IMPROVING RESERVOIR CHARACTERISATION AND SIMULATION USING NEAR-WELLBORE UPSCALING

VISWASANTHI CHANDRA

Submitted for the degree of Doctor of Philosophy

Institute of Petroleum Engineering

Heriot-Watt University

July 2014

Dedicated to my wonderful family

ABSTRACT

In this thesis, novel workflows involving high resolution near-wellbore modelling (NWM) are illustrated, which allow integration of multi-scale geological and petrophysical data from highly heterogeneous reservoirs in field-scale reservoir simulations. When applied to a clastic reservoir with high variance at small scale, NWM significantly improved reservoir characterisation and calibration of reservoir model with well test data. Results show that using NWM tools for reservoir modelling yields more precise flow calculations and improves our fundamental understanding of the interactions between the reservoir and the wellbore.

Furthermore, this thesis employs an integrated NWM workflow to identify and evaluate the geological heterogeneities that enhanced reservoir permeability in a giant carbonate reservoir with a long production history. Key among these heterogeneities are mechanically weak zones of solution-enhanced porosity, leached stylolites and associated tension gashes, which were developed during late stage diagenetic corrosion. The results of this investigation confirmed the critical role of diagenetic corrosion in enhancing the permeability of the reservoir. One of the key aims of this thesis is to develop a novel near-wellbore upscaling (NWU) workflow that addresses the challenges associated with conventional carbonate modelling workflows. The NWU workflow developed in this thesis provides a systematic geostatistical approach to obtain more realistic representation of the above multi-scale geological-petrophysical heterogeneities in the reservoir simulation model of the carbonate field. The NWU results were used to generate global porosity-permeability and vertical-horizontal permeability relationships for reservoir simulation. Instead of applying artificial permeability multipliers that do not necessarily capture the impacts of geological heterogeneities, the NWU workflow incorporates representations of fine-scale heterogeneities in the reservoir simulation model.

Another aim of this thesis is to develop a new near-wellbore rock-typing and upscaling approach to improve the integration of reservoir rock-typing and simulation in carbonate reservoirs. The rock-typing and upscaling methodology described in this work involves the geological-petrophysical classification of the reservoir heterogeneities through systematic evaluation of the key diagenetic events, including the key associations between the depositional and diagenetic features, and their impact

on reservoir flow properties. The near-wellbore rock-typing and upscaling workflow yielded consistent initialisation of the reservoir simulation model and therefore improved the calculation of volumes of fluids-in-place. Subsequently, the cumulative production curves computed by the reservoir simulation model agreed well with the historic production data. The revised simulation model is now much better constrained to the reservoir geology and provides an improved geological-prior for history matching. This thesis therefore provides valuable insights to the means by which a geologically consistent field-level history match can be achieved for complex carbonate reservoirs.

PUBLICATIONS

This thesis contains excerpts from the following papers:

- **Chandra, V.,** Barnett, A., Corbett, P.W.M., Geiger, S., Wright, P., Steele, R. & Milroy, P. Effective integration of reservoir rock-typing and simulation using near-wellbore upscaling. *Marine & Petroleum Geology*, in review.
- **Chandra, V.,** Wright, P., Barnett, A., Steele, R., Milroy, P., Corbett, P.W.M., Geiger, S., & Mangione, A. 2014. Evaluating the impact of a late-burial corrosion model on reservoir permeability and performance in a mature carbonate field using near-wellbore upscaling. SP406 *Fundamental Controls on Fluid Flow in Carbonates: Current Workflows to Emerging Technologies*, Geological Society of London Special Publications, **406**, first published June 23, 2014, doi:10.1144/SP406.11.
- **Chandra, V.,** Barnett, A., Wright, R., Geiger, S., Corbett, P.W.M., Steele, R. & Milroy, P. 2014. Novel near wellbore rock-typing and upscaling workflow to improve reservoir characterisation and modelling of carbonates. Oral presentation at 76th EAGE Conference & Exhibition, Amsterdam, SID.21329, Th-E103-07, 19 June 2014.
- **Chandra, V.,** Geiger, S., Corbett, P.W.M., Steele, R., Milroy, P., Barnett, A. & Wright, P. 2013. Using near wellbore upscaling to improve reservoir characterisation and simulation in highly heterogeneous carbonate reservoirs. Reservoir Characterization and Simulation Conference 2013 Abu Dhabi, SPE Paper 166033, September 2013.
- **Chandra, V.,** Steele, R., Milroy, P., Corbett, P.W.M., & Geiger, S. Using near wellbore modelling and dynamic calibration to improve permeability modelling in a giant carbonate field. 2013. Oral presentation at 75th EAGE Conference & Exhibition incorporating SPE EUROPEC, London, Tu-14-15, June 2013.
- Oates, M., & **Chandra, V.,** evaluating the role of meteoric karst vs. burial corrosion in an offshore Indian carbonate field. 2013. AAPG Search and Discovery Article #90163©2013AAPG, AAPG Annual Convention and Exhibition, Pittsburgh, Pennsylvania, May 19-22, 2013.
- **Chandra, V.,** Hamdi, H., Corbett, P.W.M., & Geiger, S. 2013. Improving Reservoir Characterisation and Simulation with Near Wellbore Modeling. *SPE*

Reservoir Evaluation & Engineering, **16** (2), 183-193, SPE-148104-PA, May 2013.

- **Chandra, V.,** Hamdi, H., Corbett, P.W.M., & Geiger, S. 2011. Improving reservoir characterisation and simulation with near wellbore modeling. Reservoir Characterization and Simulation Conference 2011, Abu Dhabi, SPE Paper 148104, October 2011.

Try not to become a man of success, but
rather try to become a man of value.
- Albert Einstein

ACKNOWLEDGEMENTS

First of all, I would like to express my deepest gratitude to Prof. Sebastian Geiger and Prof. Patrick Corbett for giving me the opportunity to do this PhD project. This thesis would n't have been possible without your continued support, constructive criticism and encouragement. I could not have asked for two better supervisors, thank you both for giving me ample freedom and control, while not hesitating to wear the 'supervisor hat' when needed, throughout this most heterogeneous and exhilarating journey! I would like to thank Foundation CMG for funding my PhD project through Sebastian's chair. I would like to convey my thanks to Prof. Susan Agar and Dr. Karl Stephen for agreeing to be my external and internal examiners, respectively.

I am grateful to Paul Milroy for giving me the internship opportunity at BG Group which laid the foundation for Part II of this thesis. Many thanks go to the field asset team at BG Group for providing the field data and internal reports. I would like to acknowledge, with thanks, all those at BG Group who have supported my project; special thanks go to Richard Steele for co-supervising my internship at TVP. Thank you Richard, for keeping me in loop with the reservoir management reviews and for the much needed approvals without which I could not have published the papers that are based on the BG field data. I want to thank Andrew Barnett, Paul Wright and Michael Oates for the intriguing geological discussions and technical contributions. I would also like to thank Alex Assaf, Zoe Watt, Ferney Moreno, Raheel Baig and Abdul Olanurosa for the fruitful discussions in reservoir engineering.

I am thankful to the staff of Institute of Petroleum Engineering, especially the Computer Support team for their wonderful support throughout my PhD. I would like to acknowledge, with thanks, ICCR for 'adopting' me, and providing me the opportunity to present my research in their meetings from time to time. I want to thank Hamidreza Hamdi for the engaging well testing discussions and his contribution to the SPE REE publication. I would also like to thank Eric Mackay, Helen Lewis, Obinna Chudi and Zeyun Jiang for the technical discussions that contributed to this thesis. I am grateful to

Computer Modelling Group for providing access to the CMG reservoir modelling and simulation software suit. I am thankful to the Geomodeling Corporation for providing access to SBED^{TM} and the Geomodeling team, especially Les Dabek and Rex Knepp, for the technical support they have provided. I would also like to acknowledge Schlumberger for providing access to Petrel and Eclipse, Weatherford for PanSystem and Kappa for Saphir.

I would like to thank my colleagues in the Carbonate Research group for being such fantastic officemates and friends all through these years. We have shared many joyful moments and great coffee times together. I will forever cherish those memories. In no particular order, Karen, Claudia, Yan, Robert, Adnan and Christine, thank you so much for warmly welcoming me into the office at the beginning of my PhD. Mohamed, Simeon, Chen, Alessandro and Qing, thank you for the wonderful support throughout these years. Yan and Karen, thank you for all the motivating conversations. Adnan, Mohamed and Robert, I truly appreciate how humble you are; thank you for the many pep talks. Mohamed, thank you for all the Eclipse and Petrel RE discussions. Claudia and Christine, thanks for sharing the 'Mathematicians' perspectives' where needed, and the many cakes you baked for the office. Simeon, thank you for your helpful insights on the CMG software and reservoir simulation. Alessandro, thank you for all the many extensive discussions on carbonate geology, especially about H-Field and G-Field.

I can't thank my family enough for the love and moral support they have given me throughout my PhD. Bernd, thank you for being the most wonderful partner, and for being by my side every step of my PhD journey! I dedicate this work to you and our family.

Edinburgh, July 2014

ACADEMIC REGISTRY
Research Thesis Submission

Name*:*	Viswasanthi Chandra		
School/PGI:	IPE		
Version: *(i.e. First, Resubmission, Final)*	Final	Degree Sought (Award **and** Subject area)	PhD in Petroleum Engineering

Declaration

In accordance with the appropriate regulations I hereby submit my thesis and I declare that:

1) the thesis embodies the results of my own work and has been composed by myself
2) where appropriate, I have made acknowledgement of the work of others and have made reference to work carried out in collaboration with other persons
3) the thesis is the correct version of the thesis for submission and is the same version as any electronic versions submitted*.
4) my thesis for the award referred to, deposited in the Heriot-Watt University Library, should be made available for loan or photocopying and be available via the Institutional Repository, subject to such conditions as the Librarian may require
5) I understand that as a student of the University I am required to abide by the Regulations of the University and to conform to its discipline.

* *Please note that it is the responsibility of the candidate to ensure that the correct version of the thesis is submitted.*

Signature of Candidate*:*		Date:	

Submission

Submitted By *(name in capitals):*	
Signature of Individual Submitting:	
Date Submitted:	

For Completion in the Student Service Centre (SSC)

Received in the SSC by *(name in capitals):*			
Method of Submission *(Handed in to SSC; posted through internal/external mail):*			
E-thesis Submitted (mandatory for final theses)			
Signature:		Date:	

CONTENTS

LIST OF FIGURES

LIST OF TABLES

LIST OF ABBREVIATIONS

ETR Early time region

FMI Formation micro-imaging

FWBS Fake wellbore storage

FZI Flow zone indicator

K_g Geometric average permeability

K_h Horizontal permeability

K_r Relative permeability

K_v Vertical permeability

LGR Local grid refinement

LTR Later time region

MICP Mercury Injection Capillary Pressure

MSCF Thousand Standard Cubic Feet

MTR Middle time region

NWM Near-wellbore model

P_c Capillary pressure

RCA Routine Core Analysis

SCAL Special Core Analysis

S Skin factor

SDV Standard Deviation

SGS Sequential Gaussian simulation

SIS Sequential indicator simulation

STB Stock Tank Barrels

TVDSS True Vertical Depth Sub-Sea

Chapter 1. INTRODUCTION

1.1. Preamble

Accurate simulation of fluid flow is essential to optimise hydrocarbon recovery as part of reservoir development and resource management. Performance predictions of reservoir simulation are sensitive to a number of parameters including, but not limited to, permeability, horizontal-vertical permeability anisotropy, relative permeability, and wettability, which can be difficult to constrain in heterogeneous reservoirs. These parameters are in turn controlled by geological systems in the subsurface (e.g., Weber 1982; Haldorsen 1986; Hurst 1993; Lucia 1999; Akbar *et al.* 2001; Nordahl 2004; Ringrose 2005). Data related to the variability of geological systems in a hydrocarbon reservoir are acquired over several orders of magnitude in scale, ranging from centimetre scale core plug data to kilometre-scale seismic data (e.g., Ringrose *et al*. 2008). This variability complicates the process of reservoir modelling and simulation because it involves several stages of upscaling, downscaling, and averaging of the measurements at various scales. The averaging and re-scaling of geological data raises questions about the representativeness of a reservoir model and its calibration with dynamic data (e.g., Brandsæter *et al*. 2001; Corre *et al*. 2000). Reliable dynamic calibration of reservoir models is hence very challenging for heterogeneous reservoirs containing centimetre to decimetre scale geological features formed by depositional and diagenetic processes. Therefore, new reservoir characterisation methods are needed to integrate multi-scale reservoir data and modelling workflows seamlessly. This thesis demonstrates how such techniques can be developed using high resolution near-wellbore modelling (NWM) tools in novel ways to improve reservoir characterisation and simulation. In this thesis, near-wellbore modelling refers to high resolution numerical representation of subsurface in the vicinity of the wellbore based on the geological and geophysical information obtained from the wellbore data. Chapter 3 presents an overview of the NWM tools used in this thesis. Hereafter, the terms *near-wellbore modelling* is referred to as NWM and *near-wellbore upscaling* as NWU.

The data sets used in this thesis come from clastic and carbonate data from two producing reservoirs, Field A and Field X. Field A is a heterogeneous clastic reservoir of braided fluvial depositional environment. Chapter 4 presents a novel NWM workflow adopted to improve the calibration of the reservoir model of Field A with well

test data. Field X is a giant offshore carbonate field comprising a limestone reservoir with a complex diagenetic history. The geological background and challenges associated with the reservoir simulation model of Field X are presented in Chapter 5. Modelling and simulating fluid flow is generally much more complicated in carbonate reservoirs than in clastic reservoirs due to the intrinsic depositional and diagenetic heterogeneities that occur in the former at a broad range of scales of observation and measurement. Several authors have reviewed the dominant challenges in carbonate reservoir characterisation which result from high variability of rock properties associated with geological processes (e.g., Lucia 1999; Akbar *et al.* 2001; Cerepi *et al.* 2003; Burchette 2012). Carbonate depositional environments typically cause a variety of porosity types with variable degrees of connectivity, thus yielding complex and irregular pore networks. Diagenetic processes are often key controls on the development of reservoir properties in carbonate rocks owing to the high susceptibility of carbonate minerals to chemical effects of various fluids migrating through them during syn- and post-depositional life times. The heterogeneities produced by diagenesis can significantly affect the measurement and interpretation of reservoir properties through conventional petrophysical analysis, leading to high uncertainty in the estimation of reservoir parameters. The extensive multi-scale geological and petrophysical variability inherent to carbonate reservoirs is difficult to represent in the reservoir simulation model.

Permeability has been identified as one of the biggest uncertainties associated with the reservoir simulation model of Field X during field optimisation studies that were carried out by the operator. A reduction in the uncertainties for the permeability distribution is needed to evaluate the feasibility of the next development phase. Geological studies carried out in Field X suggested that the key permeability pathways are strongly related to the mechanism of reservoir porosity and permeability evolution during late-burial corrosion (Wright & Barnett 2011). Late-burial corrosion in this thesis is referred to as deep burial/mesogenetic corrosion associated with the corrosion of limestone by burial-derived (hypogene) fluids and is considered the most critical diagenetic phase that occurred in Field X. However, it is unclear how a diagenetic model that accounts for late-burial corrosion should be included in the reservoir simulation model and how such an updated reservoir simulation model could impact production forecasting. These issues are addressed in Chapter 6 of this thesis through a systematic re-evaluation of the

reservoir simulation model of Field X, considering, in particular, the field's diagenetic history.

Estimating and upscaling permeability from the available well log and core data to obtain appropriate input permeability in the geomodel or simulation grid block scale persists to be a major concern in carbonate reservoirs such as Field X. This is because, there is no reliable direct measurement of permeability in the subsurface and the resolution of the measurements used is generally inadequate to describe the small-scale variability that influence on the flow properties (e.g., Nordahl 2004). Routine averaging methods of upscaling such as 'log-blocking' or simple averaging are ineffective in most cases, since permeability and permeability anisotropy are highly scale-dependent (Bear 1972; Elfenbein *et al*. 2005; Nordahl *et al*. 2005). Conventional geostatistical methods that are based on the idea that average petrophysical properties of a reservoir can be defined for representative elementary volume (REV) are not readily applicable to carbonate reservoirs either, due to the high extremes of multi-scale heterogeneities associated with depositional and diagenetic events in the reservoir (Deutsch 2010). Deutsch (2010) has referred to this scale as the missing scale between core plugs and well logs. Chapter 7 illustrates a novel near-wellbore upscaling (NWU) workflow which can address the above issues in Field X and provide more accurate estimates of upscaled permeability values to be input into reservoir simulation.

The performance predictions of the reservoir simulation model of Field X were found to be highly sensitive to the volumes of fluids initially-in-place and the critical oil saturation, in addition to permeability. The extensive modifications applied to water-oil relative permeability endpoints and local initial saturation in the reservoir simulation model suggested that these parameters required better characterisation. In order to revise these parameters with considerations to the proposed late-burial corrosion model (Wright & Barnett 2011), it is essential to obtain a fit-for-purpose rock-typing scheme for Field X that adequately incorporated the late-burial corrosion heterogeneities. However, it is highly challenging to obtain such a fit-for-purpose rock-typing scheme that adequately represents the influence of diagenetic processes on the reservoir petrophysical properties. This is a classic issue for carbonate reservoirs, which typically contain multi-scale and multi-modal pore types that are difficult to be adequately incorporated into rock-typing (e.g., Hollis *et al*. 2010; van der Land *et al*. 2013; Skalinski & Kenter 2014). Another common challenge is to integrate the dynamic data

during rock-typing and upscale the petrophysical properties of the rock types to the reservoir model scale using appropriate geostatistical tools to correctly initiate the reservoir simulation model. Chapter 8 addresses these issues through an integrated near-wellbore rock-typing and upscaling approach and demonstrates how this approach improves reservoir characterisation and simulation in Field X.

Numerous earlier workers such as Wen *et al*. 1998, Nordahl 2004, Ringrose 2005, Ringrose *et al*. 2008, have developed and used near-wellbore modelling techniques to address the multi-scale modelling and upscaling challenges associated with heterogeneous reservoirs. The workflow presented in Part I of this thesis is different from earlier works in that the near-wellbore model generated along the wellbore can be directly integrated into the reservoir scale simulation model without further upscaling, thus retaining as much geological and petrophysical detail as possible in the simulation model. The novel aspect of using the NWU tools in Part II is that the workflow enables the explicit representation of typical carbonate heterogeneities such as leaching, stylolites and associated small-scale fractures, which improved the permeability model and eventually fostered more realistic representation of these features in the simulation model. Another novel aspect of Part II is that the NWM tools were applied to enhance the coupling of rock-typing and reservoir simulation, thus aiding seamless integration of multi-scale and multi-disciplinary data for improved reservoir simulation. The NWU workflow formulated in Part II hence increased the scope of application of NWM tools further for carbonate reservoirs.

1.2. Objectives and aims

The overarching aim of this thesis is to develop novel workflows using NWM and NWU tools to improve reservoir characterisation and simulation in highly heterogeneous hydrocarbon reservoirs. The specific objectives of this thesis with respect to the field data used are:

Field A:

- Use NWM to incorporate centimetre to decimetre scale high-permeability features in the reservoir simulation model of Field A.
- Develop a novel workflow involving high resolution NWM to improve the calibration of the reservoir simulation model of Field A with well test data.

Field X:

- Address the uncertainty associated with permeability by understanding the fundamental controls on fluid flow that need to be adequately captured in the reservoir simulation model of Field X.
- Use NWM tools in conjunction with historic production data to understand the impact of late-burial corrosion heterogeneities on horizontal and vertical permeability in Field X.
- Analyse the sensitivity of simulated cumulative production profiles to several model scenarios that incorporated the modified permeability distributions based on Lucia's (1986) porosity-permeability transforms.
- Derive new global permeability transforms for Field X using only NWU tools.
- Resolve the uncertainty related to modelling and upscaling horizontal permeability, K_h, and permeability anisotropy ratio, K_v/K_h, in Field X using NWU tools.
- Compare the uncertainty analysis results between the original history matched model and the simulation model that employed new permeability transforms derived from NWU.
- Revise the full field geomodel of Field X with consideration to the late-burial corrosion heterogeneities to obtain a properly initialised reservoir simulation model with consistent static and dynamic reservoir properties.
- Address the uncertainties associated with volumes of fluids initially-in-place and the critical oil saturation in Field X in addition to permeability by obtaining a fit-for-purpose rock-typing scheme that adequately incorporates the late-burial corrosion heterogeneities.
- Develop a novel near-wellbore rock-typing and upscaling workflow that consistently integrates static and dynamic reservoir simulation parameters and thus provide improved geological prior for history matching of Field X.

The following section describes the structure of the thesis.

1.3. Structure of the thesis

This thesis comprises nine chapters in addition to the appendix. The chapters in this thesis are divided into three main sections; i) Theoretical background, ii) Part I and iii) Part II. Part I presents how a novel NWM workflow is applied to Field A to improve the

calibration of reservoir model with well test data. The chapters of Part II present the NWU workflows developed to address the reservoir characterisation and simulation challenges in Field X with the aid of historic production data.

Theoretical background

- Chapter 2 presents an overview of the fundamental reservoir characterisation and simulation concepts that are relevant to this thesis. Due to the cross-disciplinary nature of this thesis, it is considered important to review some topics comprehensively for the benefit of readers with multi-disciplinary backgrounds. Furthermore, these detailed sections are convenient to refer to later in the subsequent chapters.
- Chapter 3 provides the definition of near-wellbore model and introduces the NWM tool, SBED^{TM}, used in this thesis. This chapter reviews the modelling concepts used by SBED^{TM} and presents a preface to the NWU workflows used in this thesis.

Part I

- Chapter 4 illustrates a novel workflow involving high resolution NWM to improve the calibration of the reservoir simulation model of Field A with well test data. The reservoir simulation model of Field A was incorporated with high resolution near-wellbore models representative of the key geological heterogeneities in the studied well. Subsequently, the numerically simulated pressure transient response compared well to actual well test data.

Part II

- Chapter 5 provides an overview of the geology of Field X before detailing the available dataset. The major uncertainties associated with the field's geomodel and reservoir simulation model are discussed.
- Chapter 6 first describes the multi-scale geological and petrophysical heterogeneities caused by late-burial corrosion in Field X. Then a new small-scale and high-resolution reservoir modelling approach, which is based on NWU results, is discussed. The simulated cumulative fluid production profiles of several model scenarios that incorporate new permeability distributions

corroborated that the late-burial corrosion heterogeneities in Field X have significant impact on reservoir flow performance.

- Chapter 7 focuses on resolving the uncertainty related to modelling and upscaling horizontal permeability, K_h, and permeability anisotropy ratio, K_v/K_h, in carbonate reservoirs. A novel NWM workflow is developed to obtain more realistic horizontal permeability, K_h, and permeability anisotropy ratio, K_v/K_h, distributions in the reservoir model. This workflow is demonstrated on Field X, to improve permeability modelling and obtain simulation model that is much better suited for production forecast.
- Chapter 8 describes how a novel near-wellbore rock-typing and upscaling workflow is developed for Field X to obtain a properly initialised reservoir simulation model with consistent static and dynamic reservoir properties which incorporate the late-burial corrosion heterogeneities. The prime objective of the work presented in this chapter is to obtain a new simulation model which is well constrained to the reservoir geology and provide an improved geological-prior for history matching.

Finally, Chapter 9 summarises the main results and conclusions derived from the previous chapters before providing recommendations for future work.

Chapter 2. BACKGROUND

This chapter provides an overview of some key reservoir characterisation and simulation issues as a means of introducing the fundamental concepts, ideas and terminology used throughout this thesis. First, a brief discussion of the geological processes and porosity types occurring in carbonate reservoirs is presented. A review of the various methods of characterising permeability of reservoir rocks is then provided, including the key issues related to permeability upscaling and cross-scaling. Finally, a brief review of present day geomodelling methods, laying emphasis in the modelling concepts used in this thesis, is presented. It must be noted that some sections in this chapter are deliberately detailed in order to facilitate readers with diverse backgrounds to be acquainted with the terminology and assumptions used in this thesis.

2.1. Carbonate reservoirs: Review of key geological processes

A major portion of this thesis constitutes the work presented in Part II, which is to address the modelling and simulation challenges of the carbonate reservoir Field X using near-wellbore modelling (NWM) workflows. The main motivation for including this section is hence to provide an introduction to the key terminology related to carbonate reservoirs relevant to this thesis. Other aspects such as fracturing in carbonate reservoirs are not presented as they are not relevant to this work.

2.1.1. Depositional processes

Carbonate rocks are typically formed in-situ via the growth of organisms and/or precipitation in warm, low energy, shallow marine environments with little or no siliciclastic supply, at depths upto 6000 m below sea level. The most common types of carbonates that are encountered in the subsurface are limestone ($CaCO_3$) and dolostone ($CaMg(CO_3)_2$), which are at times associated with evaporites. A limestone is defined as any sedimentary rock containing over 50% of calcium carbonate ($CaCO_3$) (Nichols 2009). Most dolomite is a product of diagenetic modification of limestone and dolostone is defined as a carbonate containing over 75% of dolomite (Machel 2003). The depositional settings of carbonate deposition can be divided into five broad groups recognised on the basis of their morphology; i) shelf (rimmed), ii) ramp, iii) epeiric platform, iv) isolated platform and v) drowned platform (Figure 2.1). The carbonate field in this study, Field X, formed in a shallow ramp depositional system.

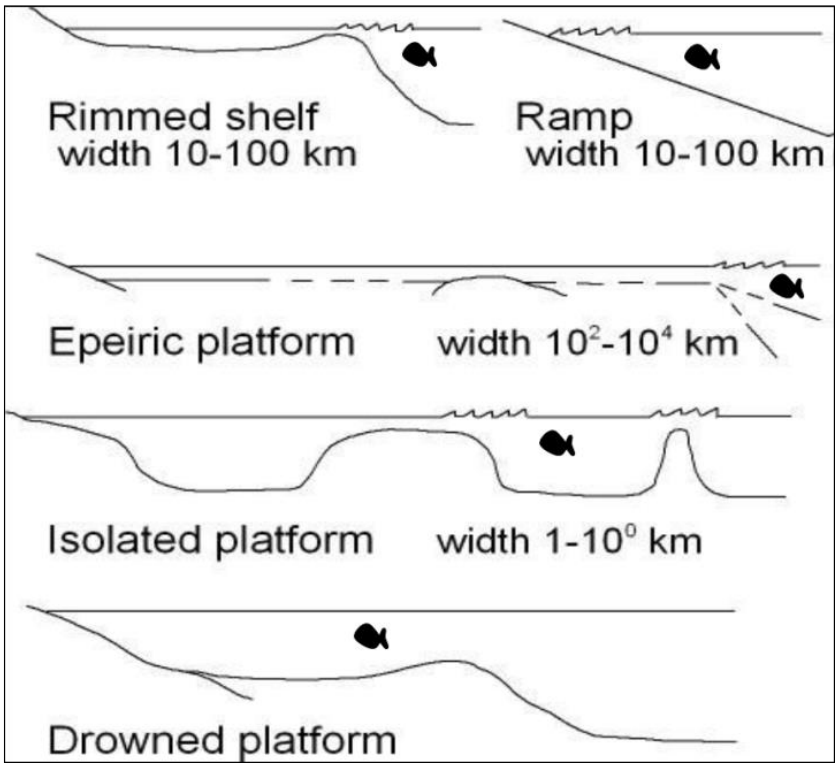

Figure 2.1. Sketches illustrating the 5 main categories of carbonate depositional settings, or platforms, i.e. rimmed shelf, ramp, epeiric platform, isolated platform and drowned platform. Modified from Tucker & Wright (1990).

Carbonate rocks are classified in numerous ways depending upon their mineralogical and/or component content and distribution. The classification scheme used in this thesis is provided by Dunham (1962), modified by Embry & Klovan (1971) (Figure 2.2). Dunham (1962) classification is the most commonly used and simplest classification for carbonate description. The Dunham (1962) classification categorises carbonate rocks in terms of being matrix- or grain-supported, crystalline, and/or biologically bound based on the fabric and nature of the matrix, grains and rock framework (Nichols 2009; Tucker & Wright 1990). According to Tucker & Wright (1990), the significance of each carbonate class in terms of energy level is relatively clear, for example the mud-supported classes (mudstone and wackestone) clearly represent low-energy environments. Embry & Klovan (1971) added the subdivision of boundstones to Dunham (1962) scheme (Figure 2.2).

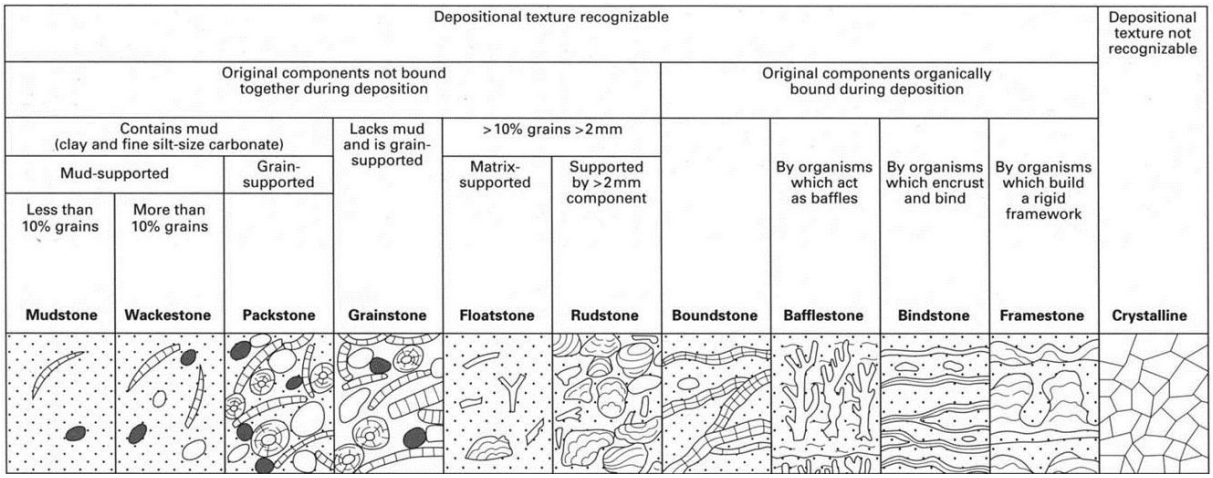

Figure 2.2. The Dunham (1962) classification of carbonate sedimentary rocks. Note that Embry & Klovan (1971) added the subdivision of boundstones to Dunham's original scheme. From Nichols (2009).

2.1.2. Diagenesis of carbonate rocks

The term diagenesis is used to describe the post-depositional processes that cause physical and chemical modifications to deposited material (Milliken 2003). The final fabric of a sedimentary rock is governed by both, depositional and the subsequent diagenetic processes. The diagenesis of carbonate sediments is significantly different from clastics due to the contrast in their prevailing chemistry and minerals. Carbonates are more readily soluble in water and are often highly susceptible to the chemical effects of various fluids migrating through them during syn- and post-depositional life times. The diagenetic alteration of carbonate rocks is commonly due to compaction and pressure solution, precipitation and re-crystallisation of cements, dolomitisation and dissolution.

Choquette & Pray (1970) have proposed one of the most popular classification schemes of diagenetic processes, which divides diagenetic regimes in carbonates into three stages; i) eogenesis, ii) mesogenesis, and iii) telogenesis. Eogenesis is the earliest stage of diagenesis. The post-depositional processes occurring during eogenesis are significantly affected by their proximity to the surface and the principal control of the reactions is the chemistry of the pore water in the sediments. Telogenesis is the stage during which long-buried rocks are affected by processes associated with uplift and erosion. Mesogenesis, also referred to as burial diagenesis, is dominated by modifications to the sediments that are buried to such depths where they are no longer dominated directly by surface processes. Massive dissolution, cavern collapse and

fracturing are among the diagenetic events that often occur in carbonate rocks in the intermediate to late burial stage. In some carbonate reservoirs such as, for example Field X, late burial (mesogenetic) dissolution can extensively modify the host rock fabric.

2.2. Stylolites and fractures

Post deposition, the contact points between mineral grains are susceptible to dissolution, typically in response to the weight of the overburden (Nichols 2009). Under high pressures, the mineral solubility increases locally at the grain contacts, typically resulting in sutured pressure solution features called stylolites (Tucker & Wright 1990; Akbar *et al*. 1995; Nichols 2009). Formation of stylolites within the rock resulting from pressure solution of calcite is a common phenomenon in the early to intermediate burial stage of carbonates. The process of pressure solution is generally associated with the removal of huge amounts of calcium carbonate and the concentration of residual clay components such as nodules or wispy clay seams. Figure 2.3 shows examples of stylolites observed in Field X.

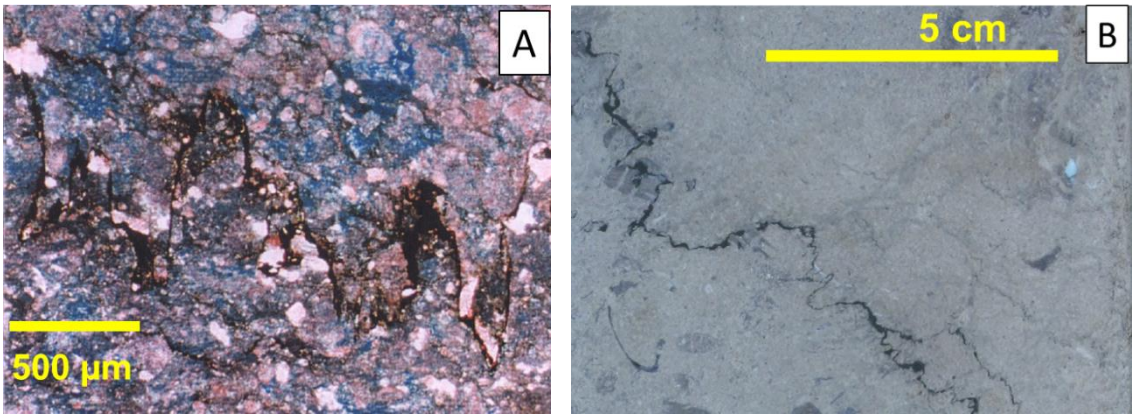

Figure 2.3. (a) Photomicrograph of stylolite in a limestone matrix in Field X. Blue resin indicates porosity. (b) Stylolite observed on the core from one of the wells of Field X. Note that the well is highly deviated and the stylolite is parallel to the bedding plane.

2.2.1. Structural aspects of stylolites

There is an extensive amount of literature available on the formation, distribution, propagation and scaling relationships of stylolites (e.g., Goldman 1940; Glover 1968; Kaplan 1976; Braithwaite 1989; Drummond & Sexton 1998; Peacock & Azzam 2006; Aharanov & Katsman 2009 and Koehn *et al*. 2012). The geometry of the stylolites is essentially controlled by the fabric and morphology of the matrix grains. Fletcher & Pollard (1981) have observed that the amplitudes of stylolites are largest in the middle

and taper off towards the tips. It has been shown that stylolites are often localised and laterally extensive, rough-walled, non-planar surfaces that are remnants of self-localised pressure solution (e.g., Fletcher & Pollard 1981; Peacock & Azzam 2006; Ebner *et al*. 2010; Koehn *et al*. 2012).

The distribution and spacing of stylolites varies from a few centimetres to several meters (Wilson & Evans 2002). Several authors have attempted to account for the topography of stylolites (e.g., Bayly 1986; Gal *et al*. 1998; Renard *et al*. 2004). Renard *et al* (2004) have studied sedimentary stylolites in limestone that can be separated to reveal the delicate three-dimensional geometry of their two sides. Figure 2.4 shows the roughness of the stylolite surfaces in 3D at various scales in the limestone samples studied by Renard *et al* (2004). Numerous studies have shown that stylolites are fractal surfaces whose geometry exhibits long-range correlation (e.g., Aharonov & Rothman 1996; Karcz & Scholz 2003). These studies suggest that due to the fractal geometry of stylolites, the dissolution and precipitation at one point along the stylolite impacts dissolution and precipitation at other points This aspect of stylolites is reflected by the collective behaviour of an ensemble of stylolites in a rock which tend to anastomose and cut across each other (Renard *et al*. 2004; Aharanov *et al*. 2014).

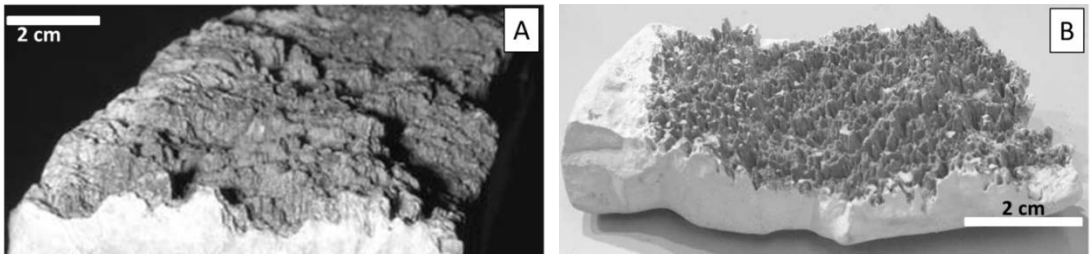

Figure 2.4. Examples of stylolites at different scales in limestones showing the variety of morphologies and amplitudes. (a) Sample with a roughness of up to 2 millimetres. (b) Sample with a roughness of up to 5 millimetres. Modified from Renard *et al*. (2004).

2.2.2. Stylolite associated fractures

The term fracture refers to any kind of brittle failure. Stylolites are often associated with wedge-shaped fractures that are considered to be Mode I type based on Kulander *et al*.'s (1979) classification of fractures. The term Mode I fracture means that the walls moved perpendicularly away from the fracture plane when the fracture formed. Several authors have postulated the theory behind the possible mechanisms of formation of stylolite-related fractures (e.g., Nelson 1981; Eren 2005; Karcz *et al*. 2011). Nelson (1981)

supports the conclusion that the coexistence of wedge-shaped fractures (tension gashes) with stylolites indicates that fracturing and stylolite formation were contemporaneous. Eren (2005) pointed out that the axes of stylolite-related fractures are parallel to the maximum stress direction, which is perpendicular to bedding parallel stylolite (e.g., Figure 2.5a). Figure 2.5b shows the general geometric relationships observed among stylolites and fractures relating to paleostress orientations proposed by Nelson (1981).

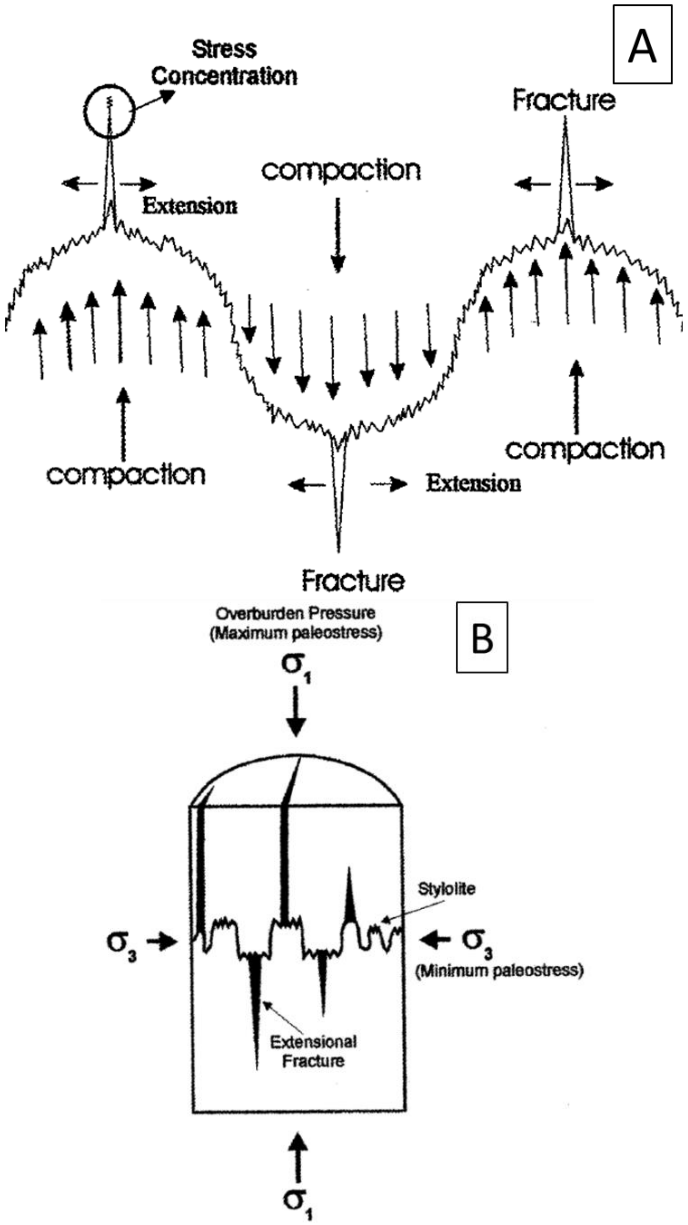

Figure 2.5. (a) Illustration of the conceptual model of the geometry of a stylolite and its effect on an occurrence of a wedge-shaped fracture. The fractures are located at crestal areas of a wave-form. From Eren, (2005). (b) A schematic diagram illustrating general geometric relationships observed between stylolites and fractures, relating to paleostress orientations. From Nelson (1981).

2.2.3. Impact of stylolites on porosity and permeability

Depending on whether the porosity of the infill material is less or more compared to the surrounding matrix, stylolites will act as either permeability barriers or pathways, respectively (Braithwaite 1989). The various porosity types associated with stylolites in carbonate reservoirs have been reviewed by Dawson (1988). The prevalent views about stylolites are that they are permeability barriers and that the porosity decreases towards the stylolites. Several case studies indeed support this theory by indicating a reduction of porosity and permeability in the matrix around the stylolites, resulting in the stylolite acting as a permeability barrier (e.g., Koepnick 1984; Burgess & Peter 1985; Thomas *et al*. 1999; Heydari 2000; Ghafoori *et al*. 2008). However, there are also many cases recorded in literature which have shown that stylolites can act as conduits to fluid flow and increase in porosity is observed around the stylolites, resulting from much more complicated diagenetic history (e.g., Mazullo & Harris 1991; Esteban & Taberner 2002; Zampetti *et al*. 2005). The carbonate field, Field X, used in this thesis is a good example of stylolites acting as permeability enhancers and will be extensively discussed in the chapters of Part II.

2.3. Secondary porosity in carbonates

Secondary porosity is defined as the porosity created in the subsurface post deposition. Primary porosity commonly consists of small-scale pore types such as matrix and intergranular porosity resulting from original deposition, whereas secondary porosity includes larger-scale porosity types such as vuggy and moldic porosity, and fractures. Many case studies have demonstrated that secondary porosity is one of the main controls of fluid flow in carbonate reservoirs (e.g., Ghafoori *et al*. 2008). Early secondary porosity is produced by meteoric (eogenetic) diagenesis, whereas late secondary porosity is formed during deep burial mesogenetic conditions by corrosive diagenetic fluids of diverse nature (e.g., Esteban *et al*. 2002, 2003; Mazzullo & Harris 1991; Sattler *et al*. 2004). Sattler *et al*. (2004) note that a close relationship is observed between the depositional environment, early diagenetic cementation and later burial processes. A detailed overview of the various mechanisms of porosity evolution in carbonate reservoirs can be found in Mazullo (2004).

Of the various mechanisms of secondary porosity evolution discussed by Mazullo (2004), the Mesogenetic model is of particular interest for this thesis due to its strong relevance to Field X. The organic matter in source rocks matures with burial and is

eventually converted into hydrocarbons. During this process, organic acids, carbon dioxide and hydrogen sulfide are expelled from the source rock. The gases combine with subsurface waters, producing carbonic acid and sulphuric acid, respectively (Mazullo 2004). These acids migrate laterally and vertically dissolving carbonates and creating porosity along their paths (e.g., Hanor 1987). Once the acids are spent, the fluids precipitate carbonate cements (e.g., Burruss *et al*. 1985). Mazullo (2004) notes that some visible signatures of deep burial dissolution porosity are; i) porosity along and associated with stylolites or which cuts across stylolites, ii) pores that cut across cements that contain hydrocarbon inclusions, iii) pores associated with fluorite, metal sulfides (e.g., galena and sphalerite), pyrite/mascarite and, iv) saddle dolomite (c.f. Radke 1980). Further details about recognising mesogenetic dissolution porosity are discussed by Moore & Druckman (1981), Heydari & Moore (1989), Moore (1989) and Mazzullo & Harris (1991). Chapter 5 presents the details of the late-burial (mesogeneteic) diagenesis model that has been proposed to be the key mechanism of porosity evolution in Field X.

2.4. Carbonate pore systems

It is important to have a good understanding of pore types and pore-size distributions in order to estimate the porosity and permeability of carbonates accurately (Akbar *et al*. 2001). Choquette & Pray (1970) have identified up to 15 types of porosity in carbonates based on the rock fabric and pore-space formation. Earlier work by Lucia (1983, 1995, 1999) suggests that these pore systems have different effects on the petrophysical properties. Lucia (1983) proposed that they should be grouped accordingly (e.g., Figures 2.6 and 2.7). The main porosity types in carbonates according to Lucia's (1983, 1995, 1999) classification are interparticle (intergrain and intercrystal), and vuggy porosity. Vuggy porosity is everything that is not interparticle, and includes vugs, molds and fractures. Vugs are divided into separate and touching. Lonoy (2006) further divided Lucia's interparticle classes, based on pore and grain size, and by dividing moldic pores into a micro- and macro- subgroup, to result in a total of twelve subgroups. The issues related to the estimation of correlation between porosity and permeability are discussed in further detail in a later section of this chapter.

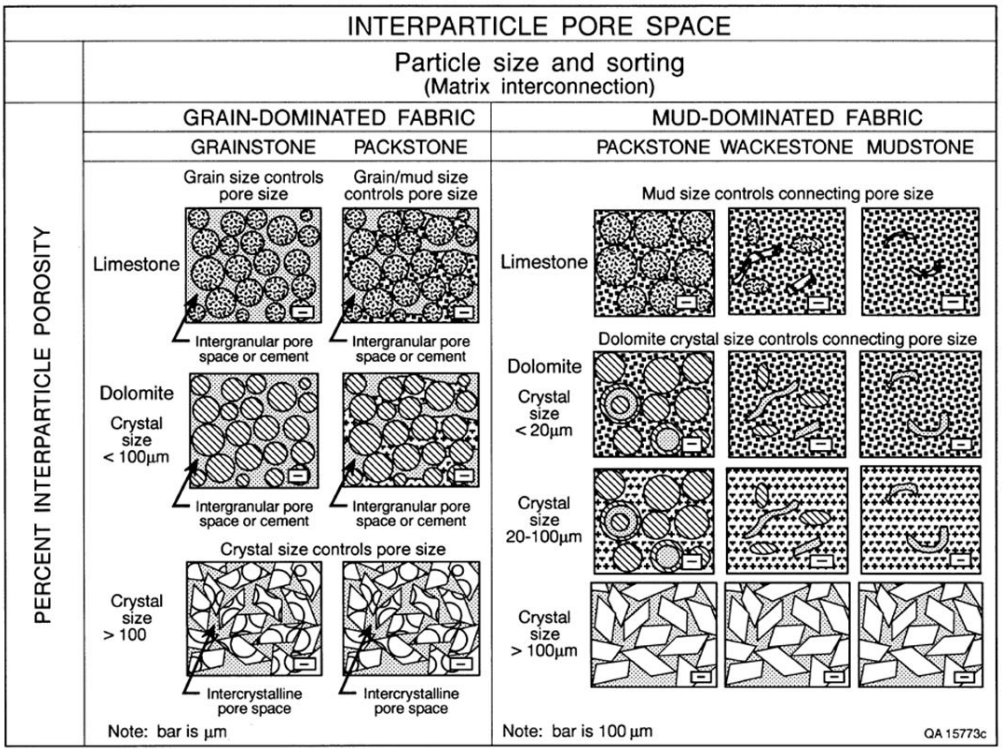

Figure 2.6. Geological and petrophysical classification of carbonate interparticle pore space proposed by Lucia (1995). From Lucia (1995).

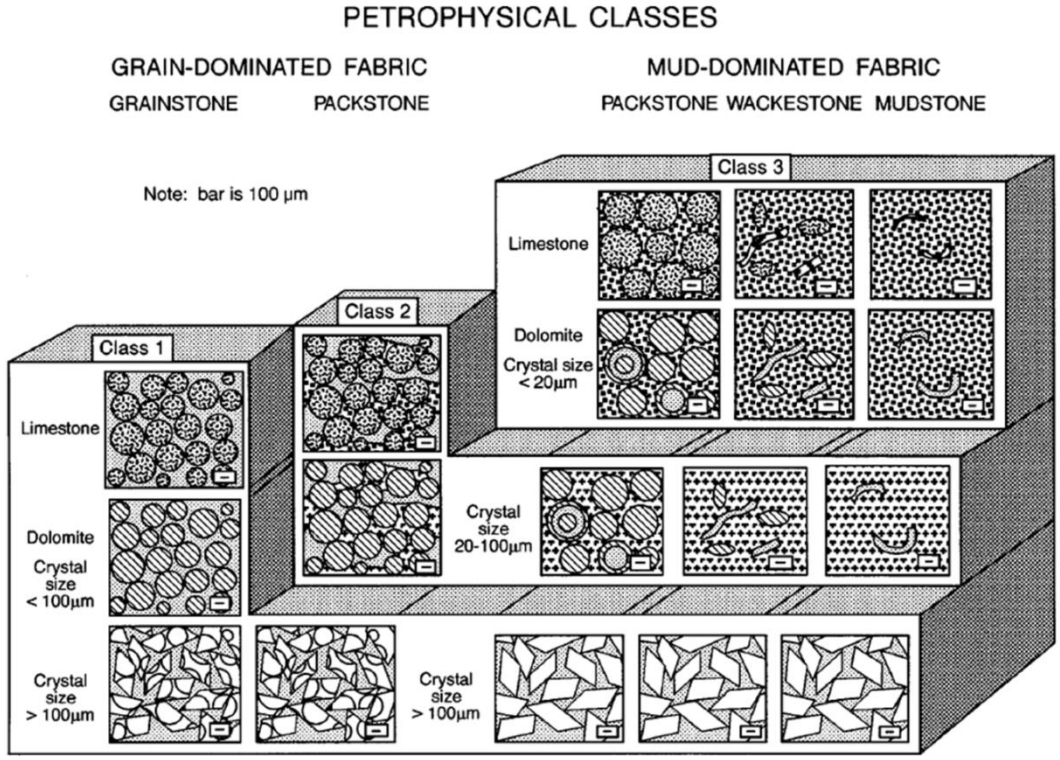

Figure 2.7. Lucia's (1995) geological and petrophysical classification of vuggy pore space, based on vug interconnection. From Lucia (1995).

2.5. Rock-typing challenges in carbonates

Rock-typing describes the process of characterising geological facies in terms of their dynamic behaviour. However, it is highly challenging to obtain a fit-for-purpose rock-typing scheme that adequately represents the influence of diagenetic processes on the reservoir petrophysical properties. This is a classic issue for carbonate reservoirs, which typically contain multi-scale and multi-modal pore types that are difficult to be adequately incorporated into rock-typing (e.g., Gomes *et al*. 2008; Hollis *et al*. 2010; van der Land *et al*. 2013; Skalinski & Kenter 2014). Another common challenge is to integrate the dynamic data during rock-typing and upscale the petrophysical properties of the rock types to the reservoir model scale using appropriate geostatistical tools to correctly initiate the reservoir simulation model. Furthermore, the difficulties of predicting reservoir quality variations at inter-well scales have long hindered the efficacy of carbonate reservoir rock-typing and simulation (Burchette 2012). These issues are addressed in Chapter 8, which presents an integrated near-wellbore rock-typing and upscaling approach and demonstrates how this approach improves reservoir characterisation and simulation of Field X.

2.6. Characterisation of reservoir permeability

2.6.1. Key controls on porosity and permeability

In order to understand the effect of geological structures on reservoir performance at the large scale, it is important to understand the fundamental controls on porosity and permeability at the pore-scale (Brayshaw *et al*. 1996). In clastic reservoirs porosity, permeability and their inter-relationship is controlled mainly by the texture and fabric of the deposited sediment. Porosity is mainly influenced by grain sorting while permeability is controlled by grain size and sorting. Corbett & Jensen (1993) have demonstrated the close association between the distribution of permeability and the sedimentary structures. The degree of anisotropy of permeability is dependent on the packing and orientation of grains (e.g., Weber 1982; Gibbons *et al*. 1993; Brayshaw *et al*. 1996). The evolution of porosity and permeability in carbonates reservoirs, on the other hand, is a much more complex issue compared to clastics. The main controls on porosity and permeability in carbonates are generally associated with the post-depositional processes that occurred in the reservoir as discussed in the earlier sections. The main challenges of characterising porosity and permeability in carbonates involve

multiple porosity systems and the presence of fractures. The following section reviews the published methods of estimating permeability in a reservoir.

2.6.2. Estimation of permeability from near-wellbore data

Permeability is a dynamic parameter and is often one of the biggest uncertainties in heterogeneous reservoirs. The most common methods of estimating permeability involve well data acquired from the near-wellbore region, i.e. core and well log data and the reservoir formation away from the well, i.e. well test data. Here, near-wellbore region means the area around the wellbore corresponding to the wireline tool resolution, which normally varies from few centimetres to few decimetres. The estimation of permeability generally involves the characterisation of relationship between pressure and fluid flow rate, in other words using variations of Darcy's law. In addition to the data mentioned above, reservoir dynamic data such as production and tracer data provide insights to the lateral connectivity of the reservoir and the horizontal and vertical permeability pathways in the reservoir scale. The following section provides a brief review of estimating permeability using the near-wellbore data.

i) Core plug analysis

Routine Core Analysis (RCA) of horizontal and vertical core plugs extracted from cores is primarily used to measure permeability in the near-wellbore region. The cores drilled from the well normally vary in diameter from 10-20 cm and, as per standard industry practice, the core plugs are approximately 2.5 cm in diameter. The core plugs are normally cylindrical and are oriented relative to the borehole such that any heterogeneity or anisotropy within the formation is reflected in the measurements. Monicard (1980), Blackbourn (1990) or Torsæter and Abrahi (2003) provide elaborate overviews of the common measurements made on core. Even though the core plug data represents a direct measure of the reservoir porosity and permeability, their volume is only a fraction of the near-wellbore volume. Hence, conventional practice of retrieving core plugs at regular intervals of one or two samples per meter may not be fully representative of the reservoir variability, especially in heterogeneous carbonate reservoirs.

ii) Probe permeameter

A probe permeameter measures permeability at the millimetre scale, i.e. at the lamina scale by pressing the tip of the measuring probe against the surface of a sample while flowing gas through an aperture into the sample. When gas flow rate and pressure are judged to have reached steady-state, they are recorded and converted to air permeability through a modified version of the Darcy law (Goggin *et al*. 1988; Halvorsen & Hurst 1990). Dykstra and Parsons (1950) first detailed the technique of characterising permeability patterns using a probe permeameter. Probe permeameter measurements are readily repeatable (Hurst & Goggin 1995). As a standard procedure, probe permeameter data are collected on orthogonal grid patterns with each measurement at 1 or 2 cm intervals on the core slab. Such a measurement grid is used to ensure reliability and repeatability of the probe permeameter, and a single measurement is taken for each point on the grid. In addition, the rock samples with highly fractured areas are normally avoided to prevent gas slippage effects.

Numerous authors have studied the applications of probe permeameter for the measurement of permeability at the lamina scale (e.g., Dreyer *et al*. 1990; Halvorsen & Hurst 1990; Corbett & Jensen 1993; Corbett 1993). An error is introduced into probe permeability measurements of heterogeneous samples with complex pore types (Corbett *et al*. 1999), but fortunately this error is only within 10% of conventional core plug analysis measurement (Goggin 1988). The close relation between permeability distribution and sedimentary structures can be shown if sample spacing is close enough, as demonstrated by Corbett & Jensen (1993) using probe permeameter. The main advantage of probe permeameter in contrast to conventional core plug method is that the measurement process is non-destructive and cheap (Halvorsen & Hurst, 1990). According to Jensen (1990), even though the accuracy of probe permeameter measurements is less than for core plugs, their greater sampling density allows for more robust correlation with wireline log data. Furthermore, the probe permeameter data can be readily correlated with image logs to identify the trend between geological structures and permeability distribution.

2.6.3. Well test analysis

Well testing is a powerful reservoir characterisation tool and provides key information on the reservoir and the well, including effective permeability, reservoir heterogeneities

and boundaries, pressure, well production potential and well geometry. The term effective permeability refers to the permeability of a large scale, statistically homogeneous medium and that is independent of the macroscopic boundary conditions. The depth of investigation of well testing tool depends on the duration of the test period and can range up to a diameter of few tens of meters around the well. There is extensive amount of literature about the principles and applications of well testing (e.g., Agarwal 1980; Ramey 1980, 1982, 1992; Gringarten 1986; Bourdet 2002). An overview of the evolution of well test analysis and interpretation techniques over the years can be found in Gringarten (2008).

i) Review of well testing concepts

During a well test, a transient pressure response is created by a temporary change in production rate (Bourdet 2002) (Figure 2.8). Reservoir parameters, including effective permeability can be estimated from the pressure derivative and other specialized plots obtained through the drawdown and build-up of reservoir pressure.

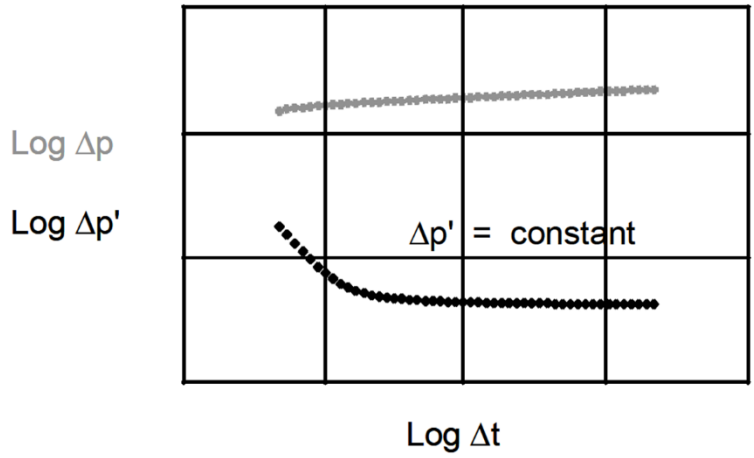

Figure 2.8. Example of derivative type-curve plot showing pressure (Δp) and pressure derivative (Δp') responses on log-log scale for well with wellbore storage and skin in a homogeneous reservoir. From Bourdet (2002).

Wellbore storage occurs in the beginning of a well test, i.e. when a well is opened, the production observed at the surface is due to the expansion of the fluid in the wellbore with negligible contribution from the reservoir. The skin factor, S, is a dimensionless parameter and characterises the well condition (e.g., Brons & Marting 1961; Ramey 1970). S has a positive value for a damaged well and a negative value when a well is stimulated. A negative skin value represents an increased surface of contact between the

well and the reservoir, for example in the case of fractures, or horizontal wells, or in an acid stimulated zone. Although reservoirs are different from each other in terms of physical description, their dynamic behaviours during well test are limited (Gringarten 2008). The dynamic behaviours of all reservoirs are obtained from the combination of three main components (Gringarten *et al*. 1979) that dominate at different times of the well test (Gringarten 2008). They are; i) Early Time Region (ETR), ii) Middle Time Region (MTR), and iii) Late Time Region (LTR). The ETR represents the near-wellbore effects at early times resulting from the well completion (e.g., Brons & Marting 1961; Ramey 1970) or high contrast in permeability distribution due to the near-wellbore geology (e.g., Corbett *et al*. 1996, 2009, 2012). The MTR is representative of the dynamic behaviour of the reservoir in the middle times of the well test and is usually the same for all the wells in a given reservoir. The LTR is representative of the boundary effects at late times and may differ from well to well in a given reservoir depending on the nature of the reservoir boundaries and the distance of the well from the boundaries.

ii) Geoengineering methods of well-testing

Geoengineering methods of well-testing (Corbett *et al*. 2009) use detailed sector-scale geological models comprising well-defined heterogeneity characteristics to numerically simulate drawdown and recovery for a wide range of parameters (Corbett *et al*. 2009, 2010; Hamdi 2012). This allows the analysis of the resulting pressure transients using standard well-testing software to correlate known geological features in the reservoir model to actual production data and well-test parameters (Figure 2.9). It must be noted that forward simulation of pressure transient data must be done cautiously such that the reservoir simulator does not add unnecessary numerical artefacts in the early time, resulting in pseudo (artefact) wellbore storage (Archer & Yildiz 2001). Standard finite-difference reservoir simulators, such as the one used in this thesis, use the Peaceman (1977) well index. The Peaceman (1977) well index is based on the solution to single-phase, steady-state, incompressible flow. However, for a pressure transient test, the assumptions of steady-state and incompressible flow are not applicable. Hence standard finite-difference reservoir simulators cannot always reproduce known pressure transient solutions due to limitations in the well index models and discretization errors caused by gridding and time stepping (Archer & Yildiz 2001). The work presented in Chapter 4 demonstrates how these issues can be mitigated by using highly refined grids around

wells and selecting time step sizes carefully during reservoir simulation to model well tests more accurately.

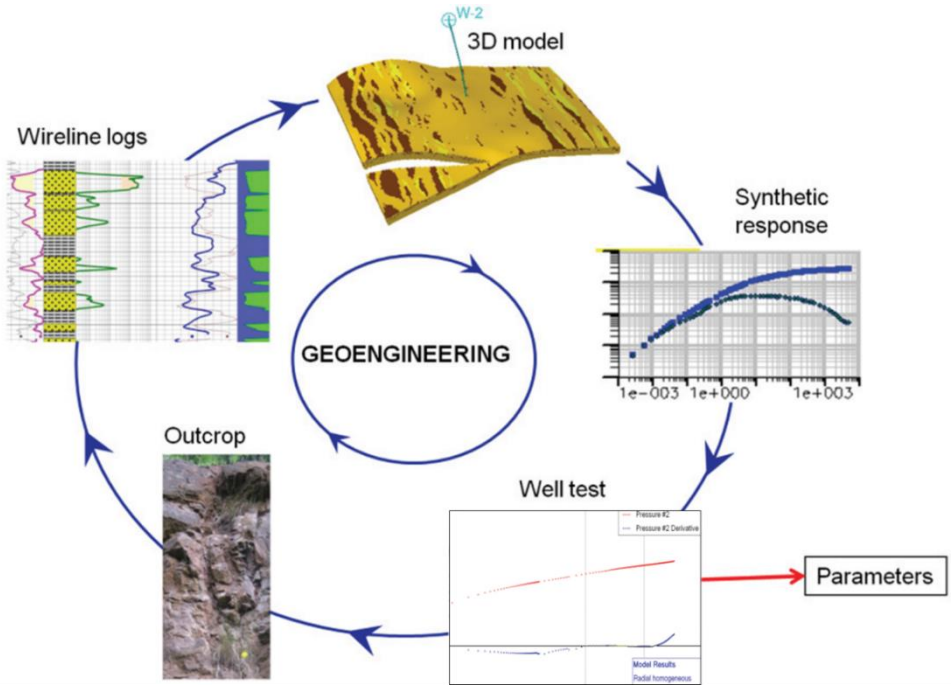

Figure 2.9. Overview of geoengineering methods of well testing. A 3D reservoir model is built based on outcrop and well log data. Pressure transients are simulated and analysed to correlate with the interpretations from real well test data. Modified from Corbett *et al*. 2010.

Overall, geoengineering workflows help to improve and validate the reservoir model. However, the question as to how to include small-scale heterogeneous geological features in large reservoir simulation models remains open. Yet their adequate incorporation is important because they can provide key flow connections or baffles and hence influence the ETR in a well-test and lead to "geoskin" (c.f. Corbett *et al*. 1996) that affects production. Geoskin represents high permeability geological features of limited lateral extent that result in well test signature similar to fractured reservoirs and show negative skin, despite the absence of any natural or induced fractures (Corbett *et al*. 1996). Geoskin thus results from a purely geological phenomenon. The NWM workflow employed in Chapter 4 extends geoengineering methods of well-testing (Corbett *et al*. 2009; 2012) using NWM with the specific aim of overcoming the challenges of incorporating small-scale geological structures into sector-scale reservoir models.

2.7. Reservoir heterogeneities vs. well data support and stationarity

In the context of geostatistics the term *support volume* refers to the volume of a sample and is related to the method of measurement. *Local stationarity* is defined as the local average and variance of a property that remains relatively constant or change gradually with location (Journel & Huijbregts 1978). Stationarity of the data is represented by gradual changes between measurements along a profile (Corbett *et al*. 1999). Koltermann & Gorelick (1996) point out that there is a conceptual difference between the volume of a sample and the characteristic length scales in the porous media. It can be observed from the discussions presented earlier in this chapter that the various methods of well data measurements used to estimate permeability represent different support volumes. Corbett (1993) demonstrates that standard industry practice of retrieving core plugs from heterogeneous reservoirs can result in sample bias issues as shown in Figure 2.10. It is difficult to sample core plugs in lithologies which are mechanically weak, for example within mud layers or highly leached carbonate rock, without breaking or splitting them. Often there is an operator bias to preferentially sample high or low permeability zones, which will induce sample bias in the permeability estimation (Nordahl 2004).

Corbett & Jensen (1992a) have found that the range of permeability values measured by the probe permeameter is wider than that of core plugs due to the smaller volume of investigation of the probe permeameter which resulted in increased number of samples. The variation of sample spacing and support volume must be done in a fit-for-purpose manner based on the geological variability and the intended use of the data (Corbett & Jensen 1992a, b). This approach is especially useful in heterogeneous carbonate reservoirs, which have high multi-scale variability of porosity and permeability. Corbett *et al*. (1999) have shown how probe permeameter can be used to assess permeability support and stationarity in a variety of carbonate pore types. Corbett *et al*. (1999) also raised the concern of sample support problems in heterogeneous carbonates and that the probe permeameter is very sensitive to the local pore geometries in vuggy pore system. The probe permeameter cannot be used quantitatively to assess permeability in such carbonate rocks but can be used as a qualitative method to map the connectivity of the vugs.

Numerous authors have discussed the scale dependency of permeability in heterogeneous reservoirs and the associated problems in reservoir simulation (e.g., Bear

1972; Jackson *et al*. 1999; Morton *et al*. 2002; Nordahl 2004). It is often difficult to bridge the scale gap between core plug permeability measurements and the permeability value interpreted from well test data. Elfenbein *et al*. (2005) compared petrophysical data with the observed variations in reservoir lithology and indicated that the core plug data do not give a realistic picture of the permeability anisotropy on the larger reservoir grid block scale. Furthermore, the scale dependency of permeability usually gives misleading results when averaged core plug permeability values are compared with the effective permeability estimated from large-scale well test. The NWM workflows presented in Part II of this thesis address the above issues by facilitating the calibration of the near-wellbore data with historic production data.

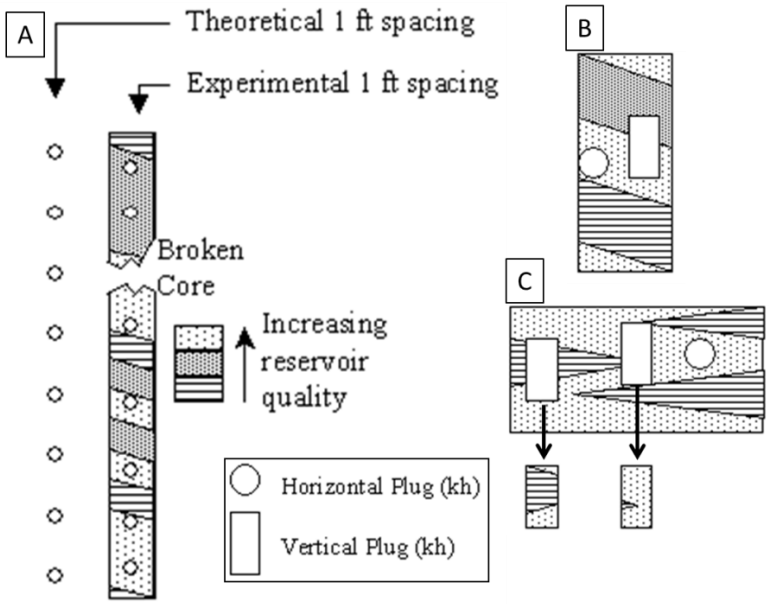

Figure 2.10. (a) Illustration of core sampling showing how sample bias may arise when using a nominal spacing of 30 cm when collecting core plugs. (b) Sample bias affects the estimation of permeability anisotropy when the vertical scale of heterogeneity is not captured by the core plugs. (c) Sample bias arising in vertical permeability depending on where the core plug is taken in relation to the representative geometry of geological heterogeneities. Modified from Corbett (1993).

2.8. Permeability upscaling and cross-scaling issues

2.8.1. Upscaling

Corbett *et al*. (1998), defined the term up-scaling as "the determination of an effective (or pseudo) property at a scale larger than that of the original measurement". As discussed in the previous sections, the sample support used for estimating permeability

using conventional near-wellbore measurement methods is normally limited to small-scale, i.e. millimetre to centimetre scale. However, the numerical model used for reservoir simulation normally employs grid-blocks that are several tens of meters wide. It is hence essential to upscale the permeability data for reservoir simulation or to be compared with well test data. Renard & Marsily (1997) provide an extensive review of the many methods proposed to calculate the effective permeability of porous media. These include effective medium theory (Dagan 1979), percolation theory (Begg & King 1985) and deterministic modelling of sedimentary structures (Corbett et al. 1992; Pickup et al. 1994, 1995; Ringrose et al. 1999; Pickup & Stephen 2000). Of these, flow-simulation-based upscaling methods are of particular interest for this thesis, and are discussed in detail in Chapter 3.

A prevalent challenge of upscaling is associated with the multistage upscaling of the flow properties obtained from well data such as core and wireline data into the reservoir simulation grid-block scale. The aspects of multistage upscaling of flow parameters from mm-scale to reservoir grid-block scale using the hierarchy of geological length scales has been widely published by earlier workers. A major step ahead in this area was taken by Pickup et al. (1994, 1995, 1998), who developed the Geopseudo method that integrates reservoir simulation with geological modelling, and yields the effective multi-phase fluid flow properties. The Geopseudo Atlas software package was developed by Pickup et al. (1994) at Heriot-Watt University in a joint industry research project. The Geopseudo Atlas incorporates templates of clastic sediment architecture models, data banks of petrophysical properties, and flow scale-up codes (Pickup et al. 1994). These methods have been adapted and assessed by Corbett et al. (1999), Pickup & Stephen (2000) and Stephen et al (2002), among others, to represent the effects of small-scale geological features in reservoir simulation. The Geopseudo method inspired the development of the near-wellbore modelling software used in this thesis (SBED^{TM}). The Geopseudo Atlas and SBED^{TM} share the common goal of integrating geological modelling with reservoir simulation, and use similar numerical methods for the calculation of upscaled single and two phase permeability values. The Geopseudao Atlas was developed as a Unix-based package and runs in X-Windows environment with user interface being written using a combination of X and Motif functions calls (Pickup et al. 1994). SBED^{TM}, on the other hand, has been developed as a commercial software package with a robust graphic and interactive user interface and is compatible

with both Windows and Unix environments. An important difference between the two software packages is that the Geopseudo Atlas uses rectangular grids for modelling the geological heterogeneities whereas SBED^{TM} uses unstructured grids to generate the geomodels based on sinusoidal functions. The geometrical models generated by SBED^{TM} hence conform to the geological features to be modelled and represent the natural variability more accurately for the same number of grid-blocks. The modelling methods used in SBED^{TM} are discussed in greater detail in Chapter 3.

As discussed above, it is a critical decision to decide the scale that the well measurements should be upscaled to (Nordahl & Ringrose 2008). The concept of Representative Elementary Volume (REV) becomes important in this context, which was introduced by Bear (1972). REV is the volume at which the desired flow parameter is homogenous and statistically stationary and is considered to ensure consistent upscaling in flow simulation studies (Bear 1972, 1988). Several authors have discussed the concept of REV in relation to the calculation of effective flow properties (e.g. Haldorsen 1986; Hurst 1993; Corbett et al. 1999; Jackson et al. 2003, 2005; Keehm & Mukerji 2004; Nordahl & Ringrose 2008). However, the application of REV is quite challenging in carbonate reservoirs due to their notoriously complex distribution of geological and petrophysical heterogeneities. Chapter 7 addresses the aforementioned issues through the near-wellbore upscaling workflow developed for the complex carbonate reservoir, Field X.

i) Upscaling in carbonate reservoirs

Upscaling permeability in carbonate reservoirs is a particularly challenging issue, owing to the extensive multi-scale geological and petrophysical variability caused by complex depositional and diagenetic processes. Numerous case studies have been published about upscaling in carbonate reservoirs involving scaling up of multimillion cell geomodels into models with thousands of grid-blocks suitable for reservoir simulation. The general aim of these studies is to integrate the geological information represented in the fine scale geomodel into the reservoir simulation model with the least possible loss in detail. In a case study of upscaling the geomodel of a giant Middle East carbonate reservoir into reservoir simulation model, Ghedan et al. (2002) used flow-based upscaling involving numerical pressure solver technique to scale up permeability from geomodel to simulation model scale. On a similar note, Suzuki et al. (2004)

demonstrated a fast upscaling technique to loop geomodel with history matching in their case study of a giant Middle East carbonate reservoir to upscale geomodel with 2 million grid block into reservoir simulation model with 6000 cells. In another case study of a Middle East carbonate reservoir, Ates et al. (2005) evaluated multiple geostatistical models using streamline simulation to find optimal level of vertical upscaling for finite difference simulation. They have used field wide sweep-efficiency as the performance measure and subsequently selected three realizations to be upscaled for the purpose of comprehensive history matching and performance prediction. In a similar case study of the Marrat reservoir of the Magwa field, Kuwait, a deep and elongated carbonate shoal reservoir, Samantray et al. (2006) evaluated multiple earth models to capture reservoir heterogeneity and assess its impact on the flow behaviour. In a case study of the Kashagan field, a giant carbonate field in the North Caspian Sea containing three different porosity systems (matrix, karst and fractures), Panfili et al. (2012) demonstrated a methodology of to obtain effective transmissibility to be used for reservoir simulation. Using a fine grid geomodel based on outcrop data from the San Andreas formation, Kazemi et al. (2012) studied the sensitivity of flow behaviour to various methods of upscaling. They have compared single-phase upscaling methods including averaging and flow-based upscaling, and Well Drive Upscaling method (Zhang et al. 2008). Note that the above discussed works involve optimal coarsening of fine scale geomodels obtained from conventional modelling techniques whereas the upscaling methods discussed in this thesis involve improving the geomodel itself through the incorporation of crucial multi-scale heterogeneities, subsequently leading to improved reservoir simulation.

Several earlier workers have demonstrated the importance of characterising and upscaling multi-scale geological-petrophysical heterogeneities pertaining to carbonate reservoirs in order to improve the reservoir simulation model and the accuracy of flow performance predictions (e.g., Wang et al. 1994; Delhomme et al. 1996; Greder et al. 1996; Prasad et al. 1996; Zhang et al. 2004; Creusen et al. 2007; Ringrose 2007; Popov et al. 2009; Rebelle et al. 2009; Buiting 2011; Correia et al. 2011; Khalili et al. 2013). In their study of the Seminole San Andres field, comprising a shallow-water carbonate reservoir, Wang et al. (1994) have investigated upscaling horizontal and vertical permeability values into simulation grid block sizes using outcrop and core data. They have estimated the effective vertical permeability using the ratio of harmonic mean to

arithmetic mean of permeability. They note that high frequency cyclicity and rock-fabric units are the two main scales for building geologic and simulation models of shallow-ramp carbonate reservoirs and that within individual cycles rock-fabric units define flow units. Wang et al. (1994) have grouped rock properties such as capillary pressure and relative permeability based on the rock fabric. They conclude that in their study rock-fabric-averaged models provided more accurate fluid saturation distributions than cycle-averaged models. In their study, the vertical permeability values used for matching production history were much lower than those measured from cores. This phenomenon reflects the insufficient representation of the thin and discontinuous barriers that are not well handled in the reservoir simulation model during vertical upscaling. Buiting et al. (2011) on the other hand used Thomeer-fitting of MICP data from hundreds of core plugs from the Arab-D limestone to upscale saturation-height functions in order to represent the transition zone more accurately.

Delhomme et al. (1996) investigated porosity upscaling in carbonates using borehole image logs. They note that heterogeneity itself is anisotropic as the horizontal variogram range is normally larger than vertical range since geological formations normally vary more rapidly in the vertical direction than horizontal. In a study focused on two types of vuggy carbonate facies with separate vuggy porosity, Greder et al. (1996) show that conventional sampling methods overestimate the permeability distribution at log scale in vuggy carbonates. Khalii et al. (2013) characterised spatial heterogeneity in carbonate reservoirs and demonstrated pore-to-core scale upscaling with the aid of X-ray-CT images. They observed that in their study permeability increased with scale. Rebelle et al. (2009) detail a rock-typing workflow in which core-to-log upscaling is done using electrofacies modelling of petro-geological groups and log-to-grid upscaling is done using power averaging coefficient. Prasad et al. (1996), in their study based on the core and well test data from a long producing non-fractured Middle East carbonate reservoir, developed a methodology based on ‘upscaling factor’ to correlate upscaled core permeability values with effective permeability from well test analysis. In a case study of the Natih formation, Oman, Creusen et al. (2007) used 3D static mini-models to model and upscale the petrophysical properties of small-scale heterogeneities, divided into three main rock types. Correia et al. (2011) used mini-models in the form of fine grid box models to adjust fracture blocks components and well indices according to small scale fracture behaviour for representing them in the reservoir simulation model

of a naturally fractured reservoir. The common goal of the above studies and the workflows discussed in Part II of this thesis is to efficiently characterise and simulate the multi-scale geological-petrophysical heterogeneities in carbonate reservoirs. The workflows presented in this thesis differ from the earlier works discussed above in that they employ high-resolution near-wellbore modelling and upscaling tools based on multiscale mixed-finite element methods. In addition, the work presented in Chapter 8 demonstrates the integration of multi-scale, multi-disciplinary data and workflows to achieve an all-round improvement in the characterisation, modelling and flow simulation of a reservoir. Over the past years significant progress has been made by several authors in the application of multiscale mixed finite-element method for solving problems related to free-flow and porous regions. For example, Gulbransen et al. (2010) have demonstrated that carbonate heterogeneities such as vugs, caves and fractures can be accounted for in a fine scale geocellular grid. However, these methods are still highly computationally intensive to be applied at industrial scale and require extensively long time frames to model and simulate the desired geological heterogeneities at the reservoir scale. In this context, the workflow applied to carbonates in Part II of this thesis provides a bridge between the multi-scale mixed-finite element methods available in SBED^{TM} and the conventional finite-difference reservoir simulation workflows still being widely used in the industry. It is hence more flexible and less time consuming for an operator to adapt the workflows demonstrated in this thesis to existing field development projects.

2.8.2. Cross-scaling

Cross-scaling is "the determination of a relationship between two different physical properties" (Corbett *et al*. 1998). Since there is no direct measurement method of permeability using conventional wireline tools, the estimation of permeability is generally more difficult compared to porosity. In addition, identifying the reservoir flow zones is often dependent on the characterisation of porosity-permeability relationship. Consequently, several models have been developed to relate permeability to other rock properties, especially porosity. Such methods often use simplifying assumptions about the porous medium and express porosity-permeability relationship as a log-linear cross-plot (e.g., Figure 2.11) The most popular methods of estimating permeability from well data use empirical equations to relate porosity and permeability (e.g., $\log k = a * \phi + b$

), where a and b are constants and are determined from core measurements to be applied to the wireline porosity log.

Note that the above methods make an implicit assumption that the core plugs are representative of the volume of rock investigated by the wireline tool, which is often not the case in heterogeneous carbonate reservoirs. Figure 2.11 shows the general trend of porosity-permeability relationships for various reservoir rock types proposed by Tiab & Donaldson (1996). The cross-scaling of porosity and permeability estimated from core plugs is generally considered to be a valid procedure due to their same sample support. Nevertheless, applying the resulting correlation on a larger support, for example on the reservoir simulation grid block, may not necessarily be correct if the assumption for homogeneity is not satisfied. On the other hand, although the coefficients of the empirical equations relating porosity and permeability are shown to be scale dependant, they become nearly constant at larger scales (Worthington 1997).

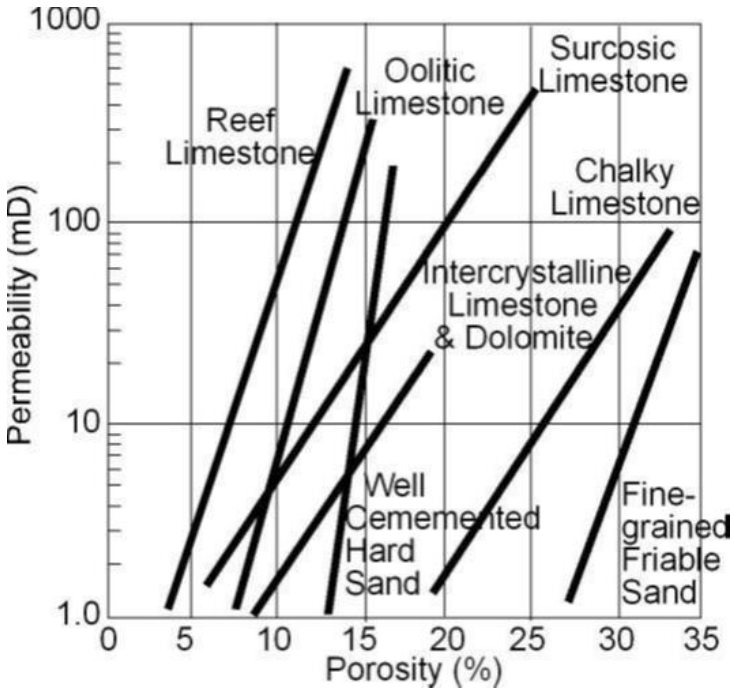

Figure 2.11. Typical porosity-permeability relationships for various rock types. From Tiab & Donaldson (1996).

Figure 2.12 shows three porosity/permeability trends derived by Lucia (1995) on a porosity-air permeability cross-plot of a variety of non-vuggy limestone rocks. Although earlier studies by Lucia (1995, 2000) suggest correlations can be derived from pore type and grain size relationships, porosity-permeability relationships in carbonates

are notoriously difficult to define. Identifying the correlation between porosity and permeability in carbonate reservoirs is a complicated issue due to the extensive range of diagenetic processes that can modify the original reservoir rock fabric. The complex pore systems in carbonates often do not allow easily recognisable clusters on the porosity-permeability cross-plot obtained from core plug data. Accurate prediction of porosity-permeability correlations in carbonates and modelling permeability in the reservoir simulation model scale continues to be an open area of research. Chapter 7 presents a novel near-wellbore upscaling workflow used to derive the global porosity-permeability correlation to be applied for reservoir simulation.

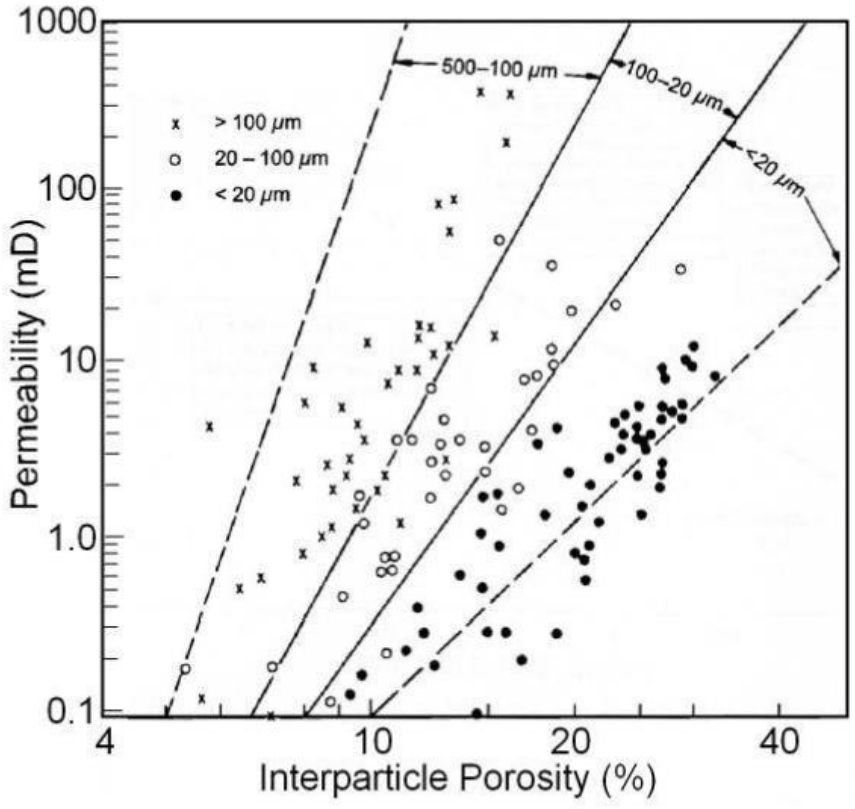

Figure 2.12. Porosity-air permeability cross-plots for various particle-size groups in non-vuggy limestone rock fabrics. From Lucia (1995).

In general, characterising the entire reservoir using a single porosity-permeability relationship will result in poor prediction of permeability. Several authors have proposed various approaches of reservoir characterisation that take into account the variation of petrophysical properties among different lithofacies (e.g., Ebanks 1987; Amaefule *et al*. 1993; Jian *et al*. 1994). Jian *et al*. (1994) employed a genetic approach to define a flow unit as a volume of rock that is subdivided according to geological and

petrophysical properties that influence the flow characteristics of the unit. Amaefule *et al*. (1993) developed a quantitative method based on the Kozeny-Carman equation to subdivide the reservoir into hydraulic units. A flow unit is different from a hydraulic unit as the former is a large-scale reservoir unit and the latter is based on classification of core plugs (Corbett *et al*. 2003). Corbett *et al*. (2003) also pointed out that the implicit assumption in the hydraulic unit approach is that the hydraulic elements are larger than the conventional core plugs. Although this seems to be a fair assumption in most clastic reservoirs, this approach must be employed cautiously when dealing with heterogeneous carbonate reservoirs. These issues are revisited in Chapter 8, where NWU workflow is applied to obtain upscaled rock types for reservoir simulation.

2.9. Review of geomodelling concepts

As a result of the complex geological processes through which a reservoir evolves, the petrophysical properties vary in space. Hence, a numerical model that solves flow equations (e.g., black oil simulation model) requires a map of the spatial distribution of the relevant properties such as porosity and permeability. The various techniques of generating porosity and permeability maps can be divided into three main types (Koltermann & Gorelick 1996); i) structure-imitating, ii) process-imitating, and iii) descriptive methods. An extensive review of these methods can be found in Kolterman & Gorelick (1996) and can be summarised as follows: Structure-imitating methods rely on spatial statistics, probabilistic rules, and deterministic constraints to depict geometric relations within aquifers and reservoirs. Process-imitating methods solve governing equations to represent either the processes through which sedimentary deposits form or the physics of subsurface fluid flow and transport. Descriptive methods divide an aquifer into zones by synthesizing hydraulic measurements and geologic observations into a conceptual depositional model.

The NWM tools used in this thesis employ process-imitating methods. Process-imitating methods construct models of heterogeneity through mathematical models of either subsurface flow or the geological processes governing sedimentary basin formation and filling (Koltermann & Gorelick 1996). One of the sub-classes of this method, the geological process method, employs fluid-flow equations and mass conservation of sediment to model depositional process such as sediment transport, depositional rate and erosion. This model class then considers erosion, transport and deposition by wind, water and mass movements by using the equations to distribute

sediments over an area and predict the sedimentological structures produced by the flow and sediment type. The geologic process modelling methods are constrained to the mathematical representation of the geological processes and can be conditioned to measured values only through trial and- adjustment of input (Koltermann & Gorelick 1996). Further details of the modelling concept applied by the NWM tools in this thesis are provided in Chapter 4.

2.10. Closing remarks

An overview of the key geological processes and porosity types typically occurring in carbonate reservoirs has been provided in this chapter. Stylolites and associated small-scale fractures are one of the crucial diagenetic features observed in the carbonate field used in this thesis (Field X). A background to the formation, distribution and propagation of stylolites has been presented. Secondary porosity is one of the main controls of fluid flow in carbonate reservoirs as demonstrated by several case studies. The various pore types and their multi-scalar aspects can impact permeability and reservoir quality in carbonate reservoirs. The key issues related to the characterisation, upscaling and cross-scaling of reservoir permeability have been discussed. The next chapter provides further details of the modelling concepts and an overview of the various steps involved in the NWM workflow used in this thesis.

Chapter 3. NEAR-WELLBORE MODELLING TOOL

In this thesis, near-wellbore modelling (NWM) refers to high resolution numerical representation of subsurface in the vicinity of the wellbore based on the geological and geophysical information obtained from the wellbore data. In the following parts of the thesis, Part I and Part II, near-wellbore modelling and upscaling tools will be used to characterise and model the multi-scale geological-petrophysical heterogeneities in a clastic reservoir, Field A, and a carbonate reservoir, Field X, respectively. The NWM tool used in this thesis is a commercialised modelling software suit called SBED^{TM}, which stands for 'Sedimentary BEDding'. SBED^{TM} is trademark software developed by Geomodeling Technology Corp. This chapter presents the modelling concept employed in SBED^{TM} and an overview of near-wellbore upscaling (NWU) workflow used in this thesis. In Part I, SBED^{TM} was employed to simulate the sedimentological components and the corresponding petrophysical properties in a rectangular shaped volume along the wellbore interval that is represented within the reservoir simulation model. In Part II, however, SBED^{TM} was used to simulate the various geological-petrophysical reservoir heterogeneities based on well data only for representative well intervals, and the upscaled properties were applied to the entire reservoir simulation model.

3.1. Modelling concept

SBED^{TM} was originally developed to bridge gaps between core-scale and well-log data through detailed modelling of centimetre to decimetre scale features such as bedding structures (Wen *et al*. 1998). In contrast to the conventional cell- or object-based geostatistical modelling methods, NWM workflow in SBED^{TM} utilizes process-oriented modelling approach. Process-oriented modelling approach can formulate deterministic geological processes such as migration and deposition of sedimentological components in a stochastic framework (e.g., Nordahl 2004; Elfenbein *et al.* 2005). Hence, the NWM workflow in SBED^{TM} leverages the advantages of both deterministic and stochastic modelling methods. In summary, the modelling approach in SBED^{TM} is process-oriented, rule-based and stochastically formulated.

Before proceeding into further discussion of modelling concepts, several sedimentological terms need to be defined. Figure 3.1a illustrates the bedform classification theme used in this thesis. A bedform is a morphological feature formed by the interaction between cohesionless sediment on a bed and the overlying fluid flow

(Nichols 2009). A lamina is the smallest bedform in a sedimentary sequence, which is relatively uniform in composition and texture and not internally layered (c.f. Campbell 1967). A bed is a unit of sediment which is generally uniform in character and contains no distinctive breaks; it may be graded, or can contain different sedimentary structures. A laminaset consists of a group or set of conformable laminae that compose a distinctive structure within a bed (Campbell 1967). The three main forms of sedimentary depositional processes are deposition, migration and erosion. Deposition is the accumulation of sedimentary particles following transport by gravity, water, air, ice or mass flows or the chemical or biological growth of the material in place. Bedform migration is the process of development of bedforms in time and space (Simons *et al.*1965). Erosion is the removal of material from bedforms by various transport processes.

The size, shape and evolution of bedforms, in addition to their internal structure, have been found to depend on the physical properties of the sedimentary grains and the transporting fluid, and the depositional process *(*e.g., Brush 1965; McKee 1965; Allan 1968; Southard & Boguchwal 1973; Reineck & Singh 1980; Allan 1982a, b). Several authors have worked on synthetic modelling of small-scale, i.e. centimetre to decimetre scale, sedimentological bedforms. Rubin (1988) was one of the pioneers in synthetic bedform modelling, who developed an algorithm based on sine curves that are displaced in time and space to mimic the migration of lamina surfaces based on earlier work by Allen (1968). Wen *et al*. (1998) made a significant step forward by combining sedimentation pattern imitation methods, partly derived from the Rubin (1988) code, and stochastic methods. The main advantages of the approach developed by Wen *et al*. (1998) is that the bedform modelling is in 3D and is paired with property modelling and flow based upscaling features. The following surface function (Wen *et al*. 1998) is manipulated in SBED^{TM} to implement process-oriented modelling:

$$z(x,y)^t = A\sin\left(\frac{x}{L_x}+\theta_x\right) + B\sin\left(\frac{y}{L_y}+\theta_y\right) + g(x,y) \qquad (1)$$

where x and y are spatial coordinates and t is a nominal time increment. A and B are amplitudes of the bedform in the current (x) and crest (y) directions, respectively. Lx and Ly are wavelengths of the bedform in the current (x) and crest (y) directions, respectively. θ_x and θ_y are initial phase angles (radians) and g(x,y) is a 2D Gaussian

random function. Additionally, SBED^{TM} also contains a proprietary code for object modelling to superimpose post-depositional features such as biogenic structures on simulated bedforms. Figure 3.1b shows the various components of bedform surfaces included in the above algorithm.

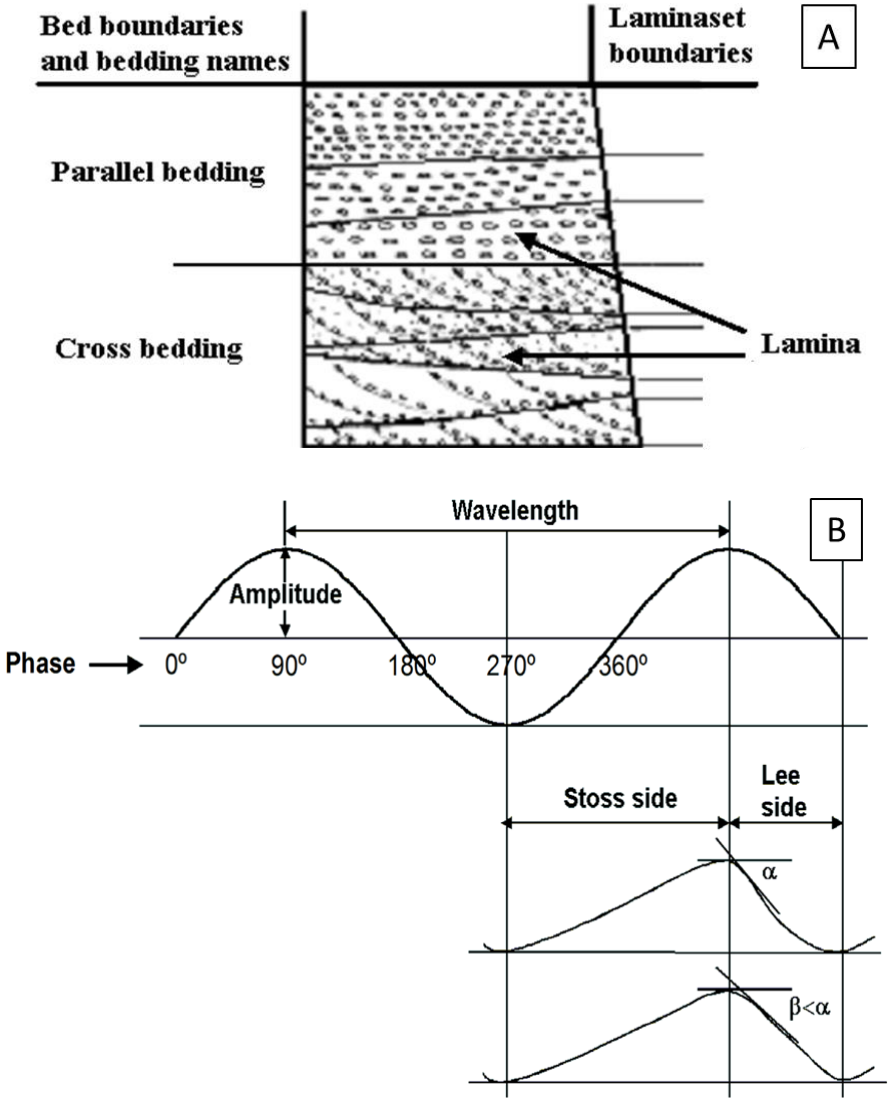

Figure 3.1. (a) Illustration of bedform classification theme used in this thesis. Modified from Reineck and Singh (1980). (b) Conceptual bedform model showing the bedform terminologies wavelength, amplitude, and phase. Modified after Allen (1968).

Figure 3.2 illustrates how the bedform surfaces are migrated in a time series to simulate sedimentary processes. The surfaces generated in SBED^{TM} using equation (1) are displaced by vectors to simulate the migration of bedforms (Nordahl 2004). The 3D volume between the displaced surfaces is created with an irregular grid and represents a simulated lamina. The stochastic components included in SBED^{TM} enable the

simulation of the natural variability of the bedforms between the bedding boundaries. Correlated random variables are added to each of the control parameters that are used to simulate the bed forms (Ringrose *et al*. 2003). After a series of such lamina sets are created using equation (1), a hiatus is simulated. This hiatus can then be eroded by a new time series using different set of control parameters (Ringrose *et al*. 2003; Nordahl 2004). In this way the deposition, migration and erosion of lamina sets, beds and bed sets can be simulated. The 3D volume between the simulated surfaces in the irregular grid comprises the grid cells at the lamina scale. These grid cells can then be populated with porosity and permeability of the respective lamina set drawn from the input geostatistical data.

Using the methodology discussed above, the algorithms in SBED^{TM} facilitate the modelling of geological features at various spatial scales. Once a conceptual sedimentological model is available, a wide variety of stratigraphic geometries can be modelled in 3D owing to the flexibility of the process-oriented modelling approach. The modelling algorithms can be tailored to specific clastic depositional settings such as fluvial, shoreface and deep-water environments (e.g., Figure 3.3). The following sections provide an overview of the various steps involved in the near-wellbore modelling and upscaling workflow in SBED^{TM}.

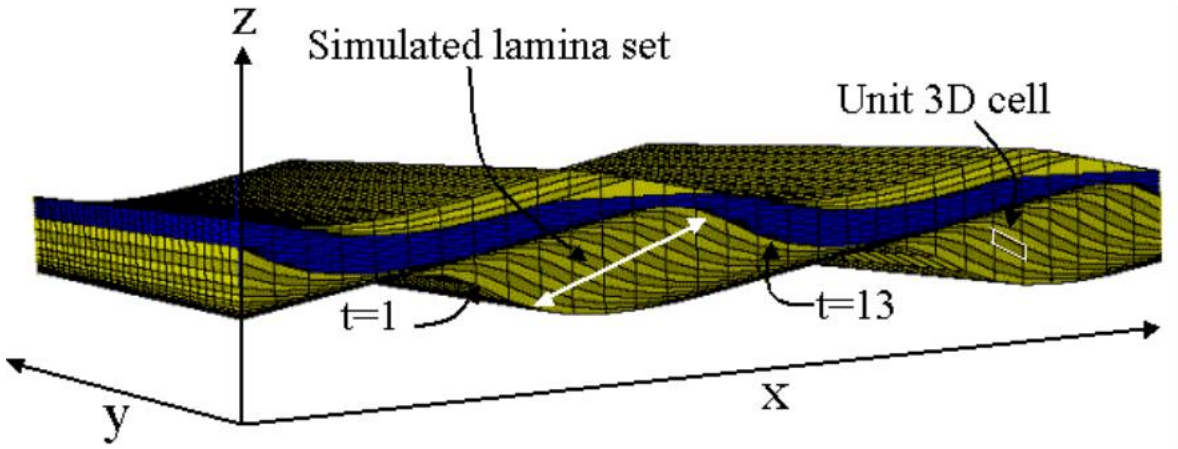

Figure 3.2. Schematic illustration of the generation of sand (yellow) and mud (blue) lamina surfaces in SBED between times t=1 and t=13 in the time series of equation 1. The length of the white arrow indicates the migration direction and speed. From Nordahl (2004).

Figure 3.3. Example of high resolution near-wellbore model representing the bedding structures of a thin-bedded turbidite section with high vertical heterogeneity. The above image was taken during an outcrop study of the Permian Reef Complex of the Guadalope Mountains region, New Mexico.

3.2. Overview of near-wellbore modelling workflow

Before discussing the details of SBED^{TM} workflow, some terms need to be defined specifically. A *lamina template* in SBED^{TM} is a set of control parameters that defines a lamina set or the volume within a biogenic structure. A lamina template is the smallest modelling element in SBED^{TM} by means of which the porosity and permeability distributions of a lamina set or biogenic structure are defined. A *sub-model template* constitutes a set of lamina templates whose spatial distribution is defined by a set of control parameters. The term *sub-model boundary* is used to describe a bedding boundary that separates two different lithofacies intervals. A *sub-model* is a bedding structure realisation created by assigning a sub-model template between the sub-model boundaries. A stack of sub-models assigned with respect to the sub-model boundaries within a well interval constitute a *near-wellbore model*. The various steps of the NWM workflow in SBED^{TM} are discussed in detail in the following sections.

3.3. Core and petrophysical analysis

The reservoir data that can aid the NWM workflow in SBED^{TM} include borehole images, core samples and photos, thin sections, core descriptions and interpretations, core plug porosity and permeability data, probe permeameter data and well log curves. These data are interpreted to understand the crucial reservoir and fluid heterogeneities and to identify the representative lithofacies in the well interval. These interpretations are then used to define the sub-model boundaries and generate the sub-models for each

lithofacies type in the well. The core images in white light complemented by thin-section and core description logs can be used to define the sub-model boundaries and classify the lithofacies in the well interval. The wellbore images are useful to interpret the major lithofacies and reservoir heterogeneities, and help identify sub-model boundaries. The core plug porosity and permeability data can be used to calculate the porosity and permeability distributions of the various lamina templates within a sub-model. The probe permeameter device, as discussed in Chapter 2, is a valuable tool to understand the variability of permeability at the lamina and bed scale. Probe permeameter measurements are hence very useful to obtain the permeability distributions to be input in the lamina templates. Wireline data can be used to calibrate the petrophysical input for near-wellbore models and check the quality of the resulting effective petrophysical properties. In addition to the static reservoir data discussed above, NWM workflow can also benefit from the insights gained from the interpretation of reservoir dynamic data such as well-testing and production logging data. In this thesis, the NWM workflow was coupled with well testing data and production data to improve reservoir characterisation as demonstrated in Part 1 and Part 2, respectively.

3.4. Grid specifications

The first step in the process of building a near-wellbore model is to define the grid and cell dimensions of the model. The grid and cell sizes are specified using the Graphic User Interface (GUI) window shown in Figure 3.4. The model units and the grid cell dimensions are input in the X- and Y-directions i.e., ‘dx’ and ‘dy’ and the number of cells i.e., ‘Nx’ and ‘Ny’. The grid cell size in the vertical direction, i.e., ‘dz’ varies according to the geometrical parameters designated in the sub-model template. The model size (X, Y, Z) is given by the product of the cell size and number of cells in each direction (Nx, Ny, Nz).

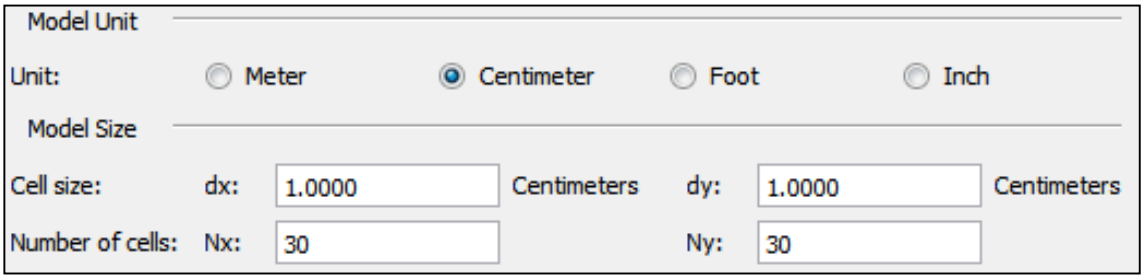

Figure 3.4. Part of the Graphic User Interface (GUI) window used to specify the cell and model dimensions in a NWM scenario.

3.5. Bedding structure modelling

As discussed before, the near-wellbore models in SBED^{TM} are created with irregular grids. These irregular grids adapt to the sub-model templates in the vertical direction such that the structural details and boundaries of the bed forms are captured. Each grid cell within a sub-model represents a designated lamina template, for example sand or shale lamina, and a petrophysical property associated with that grid cell. The spatial distribution and volume of the cells is controlled by the geometry of the bed form surfaces, which is defined using the GUI window shown in Figure 3.5. Firstly, this window is used to define the output parameters that control the number of equally probable realisations desired as output, and the seed number. In SBED^{TM} random seed numbers are used to initiate and displace the bed form surfaces (Ringrose *et al*. 2003). The realisations can be reproduced for a given seed number to check the repeatability of the results.

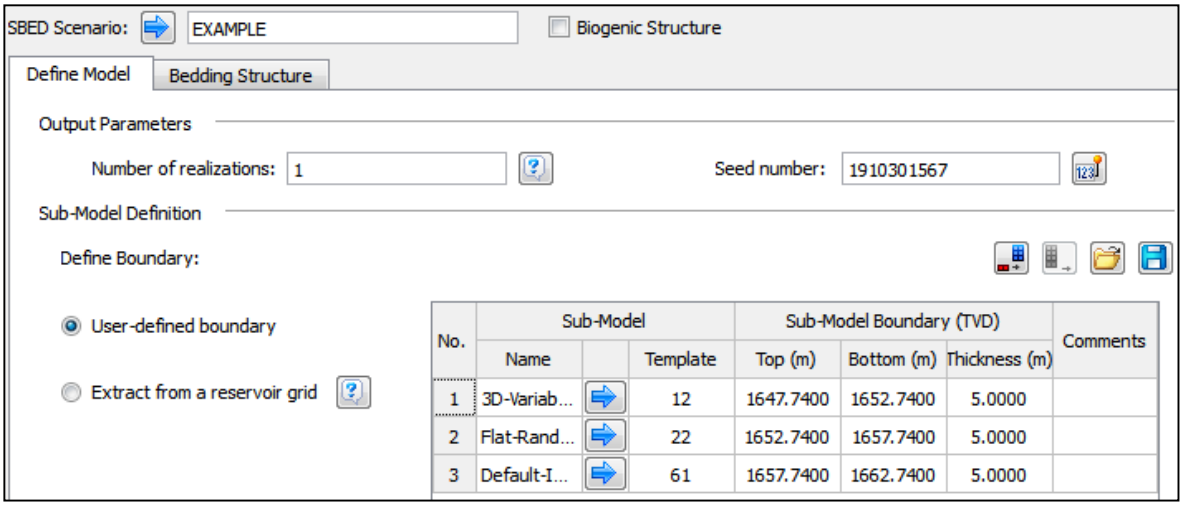

Figure 3.5. The Define Model tab used to input the output parameters and sub-model definition.

Secondly, this GUI is used to input the sub-model boundaries and sub-model templates of the near-wellbore model. As discussed earlier, the physical or conceptual representations of the actual reservoir rock in the well, like core descriptions and borehole image logs, are used to identify the sub-model boundaries. These sub-model boundaries are input by specifying the top and bottom depths of each sub-model as shown in Figure 3.5. The respective sub-model templates are then assigned. Then the lamina templates and geometrical parameters are assigned for each sub-model individually, which vary according to the sub-model template used. The geometrical

parameters can be defined using the mean value and linear or periodic trend, or impart a random component. The mean value represents a constant average value of the parameter. Alternatively, a linear component can be assigned to the parameter to vary with an increasing or decreasing upward trend. A periodic component represents cyclicity in the vertical succession of the lamina surfaces and is modelled by a sine function described in terms of amplitude, phase and wavelength. A random component imparts noise in a vertical succession and is controlled by a standard deviation value. Further details of input parameters for bedding structure modelling are discussed only for the sub-model templates used in this thesis in the following sections. After all the required parameters have been entered the 3D geometry of the near-wellbore model will be generated for that well interval.

Over 100 3D sub-model templates are available in SBED^{TM} that are representative of sedimentological features typically observed in clastic depositional environments. The main types of sub-model templates in SBED^{TM} include cross bedding, parallel bedding, hummocky cross stratification bedding, flaser bedding, wavy bedding, lenticular bedding and massive bedding. The available sub-model templates in SBED^{TM} are representative of clastic depositional features. For this reason, the GUI windows in SBED^{TM} use the terms ‘Sand’ and ‘Mud’ to represent the geometrical parameters of the individual lamina templates. However, in this thesis diagenetic features such as stylolites are also modelled by manipulating the suitable lamina and sub-model template parameters as discussed in a later section.

3.5.1. Cross bedding

Cross-bedding is defined as an arrangement of strata thicker than 1 cm and inclined at an angle to the main planes of stratification (Nichols 2008). Cross-bedding is primarily produced by the migration of bedforms such as ripples and dunes (Jackson 1997; Rubin 2003). The cross-bedding templates in SBED^{TM} are based on the classification scheme by Rubin (1987). The clastic field used in this thesis, Field A, contains multi-storey minor channel fills of cross bedded sandstone. These cross bedded channels were interpreted to be high permeability reservoir zones. It was important to model them to evaluate their influence on fluid flow in the near-wellbore region. Figure 3.6 shows one of the sub-model templates available in SBED^{TM} to model cross bedding of sand laminae.

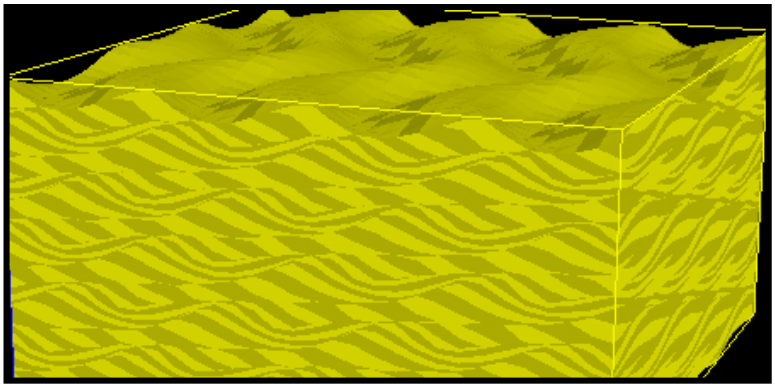

Figure 3.6. Example of 3D sub-model template in SBED used to model cross-bedding.

Figures 3.7 and 3.8 shows the GUI windows used to input geometrical parameters for the cross bedding sub-model. Up to three different lamina types can be modelled within each sub-model as shown in Figure 3.7a. However, sedimentological interpretations of Field A based on core description logs and outcrop analogues suggest the presence of only one dominant type of sand lamina in the cross bedded facies, which was represented using the respective lamina type. The geometrical parameters used to model cross bedding are divided into three main groups; 1) Bedform parameters, 2) Migration parameters, and 3) Deposition parameters. The core photographs and the sedimentological descriptions of Well A of Field A, were available for the study presented in this thesis. The above mentioned geometrical parameters were hence adjusted for Field A iteratively to reflect the core image and sedimentological descriptions.

i) Bedform parameters

The bedform parameters of cross bedding sub-model describe the bedform geometry in the directions parallel and perpendicular to the direction of deposition (Figure 3.7b). The parameters that need to be specified are wavelength, amplitude, symmetry and steepness, which were defined earlier as shown in Figure 3.1. Each parameter can be associated with the respective Mean, Linear, Periodic and Random components (see Figure 3.7). The wavelength defines the number of cells in the horizontal direction within a bedform while amplitude defines the bedform heights parallel to the direction of deposition. Symmetry and steepness are indices that describe the symmetry and steepness of the bedform respectively and range from 0 to 1. The mean wavelength and amplitude used in Field A in the direction of deposition were 8 cm and 0.25 cm,

respectively. The mean steepness and symmetry values were 0.2 and 0.4, respectively. The mean wavelength and amplitude perpendicular to the direction of deposition were 15 cm and 5 cm, respectively. A periodic component with wavelength of 10 cm was imposed on all the above parameters. A random component with standard deviation of 0.245 was imposed on the amplitude perpendicular to the direction of deposition, based on the visual correlation between the geometrical model and the core photographs.

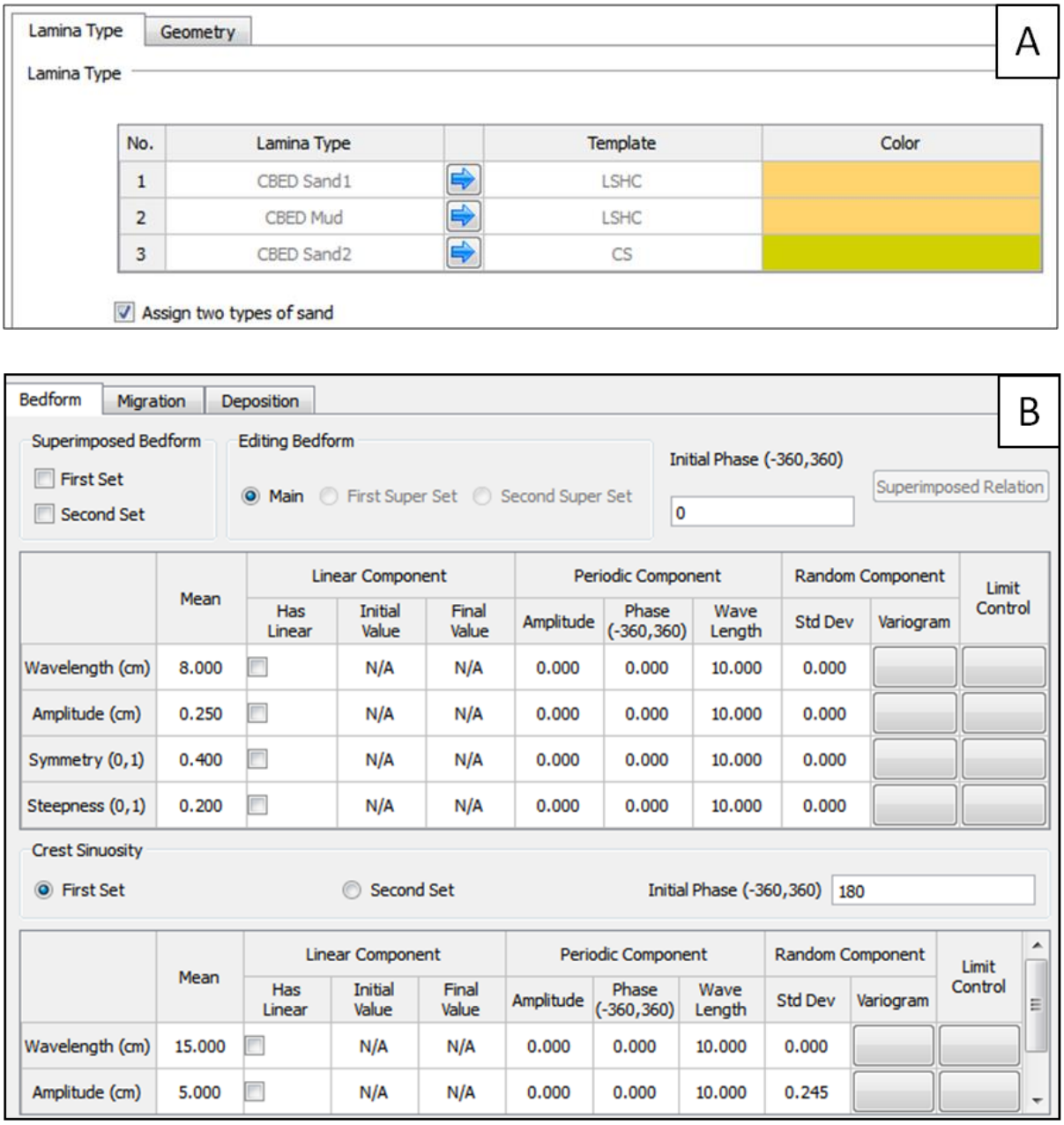

Figure 3.7. GUI windows used in SBED^{TM} to define (a) Lamina templates within cross bedding sub-model and (b) Bedform parameters.

ii) Migration parameters

The migration parameters of the cross bedding sub-model describe the bedform migration with respect to the direction and distance per layer (Figure 3.8a). The direction of bedform migration is defined as the azimuth of migration relative to the x-axis if the bedforms. The horizontal distance that the bedform surfaces extend on the stoss and lee sides is termed as the distance per layer. In the case of Field A, a mean value of 0^o was used as the direction of migration associated with a period component with wavelength of 10 cm. The mean distance per layer value used in Field A was 7 cm associated with a periodic component with wavelength of 2 cm and random component with standard deviation 1.

iii) Deposition parameters

The deposition parameters describe the aggradational distance and the number of laminae for the lithological components of the bedforms (Figure 3.8b). The main lithological components in cross bedding sub-model template are sand and mud. However, as mentioned earlier, sand is the major lithological component of the cross bedded facies in Field A. Hence the number of mud laminae used was 0. The mean number of sand laminae used was 3, associated with a periodic component with wavelength of 10 cm. The mean aggradational distance used for the sand laminae was 0.4 cm associated with a periodic component with amplitude 0.2 cm, phase angle of 90^o and wavelength of 1 cm was used.

3.5.2. Parallel bedding

Parallel bedding is defined as a sedimentary structure marked by beds that are parallel and without angular junctions (c.f. Jackson 1997). Parallel bedding typically occurs on beaches or other sandy areas exposed to wave action, but are also produced in high flow regimes, during ripple formation, and by suspension clouds and turbidity currents (Reineck and Singh 1980). Figure 3.9 shows one of the sub-model templates available in SBED^{TM} to model parallel bedding, which comprises alternating mud and sand laminae. In this thesis, the parallel bedding sub-model template parameters are manipulated to model stylolites in Field X. Stylolites are one of the crucial geological features present in Field X and it was essential to model these features to evaluate their impact on fluid flow. Figure 3.10 shows the GUIs in SBED^{TM} used to input geometrical parameters for the parallel bedding sub-model. Two lamina templates were used to

represent the back ground carbonate matrix and stylolites, respectively (Figure 3.10a). The lamina type that refers to mud was used to represent stylolites. The GUI shown in Figure 3.10b was used to enter the bedform geometry parameters, which are of four main types; 1) lamina thickness parameters, 2) vertical distribution parameters, 3) dip and azimuth, and 4) bedding plane roughness.

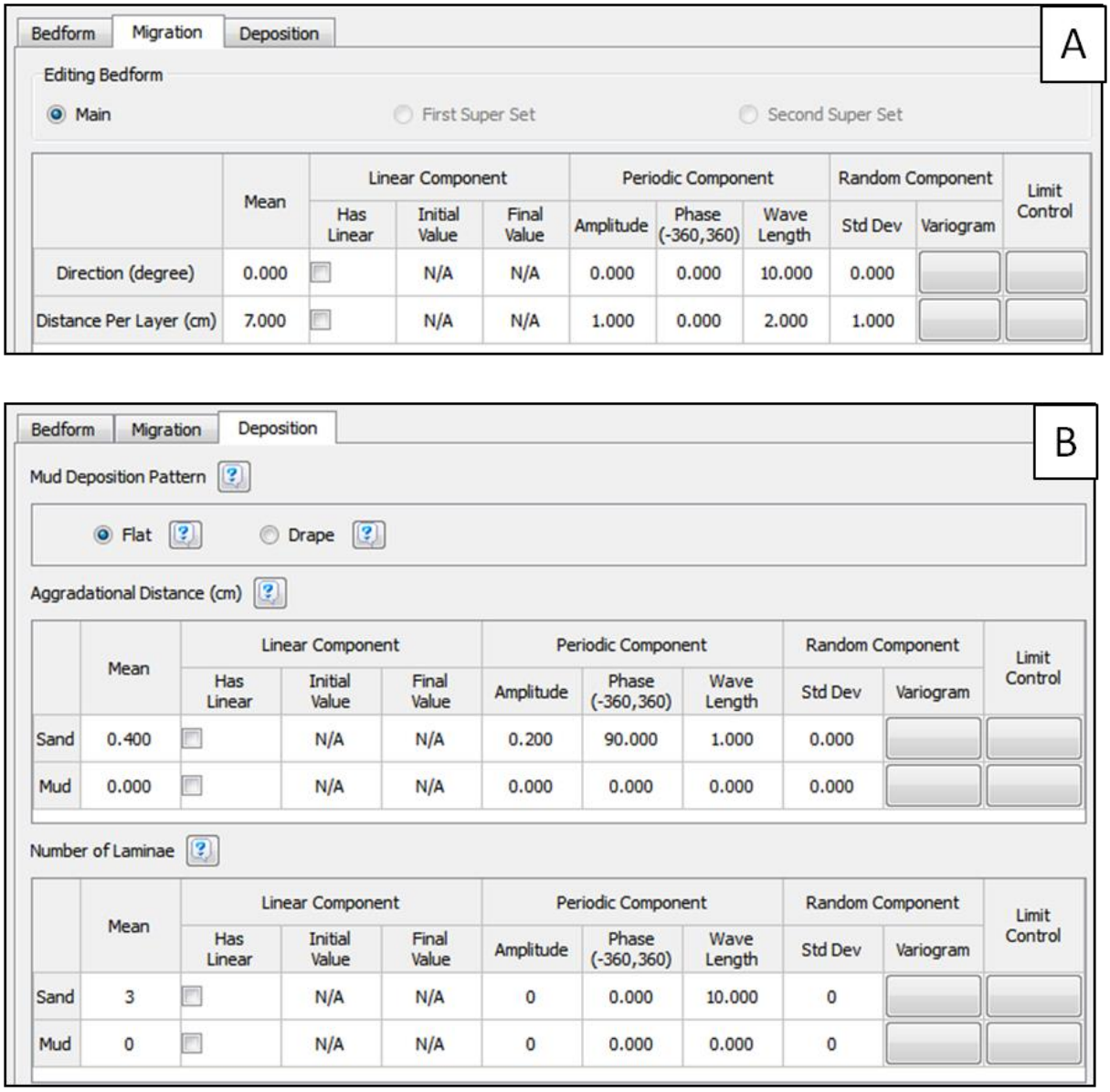

Figure 3.8. GUI windows used in SBED^{TM} to define (a) Migration parameters and (b) Deposition parameters.

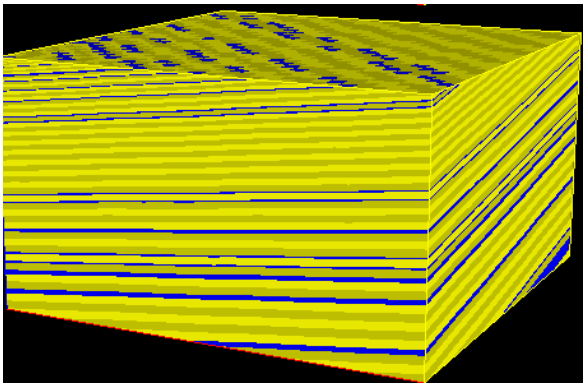

Figure 3.9. Sub-model template representing parallel bedding of randomly interbedded sandstone (yellow) and mud (blue) laminae.

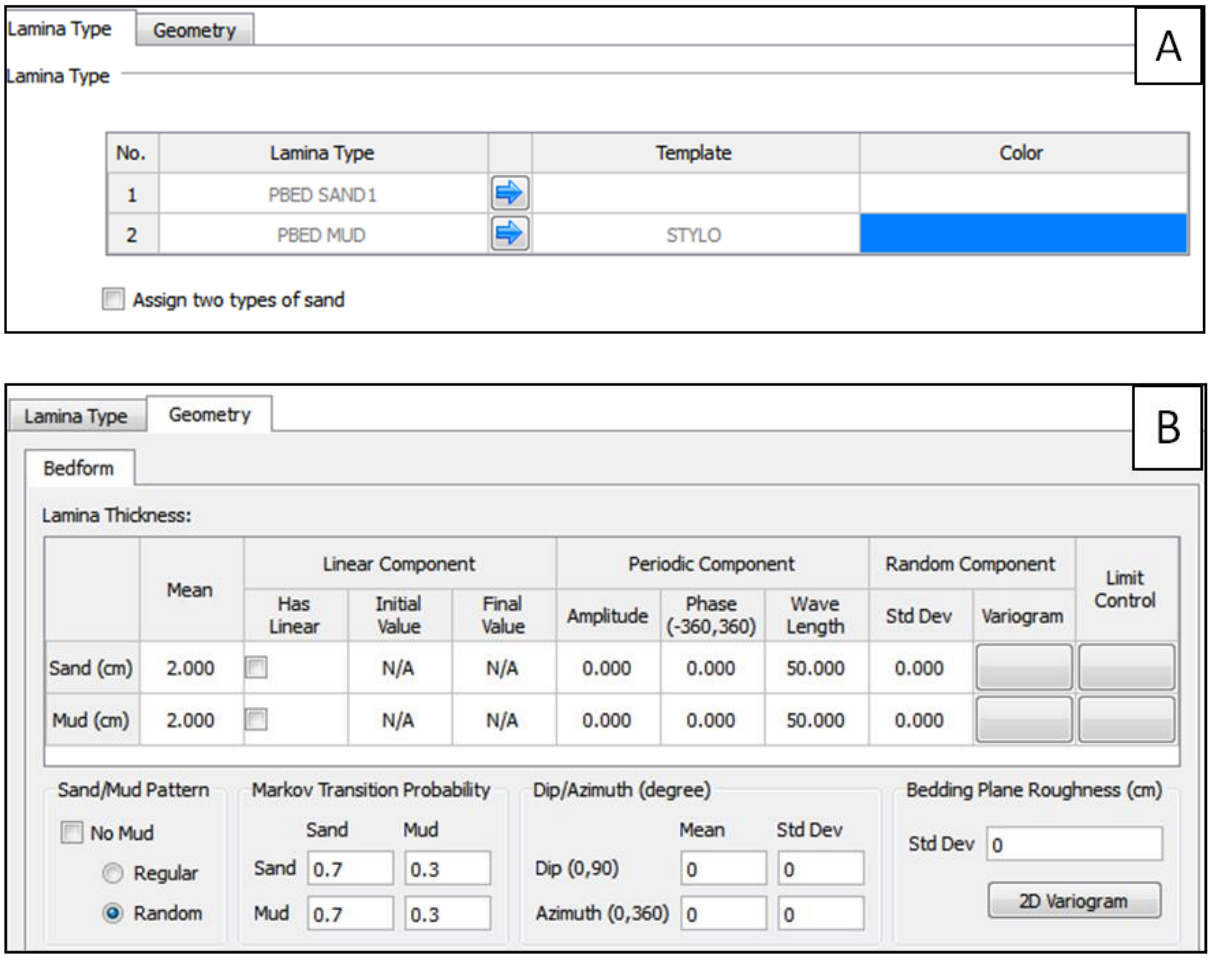

Figure 3.10. GUI windows used in SBED^{TM} to define (a) Lamina templates within each sub-model and (b) Geometrical parameters of the Lamina types.

i) Lamina thickness parameters

The lamina thickness parameters are used to describe the vertical distribution of the laminae as shown in Figure 3.11. The thickness of each lamina type can be defined by entering a deterministic mean value of thickness or as a stochastic distribution by defining a linear or periodic trend, or impart a random component. The migration of the lamina surfaces in the stochastic case is simulated as a linear combination of the defined stochastic components. In this thesis, constant mean thickness values of the stylolite and background carbonate matrix are used within each sub-model.

ii) Vertical distribution parameters

The laminae can be distributed in the vertical direction using regular or random distributions. When random distribution is used Markov Transition Probability method is employed, which calculates the probability of adjacent stylolite (Mud) and/or carbonate (Sand) laminae. This is a fixed (and only) method of controlling the proportion and distribution of 'sand' and 'mud' laminae in the SBED^{TM} version used for this thesis. Numerous earlier workers discuss the various approaches of geostatistical modelling of subsurface spatial structure based on indicator-based methods for categorical variables, such as sequential indicator simulation, simulated quenching and so on (e.g., Johnson and Driess 1989; Deutsch and Journel 1998; Desbarats 1993; McKenna and Poeter 1994, 1995; Ritzi et al. 1995; Weissmann et al. 1999). Markov transition probability method bears the advantage that it can simulate volumetric proportions of observable geological attributes, through a combination of fitting transition probability measurements and inference from geologic information (Weissmann et al. 1999).

The input values entered for each lamina type in the Markov Transition Probability matrix that are shown in Figure 3.12a define the proportions of the stylolite and carbonate laminae within the sub-model. For example, according to the input parameters shown in Figure 3.12a, if the sub-model starts with sand (the first row), the probability of sand being adjacent to sand is 20%, and so of mud being adjacent to sand is 80%. If the sub-model starts with mud (the second row), the probability of sand being adjacent to mud is 40% and of mud being adjacent to mud is 60%. The resulting model in this example thus contains higher proportion of mud than sand.

iii) Dip and azimuth

Azimuth is defined as the geological strike of the bedding features, where north is the y-axis and the azimuth is counter clockwise to the y-axis. Dip is the angle perpendicular to the direction of Azimuth. The mean and standard deviation values can be entered to model constant or variable dip and azimuth of the laminae as shown in Figure 3.12b. The mean value for the dip of the laminae can be varied between -90^{o} and 90^{o} and the standard deviation to the mean value can be varied from 0 to 10. The mean value of azimuth can be varied between 0^{o} and 360^{o} and the standard deviation to the mean value can be varied from 0 to 10. In this thesis, the stylolites are modelled parallel to the bedding plane.

iv) Bedding roughness

Bedding roughness is defined as the undulation of the bedding planes. The bedding roughness within the sub-model can be controlled by entering a value for standard deviation ranging from 0 to 10 (Figure 3.12c). A standard deviation value of 0 yields bedding surfaces that are even (Figure 3.13a), while the value 10 results in very rough bedding surfaces. In this thesis, sub-model scenarios with stylolites were modelled by using standard deviation to the bedding roughness ranging from 0.1 to 1(Figure 3.13b).

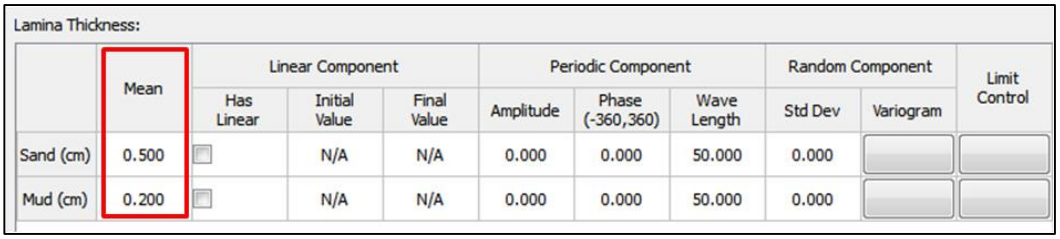

Figure 3.11. Input parameters used to specify the mean thickness of the lamina types. The Linear, Periodic and Random components are used to model the thickness stochastically.

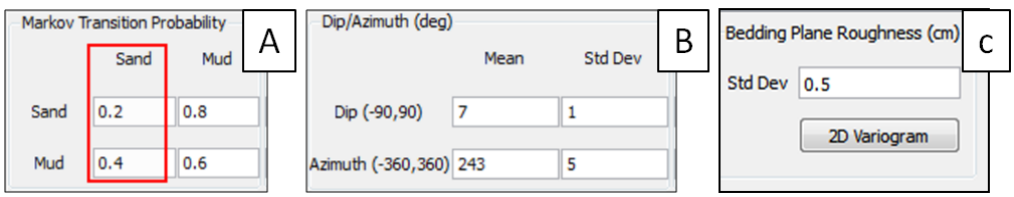

Figure 3.12. (a) Markov Transition Probability Matrix used in SBED^{TM} for random distribution of lamina templates. (b) Input parameters used to define dip and azimuth of the bedding surfaces.

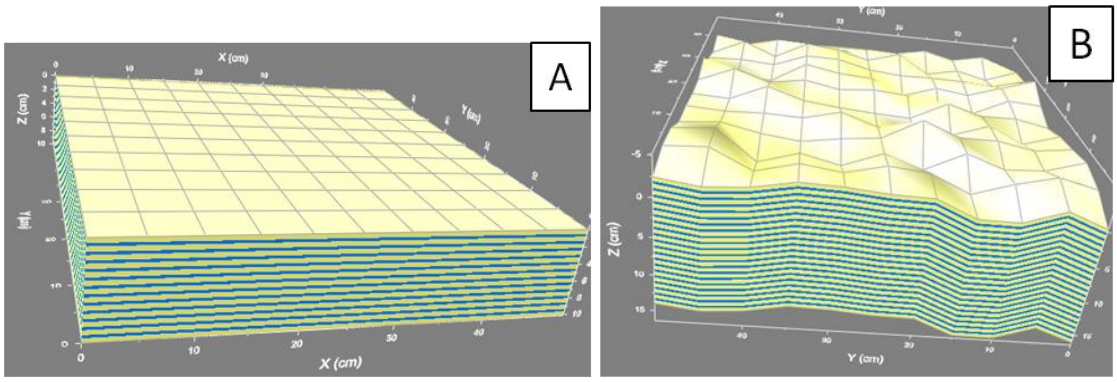

Figure 3.13. Parallel Bedding Models with standard deviation to bedding plane roughness 0 (a) and 1 (b).

3.5.3. Massive bedding

Massive bedding is defined as a stratified rock that is obscurely bedded, i.e. appears to be without any internal structure, regardless of thickness (Nichols 2009). Massive bedding can form by very rapid sedimentation or due to post depositional processes such as intense bioturbation (Reineck & Singh 1980). In this thesis, the massive bedding template is used to model the amalgamated channel sands in Field A and the carbonate lithofacies in Field X. Figure 3.14 illustrates an example of massive bedding sub-model template in SBED^{TM}.

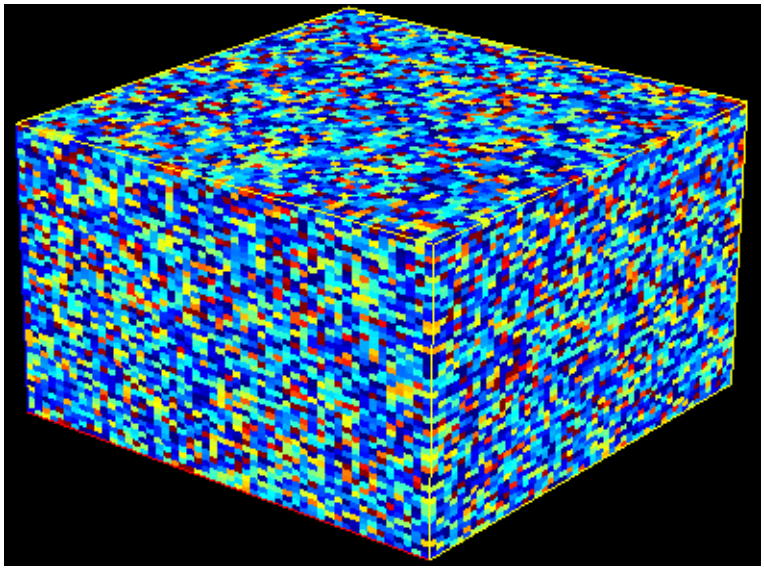

Figure 3.14. Example of a 3D sub-model template used to model massive-bedding. Note that the variation in the above model is due to heterogeneous property distribution within a massive bed.

3.5.4. Assigning biogenic structures

Bioturbation refers to the mixing of unconsolidated sedimentary particles through the activities of biological organisms (Bromley 1996; Soetaert *et al*. 1996). The term *biogenic structure objects* refers to bioturbation structures that were formed by sediment burrowing or mixing by animals. SBED^{TM} facilitates the modelling of bioturbation structures using object modelling method that can superimpose biogenic structure objects on the bedding structure model. Each biogenic structure object can be assigned with a lamina template that is associated with its respective geometrical parameters as well as porosity and permeability distributions. The workflow used for using the bioturbation modelling feature in SBED^{TM} in this thesis is as follows.

The five different types of biogenic structure object templates (Figure 3.15) available in SBED^{TM} were; 1) U-shaped rod, 2) U-shaped body, 3) curved rod, 4) star rod, and 5) network rod. In this thesis the geometrical parameters of U-shaped body and Network rod are modified to model the crucial diagenetic features in Field X, the details of which are presented in Chapter 7. Firstly, the suitable biogenic structure object was selected based on the geometry of the diagenetic feature to be modelled. Then the corresponding geometrical parameters were specified to reflect the shape of the diagenetic feature as observed from the core and/or image log data. The set of geometrical parameters to be specified varied with the type of biogenic structure object.

Secondly, the spatial distribution parameters of the biogenic structure objects were specified to define the intensity of the diagenetic features. The three control types used to define the number and distribution of the biogenic structure objects were; 1) constant, 2) percentage and 3) bioturbation index. The constant type distribution was a deterministic method in which the total number of bioturbation structure objects to be modelled in the sub-model was specified. The percentage and bioturbation index types of distribution were stochastic methods. The percentage type required the input of the mean and standard deviation values of the percentage volume of the sub-model that was to be occupied by the bioturbation structure objects. The bioturbation index type was used to define the distribution of bioturbation structure objects in terms of bioturbation intensity. Bioturbation intensity in a body of sediment is defined as an indication of the number of animals living in there and the length of time over which they are active (Droser & Bottjer 1986). The six grades of bioturbation intensity are defined in SBED^{TM} are detailed in Table 1 below.

Table 3.1. Grades of bioturbation intensity (Droser & Bottjer 1986).

Grade	Description
1	A few discrete traces
2	Bioturbation affects less than 30% of the sediment, bedding is distinct
3	Between 30% and 60% of the sediment affected, bedding is distinct
4	60% to 90% of the sediment bioturbated, bedding indistinct
5	Over 90% of sediment bioturbated, and bedding is barely detectable
6	Sediment is totally reworked by bioturbation

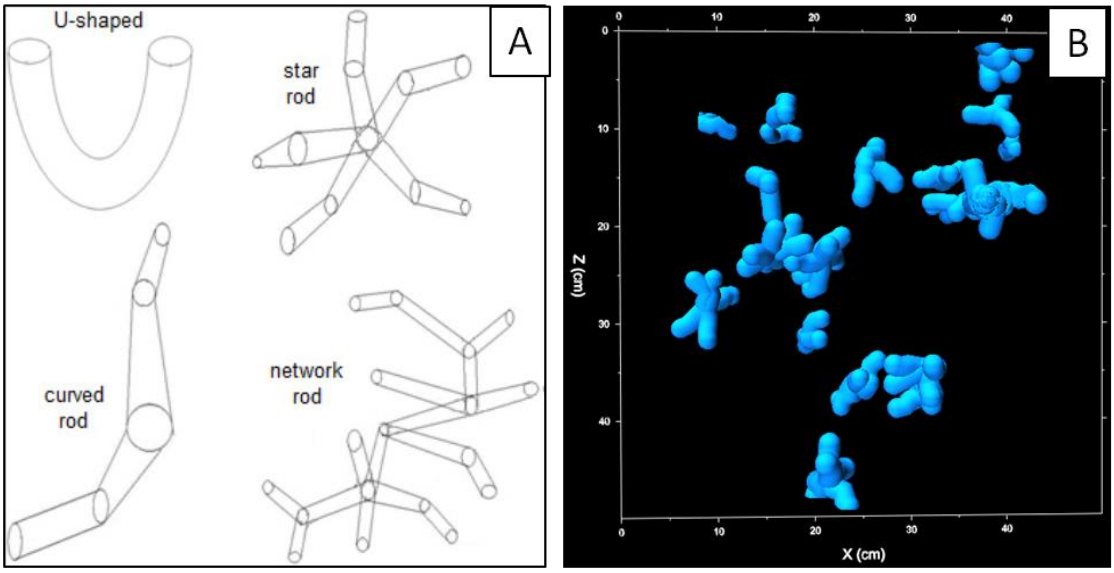

Figure 3.15. (a) Illustration of the types of bioturbation structure objects in SBED^{TM} (b) Example of star rod bioturbation structure distribution in 3D.

3.6. Property modelling

As discussed earlier, the grid cells representing the volumes between the bedform surfaces can be populated with porosity and permeability of the respective lamina set drawn from a Gaussian field (Ringrose *et al*. 2003, 2004). The mean, standard deviation, minimum and maximum values of porosity and permeability are input for each lamina type present in the sub-model. It is also possible to employ a suitable variogram to define the porosity and permeability distributions. When geostatistical data for the variogram are available, the suitable variogram model, trend and poro-perm correlation can be selected accordingly. Otherwise, the porosity and permeability distributions are derived from a random Gaussian field using the mean, standard deviation, minimum and maximum values. Random Gaussian field is the default and only option available in the current SBED^{TM} version used in this thesis for the latter method of property distribution. The Random Gaussian field distribution is hence used

for property modelling throughout this thesis, due to limited geostatistical data, especially for the carbonate field, Field X.

The input for porosity and permeability for the lamina templates were obtained from the Routine Core Analysis data in conjunction with the wireline log data and quality controlled using thin-section analyses. The permeability distribution obtained from core and probe permeameter data for both Field A and Field X indicated log normal distribution, while porosity indicated normal distribution. Further details of the statistical analysis of porosity and permeability data in Field A and Field X are discussed in Chapter 4 and Chapter 5 of this thesis, respectively. Unless otherwise stated, log normal distribution of permeability and normal distribution of porosity are hence used hereafter in this thesis. The porosity and permeability grids can be generated in irregular and regular formats as discussed in the following sections.

3.7. Upscaling

As discussed earlier, all NWM geometrical and property model grids are irregular grids, usually containing millions of cells. In order to apply a NWM grid in conventional field scale reservoir modelling and simulation workflows, it is necessary to upscale the grid properties. Upscaling can reduce the number of cells by orders of magnitude by coarsening and homogenising the 3D grid. There are two ways of upscaling the grid in SBED^{TM}; i) convert the irregular grids into regular grids and ii) use the built in flow based upscaling code to calculate the effective properties of the sub-models. The following sections provide the details of these two upscaling methods. In both methods porosity of the upscaled sub-model realisations is computed as the arithmetic average of the cell values.

3.7.1. Irregular and regular grids

In an irregular grid the individual cell dimensions Δx and Δy are the same, but the vertical dimension Δz varies for each cell (Figure 3.16). In contrast, the value of Δz is constant for all the cells in a regular grid (Figure 3.16). In SBED^{TM} the irregular porosity and permeability grids can be converted into a regular grid format (without changing the Δx and Δy values). This approach involves re-sampling of the property values using simple arithmetic averaging, using Δz for the regular grid as input. The Δz value should be selected such that the geological structures of interest are represented at sufficient resolution. The bed form structures can be preserved by increasing the

number of cells in the regular grid to capture the geometric details, although this could significantly increase the simulation time and required memory. The resulting NWM is still a high resolution centimetre scale model but is now more convenient to integrate in a conventional flow simulator workflow applying local grid refinement. The regular grid properties are then transferred into the reservoir model without any further upscaling. This upscaling approach will be applied in Chapter 4 to obtain the regular grid of the NWM to be incorporated in the reservoir simulation model of Field A.

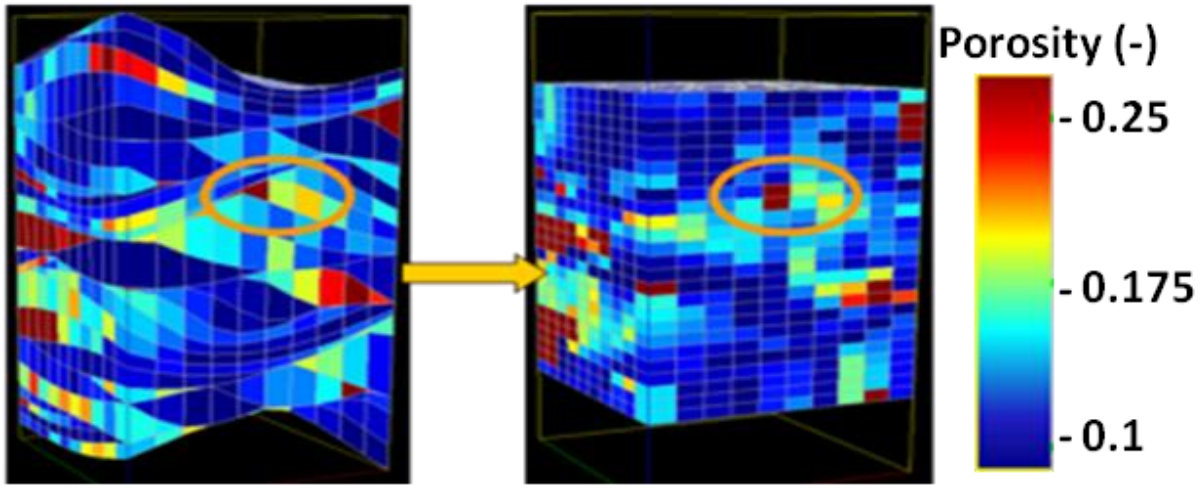

Figure 3.16. Unstructured porosity grid (left) after upscaling into regular grid (right).

3.7.2. Flow based upscaling

The upscaling concept in SBED^{TM} is based on the pressure solver method developed by Pickup and Sorbie (1996) and Pickup *et al*. (1995, 2000). The single-phase upscaling algorithm embedded within SBED^{TM} allows the upscaling of permeability grid to derive effective permeability, K_{eff}, (e.g Figure 3.17a) by employing flow-simulation-based numerical method. Single-phase upscaling refers to the process in which effective property values for a petrophysical grid are derived by assuming that flow simulation is for a single fluid phase. The upscaling algorithm used in SBED^{TM} is based on mixed finite-element method developed by The Foundation for Scientific and Industrial Research in Norway (Aarnes *et al*. 2008). The calculated effective permeability value represents the impact of the sub-grid scale heterogeneities in a sub-model on fluid flow and can be used as input to the reservoir simulation grid. The K_{eff} is a tensor as shown in Figure 3.17b. For example, k_{xy} here represents flow in the *x* direction because of a pressure gradient in the *y* direction.

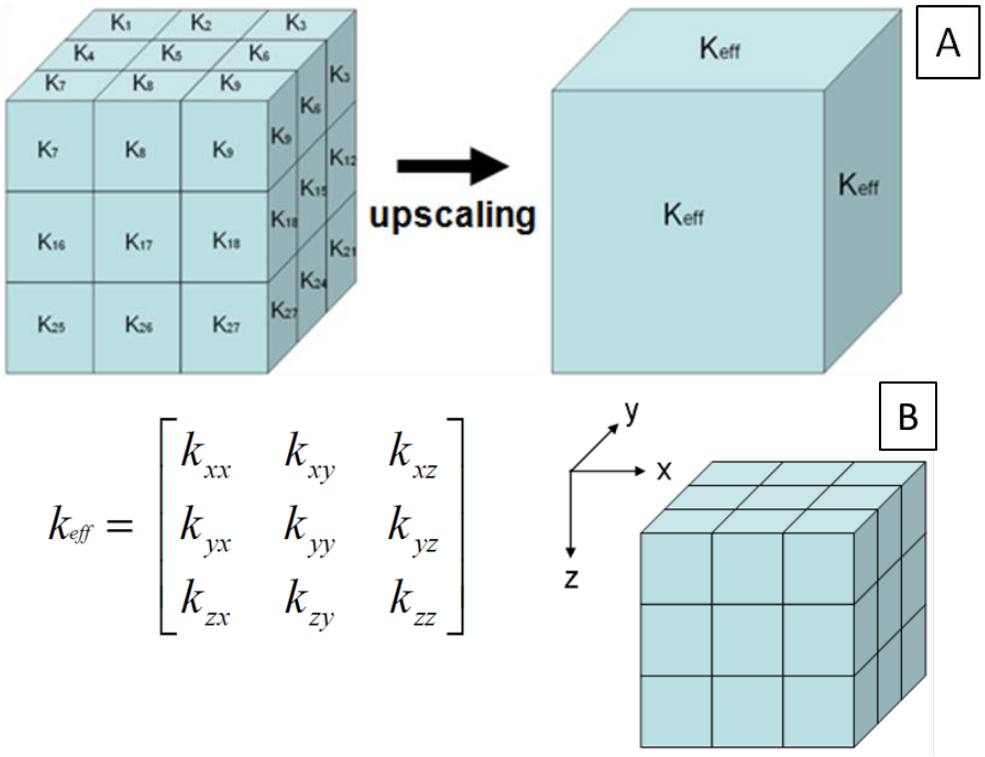

$$k_{eff} = \begin{bmatrix} k_{xx} & k_{xy} & k_{xz} \\ k_{yx} & k_{yy} & k_{yz} \\ k_{zx} & k_{zy} & k_{zz} \end{bmatrix}$$

Figure 3.17. (a) Upscaling a grid to derive effective permeability, $K_{eff.}$ (b) Components of effective permeability tensor. Modified from SBED^{TM} technical manual (2012).

In order to calculate K_{eff} numerically using the pressure solver method (Pickup & Sorbie 1996) boundary conditions must be applied to the grid. The three types of boundary conditions that can be applied for upscaling are; i) fixed boundary conditions, ii) linear boundary conditions, and iii) periodic boundary conditions. Fixed boundary conditions refer to no-flow boundary conditions and are appropriate to be used for homogeneous reservoirs with negligible cross-flow. Linear and Periodic boundary conditions refer to open flow boundary conditions. Linear boundary conditions assume that the pressure on boundary surfaces of the grid parallel to the pressure gradient in the XY and XZ planes changes linearly. Periodic boundary conditions assume that the pressure gradients at the top and bottom boundary surfaces (i.e. the x-y plane) are equivalent, the pressure-gradients at the front and back boundary surfaces (i.e. the x-z plane) are equivalent and flow across these surfaces is unrestricted. This method is illustrated in Figure 3.18 below. The selection of boundary conditions is dependent on the extent of heterogeneity and 'crossflow of fluid' to be represented in the 3D geomodel to be upscaled. Periodic boundary conditions apply no limitations to flow across boundary surfaces and allow the calculation of the full permeability tensor. Hence periodic boundary conditions are suitable to be applied for heterogeneous reservoirs with repetitive, alternating geological

structures. The pressure solver used with periodic boundary conditions in SBED™ accounts for 'crossflow', thus yielding the full permeability tensor shown in Figure 3.17b, and more accurate results compared to linear boundary conditions. In order to obtain more realistic K_{eff}, periodic boundary conditions will be used throughout this thesis where near-wellbore upscaling is employed (i.e. in Field X).

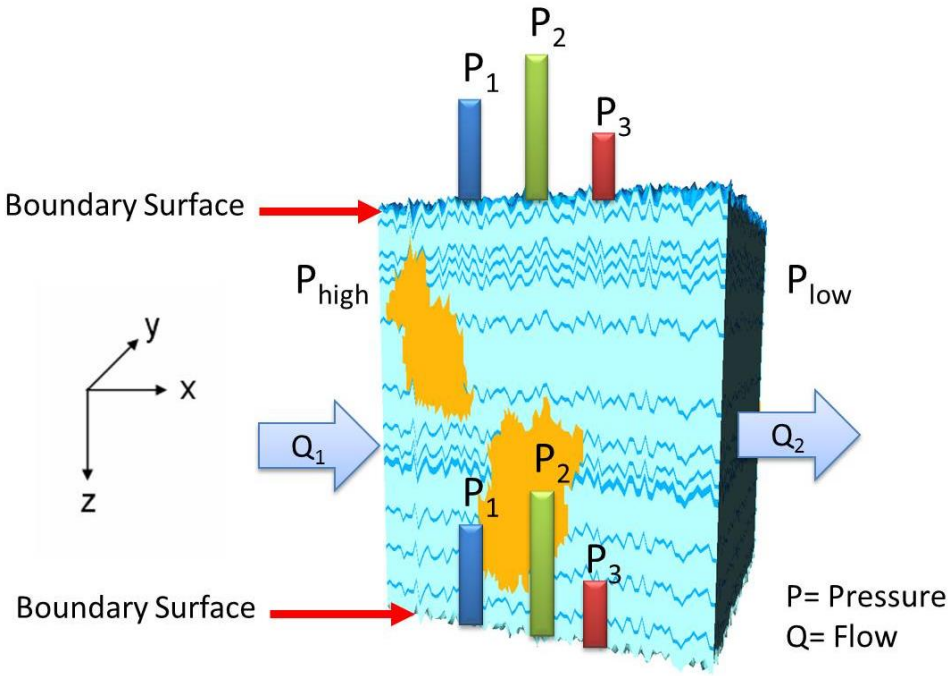

Figure 3.18. Illustration of periodic boundary conditions during flow-based upscaling of a sub-model. Here, the distribution of pessures at P_1, P_2 and P_3 represents the same pressure gradient at the top and bottom boundary surfaces and Q_1 and Q_2 represent the inlet and outlet flowrates respectively.

3.8. Discussion: NWM advantages and challenges

It is difficult to compare SBED™ with other modelling tools as there are only very few, if any other, commercially available modelling tools that are specifically designed to model the bedform scale in the near-wellbore region. Nevertheless, some advantages and practical challenges of the NWM tools and methods currently used in SBED™ have been discussed below.

3.8.1. Advantages

Geological and petrophysical heterogeneity at the core scale impact the effective flow properties at the reservoir grid-block scale (Nordahl *et al*., 2004; 2005; Ringrose *et al*., 2005). Hence, the first and obvious advantage of the NWM tools in SBED™ is that they model sedimentary structures in a way few other modelling tools do (Nordahl 2004).

Furthermore, the NWM tools employed in SBED^{TM} generate geological models that represent the scale at which the input data were collected. Earlier works by Nordahl *et al*. (2004) and Ringrose *et al*. (2005) demonstrate that the application of these NWM tools with the collaboration of sedimentological and petrophysical well data allows capturing the lamina scale and/or bed scale heterogeneity in the reservoir model. NWM methods provide a solution to the biased sampling and scale transition issues and results in better estimates of porosity, permeability and Net-to-Gross values of the reservoir (Nordahl *et al*. 2004 2005; Ringrose *et al*. 2005). The effective property values calculated through near-wellbore upscaling can be incorporated into the existing reservoir simulation workflows. The NWM tools in SBED^{TM} thus facilitate the integration of multi-scale data to provide accurate property statistics for reservoir modelling (Ringrose *et al*. 2003, 2004).

As discussed in the earlier sections of this chapter, the geometrical parameters controlling the sedimentary bedform modelling and the petrophysical properties are specified by the user. Since the effect of the input parameters on the output, geometrical and petrophysical, is well understood the NWM tools are not used as a 'black-box', which is an important aspect to generate realistic models of sedimentary structures (Nordahl 2004). The distribution of petrophysical properties within the near-wellbore model is not a random process as they are spatially and statistically conditioned to the lamina types within a sub-model. This link between the sedimentary structures and the petrophysical properties is observed to be particularly advantageous when probe permeameter measurements are available. Finally, the NWM tools in SBED^{TM} enable the generation of numerous equally probable realisations of a range of bedform heterogeneities that could be representative of reservoir rock. This aspect is beneficial to understand the uncertainty associated with the distribution of geological heterogeneities in the near-wellbore model outside the plane of view of core slabs.

3.8.2. Challenges and limitations

One of the main challenges of using SBED^{TM} is to obtain reasonable input values for the various geometrical parameters in order to ensure that the simulated sedimentological structures are realistic. This is because SBED^{TM} approximates the geological processes with the migration of sine curves and does not simulate the actual depositional and migration process. Although the overall geometry of bedforms can be imitated reasonably well with this method, it is challenging to incorporate all the natural

variability and there is a tendency to create overly simple structures compared to actual observations on well data (Nordahl 2004). However, as discussed before, this can be overcome by choosing the geometrical parameters carefully and not using SBED™ as a 'black-box'. An additional difficulty is that the observations used to derive the lamina scale input parameters are often in 2D, for example sedimentological description of core slabs, while the modelling process is in 3D. NWM in SBED™ is hence an iterative process between the input parameters, the output models, and the geophysical data used for quality control. In this context, it is worth noting that one of the limitations of SBED™ in its current version (SBED™ 4.2) is that the geological features cannot be modelled deterministically, for instance to reproduce a 3D model based on 3D X-Ray tomography data of a certain core slab. Exact duplication of the well cores is hence not possible using SBED™. Another key challenge is to obtain the porosity and permeability distributions that are to be specified for each lamina type if the probe permeameter measurements are not available. Where applicable, the core plug values can be used to mitigate this issue and to derive the input parameters for porosity and permeability at the lamina scale (e.g., Nordahl 2004). Nevertheless, the input values obtained from core and probe permeameter must be carefully evaluated to mitigate the risks of sample bias and under- or overestimating the upscaled permeability value.

Another challenge is that certain post-depositional aspects cannot be simulated directly using the NWM tools in SBED™, especially compaction. However, effects of compaction can be addressed implicitly in the form of the petrophysical data input. It must be noted the NWM tools in SBED™ are tailored to model clastic depositional environments. It is hence challenging to model carbonate reservoirs, which have typically undergone complex diagenetic processes. However, it is shown in Part II of this thesis how these challenges are addressed by using various NWM tools to model diagenetic features such as stylolites, centimetre scale fractures and corrosion-enhanced porosity in the carbonate field Field X. Depending on the nature of geological detail to be represented in a near-wellbore model, the output grids from SBED™ could often occupy large amount of disc space and take long CPU time to run flow-simulation-based upscaling calculations. Such hardware and time limitations could become especially cumbersome when the NWM workflow need to be employed for large hydrocarbon fields with numerous wells. This challenge will be addressed in Chapter 7

using a novel near-wellbore upscaling workflow which employs the NWM tools in SBED^{TM} to obtain upscaled porosity-permeability transforms for reservoir simulation.

3.9. Concluding remarks

The modelling approach employed by the NWM tools in SBED^{TM} is process-oriented, rule-based and stochastically formulated. Overviews of the NWM workflow and the various tools involved in each step have been described in this chapter. Furthermore, the main advantages of the NWM tools in SBED^{TM}, the limitations and associated challenges have been discussed. It will be shown in the following chapters of this thesis how NWM workflow is coupled with dynamic data to improve the reservoir characterisation and simulation of highly heterogeneous clastic and carbonate reservoirs. Chapter 4 presents how this workflow will be used to obtain near-wellbore model of a heterogeneous fluvial reservoir to be calibrated with well test data. NWM workflow will be used to build detailed geological model of a selected interval of the Sherwood formation in Well A of Field A. Chapters 6, 7 and 8 present how the near-wellbore modelling and upscaling workflow was used to model and upscale the multi-scale heterogeneities in Field X, a highly heterogeneous carbonate reservoir, to improve reservoir characterisation and simulation. In Field X, a generic near-wellbore modelling workflow was used to generate high resolution core-scale sub-models of representative volume of core rather than building a geological model for the entire well interval.

Part I

NEAR-WELLBORE MODELLING APPLIED TO A CLASTIC RESERVOIR

In this part a novel workflow to improve dynamic calibration of reservoir simulation models involving high resolution near-wellbore modelling (NWM) is illustrated. This workflow enabled the integration of seismic, wire-line data and well core logs from highly heterogeneous reservoirs in field-scale reservoir simulations. The chapter presented in this part demonstrates that a NWM-enhanced-geoengineering workflow can improve reservoir characterisation by applying NWM to a real clastic reservoir; Field A. Field A has a high variance of permeability distribution at core scale. Centimetre-scale models, containing several million cells, representing the fine geological details of the near-wellbore region, were constructed using available data from core and open-hole well-log suits. The resulting unstructured well models were upscaled to centimetre-scale regular grids and the latter were incorporated into a field-scale simulation model to evaluate the dynamic behaviour of the reservoir employing static model transient test. A number of flow simulation sensitivities were performed, comparing conventional local grid refinement in the near-wellbore region with that involving NWM. A significant improvement in the reservoir characterisation and the calibration of dynamic models was observed when NWM tools were employed. The results of this chapter showed that using NWM tools for reservoir modelling yielded more precise flow simulations consistent with observed dynamic data and improved our fundamental understanding of the interactions between the reservoir and the wellbore.

Chapter 4. APPLICATION OF NWM-ENHANCED GEOENGINEERING WORKFLOW TO A HETEROGENEOUS CLASTIC FIELD

This chapter illustrates a novel workflow involving high resolution near-wellbore modelling (NWM), which allows us to accurately include seismic, wire-line data, image logs, and well core logs from highly heterogeneous reservoirs in field-scale reservoir simulations.

4.1. NWM-enhanced geoengineering workflow

The NWM-enhanced geoengineering workflow involves the integration of NWM techniques with local grid refinement (LGR) of the near-wellbore region into the classical geoengineering workflows described in Chapter 2 (Figure 4.1). Using well-log and outcrop data, detailed geological models of the near-wellbore region were built and upscaled such that they could be incorporated into the sector- or field-scale models using local grid refinement (LGR). Numerical simulation of transient test response of these static models enabled the correlation of known geological features in the reservoir model to the actual production data and well-testing parameters, which helped to improve the calibration of static and dynamic models. This workflow yielded more realistic static and dynamic model realisations of the reservoir. In particular, the aim of this workflow was to understand the effects of structural complexity, diagenetic alterations and textural variations on reservoir property modelling and simulation studies by bridging the gap between NWM scale and field scale. NWM preserved the geological details of the reservoir in the near-wellbore region and the corresponding petrophysical properties in the upscaled model, which were exported into a conventional reservoir simulator. The upscaled NWMs complemented the nested, locally refined grids centred at the well and contributed to the accuracy of the simulation results significantly, particularly in the Early-Time Region (ETR), and allowed for a more robust validation of static and dynamic models.

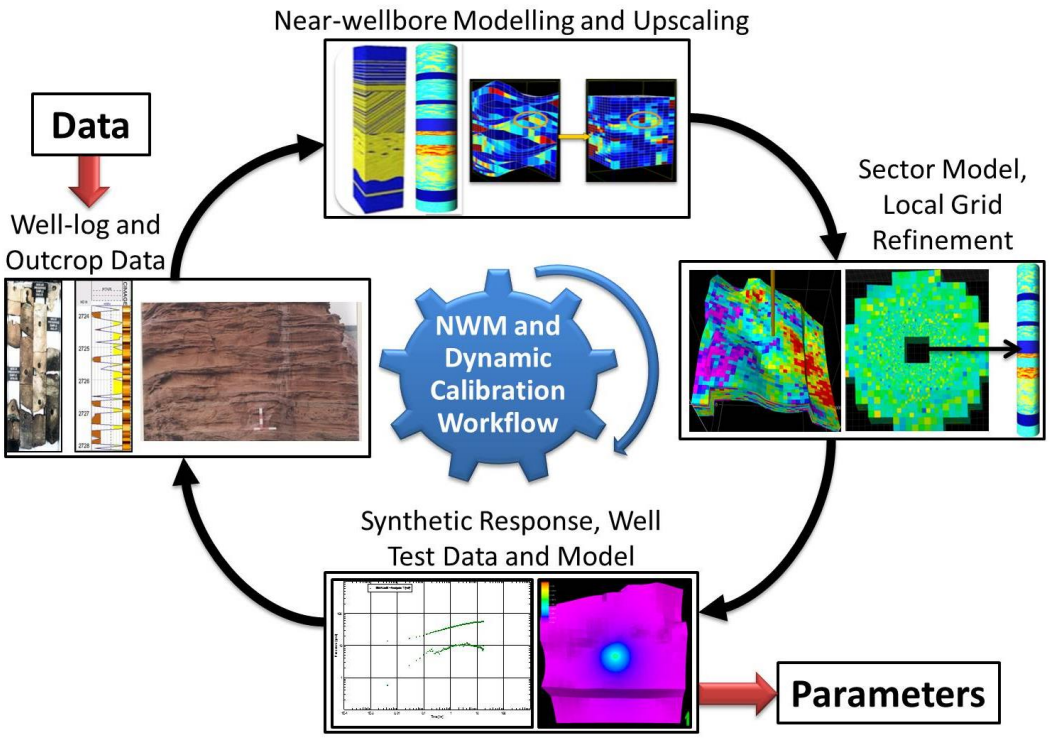

Figure 4.1. Geoengineering workflow that incorporates near-wellbore modelling (NWM), upscaling and dynamic model calibration.

4.2. Heterogeneous onshore clastic reservoir, Field-A

4.2.1. Field-A background

NWM was incorporated into a geoengineering workflow using real well data from Well-A, a vertical production well in an onshore clastic reservoir, named Field-A. The main sources of data used in this chapter are the well log data, core data and well testing data, all from Well-A. Field-A comprises a Triassic sandstone reservoir (Colter & Harvard 1981) overlying an onshore and offshore aquifer. The geological context of Field A is described in detail by Colter & Havard (1981). The chief reservoir zone comprises a Triassic broadly fining- and muddying-upward succession approximately 150 m thick, overlain by over 300 meters of playa mud rocks. The reservoir itself can be divided into two main intervals, a lower section of high net to gross fluvial deposits and an upper section comprising more common lacustrine and floodplain mudrocks (McKie et al. 1998). The sedimentary sequences in Field-A were interpreted to be of braided fluvial environment of deposition. The deposition of sediments in braided fluvial environment is majorly controlled by the flow of water in rivers and streams. Figure 4.2 illustrates the main morphological features of a braided fluvial depositional system. The key mechanism of accumulating sediment in a braided fluvial system is found to be

associated with the processes of deposition on the mid-channel bars (Nichols 2009). The principal reservoir sand bodies in braided fluvial systems originate within the channels and are often discontinuous (Davies *et al*. 1992).

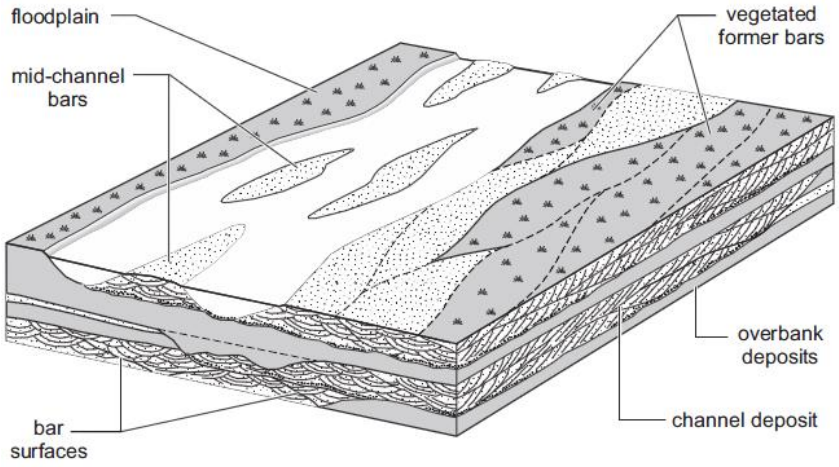

Figure 4.2. Conceptual model of braided fluvial depositional environment illustrating the main morphological features. Modified from Nichols (2009).

The reservoir of Field-A is dominated by arkosic sandstones and contains significant amounts of mudstone, calcrete and calcrete conglomerates (such as rhizocretions) (Bowman *et al*. 1993). Here, calcrete is defined as secondary carbonate formation of calcareous, semi-conducted aragonite or early diagenetic calcite forming in unconsolidated sediments in semi-arid and arid climate regimes (Walls *et al*. 1975). Hay & Reeder (1978) provide a detailed mineralogical and petrological description of calcretes. The reservoir facies can be broadly classified into channel sand, sheetflood and floodplain. Here, facies is defined as a body of rock with specified/distinct characteristics that formed under certain conditions of sedimentation, which indicate a particular process, set of conditions or environment (Reading 1996). The parameters controlling the reservoir quality are mainly the grain size, clay content and localized small scale heterogeneities that can influence the K_v/K_h ratio (Bowman *et al*. 1993). Well-A in particular is dominated by multi-storey minor channel-fills of cross-bedded sandstone (Bowman *et al*. 1993), which have been characterized as the best reservoir zones in this well based on core and petrophysical analysis. These minor channel fills are sandwiched between the flood plains and the rhizocretion bearing sandstones (Toro-Rivera *et al*. 1994). Outcrop analogue studies done at a nearby outcrop analogue have provided better understanding of the heterogeneities in this reservoir and show that the

calcrete nodules and conglomerates caused a significant reduction in permeability and porosity (Newell 2006; McKinley *et al*. 2004) in the rhizocretion bearing sandstones. On the other hand, well-test analysis of the pressure transient data of Well-A indicates that the minor channel fills could act as high permeable conductive zones in the well interval, as detailed in the following section. The working hypothesis for this chapter was hence that the small-scale channel fills impact the pressure transients observed at Well-A. We conjecture that a geological model, which can capture these small-scale heterogeneities, will be able to represent the observed transient data more accurately, both qualitatively and quantitatively. Therefore, it was attempted to capture the combination of multi-scale heterogeneities, which are believed to significantly affect the flow behaviour of this reservoir, using NWM as they are otherwise challenging to model through conventional simulation workflows. The main focus is the ETR and Middle-Time region (MTR) of the transient data and not the Late-Time Region (LTR) where aquifer support affects the pressure derivative and small-scale heterogeneities become less important.

4.2.2. Data analysis

The well test simulation results discussed in this chapter are obtained from commercial well testing software. Figure 4.3 shows the normalised log-log plot of the pressure derivative versus time from the actual pressure build-up data in Well-A. Note that the available well-test data is for a shorter time than the simulated transient data. The synchronization of pressure and rate data was accurately checked. The transition in the derivative behaviour between 10-16 minutes was caused by the change of the hydrostatic pressure reference. Well-test interpretation results indicated a skin factor $S = -3.6$ and an effective permeability value of $K_e = 44.1\ md$, which compared well to the geometric average of the core permeability (K_g) of 42.9 md (Toro-Rivera *et al*. 1994). The high negative skin value could imply linear flow in the ETR and was supported by an approximate half slope trend of the derivative. This trend was probably due to the high permeable minor channel fills flowing linearly into the wellbore. The consequent change into radial flow in the middle time region (MTR) suggested that these high conducting channels are of limited extent present in the vicinity of the wellbore with correlation lengths much smaller than sector grid model dimensions, and do not extend over the entire well-test drainage area. Figure 4.3 also indicates a roll-over in the LTR that could be due to existence of pressure support arising from the

association between onshore and offshore aquifer (Toro-Rivera *et al*. 1994). However, this is neither discussed in further detail nor considered in the simulation scenarios as it is out of scope of the current study.

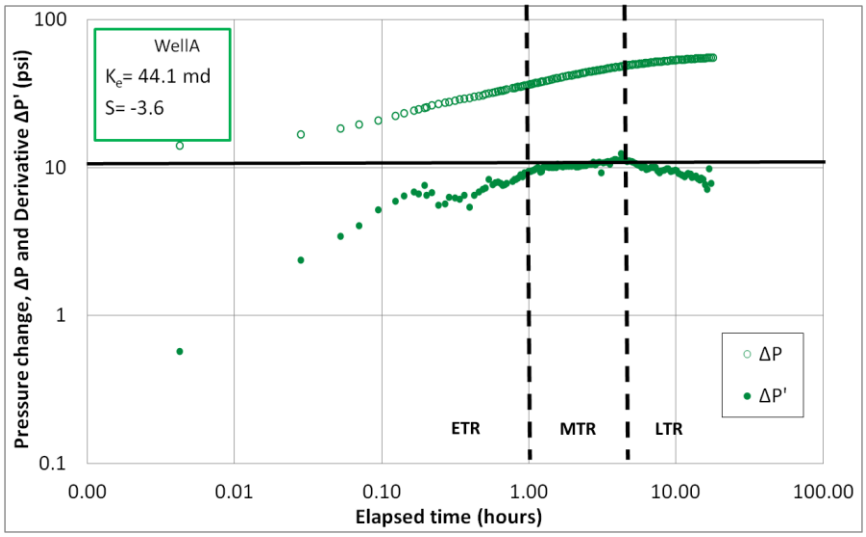

Figure 4.3. Log-log plot of the pressure and pressure derivative vs. time from the actual pressure-buildup data in Well-A (Toro-Rivera *et al*. 1994) showing the Early-Time Region (ETR), Middle-Time Region (MTR) and Late-Time Region (LTR) flow regimes.

4.3. Well-A near-wellbore model

Using the available core images, wireline and sedimentary logs from Well-A, a detailed classification of the lithofacies in the well was performed, mainly on the basis of shale volume, distribution of calcretes and extent of cementation. The lithofacies classification was corroborated in this study with the lithofacies classification previously done by earlier workers (e.g., Bowman *et al*. 1993; Toro-Rivera *et al.* 1994). The heterogeneities that were aimed to be represented explicitly in the NWM were the high permeable cross bedded minor channel fills that were only several centimetres thick, with short correlation lengths. These high permeability streaks were interpreted to have caused negative geoskin (Corbett *et al*. 1996) in the well, as theorized by Toro-Rivera *et al.* (1994). The NWM of Well-A was thus designed for a representative well interval of 65 m with areal dimensions of 50m x 50m (Figure 4.4). The choice of the preferred areal dimensions of the NWM was made with the assistance of several simulation sensitivities based on the correlation lengths of the high permeability zones, aiming to obtain a reasonable match with the ETR behaviour.

The core images and the sedimentary logs were used as reference for specifying the bedding boundaries in the well interval and customizing the bedding structure templates for each lithofacies in the near-wellbore modelling software discussed in Chapter 3, SBED^{TM}, including the high permeable streaks. The porosity-permeability models were obtained using input from core plug and well log data (Figure 4.4), as explained in the NWM workflow in Chapter 3. An optimum choice of grid cell specifications of the NWM with $\Delta x = \Delta y = 5$m and $\Delta z = 0.2$ m was made based on simulation sensitivities. More details of the sensitivity analysis are presented in Appendix A. This grid resolution minimized the total number of grid cells and thus the simulation runtimes while, at the same time, maximized the representation of geological and petrophysical heterogeneities. Once the geometrical parameters were input, in SBED^{TM}, every realisation required an average of fifteen minutes to be completed. The resulting NWM accounted for the high permeability streaks as well as the details of the lithofacies such as cross bedding, massive bedding, and calcrete nodules (Figure 4.4). The NWM resolution, which was preserved through LGR in the dynamic model, was significantly greater than the typical grid size encountered in dynamic models.

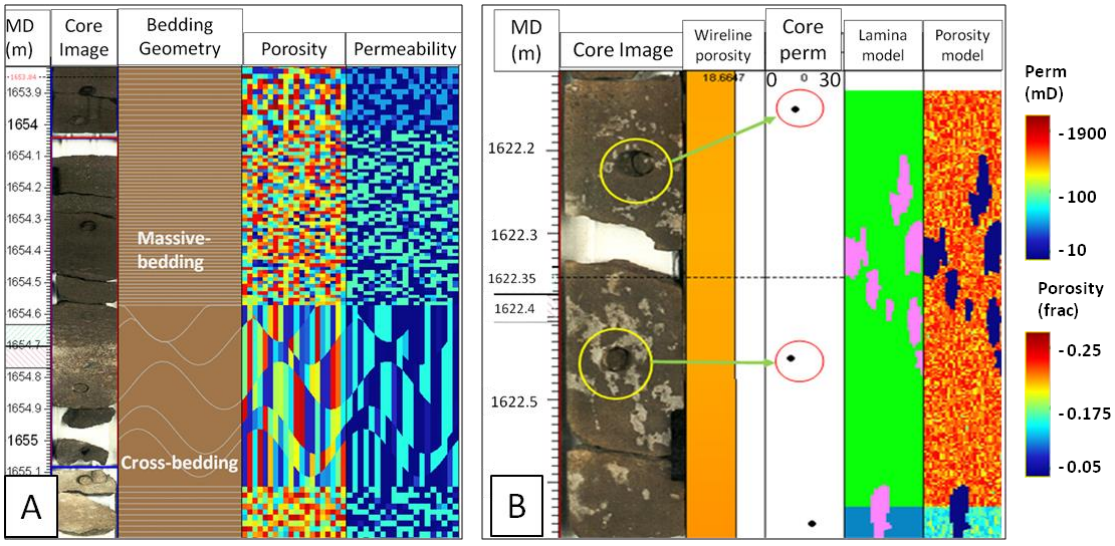

Figure 4.4. (a) Example of a well-section from Well A used to define bedding boundaries and bedding structures based on the well core and the corresponding porosity and permeability realisations. (b) Representation of the calcrete and cemented zones in the geometrical (Lamina model) and property models in the NWM of Well-A. Note that the porosity and permeability logs represent the modelled distribution, based on core and wireline data.

Three realisations of the geometrical model each with five property model realisations, and thus a total of fifteen realisations of the high resolution- near-wellbore property models (Figure 4.5) were generated to ensure confidence in the repeatability of the results. Each regular-NWM grid was then directly embedded into the centre of the Field-A sector model without any further upscaling, as described in the following section.

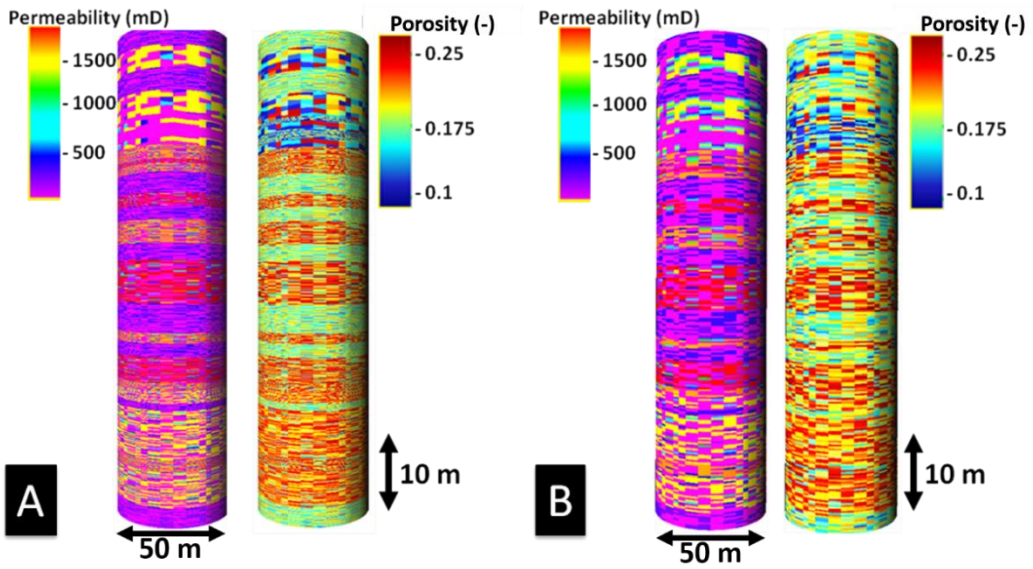

Figure 4.5. (a) Irregular grid realisations of permeability and porosity in the NWM for the 65 m interval of the well. The total number of cells is 126,800. The cell dimension in vertical direction is variable. (b) Regular grid realizations of permeability and porosity for the well. The total number of cells is 26,000. The cell dimension in vertical direction is constant.

4.4. Well-A sector model and local grid refinement (LGR)

A field scale 3D sector model of dimensions 2 x 2 x 0.65 km was built using the Well-A log data and the available seismic top surface of Field-A for the 65m vertical interval of the well. The model was built with the aim to generate synthetic pressure transients for the reservoir and analyse the impact of a detailed representation of the near-wellbore region. Several scenarios of coarse models were tested and compared to the available dynamic data of Well-A. This will be discussed in the next section of this chapter. The reservoir model was populated using commercial reservoir modelling software, with 4 facies types using Sequential Indicator Simulation (SIS) and with petro-physical properties using Sequential Gaussian Simulation (SGS) (Figure 4.6) (Deutsch *et al.* 1998; 2002). The SIS method was used to generate realisations of facies distribution by

assigning an indicator representation for each facies type within each grid block. The advantage of the SIS algorithm is that the spatial correlations can be accounted for and the distribution of facies is conditioned to the facies distribution in the well (Deutsch & Journel 1992, p 151). The facies indicators were then used in conjunction with SGS to condition the distribution of porosity and permeability in the grid blocks. SIS and SGS methods are stochastic processes which yield geostatistical representation of the reservoir properties, and do not simulate the geological processes that resulted in the distribution of reservoir properties. They are hence associated with some uncertainty in the distribution of lithofacies and associated properties. In the case of Field A, SIS and SGS could represent the MTR and LTR sufficiently accurate to conduct this study, as will be verified by the well test simulation results in a later section.

It was expected that once the fine scale NWM grid is combined with the coarse sector model, the resulting flow simulations would be associated with significant amount of numerical artefacts due to the dramatic change in the grid cell dimensions. This would render it difficult to study the actual effect of NWM on the simulation results. Hence, the optimum number of nested grids was analysed in the sector model in order to ensure that the difference in results after embedding the NWM is not just an effect of numerical artefacts but rather due to the simulation of geological details in the near-wellbore region. Hence, four scenarios of LGR were generated using the Cartesian gradual refinement method (Figure 4.7). In Cartesian gradual refinement method the degree of refinement was gradually increased towards the well in each grid direction over a number of levels. The target number of sub-divisions within the highest refinement (innermost) level and the number of levels was specified such that the cell dimensions of the innermost grid level for all the LGR scenarios are $\Delta x = \Delta y = 5$m and $\Delta z = 0.2$ m, i.e. equal to the cells of the NWM (Figure 4.7). All LGR scenarios used the same permeability and porosity distribution as the original coarse model, i.e. without any upscaling or downscaling and without embedding the NWM. The optimal LGR scenario was chosen after carefully testing that the obtained results had numerically converged. The corresponding well test results are discussed in detail in the 'Results and Discussion' section. It must be noted that although numerical results have converged, none of the LGR models captured the ETR behaviour of the transient data correctly. This is due to inadequate representation of the centimetre to decimetre scale geological structures in the dynamic model and this issue was addressed by including NWM.

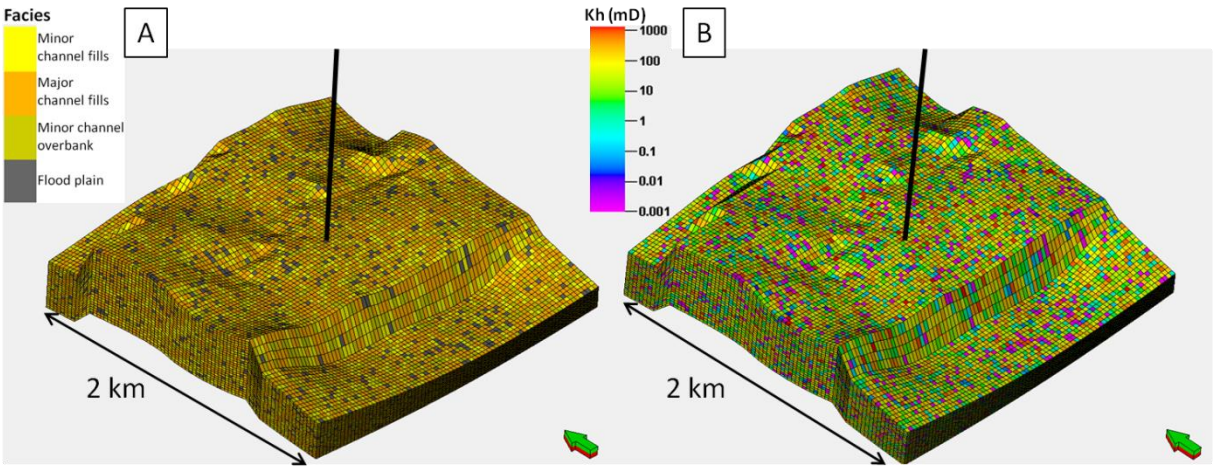

Figure 4.6. Facies (a) and permeability (b) distributions in the field scale model of the reservoir with the well placed in the center. Average grid block size is $\Delta x = \Delta y = 25$m and $\Delta z = 2$ m. The total number of cells is 158,080.

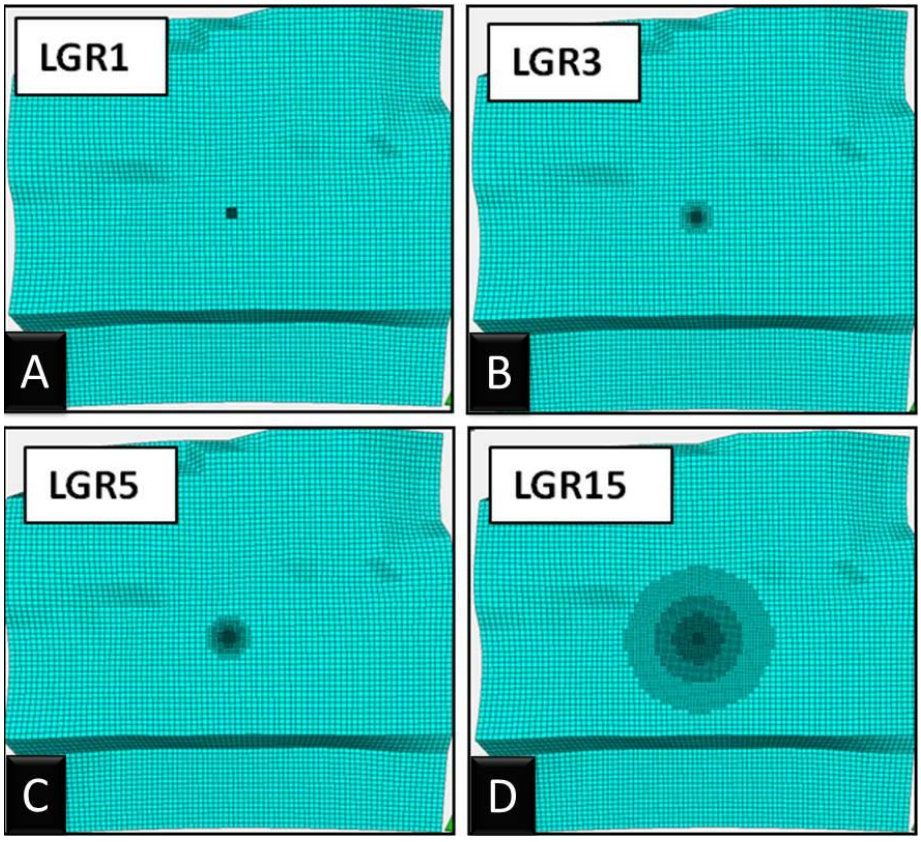

Figure 4.7. Nested grid scenarios generated for this study by the linear gradual refinement method. The cell dimensions of the innermost grid level for all the scenarios are $\Delta x = \Delta y = 5$m and $\Delta z = 0.2$ m, i.e. equal to the cells of the NWM. (a) LGR1: 1 refinement level, (b) LGR3: 3 refinement levels, (c) LGR5: 5 refinement levels and (d) LGR15: 15 refinement levels.

4.5. Combining sector and NWM grids in the flow simulator

The NWM of Well-A was fused into the sector model by carefully replacing the innermost and finest level of the local grids with the exported NWM property grids of Well-A. This ensured that the cell and model dimensions of the near-wellbore grid and the replaced locally refined grid were the same. Any further upscaling of the NWM grid properties was hence not necessary. A single-phase black oil simulator with a slightly compressible fluid was applied to generate drawdown curves of Well-A, producing at a flow rate of 990 STBO/d (157.41 m^3/day) for 300 hours. Wellbore storage was absent. The input parameters for reservoir simulation were obtained from Toro-Rivera *et al*. (1994).The density of oil and solution gas-oil ratio used in the fluid model is 50.9 lb/ft^3 (815.313 kg/m^3) and 0.35 MSCF/STB (62) respectively. Single phase flow simulations were performed for the sector model with local grid refinement before and after embedding the NWM. The flow simulations were repeated using all the fifteen realisations of the NWM and the corresponding pressure derivative curves were analysed using standard well-testing analysis software. Finally, the simulated well-test response was compared against the available real pressure transient data of Well-A.

4.6. Results and discussion

Four coarse model scenarios (Table 4.1) with varying grid specifications, facies classification, permeability predictors and spatial distribution parameters of porosity and permeability (i.e. varying correlation lengths) were tested to obtain the closest possible match to the real well data. The real well-test showed a permeability value close to the geometric average of core plug permeability values, thus indicating the random nature of permeability distribution. It must be noted, that an effective permeability value equivalent to the geometric mean is also be possible in the case of a reservoir with tilted layers. However, based on the geological model established for Field A, the possibility of tilted layers was ruled out. Hence, the equivalency of well test permeability to geometric mean of core plug permeability values was attributed to the random distribution of permeability. Therefore, the spatial correlation lengths were set to 25m to reproduce the random property field (Corbett *et al*. 2012; Hamdi 2012), causing a plateau (within 1 hr to 4 hr) in the MTR close to the middle time stabilization observed in the actual well test data. Figure 4.8 shows the log-log plot of the pressure derivative versus time, comparing the coarse grid scenarios, i.e. without LGR, with Well-A data that could match Well-A transient pressure response.

Note the dissimilarity in the extension of the pressure drops in the beginning of the test due to the difference in the grid cell sizes. The finer models showed lesser pseudo wellbore storage effect than the coarser ones (Archer & Yildiz 2001). After comparing the static transient pressure response analysis for these models, the optimum scenario for the next steps of the analysis was selected based on the skin, K_e and the trend of derivative rise in the MTR. As discussed earlier, the roll-over observed in the LTR of real well-test response of Well-A was not simulated in these scenarios. The preferred sector model, 'Coarse A', had the grid specifications $\Delta x = \Delta y = 25$ m, $\Delta z = 2$ m outside the NWM region. It contained four main facies types in the well interval, each with its individual permeability predictors (Table 4.2). The pressure transient analysis for this model yielded an effective permeability of $K_e = 27.9$ md, which compares well with the geometric average of core permeability and suggests random distribution of permeability. The skin factor was S = -2.6. The relative extent of agreement between the implications of K_e and S, of the coarse models with those from real well-test data has provided the basis for initial evaluation of the coarse model scenarios.

Table 4.1. Summary of coarse grid scenarios compared with Well-A data.

Scenario Name	**Grid block dimensions, Δx x Δy (m)**	**Facies and K_h distribution**
Coarse A	25 x 25	K_h calculated from individual permeability predictors used for each facies type as presented in Table A1
Coarse B	25 x 25	Permeability distributed using SGS from the K_h log obtained using the permeability predictors from Table A1
Coarse C	50 x 50	K_h calculated from individual permeability predictors used for each facies type as presented in Table A1
Coarse D	50 x 50	Permeability distributed using SGS from the K_h log obtained using the permeability predictors from Table A1

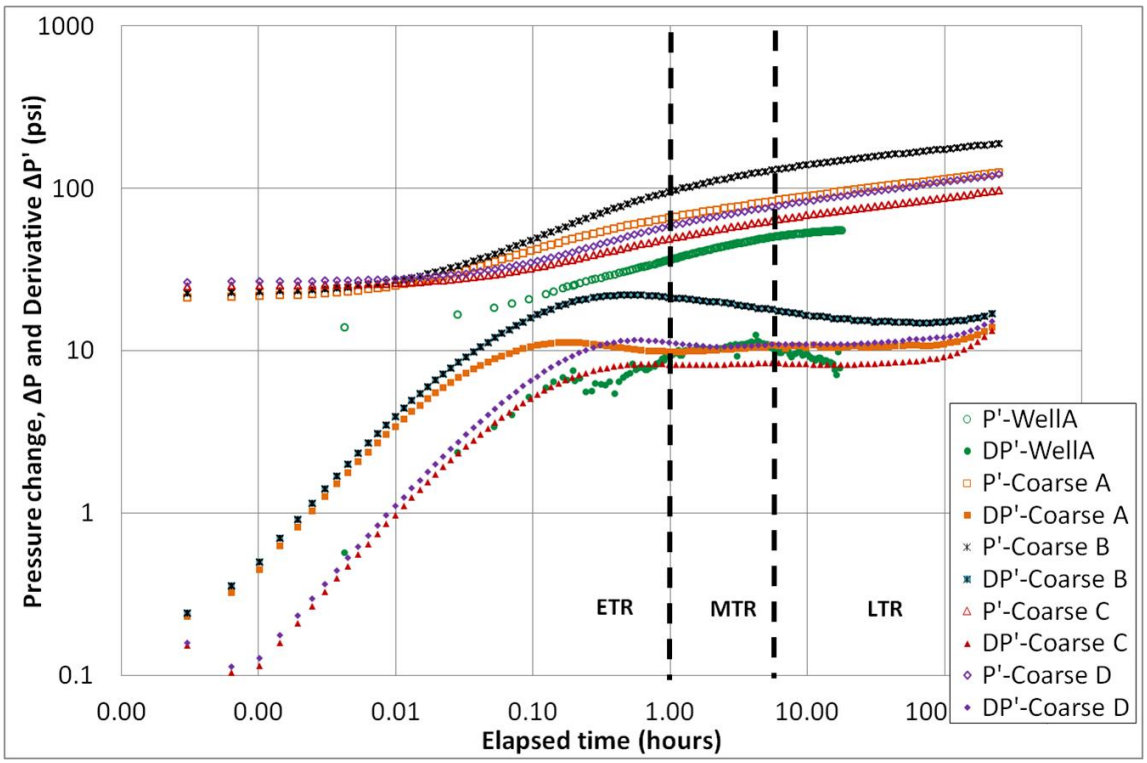

Figure 4.8. Log-log plot of the pressure derivative vs. time comparing the coarse grid scenarios with Well-A data. The details of the scenarios are explained in Table 4.1.

Table 4.2. Permeability predictors used for the sector model best case scenario.

Facies	**Permeability predictor** (**K_h = Horizontal permeability,** Φ = Porosity)
Minor Channel Fill	$\log K_h = 12.708 \times \Phi - 0.3243$
Major Channel Fill	$\log K_h = 13.681 \times \Phi - 0.3713$
Minor Channel Overbank	$\log K_h = 25.616 \times \Phi - 3.2951$
Flood Plain	$k_h = 0.01\ mD$

4.6.1. Local grid refinement results

The pressure derivative curves for the four scenarios of nested grids with varying gradual refinement and distance from the well were obtained for the sector model of Field-A. Figure 4.9 compares the different nested grid scenarios with the coarse model without local grid refinement, showing the typical log-log plots of normalised pressure derivative vs. time curves.

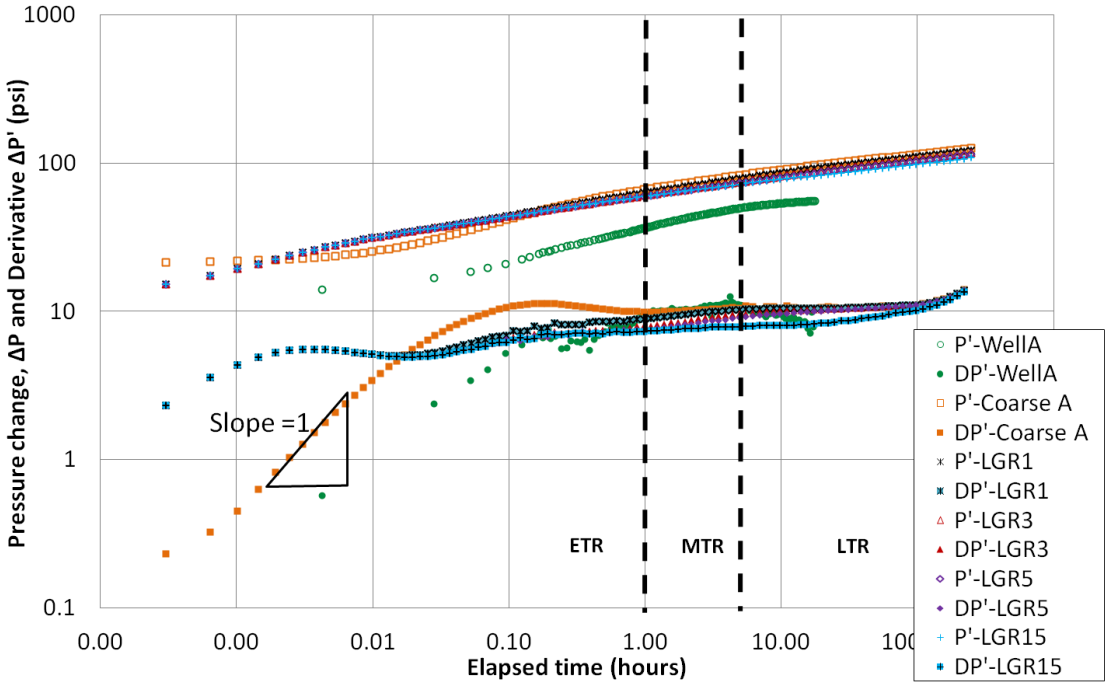

Figure 4.9. Log-log plot of pressure derivative vs. time comparing the coarse grid and nested grid scenarios of Field-A sector model. LGR1, LGR3, LGR5 and LGR15 re LGR scenarios with 1, 3, 5 and 15 nested grids, respectively.

The unit slope in the ETR indicates wellbore storage. However, wellbore storage was absent in the model and this numerical artefact was significantly reduced in the nested grid scenarios. This is fake wellbore storage effect (Archer & Yildiz 2001) and is a numerical artefact and arises from the use of pseudo steady-state well index in transient well-test simulations. It can be reduced with improved spatial discretisation although some artificial ("fake") wellbore storage would be still present in the very beginning of the test. The fake wellbore storage effect is directly proportional to the lateral dimension of the cell and is inversely proportional to the hydraulic diffusivity coefficient (Archer & Yildiz 2001). Using a transient well index (Archer & Yildiz 2001) or by employing highly refined cells in the near wellbore area can minimize this phenomenon (Hamdi 2012). The identical pressure transients for the simulations with local grid refinement showed that the numerical solution converged in the ETR starting from the scenario LGR3, which had 3 nested grids in the area within 75 m radius from the well (Figure 4.7b). This is further corroborated by Figure A4 in Appendix A, which shows the plot of pressure at a point of time in the ETR versus the inverse of number of cells within the local grid refinement zone of each LGR scenario. Note that the lateral extension of the NWM was only 50 m x 50m, which was the same as the innermost nested grid. LGR3

was chosen as the optimum nested grid scenario for the next step of this workflow that involves near-wellbore modelling since the grid refinement has reduced the numerical artefacts to the desirable extent in the region of interest (ETR and MTR) without a dramatic increase in the computation time. The grid cell specifications of the innermost level of LGR3 were $\Delta X = \Delta Y = 5$m and $\Delta Z = 0.2$ m. The static model transient pressure analysis of LGR3 sector model yielded an effective permeability of $K_e = 28.7$ md and skin factor of S = -2.96 (See Figure A2, Appendix A). Although the simulated pressure response converged for LGR3, it still did not agree with the observed pressure transient data. This indicated that the geological representation of the near-wellbore region was insufficient and the NWM workflow, discussed in the next section, was used to address this issue.

4.6.2. Near-wellbore modelling results

The 15 realisations of the near-wellbore model were embedded into the LGR3 model (Figure 4.10) and the pressure transient response was simulated and analysed for each scenario. Figure 4.11 represents the multiple well-test simulations and the corresponding interpretation statistics, i.e. the mean and standard deviation of the skin factor and of the effective permeability, for all 15 equiprobable realisations. More detailed results are presented in Table 4.3. Clearly, the effect of NWM on the pressure transient response was almost identical for all realisations when the pseudo wellbore storage effect ended (i.e. after around 0.02 hr). This was reflected by the negligible deviation of S and K_e results from analysis of the static model pressure transient analysis. The static model pressure transient analysis results for the 'LGR3+NWM' sector model were: mean $K_e = 28.55$ md and mean S = -3.53 (See Figure A3, Appendix A). The LGR3+NWM scenarios yielded pressure transient analysis results that matched well with Well-A results compared to the earlier scenarios. The skin factor was almost identical to that of Well-A, demonstrating the successful replication of the high permeable minor channels in the vicinity of the wellbore. The linear flow behaviour towards the wellbore characterised by the derivative rise in the ETR was also simulated with improved accuracy.

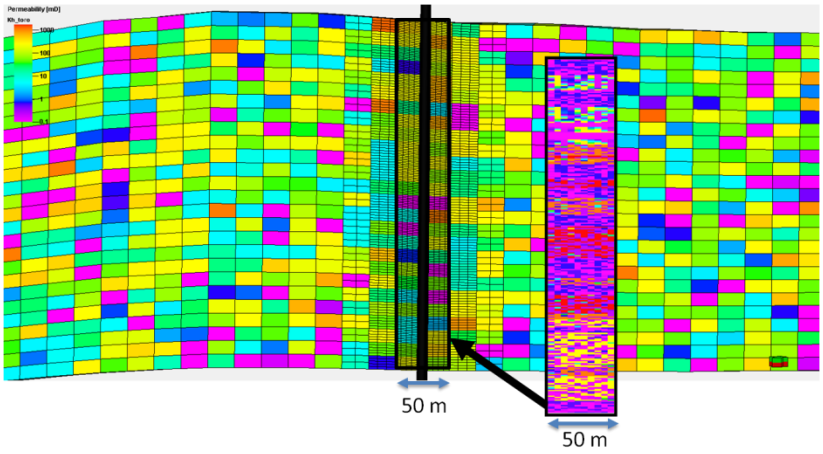

Figure 4.10. Cross-section of Field-A sector model illustrating the replacement of the finest level of the local grid refinement in LGR3 scenario by the NWM property realisation in the simulator.

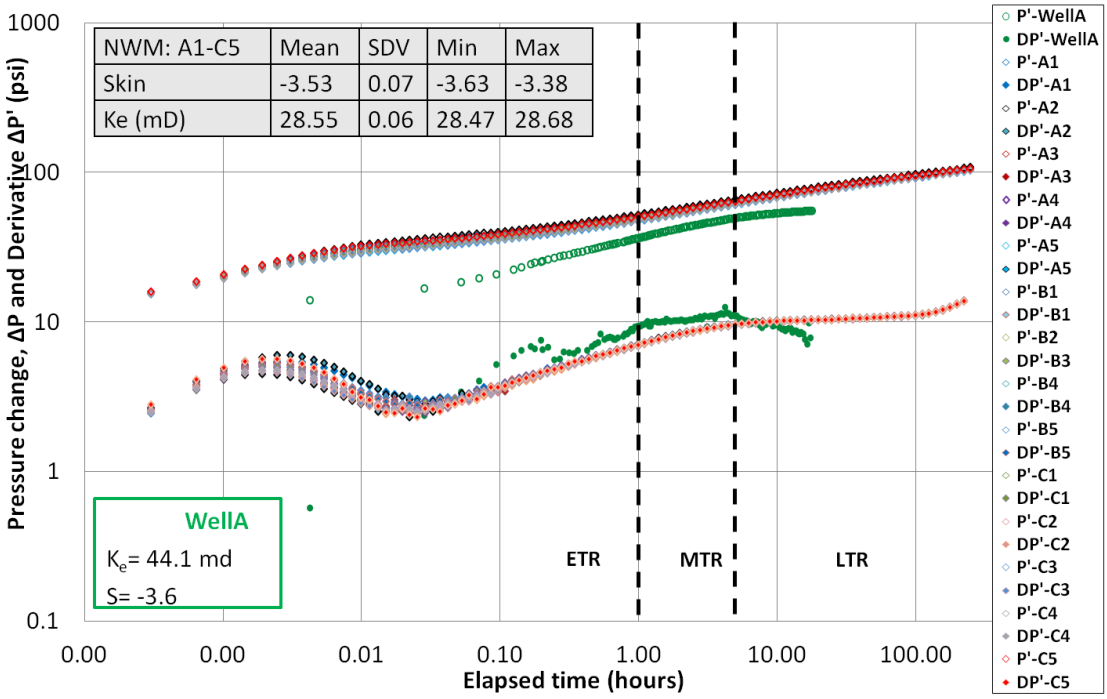

Figure 4.11. Log-log plots of pressure derivative vs. time for the LGR3 sector models each incorporated with one of the 15 different NWM realisations (Table 4.3). Note that the curves overlay each other after the end of the pseudo wellbore storage period. The multiple realisations A1 to C5 correspond to the three bedding realisations A, B and C and their respective five property realisations 1 to 5.

Table 4.3. Summary of static model pressure transient analysis results.

CASE	Skin	Ke (mD)
WellA	-3.6	44.1
Coarse A	-2.6	27.9
LGR3	-2.96	28.7
A1	-3.438	28.5
A2	-3.378	28.48
A3	-3.557	28.55
A4	-3.518	28.6
A5	-3.628	28.5
B1	-3.519	28.56
B2	-3.563	28.47
B3	-3.569	28.51
B4	-3.51	28.64
B5	-3.52	28.59
C1	-3.548	28.56
C2	-3.6	28.61
C3	-3.622	28.47
C4	-3.582	28.68
C5	-3.457	28.56

4.6.3. Comparing the Coarse, LGR and LGR+NWM models with Well-A data

Figure 4.12 compares the pressure transient response and analysis results of the coarse, LGR3 and 'LGR3+NWM' scenarios with that of Well-A. The difference between the pressure transient responses of these scenarios is significant in the ETR. Note that the aim of this study was not to obtain the exact match for the real test but to calibrate the static model with the Well-A dynamic data by reproducing the main heterogeneities affecting the ETR. In the case of Well-A these heterogeneities were the highly conducting cross bedded channel fills.

Although both local grid refinement models, LGR3 and 'LGR3+NWM', exhibited considerably lower numerical artefacts and higher negative skin than the coarse model, the derivative rise in the ETR could only be captured in the model 'LGR3+NWM', i.e. once small-scale heterogeneities were included in the dynamic model through NWM. The mean negative skin value of 'LGR3+NWM' realisations (S= -3.53) was higher than that of the LGR3 (S= -2.96), while the mean effective permeability value was similar, and closely replicated the actual skin value of Well-A (S= -3.6). This indicated that the difference in pressure response compared to the coarse model was not just due to the reduced numerical artefacts but was a result of the local geological heterogeneities, mainly the thin high permeability streaks acting as conductive zones. These heterogeneities were preserved in the NWM, which demonstrated that the geological heterogeneities could be responsible for the uncommon trends in the well-test response

of Well-A and that the skin effect was likely a negative geoskin, (Corbett *et al*. 1996) as proposed by the conventional interpretation (Toro-Rivera *et al*. 1994). Clearly, refinement of the coarse model grid alone, as in the case of LGR3, cannot reproduce this feature as effectively. Hence, NWM complements the dynamic calibration workflow by providing better understanding of the early time well-test responses and to consider the alternate geological scenarios in the test interpretations. In other words, adopting a NWM workflow can improve the representation of small scale heterogeneities (e.g., effective flow barriers or conductive zones) that are significant for flow and hence increase the representativeness of the sector model.

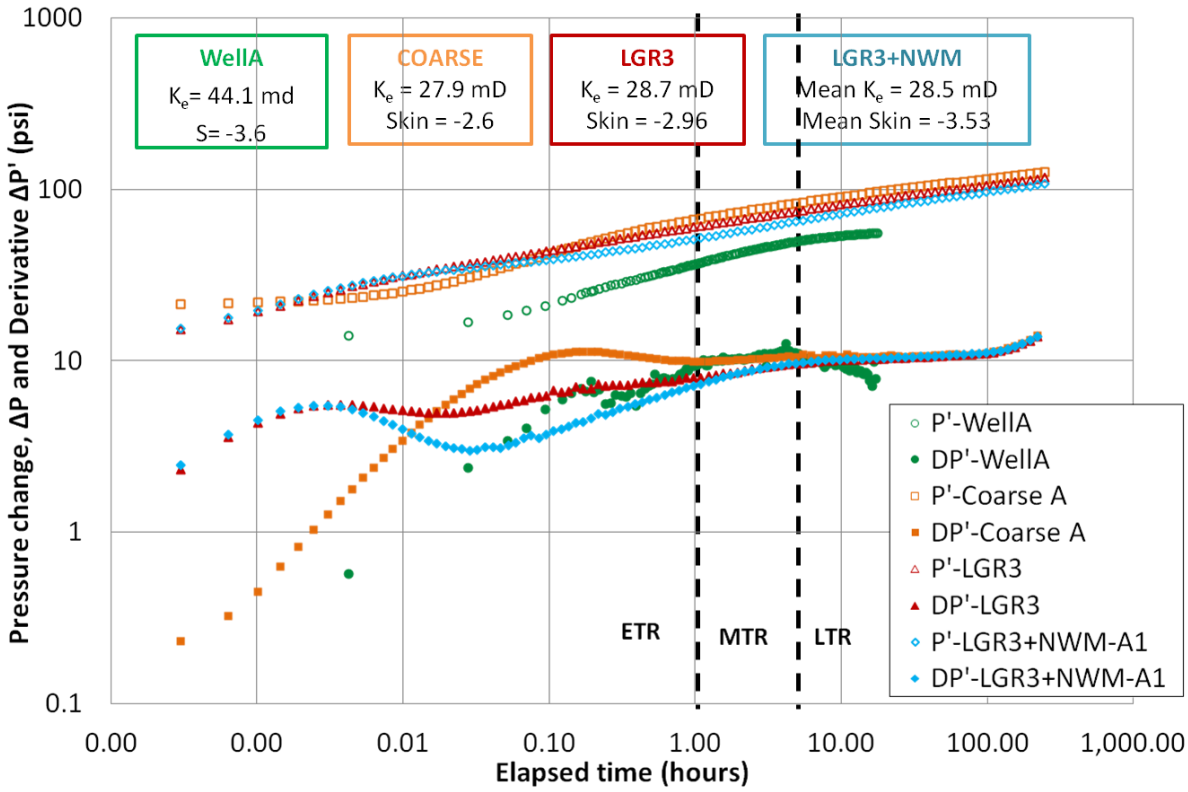

Figure 4.12. Comparison of the log-log plots of pressure derivative dp (psi) vs. time (hour) of the coarse, LGR3 (local grid refinement with 3 levels of nested grids) and LGR3+NWM (local grid refinement embedded with high resolution NWM realisation A1) with the real well data

4.7. Conclusions

The geoengineering workflow of Corbett *et al*. (2009, 2010) was extended by incorporating high resolution representations of the geological heterogeneity in the near-wellbore region through local grid refinement and near-wellbore modelling (NWM). This allowed more realistic representation of the sector model by incorporating higher

variability in the distribution of the properties, particularly in the near-wellbore region. Using numerical simulations on reservoir models with and without NWM showed that the incorporation of small-scale heterogeneity into reservoir models through NWM allowed reiteration of the real pressure transients more closely. The workflow ideally requires good ETR data sampling for dynamic calibration, but in the event of sparsely sampled ETR, the skin value and the derivative rise observed from the MTR can be used as a measure of dynamic calibration of the geostatistical NWM. In summary, the following key conclusions were drawn:

- NWM can be used to build more representative geomodels in the near-wellbore region and capture a wide range of multi-scale heterogeneities in a reservoir. This reinforced the study of skin effects in a numerical modelling environment.
- NWM was fused with field scale geomodelling, complemented by local grid refinement to minimize numerical artefacts in the ETR. This resolved the near-wellbore geology at scales that could not be achieved in conventional reservoir simulation and hence provided clear information on skin effects.
- Choosing the optimum grid cell size of the NWM regular grid enabled the replication of the highly conducting cross bedded channel fills in the near-wellbore region of Well-A. This was reflected in the well-test simulation results.

Overall, a fit-for-purpose geoengineering workflow that involved NWM improved reservoir characterisation of heterogeneous reservoirs. It is hence suggested to extend this workflow to other challenging reservoirs, such as carbonates, which have multi-scale geological heterogeneities that impact near-wellbore flow.

Part II

NEAR-WELLBORE MODELLING APPLIED TO A CARBONATE RESERVOIR

Carbonate reservoirs host a major portion of the world's remaining conventional and unconventional hydrocarbon reserves, typically containing multi-scale geological heterogeneities varying over many orders of magnitude in size. Characterising and representing the geological and petrophysical heterogeneities robustly in reservoir models is a prime challenge in carbonate reservoir simulation. The general objective of the chapters presented in Part II is to develop novel near-wellbore upscaling workflows that address the challenges and uncertainties associated with reservoir simulation of a complex carbonate reservoir, Field X.

Chapter 5. THE GIANT CARBONATE FIELD, 'FIELD X'

This chapter provides an overview of the geology of Field X, the giant carbonate reservoir investigated in this thesis, before detailing the available dataset. The diagenetic model of Field X employed in this thesis, which was proposed by earlier workers, will then be discussed in detail followed by an overview of the main porosity types present in Field X. The major uncertainties and challenges associated with the field's geomodel and reservoir simulation model will then be discussed. The contents of this chapter including Figures, specifically Figures 5.8 to 5.12, leverage the proprietary reports provided by the operator, published works and discussions with the asset specific geologists and reservoir engineers. Unless otherwise specified, the thin-section images were taken using plane polarized light. For confidentiality reasons the proprietary reports could not be cited here.

5.1. Geological overview of Field X

5.1.1. Depositional setting

Field X is a giant offshore oil and gas field comprising an Eocene-Oligocene limestone reservoir with broad, low relief anticline trap structure. Field X has a long production history and consists of a gas column up to 50 m thick, an oil rim of about 20 m thickness, and an underlying aquifer. The oil rim is being produced through gas cap drive mechanism (Oates *et al*. 2012). The stratigraphic summary of Field X is illustrated in Figure 5.1a. Field X and the basin that contains it are part of a bigger structure that is a pericratonic rift basin (Goswami *et al*. 2007). The latter is an offshore, divergent passive continental margin basin that was formed due to extensional tectonics during Late Jurassic-Early Cretaceous period with NW-SE-trending horst-graben geometry (Goswami *et al*. 2007). Earlier studies indicate that this rifting was followed by moderate subsidence during the Late Cretaceous, leading to the development of extensive carbonate platforms. Carbonate deposition occurred as a series of shallowly dipping clinoforms representing stacked facies belts prograding into the basin. The major structural feature in the block containing Field X and its neighbouring hydrocarbon fields is the East-fault zone (Figure 5.1b). The East fault zone was an extensional fault through Late Eocene time, and has undergone an episode of transpressional activity in post-mid Miocene time. The information related to the extensional offset and the shear sense of the fault is unknown. An extensive shale unit

was deposited post-Miocene, following carbonate deposition, which acted as the regional cap rock for the reservoir. However, it is noted that within the limestone localised shale beds act as local cap rocks for different pay zones (Goswami *et al.* 2007).

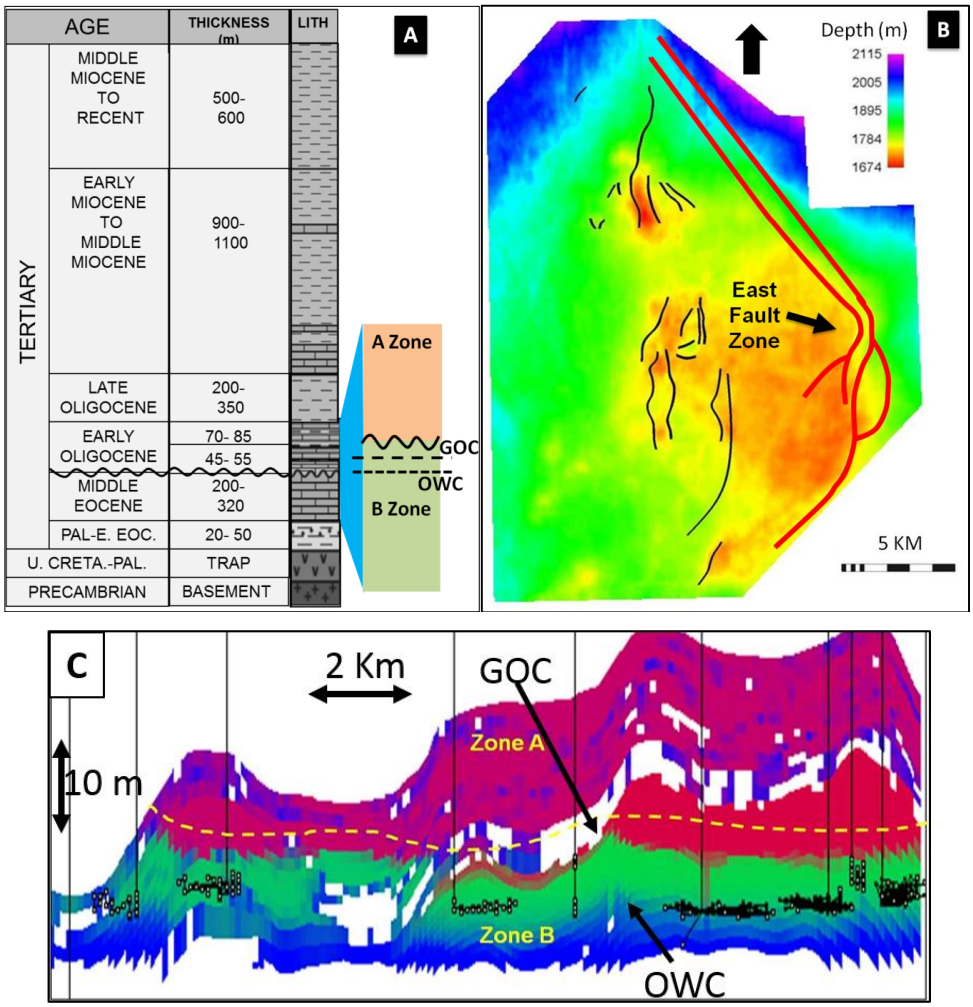

Figure 5.1. (a) Stratigraphic summary of Field X showing the main reservoir units A Zone and B Zone, the gas-oil contact (GOC) and the oil-water contact (OWC). (b) A 2D cross-section image of Field X showing the main fault polygons present in the geomodel. The East fault zone (red coloured fault polygons) is the major structural feature in the block containing Field X and its neighbouring hydrocarbon fields. (c) Cross-section image of Field X showing the oil-water contact, gas-oil contact and the hydrocarbon bearing zones A Zone and B Zone.

The overburden to the reservoir comprises offshore mudstone and limestone. The reservoir is currently at its maximum burial depth (about 1700 m) and may also be at its maximum temperature of 130˚C (Richard Steele, personal communication, June 2013).

The main reservoir zones were interpreted to be highstand systems tracts and their stratigraphic framework was summarised as a stacked depositional sequence in a distally steepened shallow ramp setting (Figure 5.2). The predominant lithofacies in the field are nodular packstones and wackstones intercalated by grainstones. The two main hydrocarbon bearing zones in Field X are the Early Oligocene A Zone and Eocene B Zone (Figure 5.1c), which are continuous across the field. A Zone is dominated by *Nummilitides* while B Zone limestones mainly contain an assemblage dominated by *Coskinolina*. The biota and facies associations indicate that the A Zone records more distal sedimentation on the ramp than the B Zone.

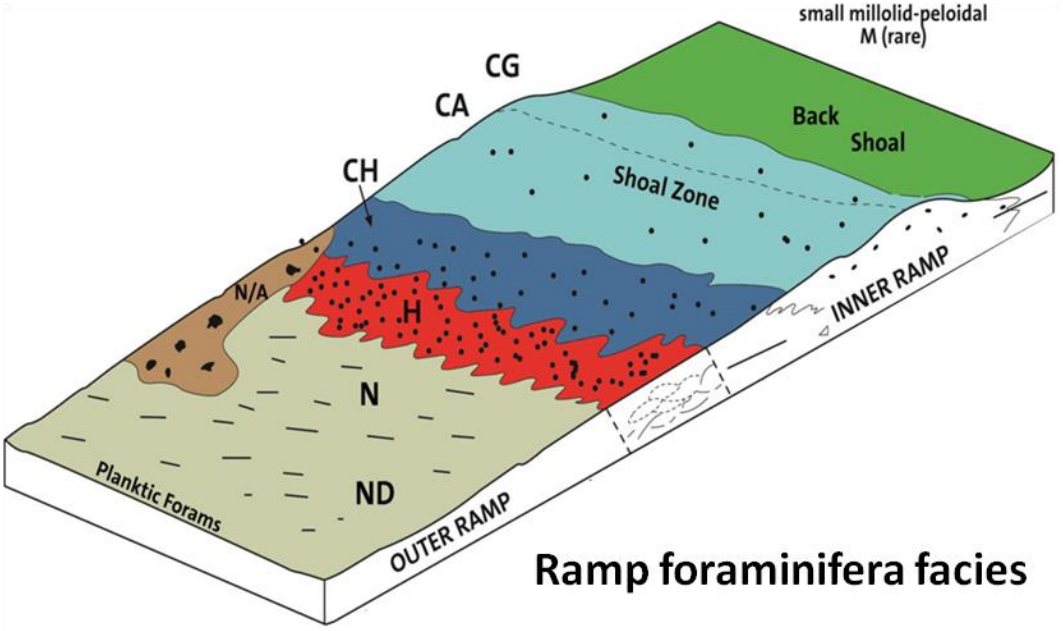

Figure 5.2. Illustration of foraminifera distribution in the limestones of Field X with reference to a carbonate ramp model zone (modified from Barnett *et al*. 2010). Facies key; CG- *Coskinolina* grainstones; CA- *Coskinolina* and *Alveolinid* facies; CH- *Coskinolina* hash facies; M- *Miliolid* facies; H- Hash facies with fine skeletal debris; N- *Nummulites* matrix-rich limestones, ND- *Nummulites-Discocyclinid* facies.

The major lithofacies types identified in Field X are summarised in Table 1 and their thin-section images are shown in Figure 5.3. A Zone and B Zone were interpreted to be of different depositional systems and were hence treated separately throughout this thesis. The oil-water contact and the gas-oil contact are located in the B Zone. Earlier works noted that A Zone and B Zone are separated by a disconformity that is associated with sub-aerial exposure corresponding to an early Oligocene fall in relative sea level. A shale unit, which has been referred as ‘A/B unconformity’ in this study, overlies this

disconformity and acts as transient local seal, capping the B Zone. The A/B unconformity is interpreted in earlier studies to be the basal part of a much thicker weathering profile truncated during the transgression proceeding the deposition of A Zone.

Table 5.1. Interpretation of lithofacies observed in Field X (Barnett *et al*. 2010).

Facies	Subfacies	Component grains	Interpretation
M	**M** - Miliolid facies	Mainly small miliolids	Restricted inner ramp (back shoal)
C	**CC**- *Coskinolina*-dominant facies	*Major:* Large specimens of *Coskinolina* and large rotalids*; Minor:* Small miliolids, rotalids, textularids and alveolinids	Inner ramp (shoal)
	CG - *Coskinolina* grainstone facies	*Major*: Commonly fragmented *Coskinolina*, small and large rotalids, miliolids and textularids; *Minor*: Alveolinids, rare *Orbitolites* and *Peneropolis*	Inner ramp (shoal)
	CA - *Coskinolina* and *Alveolina* facies	*Major: Coskinolina* and *Alveolina*; *Minor: Orbitolites*, rare undifferentiated soritids and green algae	Inner ramp (shoal)
	CP - *Coskinolina* packstone facies	*Major: Coskinolina*	Inner ramp (shoal)
	CH - *Coskinolina* "hash" packstone to wackestone facies	*Major:* Coskinolinid debris	Proximal mid-ramp
A	**AH-** Alveolinid "hash" facies	*Major: Alveolina*	Inner ramp
	AW- Alveolinid wackestone	*Major: Alveolina*	Inner ramp
Fl	**F-** Floatstone	*Floatstone dominated by platy corals.*	Shallow mid-ramp
Fr	**Fr-**Framestone	*Framestone dominated by platy corals.*	Shallow mid-ramp
H	**H** - "Hash" facies with fine skeletal debris	*Major:* Finely comminuted bioclasts, rotalid and echinoderm debris	Mid-ramp
R	**R** - Rotalid packstone facies	*Major:* Rotalids (e.g. *Lockhartia*), echinoderm debris	Mid-ramp
	RH - Rotalid "hash" packstone facies	*Major:* Rotalid fragments, finely comminuted undifferentiated bioclasts, echinoderm debris	Mid-ramp
G	**G** - *Gypsina* wackestone to packstone facies	*Major: Gypsina*; *Minor:* Nummulitids, nummulithoclastic debris, *Lepidocyclina*, *Operculina*	Outer ramp
N	**N** - Nummulitid grainstone to wackestone facies (partially dolomitised)	*Major:* Nummulitids	Outer ramp
	AN - Nummulitid wackestone to packstone facies with alveolinids	*Major:* Nummulitids, alveolinids; *Minor: Operculina*	Outer ramp
	ND - Nummulitid facies with discocyclinids (partially dolomitised)	*Major:* Nummulitids, discocyclinids	Outer ramp
PF	**PF-**Planktonic foram	*Planktic foram mudstone to wackestone.*	Deepest water facies identified

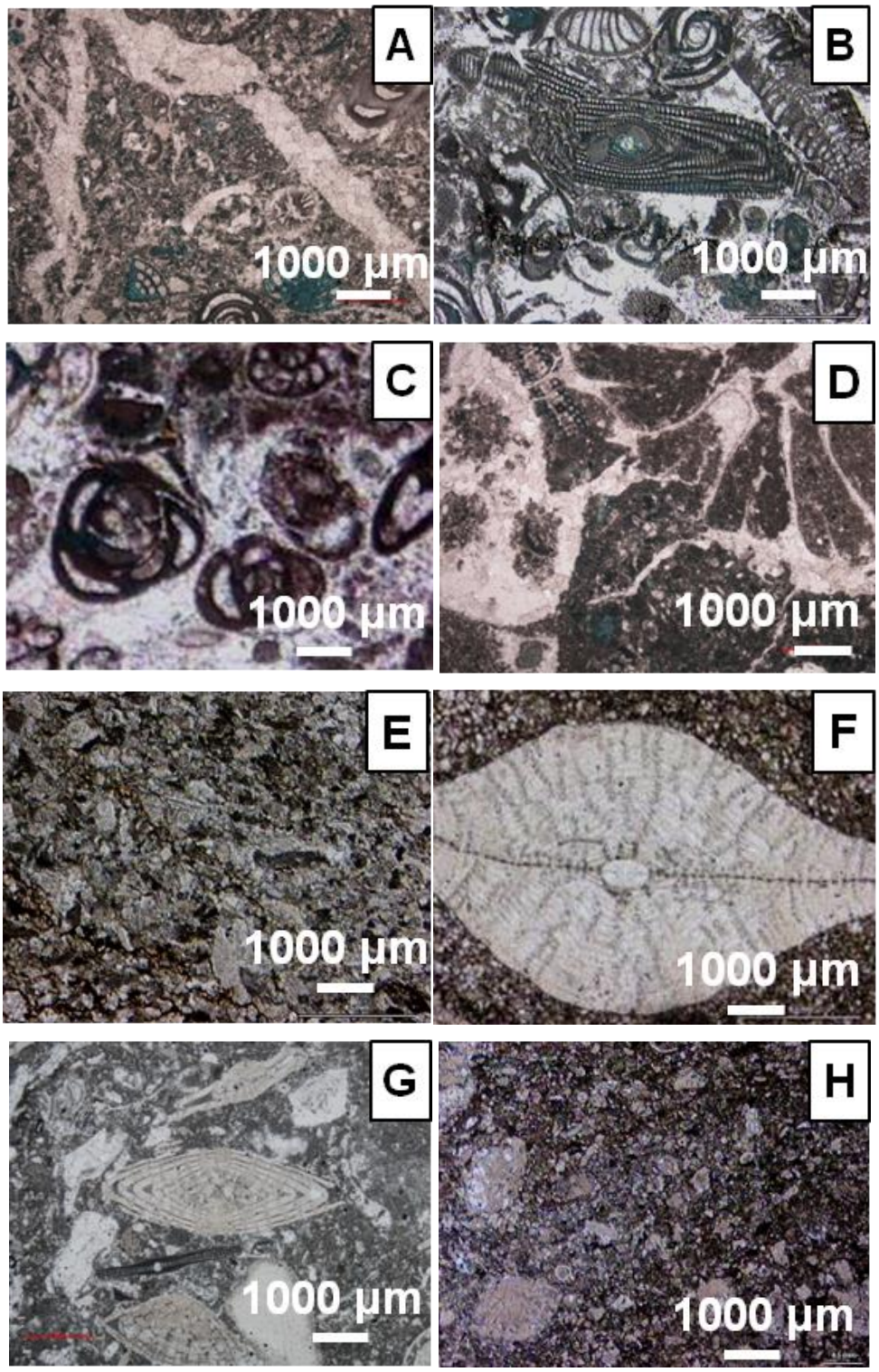

Figure 5.3.Thin section images of the main lithofacies types identified in Field X taken using plane polarized light. The images were obtained from a proprietary report given by the operator. (a) *Coskinolina* facies. (b) *Coskinolina* and *Alveolinid* facies. (c) *Miliolid* facies (d) Platy corals (e) Fine bioclastic Hash with Rotalid forams. (f) *Nummulites-Discocyclinid* facies (g) *Nummulites* (h) Hash facies with Echinoderm debris. The blue coloured resin indicates porosity.

5.1.2. Diagenetic history

The main paragenetic events that occurred in Field X were discussed by Wright & Barnett (2011) and are summarised in (Figure 5.4). The A Zone underwent deeper phreatic stabilisation after deposition, whereas the B Zone sediments were stabilised and cemented under shallow burial conditions. During intermediate burial, pressure solution features such as stylolites, microstylolites and clay seams developed ubiquitously. The majority of the stylolites were associated with tension gashes, some of which were cemented (Moshier 1989; Alsharhan 1990; Alsharhan & Sadd 2000). High amplitude stylolites and associated fractures were commonly developed in grainstones and packstones whereas microstylolites developed in finer lithologies. Nodular fabrics and clay seams were formed in the finer grained, more argillaceous facies.

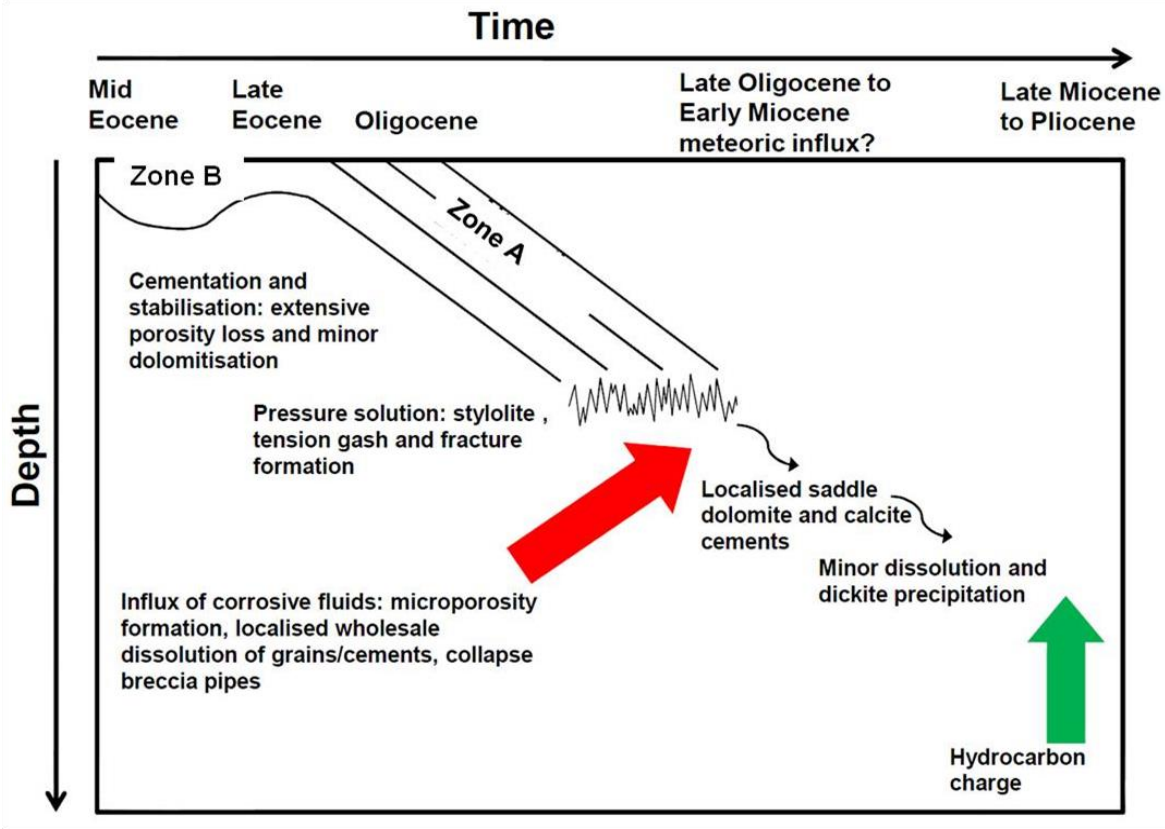

Figure 5.4. Key paragenetic events that occurred in A Zone and B Zone (modified from Wright & Barnett 2011). The depositional facies underwent extensive early cementation followed by compaction and pressure solution developing stylolites and associated tension gashes. This was followed by a major phase of dissolution associated with saddle dolomite and dickite precipitation.

It was hypothesised that the stylolites later reopened during a tectonic uplift event, allowing them to act as conduits for burial-derived fluids that caused a major phase of late-burial dissolution. During the dissolution phase the micritic grains were selectively removed initially and eventually even the spar cements were destroyed. This was followed by bladed calcite cementation and saddle dolomites. Late-burial corrosion in Field X is referred to as deep burial/mesogenetic corrosion associated with the corrosion of limestone by burial-derived (hypogene) fluids. The range of diagenetic effects associated with pressure solution and the distribution of porosity with respect to rock fabric is illustrated in Figure 5.5. Late-burial dissolution (Esteban & Taberner 2002, 2003) played a crucial role in the evolution of reservoir static and dynamic properties in Field X (Wright & Barnett 2011). Although the Eocene B Zone was exposed subaerially during the early Oligocene and a few cored wells show short intervals of cemented karst breccia, there is no widespread diagenetic signature of this event in the reservoir. The following section provides a detailed discussion about the late-burial corrosion model of Field X.

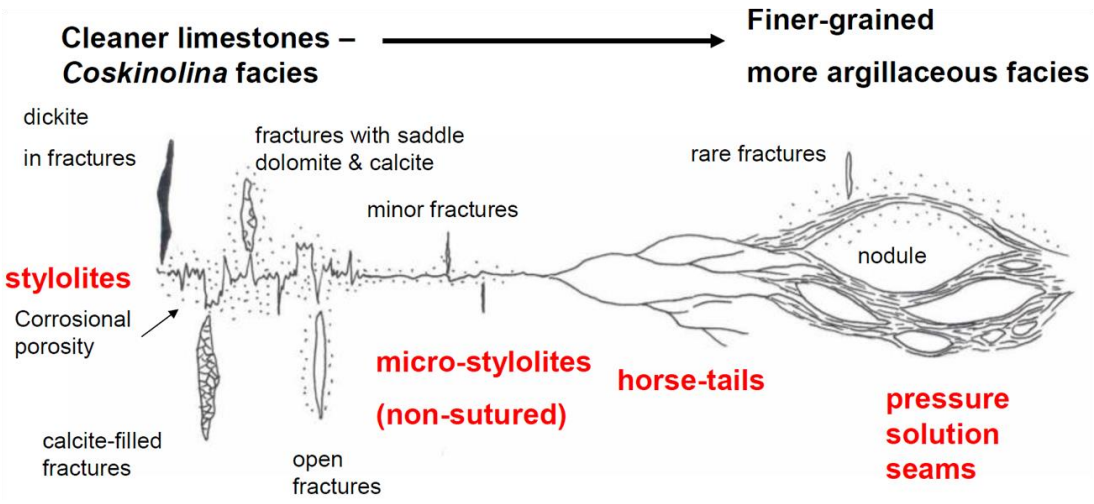

Figure 5.5. Conceptual model of the porosity distribution with respect to rock fabric and pressure solution (Modified from proprietary report). The range of diagenetic effects caused by pressure solution, including the associated fractures, is shown. High amplitude stylolites and associated fractures were commonly developed in grainstones and packstones whereas microstylolites developed in finer lithologies. Nodular fabrics and clay seams were formed in the finer grained, more argillaceous facies.

5.2. Field X database

Over 300 meters of core from 3 vertical wells and 1 highly deviated pilot well in Field X were inspected for this study. Routine Core Analysis (RCA) and Special Core Analysis (SCAL) data were used for petrophysical evaluation, along with high resolution images of the core and thin-sections from all these wells. Thin-sections were filled with a dyed resin in order to recognise the pore space with ease and to strengthen the rock to make it easier to cut samples. A blue dyed resin was used, which can be readily distinguished from other minerals or cements present in the rock sample. The porosity in the thin-section images shown in this thesis can be identified as the blue areas on the photograph. Two of the aforementioned wells also have probe permeameter data from core slabs. Core Spectral Gamma Ray logs, wellbore image logs and the typical well-log suite containing Gamma Ray, Density-Porosity and Sonic logs were used as well. In addition, the core description logs from earlier geological studies were provided for this study. These logs were supplemented by the description of the distribution of leached stylolites and tension gashes on the cores including some basic measurements of their apertures, mainly based on visual inspection.

5.2.1. Field X geomodel

The original geological-petrophysical model of Field X and the history matched simulation model were provided by the operator and serve as the base case throughout this study. Figure 5.6 shows the porosity model of Field X given by the operator and the four wells used in this study. The geomodel suggests an average permeability and porosity of 20 mD and 0.15, respectively. The geomodel grid was constructed in a North-South direction. It comprised over five million grid blocks with cell dimensions of 50 m x 50 m horizontally. The geomodel contained a total of 59 layers. Cell sizes in the vertical direction had an average thickness of 2 m.

5.2.2. Field X reservoir simulation model

A total of 170 wells were drilled in this reservoir, of which over 80 were horizontal multi-lateral wells. The reservoir contains fully saturated oil of about 40° API with the initial reservoir pressure of 2550 psia at the gas-oil contact of 1737m TVDSS. The oil-water contact occurs at 1757 m TVDSS and the free water level was calculated at 1762 m TVDSS. The operator provided the PVT properties and suggested that as Field X is a thin oil rim with no evidence of compartmentalization, there is not much areal or vertical variation in PVT properties. Based on compositional analysis of Field X crude,

it was a fairly close approximation to a black oil system. The production in the reservoir is through gas-cap drive mechanism. The reservoir simulation model provided by the operator had 1,320,759 active cells following areal and vertical coarsening of the geomodel. It was a three-phase black oil model and contained the specifications of the 170 wells and over 25 years of production history. Figure 5.7b illustrates the oil, gas and water cumulative production curves calculated by the history matched reservoir simulation model of Field X compared to the respective historic cumulative production curves.

The East Fault zone was used as simulation boundary in the full field reservoir simulation model. A proprietary report from the operator suggested that there was no clear evidence of in-field faults acting as pressure barriers in Field X. However, the operator noted that these faults can have significant influence on A to B-Zone communication and well performance. The 26 faults included in the geological model were hence retained in the simulation model as conductive faults. The model property arrays were received from the asset geologist and included NTG, V_{shale}, effective porosity (PHIE), total porosity (PHIT) and effective water saturation (SWE). The PVT properties provided by the operator for reservoir simulation were, bubble point pressure of 2550 psia, solution gas-oil-ratio of 0.677 Mscf/STB (at 2550 psia), oil formation volume factor of 1.469 (at 2550 psia) and oil viscosity of 0.32 cp (at 2550 psia). The saturation height functions used for initialising the reservoir simulation model are provided in Appendix B, Figure B1. The relative permeability curves used for reservoir simulation by the operator were derived from centrifuge relative permeability data from core samples from three wells of different well groups. The oil-water and gas-oil relative permeability curves used in the reservoir simulation model by the operator are described in Appendix B, Figure B2. In the following section the main geological controls of the distribution of late-burial corrosion enhanced-porosity are discussed.

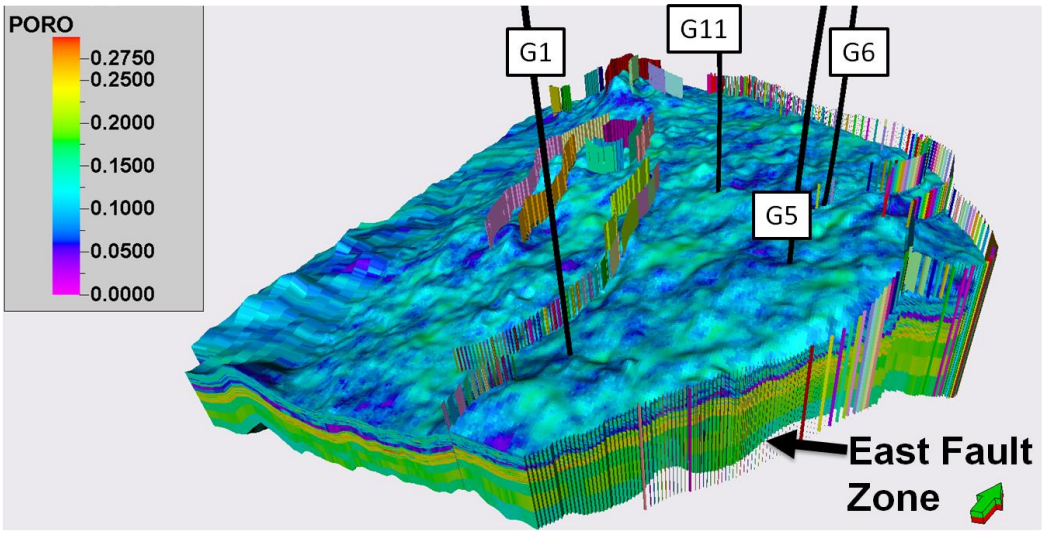

Figure 5.6. Illustration of Field X geomodel showing the porosity distribution, the fault polygons present in the model and the four wells used in this study. G1, G5, G11 and G6 are the wells used in this thesis.

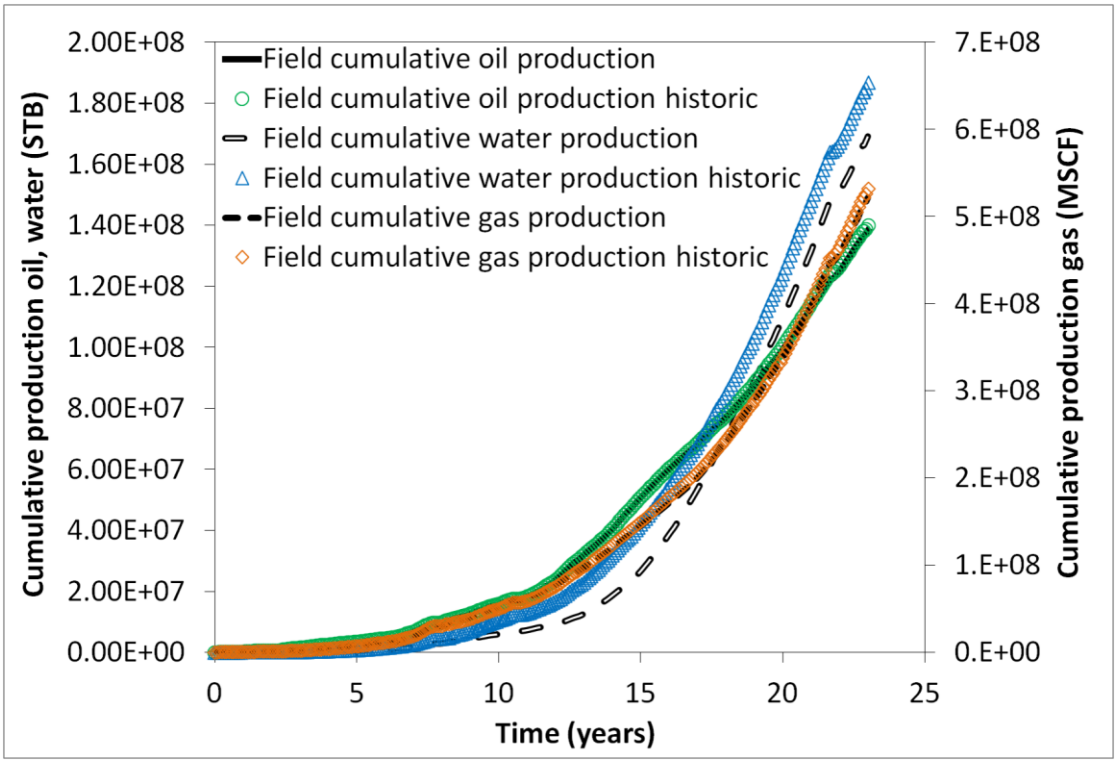

Figure 5.7. Oil, gas and water cumulative production curves as calculated by the history matched reservoir simulation model of Field X compared to the respective historic cumulative production curves. Note that the historic and simulated curves perfectly overlay each other for both oil and gas production profiles. STB refers to 'Stock Tank Barrels'. MSCF refers to 'Thousand Standard Cubic Feet'.

5.3. Late-burial corrosion in Field X

Numerous studies have demonstrated that mesogenetic dissolution is a key control for reservoir quality in other carbonate reservoirs worldwide (e.g., Mazzullo & Harris 1991; Jameson 1994; Esteban & Taberner 2002, 2003; Sattler *et al*. 2004; Lambert *et al*. 2006). Even though some authors (Ehrenberg *et al*. 2012) have questioned this, it is widely accepted that burial corrosion can extensively alter the static and dynamic properties of a reservoir, for example porosity, permeability, relative permeability and wettability. In their study of the carbonate reservoirs in the Permian Basin, including the Chapman Deep Field, Bone Spring Formation, Lower Permian Dolomites of the Southern Delaware Basin and the Griffin Penn Field, Mazullo & Harris (1991) emphasised the significance of deep-burial diagenesis in reservoir development. Jameson (1994) presented the case study of the Lisburne Field, Prudhoe Bay, Alaska and discussed the occurrence of porosity which is of late-burial origin, due to either dolomitisation or burial dissolution. In this study, Jameson (1994) discussed a model for late dissolution, based on the geological and petrophysical observations made during the case study. Furthermore, Jameson (1994) concluded that late fluids could have accentuated the initial contrast in the reservoir properties in Lisburne Field through dissolution along faults and fractures.

Zampetti et al. (2003) showed in a case study that most reservoir porosity observed in a Central Luconia Miocene platform postdates pressure solution and is related to deep burial conditions. Sattler et al. (2004) discussed the impact of the various processes and factors on the distribution of late-leached porosity and the subsequent impact on reservoir porosity types in the Miocene Zhujiang carbonates from the Liuhua 11-1 field, situated in the South China sea 220 km southeast of Hong Kong. In this study, Sattler et al. (2004) conclude that the major influencers of the spatial distribution of late-leached porosity in the Liuhua 11-1 field could have been the depositional facies and early marine cementation, meteoric cementation, and compaction and related burial cementation. Lambert et al. (2006) discussed the formation of microporosity, caused by rounded micrites resulting from burial dissolution, leading to enhanced poro-perm in three microporous reservoirs from the Middle East. Lambert et al. (2006) have developed a model for diagenesis in microporous carbonate reservoirs and discussed the relationship of stylolites with burial dissolution, which is responsible for the rounded micritic microtexture in the studied fields. Lambert et al. (2006) have hypothesised that

the burial dissolution responsible for rounded micrites in the studied fields preceded or accompanied the first oil migration induced by corrosive fluids associated with migration. Lambert et al (2006) and the earlier works cited therein confirm that the aforementioned phenomenon is "widespread and frequent throughout the Middle East". Most likely, reservoir quality in Field X is also significantly controlled by this late-burial corrosion, impacting formation porosity over several orders of magnitude in scale, varying from seismic-scale breccia pipes to strongly fabric selective micro-porosity (Wright & Barnett 2011).

Geological studies carried out by the operator suggest that the key static and dynamic reservoir properties in Field X are strongly related to the mechanism of reservoir poro-perm evolution during late-burial corrosion (Wright & Barnett 2011). As mentioned earlier, the stylolites and associated tension gashes could have opened due to a tectonic uplift event and conducted reactive fluids containing sulphides, silica and aluminium, enabling them to migrate into the surrounding host limestones. These reactive fluids corroded the formerly tight cemented matrices by selectively removing the micritic grains with high surface area (Wright & Barnett 2011). The conduits feeding the reactive fluids to the reservoir are not known with certainty. Feed through faults and from the closely underlying basement are both possible. The presence of exotic minerals in the core such as pyrite, dickite and saddle dolomite supports mixing corrosion mechanism as defined by Esteban & Taberner (2003). Figure 5.8 illustrates the mechanism of late-burial corrosion and evolution of porosity proposed by Esteban & Taberner (2003).

Both, A Zone and B Zone, clearly show the effects of a major phase of mesogenetic dissolution prior to hydrocarbon arrival. The B Zone is dominated by inner ramp *Coskinolina* grainstones to packstones, which developed high amplitude stylolites and associated fractures (Figure 5.5). These allowed the corrosive fluids to selectively remove the fine grained walls of agglutinated miliolid foraminifera in the early phase of corrosion (Wright & Barnett 2011). During later phases, the sparite and more coarsely crystalline foraminifera were extensively corroded. In contrast, there was only weak development of stylolites in the outer ramp *Nummulitic* packstones and wackestones of A Zone due to a higher clay content that prevented the formation of high amplitude stylolites (Figure 5.5). Hence the millimetre-sized clay seams and microstylolites caused only low to moderately intense corrosion, which resulted in widespread

microporosity development in these formerly tight cemented limestones. Note that micro-porosity in Field X is defined as pores with a pore throat diameter of 0.5 microns or less.

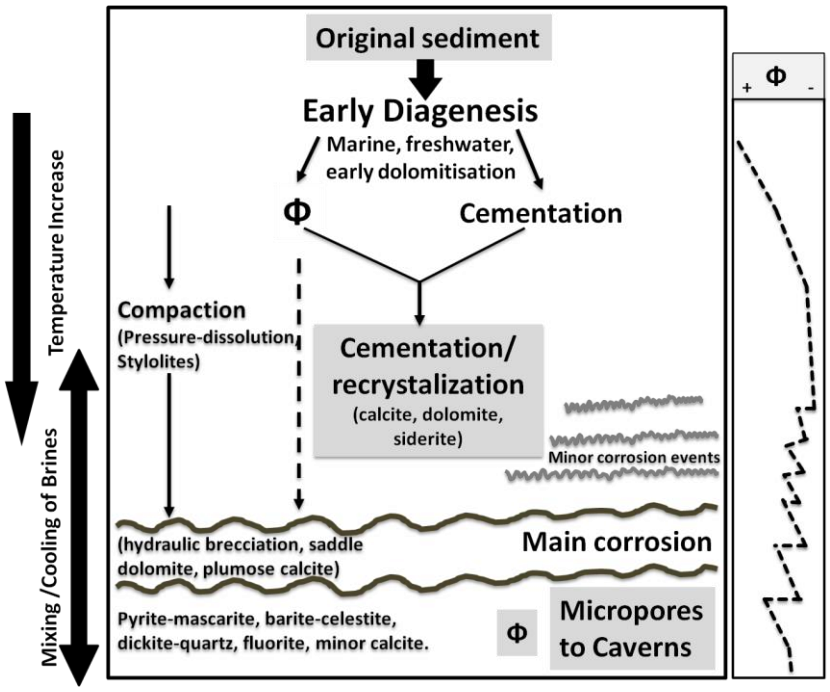

Figure 5.8. Illustration of the mechanism of late-burial corrosion and the evolution of porosity, from early diagenetic setting at top down to increasing burial depths. Modified from Esteban & Taberner (2003).

5.4. Porosity types in Field X

According to Wright & Barnett (2011), the main porosity types seen in Field X are associated with late-burial corrosion and are leached stylolites associated with fractures, moldic-vuggy porosity and matrix porosity. A comparison of core description with core plug data and thin-sections suggested the presence of extensively corroded matrix. There is evidence of intergranular porosity in the A Zone, especially above the A/B unconformity, presumably because A Zone was not stabilised and cemented under meteoric conditions, thus preserving some primary porosity. Although several types of dolomites are observed on the cores, only one of them, i.e. the dolomite associated with some nummulitic limestones, is associated with porosity formation. However, none of these dolomites are thought to contribute to the reservoir quality and hence have not been investigated in detail in the earlier geological studies. The following sections describe the main porosity types present in Field X.

5.4.1. Moldic-vuggy and matrix porosity

Earlier geological studies suggest that the occurrence of moldic porosity and associated vugs is widespread in Field X (Figure 5.9). The majority of moldic pores in Field X are the sites of former calcite forams. The formation of moldic porosity in Field X was highly selective and the miliolid and textularid forams were preferentially dissolved much earlier than the rotalids while the echinoderm debris was resistant to corrosion. Matrix porosity refers to pervasively fine, and sub-millimetre porosity within the matrix of the rock (Figure 5.10a). Not only the forams, but also the surrounding cements and matrices were corroded during the dissolution phase, resulting in pore types ranging from micron-sized pores to millimetre to centimetre-sized vugs. Microporosity was created as a leached microporous mosaic, associated with solution-enhanced intercrystalline porosity grading into larger pores (Wright & Barnett 2011) (Figure 5.10b). Classical microporosity associated with the formation of micron-sized polyhedral and rhombic micrite is locally present but is not the main type of microporosity in Field X.

5.4.2. Stylolite and fracture porosity

In contrast to the general trend observed in most reservoirs where stylolites are associated with cemented zones of poor reservoir quality (e.g. Burgess & Peter 1985; Alsharan & Sadd 2000), enhanced porosity is found extensively along stylolites, microstylolites and clay seams in Field X (Figure 5.11). Additionally, majority of the sutured, high amplitude stylolites are associated with centimetre scale fractures. The stylolite associated fractures are hereafter referred to as ‘tension gashes’ in this thesis. Tension gashes are not always present with stylolites in the cores but their frequency may be much greater than what is seen on the cores because they may occur outside the plane of the core face. Earlier geological studies suggest the presence of two generations of tension gashes, the most recent ones tending to be open or partially filled with dickite and calcite. The tension gashes observed in core were at times up to 6 mm wide and usually aligned with the direction of the stylolite peaks. They seemed to have initiated from the mechanical discontinuity along the stylolite surface and developed along the direction of the lithostatic stress. These tension gashes are predominantly associated with high amplitude stylolites in the more grain-rich facies. Most tension gashes are heavily corroded, and some are filled with blocky, non-ferroan calcite cements that are also corroded (Figure 5.12). In addition there are many small calcite-filled veins that

appear earlier than some stylolites and have been truncated by stylolites. Many of these veins also suffered later corrosion (Figure 5.13a). It is worth noting that saddle dolomite cement, which is a last carbonate phase before the final dissolution event and dickite precipitation, is widespread in the fractures (Figure 5.13b). The two types of 'fracture porosity' observed in Field X are hence; a) Stylolite associated tension gashes, which are few mm to several centimetres long and visible only on or below core-scale resolution and b) 30-40 cm long fractures with no direct relation to stylolites that truncate the stylolites and tension gashes and can be seen in FMI logs. The latter type of fractures was rarely observed in the studied wells.

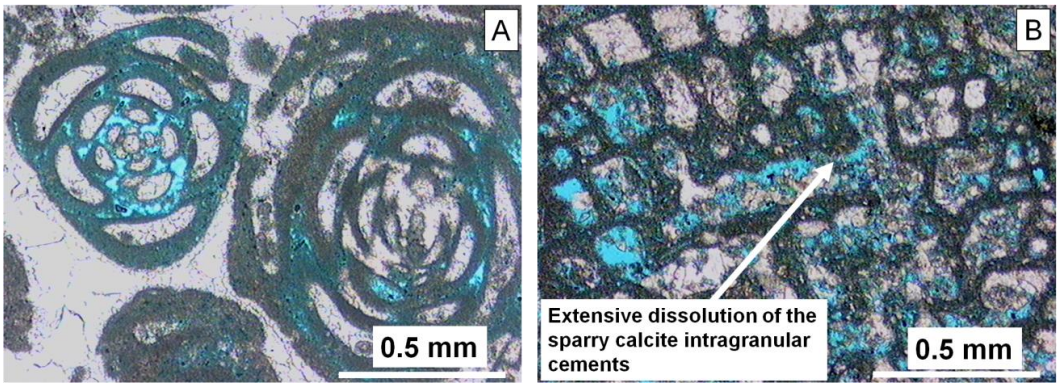

Figure 5.9. Thin-section images showing (a) corroded Miliolids with residual spar cements and (b) dissolution of walls and cements in Coskinolinas. The blue coloured resin indicates porosity (Images modified from proprietary report).

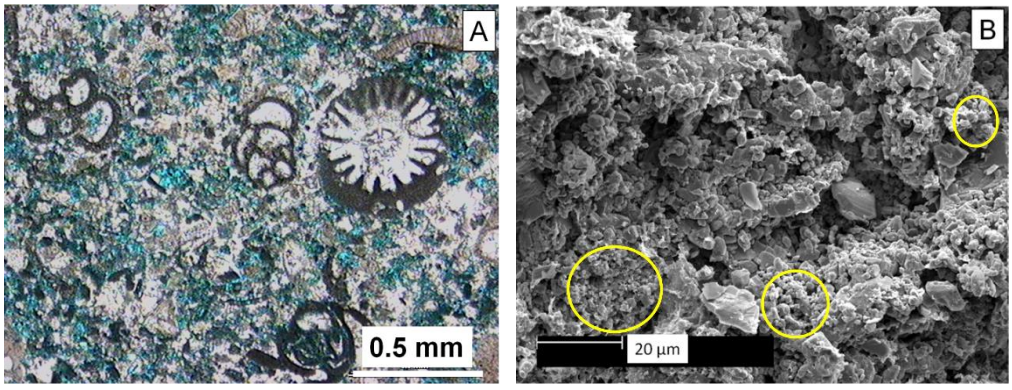

Figure 5.10. (a) Thin-section images showing matrix porosity in coarse grainstone caused by extensive corrosion of individual grains and the spar cements. The blue coloured resin indicates porosity. (b) Back Scatter Electron Microscope (BSEM) image of typical corroded matrix with microporosity. The circled regions show examples where the rock grains were corroded resulting in microporosity (Images modified from proprietary report).

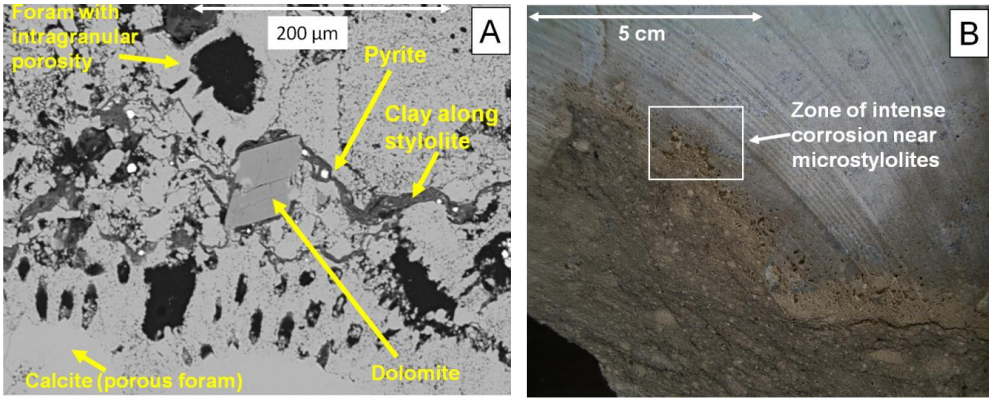

Figure 5.11. (a) Photomicrograph showing the porosity distribution and minerals along the stylolites. Here, light grey is calcite and black is porosity. (b) Core image showing intensely corroded zone of porosity associated with swarms of microstylolites (Images modified from proprietary report).

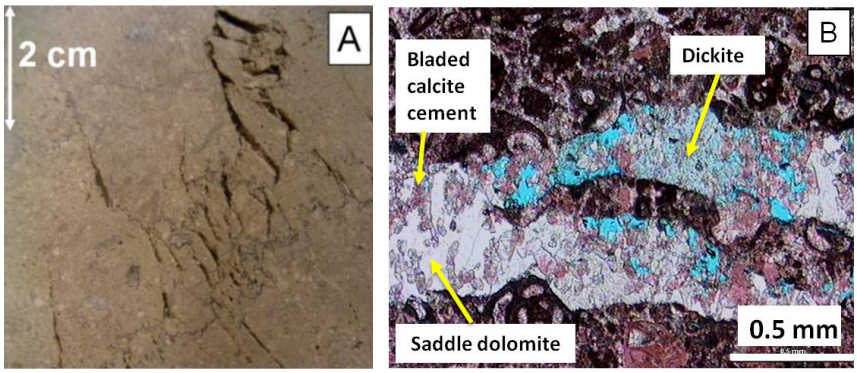

Figure 5.12. (a) Core image showing intensely corroded tension gashes associated with stylolites. (b) Thin section image showing tension gashes filled with bladed calcite cement, saddle dolomite and dickite. Note that the calcite cements were also corroded. The blue coloured resin indicates porosity. (Images modified from proprietary report).

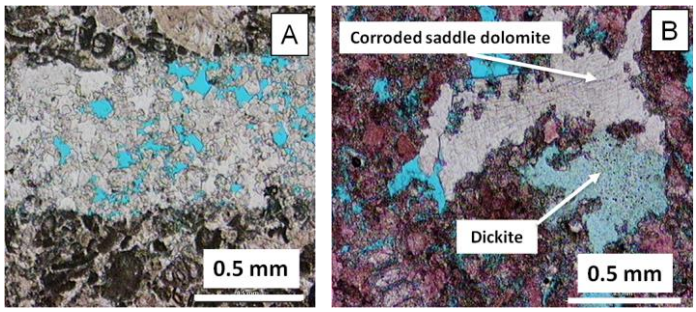

Figure 5.13. (a) Thin-section image showing tectonic vein filling calcite that suffered corrosion. (b) Saddle dolomite in a tension gash that has undergone corrosion followed by dickite precipitation. The blue coloured resin indicates porosity. (Images modified from proprietary report).

5.4.3. Summary

In summary, the main present-day porosity types and probably the majority of the reservoir porosity originated as a result of late-burial corrosion of the limestones of A Zone and B Zone, caused by the arrival of burial-derived (hypogene) fluids. The key porosity types are leached stylolites and associated tension-gashes, corrosion-enhanced intergranular and vuggy macroporosity, and microporosity. Hereafter, the intervals that contain the porosity types listed above as are referred to as Corrosion Enhanced Porosity (CEP) zones. Hence, the CEP zones comprise well-connected late-burial corrosion features, all of which contribute to a high-permeability network that significantly enhances fluid flow in the reservoir. The impact of these late-burial corrosion heterogeneities on reservoir permeability and performance of simulation model has been discussed in Chapter 6. The following sections describe the major geological controls of late-burial corrosion in Field X and the implications towards reservoir quality. These inferences have been used in Chapter 8 as part of the near-wellbore rock-typing and upscaling workflow.

5.5. Geological controls of corrosion-enhanced porosity.

The lithofacies types, stylolite types and the CEP types were characterised in the four wells were logged and digitised as part of this thesis. These logs were then used to divide the near-wellbore region of the wells into centimetre to decimetre scale intervals as shown in Figure 5.14. The logs digitised in Petrel, as shown in Figure 5.14, were used to perform the various calculations related to the characterisation and quantification of the CEP types that are discussed in this section. It must be noted that since these logs are based on the 2D observations of the well cores, the calculations are subject to some uncertainty with respect to the distribution of CEP type in 3D. This can be mitigated using image logs and X-Ray Tomography data, but since these were not available for this study, it is recommended to consider this in future studies. Based on the gross depositional model, the lithofacies observed in Field X were grouped in to 6 major lithofacies in A zone and 6 in B zone (Table 1). In order to be incorporated into the rock-typing workflow the main types of stylolite distributions observed in Field X were classified into; i) low amplitude stylolites (LAS) with low intensity of associated tension gashes and ii) high amplitude stylolites (HAS) with high intensity of associated tension gashes. The main types of CEP observed in Field X were categorised into two main groups; i) ‘CEP1’, representing the well intervals with high proportions of well-

connected chalky microporosity and some mesoporosity, and ii) 'CEP2', which is mainly macroporosity including vuggy, moldic and leached stylolites and tension gash porosity. The factors and processes that acted as key controls on the intensity and spatial distribution of CEP types in Field X were reservoir stratigraphy, depositional setting and pressure solution.

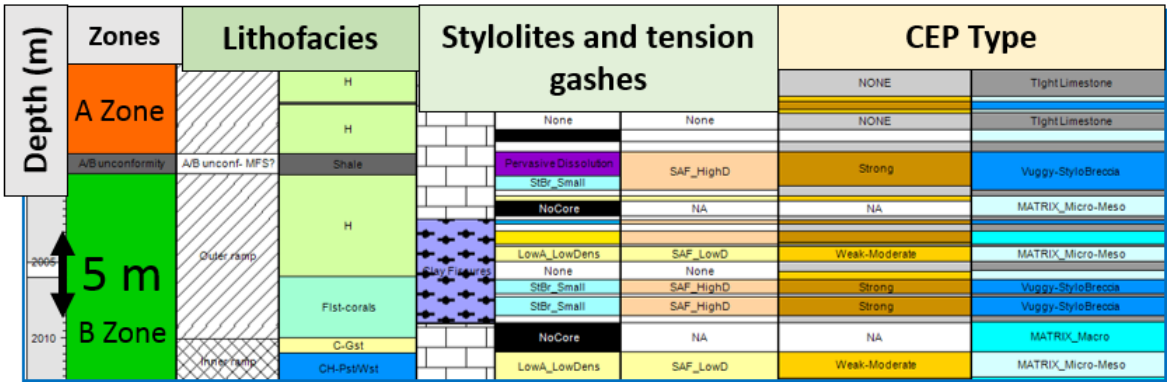

Figure 5.14 Example of well cross-section from Petrel showing how the lithofacies types, stylolite types and the CEP types were characterised in the four wells, logged and digitised in Petrel.

Table 5.2. Summary of major lithotypes present in A and B zones.

#	Description	Interpretation	Zone
1	Coskinolina-Grainstone	Inner ramp	**B**
2	Coskinolina-Packstone	Inner ramp	**B**
3	Coskinolina Hash- Packstone /Wackestone	Shallow mid ramp	**B**
4	Framestone with platy corals	Shallow mid ramp	**B**
5	Floatstone with platy corals	Shallow Mid ramp	**B, A**
6	Rotalids- packstone	Mid ramp	**B, A**
7	Nummulitides- Packstone	Outer ramp	**A**
8	Nummulitides- Grainstone /Wackestone	Outer ramp	**A**
9	Nummulitides- Wackestone /Packstone	Outer ramp	**A**
10	Shale zones	unconformities	**A**

5.5.1. Main controls of late-burial corrosion at reservoir scale

At the regional scale, the East-fault zone and the A/B unconformity seem to have played a critical role in the distributions of CEP in A Zone and B Zone (Figure 5.15a). Seismic data suggested that Field X comprises extensive breccia pipes and collapse features (Figure 5.15b) that are hundreds of meters in diameter, and which appear to be associated with the NNW-SSE trending strike-slip fault system. Based on this and earlier geological interpretations, it was hypothesised that the East-fault zone was probably one of the main conduits of the late-burial corrosion fluids to enter Field X (Figure 5.15a). Hence, in theory, it was expected to see an increasing trend in the intensity of corrosion of the reservoir formation closer to this fault zone. Statistical

analysis of the digitised CEP logs from the studied wells suggested a good correlation between the distance of wells from the fault zone and the percent of CEP2 type porosity, which was associated with high intensity of burial corrosion (Figure 5.15c). It must be noted that although the breccia pipes can act as a major vertical permeability enhancers, these were not included in the reservoir model built by the operator since they were outside the reservoir model boundaries. This is because the breccia pipes are associated with the East Fault Zone as mentioned above, which was one of the boundaries of the reservoir model.

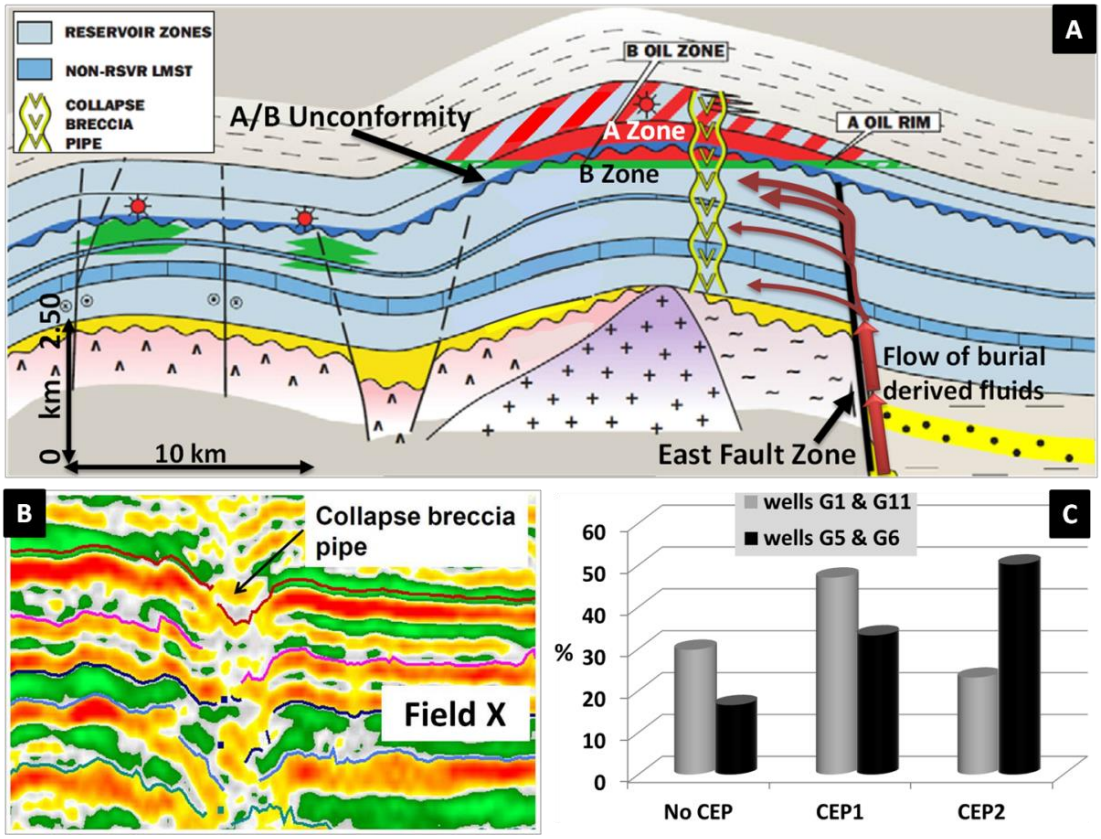

Figure 5.15 (a) Idealised cross-section of Field X illustrating the East fault zone, the A/B unconformity and the flow of burial derived fluids into the reservoir formation through the fault zone (modified from Barnett et al. 2010). (b) Collapse breccia pipe associated with the East fault zone observed on seismic data (modified from Barnett et al. 2010). (c) Histogram of cumulative percentages of CEP types in the studied wells. Wells G5 and G6, which are closer to the East fault zone compared to wells G1 and G11, show higher percentage of CEP2. CEP2 is characterised by high proportions of leached macroporosity caused by advanced and intense corrosion.

On the other hand, the A/B unconformity (Figure 5.15a) probably acted as an aquitard, causing the burial derived corrosive fluids to concentrate in the matrix of B Zone, resulting in more intense corrosion. This was evidenced by the significantly higher proportions of CEP2 type porosity in B Zone (Figure 5.16a), characterised by high proportions of leached macroporosity caused by advanced and intense corrosion. This hypothesis was also favoured by the field production data and tracer data, which suggested that B Zone acts as a stratified high permeability zone of much higher reservoir rock quality than A Zone. This inference was supplemented by the comparison of porosity-permeability values (Figure 5.16b) and pore-size distributions (Figure 5.16c) between A Zone and B Zone. Overall, it was observed that A Zone has a lower rock quality index and lower pore-size range compared to B Zone.

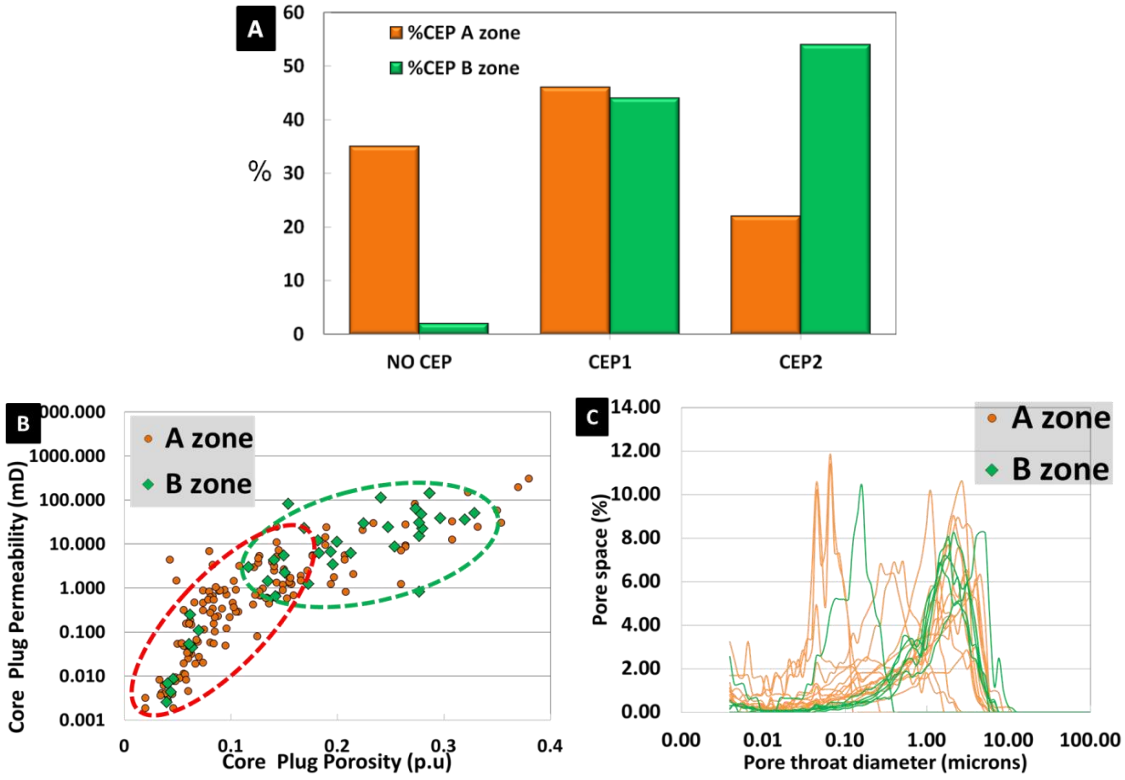

Figure 5.16 (a) Histogram of cumulative percentage of corrosion-enhanced porosity (CEP) types showing higher proportions of CEP2 type porosity in B Zone. (b) Cross-plot showing higher porosity-permeability values in B Zone compared to A Zone. Note that this plot is obtained from the core plug poro-perm data, which suffers from sample bias, and are not fully representative of the extent of corrosion-enhanced porosity in B Zone. (c) Plot of pore size distributions demonstrating higher pore size distributions in B Zone compared to A Zone.

5.5.2. Main controls of late-burial corrosion at sub-grid scale

Core and thin-section data suggested a strong correlation between the distribution and types of stylolites and the development of CEP at centimetre to decimetre scale (Figure 5.17).

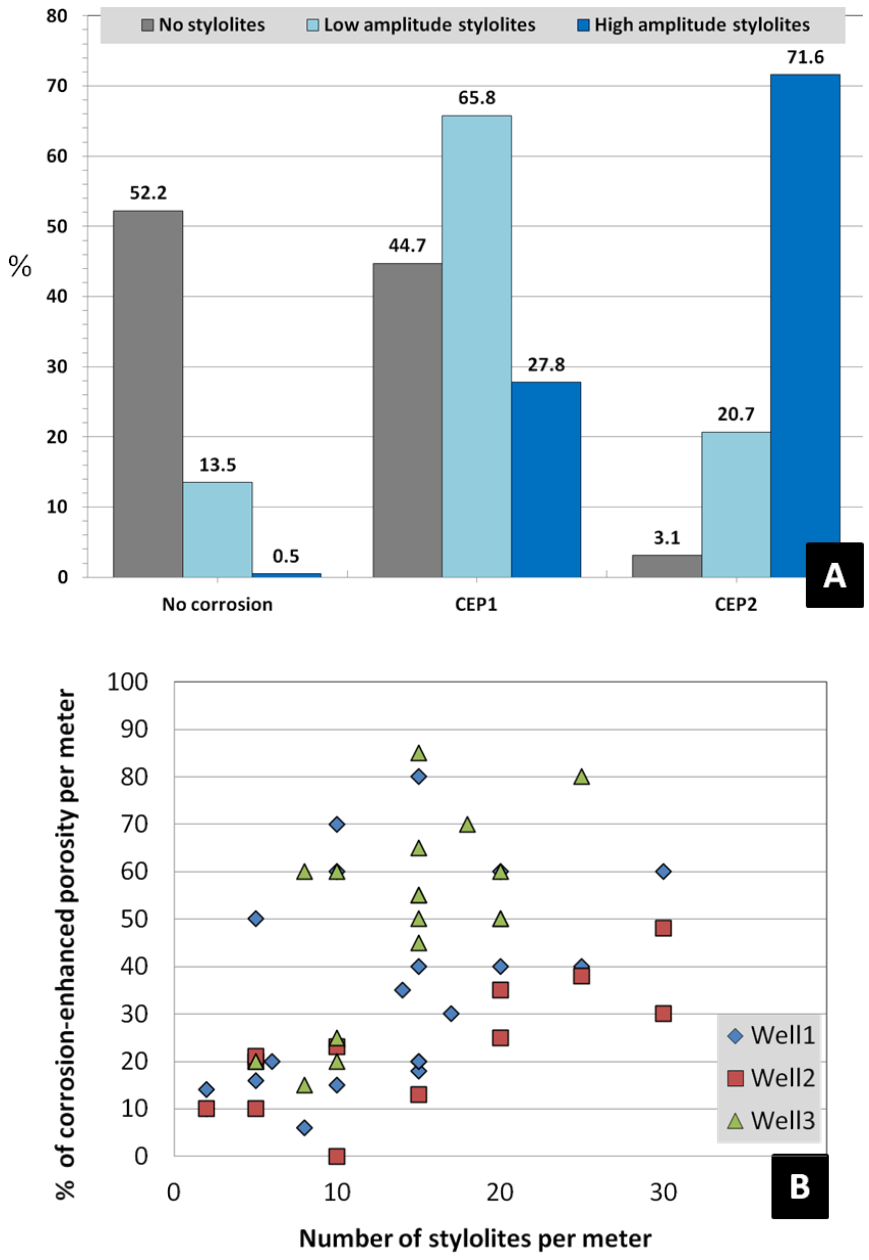

Figure 5.17 (**a**) Histogram illustrating the percent of corrosion-enhanced porosity types associated with the various stylolite types in Field X. The high amplitude stylolites are associated with higher amounts of CEP2, characterised by high amounts of leached macroporosity. (**b**) Correlation between percentage of corrosion-enhanced porosity per meter and number of stylolites per meter for the studied wells. The extent of corrosion increased with the number of stylolites per meter.

A vast majority of the stylolites and tension gashes were associated with halos of moderately to highly corroded CEP zones that were highly permeable, as observed from the probepermeameter measurements. This supported the hypothesis that, stylolites acted as conduits to the flow of the corrosive fluids into the surrounding matrix during the late-burial corrosion phase in Field X (Wright & Barnett 2011). Bitumen is found along many stylolites showing that these acted as conduits for hydrocarbon migration. Figure 5.18a illustrates the role of stylolites in the distribution of corrosion-enhanced porosity in the adjacent reservoir formation. Figure 5.18b illustrates the links between the depositional and diagenetic processes in Field X at core scale.

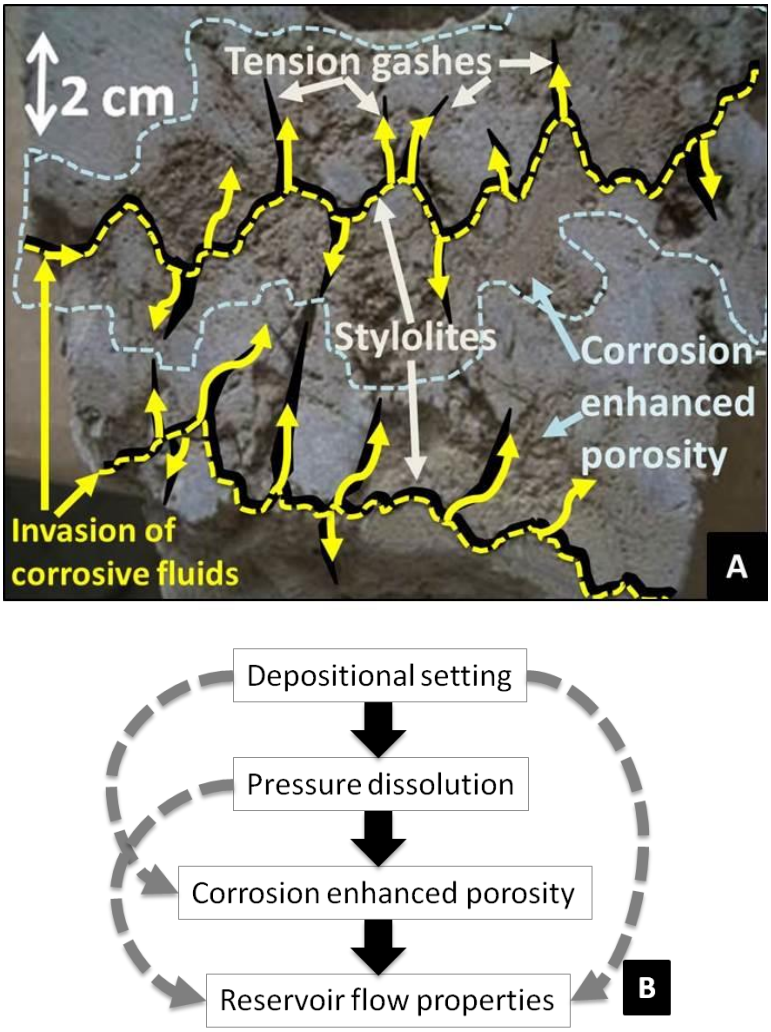

Figure 5.18 (a) Illustration of stylolites and tension gashes acting as conduits to the flow of the corrosive fluids into the surrounding matrix. (b) Illustration of the main controls of reservoir properties at core-scale and the links established between the lithofacies types, stylolite types and extent of corrosion-enhanced porosity in Field X.

The distribution of stylolite types was strongly related to the lithofacies distribution in the reservoir zones. Stylolitisation was relatively low in the outer ramp Nummulitic packstones and wackstones of A Zone due to higher clay content.A Zone mainly consisted of low amplitude stylolites (LAS type) and comprised a much lower percentage of CEP2 type porosity compared to B Zone. The millimetre-sized clay seams and microstylolites in A Zone caused only low to moderately intense corrosion, which resulted in widespread microporosity development in these formerly tight cemented limestones. B Zone is dominated by inner ramp Coskinolina grainstones and developed high amplitude stylolites and associated tension gashes. The HAS type stylolites in B Zone allowed the corrosive fluids to selectively remove the fine grained walls of agglutinated miliolid foraminiferas in the early phase of corrosion. At a more advanced stage, the sparite and more coarsely crystalline foraminiferas were extensively corroded. Hence, B Zone, which is predominated by HAS and LAS type stylolites, contains higher percentages of CEP1 and CEP2 compared to A Zone. This contrast in distribution of porosity types in B Zone and A Zone could have also been amplified by the effect the of A/B unconformity as discussed before.

5.6. Field X reservoir uncertainties and simulation challenges

Several reservoir engineering studies have been undertaken by the operator to understand the impact of individual reservoir simulation parameters on the incremental oil recovery of the proposed reservoir development schemes. Table 2 details the full list of reservoir simulation parameters used for this sensitivity study. Figure 5.19 illustrates the main uncertainties identified in the Field X reservoir simulation model during one such earlier study. The factors which are most influential to incremental oil recovery are critical oil saturation, alternative geomodel scenarios with varying fluid-in-place distributions and the horizontal and vertical permeability multipliers applied to the reservoir zones. Here, critical oil saturation refers to the maximum oil saturation at which oil relative permeability is zero. The following sections discuss the uncertainty associated with these reservoir simulation parameters and how they have been addressed in the chapters to follow.

Table 5.3. Uncertainty parameters used in sensitivity study.

Model Parameters	Code of parameter	Comments	Base	High	Low
Aquifer pore volume multiplier	AQUPV	Multiplier of aquifer pore volume	1	1.5	0.5
Maximum relative permeability to oil	Kromax	Maximum relative permeability to oil	0.6	0.9	0.4
Maximum water relative permeability in A Zone	Krwr1	Applied to Zone A, equivalent to layers 1 – 17 in reservoir model	0.15	0.3	0.1
Maximum water relative permeability in B Zone	Krwr2	Applied to Zone B, equivalent to layers 18-36 in reservoir model	0.3	0.4	0.1
Horizontal permeability multiplier in A Zone	MULTPERM1	Horizontal permeability multiplier in A Zone, equivalent to layers 5-17 in reservoir model	20	30	10
Horizontal permeability multiplier in upper B Zone	MULTPERM2	Horizontal permeability multiplier in upper layers of B Zone, equivalent to layers 18-25 in reservoir model	10	20	5
Horizontal permeability multiplier in lower B Zone	MULTPERM3	Horizontal permeability multiplier in lower layers of B Zone, equivalent to layers 26-36 in reservoir model	5	10	1
Vertical permeability multiplier in upper A Zone	MULTPERMZ1	Vertical permeability multiplier in upper layers of A Zone, equivalent to layers 5-7 in reservoir model	0.1	1	0.01
Vertical permeability multiplier in lower A Zone	MULTPERMZ2	Vertical permeability multiplier in lower layers of A Zone, equivalent to layers 8-15 in reservoir model	0.1	1	0.01
Vertical permeability multiplier of A/B unconformity	MULTPERMZ3	Vertical permeability multiplier in the unconformity, equivalent to layers 16-17 in reservoir model	0.1	0.5	0.01
Vertical permeability multiplier of B Zone reservoir	MULTPERMZ4	Vertical permeability multiplier in B Zone, equivalent to layers 18-33 in reservoir model	0.1	1	0.01
Vertical permeability multiplier of lower B Zone - non-reservoir	MULTPERMZ5	Vertical permeability multiplier in non-reservoir layers of B Zone, equivalent to layers 34-36 in reservoir model	0.1	1	0.01
Maximum water-oil capillary pressure	PCW	Scaled water-oil capillary pressure increases or decreases the transition zone effects	8	12	4
Initial gas-in-place (GIIP) in BCF	POROINC	Different gas-in-place distributions	2405	3205	1604
Critical gas saturation	SGCR	The maximum gas saturation at which gas relative permeability is zero	0	0.05	0
Critical oil in water saturation in A Zone	SOWCRA	Critical oil saturation in A Zone	0.1	0.15	0.05
Critical oil in water saturation in B Zone	SOWCRB	Critical oil saturation in B Zone	0.1	0.3	0.05

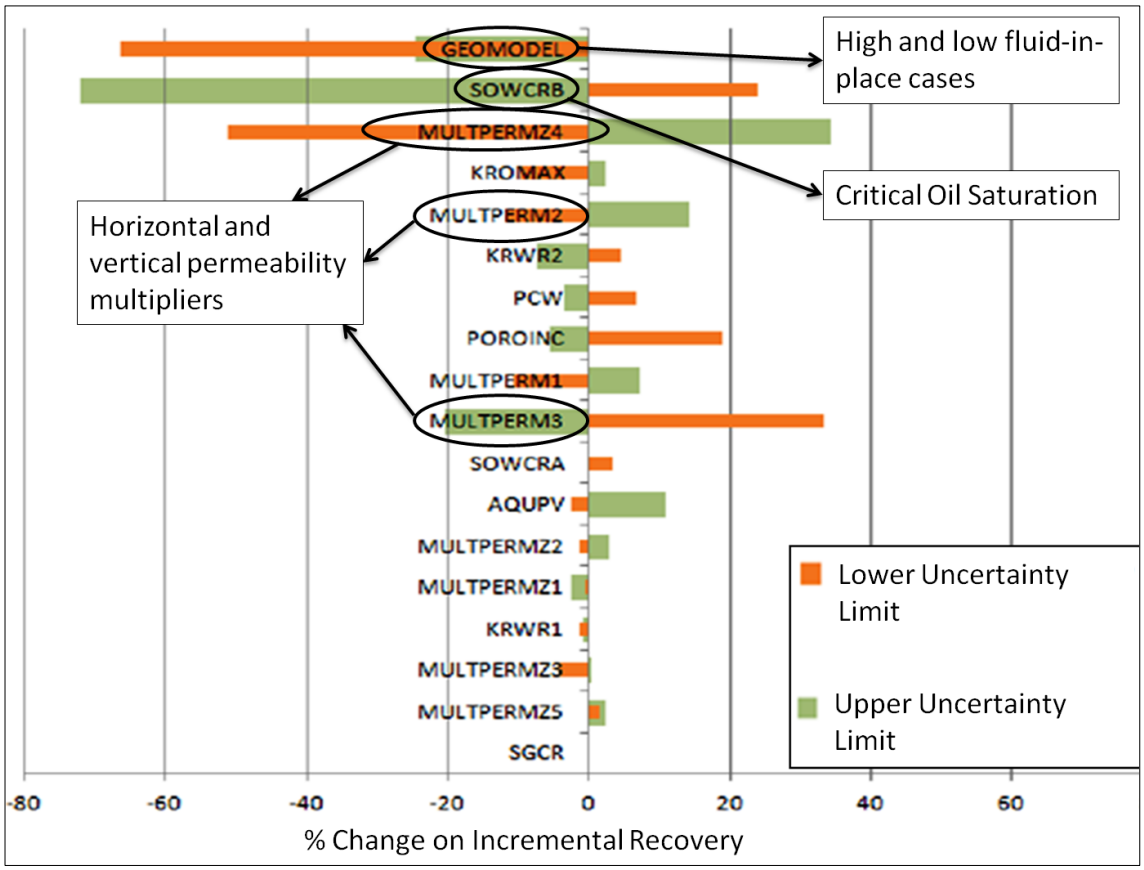

Figure 5.19 Tornado chart showing the sensitivity of incremental oil recovery to the reservoir simulation parameters (modified from proprietary report). Incremental oil recovery is most sensitive to changes in critical oil saturation, alternative geomodel scenarios with varying fluid-in-place distributions and the horizontal and vertical permeability multipliers applied to the reservoir zones.

5.6.1. Permeability modelling challenges

As discussed earlier, permeability has been identified as one of the biggest uncertainties in the reservoir simulation model of Field X during the sensitivity studies. A reduction in the uncertainties for the permeability distribution is thus needed to evaluate the feasibility of the next development phase. The permeability model, used for reservoir simulation and history matching of Field X, has been obtained solely by using a permeability transform derived from core data (Figure 5.20), which constrains the average reservoir permeability to be 20 mD. However, over 25 years of production history supports an interpretation of a stratiform high-permeability network with horizontal permeability on the order of 200 mD. Core recovery was poor as significant parts of the reservoir comprise high-permeability and probably mechanically weak carbonates, which have been altered by mesogenetic corrosion. The available core plug

data suffers from inherent sample bias and insufficiency due to rock-mechanical constrictions and due to the shortcomings of using a regular sampling interval of 1 meter (Oates *et al*. 2012). Hence the resulting core analysis hardly sampled any high-permeability features. Yet, such high-permeability features were clearly apparent in the dynamic data.

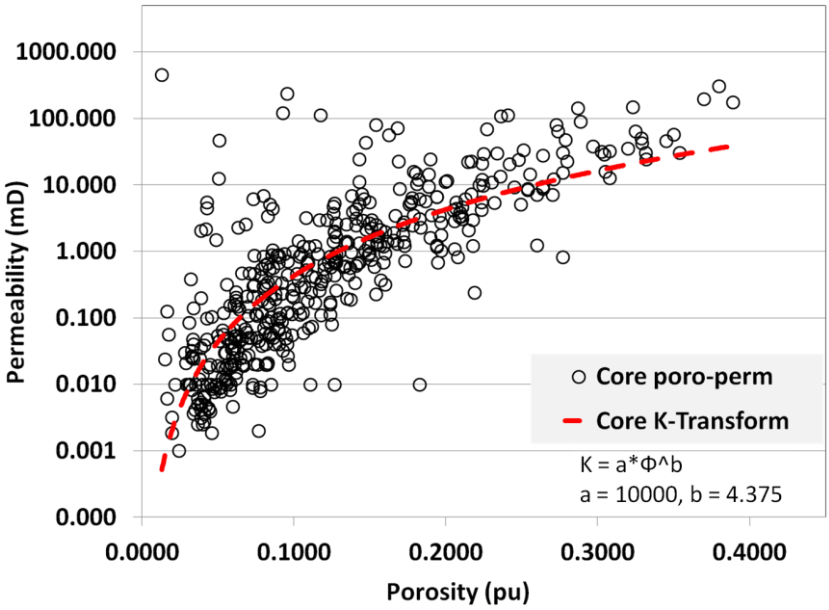

Figure 5.20 Core data and permeability transform used for generating the original geomodel of Field X. Here, K is horizontal permeability and Φ is porosity.

Because core sampling was biased to lower permeability values, the reservoir simulation model required major modifications to obtain the satisfactory history match shown in Figure 5.7. These modifications were exclusively of numerical nature, comprising, for example, horizontal permeability multipliers of 10 and 20 in the main reservoir zones. In addition, vertical permeability, local well permeability and well productivity index multipliers were also needed. These multipliers imply that the mechanism of fluid flow taking place in the reservoir formation was not successfully represented through the core permeability data input into the static geomodel and ultimately into the simulation model. According to an internal report provided by the operator, whilst quantitative well test interpretation in Field X was very difficult due to the well architecture (horizontal and multilaterals) and geological set up (gas cap and aquifer), the well test results were used as a guide to deriving permeability multipliers during the history matching process. Although collectively these permeability

multipliers lead to a good history match, it appears that the “right” history match was achieved for the “wrong” geological reason.

Removing the different permeability multipliers, hereafter referred to as K-multipliers, caused the quality of the history match to degrade significantly. Figure 5.21 demonstrates the sensitivity of simulated cumulative oil production curves to the applied numerical permeability multipliers in Well Group 1, the well group containing Well G11 (Figure 5.6). The computed cumulative oil production dramatically decreased with the removal of the numerical permeability enhancers applied to the simulation model. This decrease can be seen in Figure 5.21 from the difference between curves OPT, original simulation model with K-multipliers, and OPT3, model with all the K-multipliers removed. Hence, the original geomodel permeability was inadequate to simulate the fluid flow mechanism in Field X, although it could be calibrated using artificial multipliers. However, these K-multipliers were not based on geological constraints.

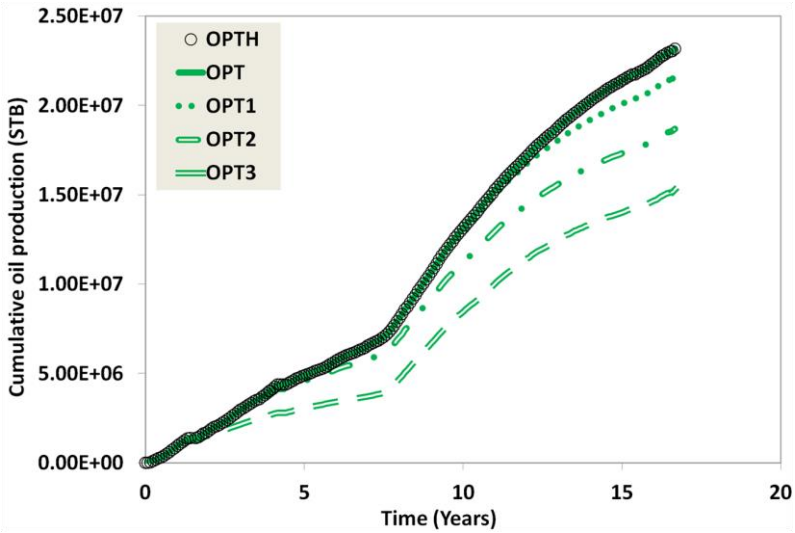

Figure 5.21. Cumulative oil production curves from Well Group 1. OPT corresponds to the history matched simulation model, which aligns perfectly with the historic production data OPTH. OPT1 is the simulated production after removing horizontal permeability multipliers (K-multipliers) from the zones. OPT2 is the simulated production after removing zone and local well K-multipliers. OPT3 is the simulated production after removing the well productivity multipliers in addition to the zone and well K-multipliers. STB is the abbreviation for ‘Stock Tank Barrels’.

Earlier studies, supported by a steady water-cut profile over the field's long production history (Figure 5.22), indicate that a connected natural fracture network is probably absent in Field X (Oates *et al*. 2012). The two key questions for evaluating future development scenarios in Field X were hence: What is the geological nature of the high-permeability zones that were required in the reservoir simulation model to obtain an adequate history match? How could these zones be quantified and represented to update the reservoir simulation model in a geologically consistent way rather than using artificial multipliers?

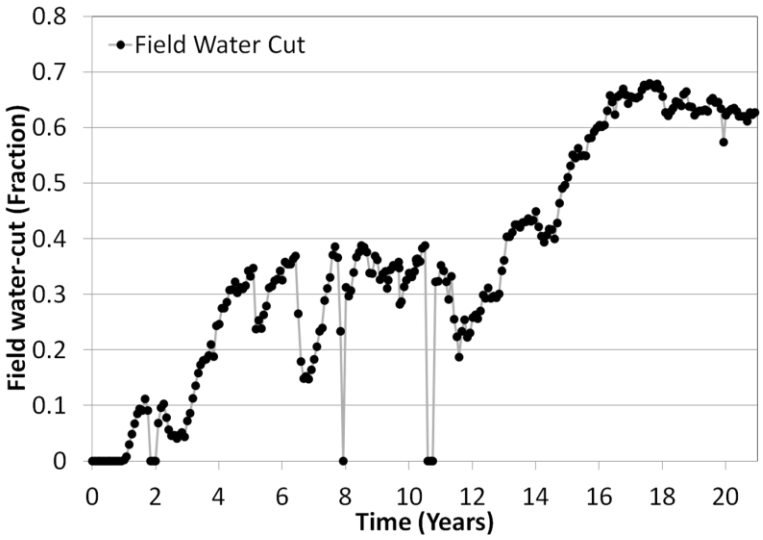

Figure 5.22. Gradual water-cut profile of Field X. Erratic water break-through was not observed during the field's production life and hence fractures are probably not controlling fluid flow in the reservoir. The periods of zero water-cut correspond to the times when field production operations were temporarily suspended.

This study employs the hypothesis that the enhanced permeability in Field X was caused by late-burial corrosion, as discussed in the earlier sections, and this needed to be accounted for in the geomodel. Figure 5.23 below illustrates the conceptual model of the multiscale connectivity of the CEP zones discussed earlier in this chapter across the Field X reservoir.

The lateral extent of the CEP zones in Figure 5.23 was guided by the core description logs from the highly deviated Well G6. Theoretically, the leached stylolites and tension gashes, in conjunction with the corrosion enhanced matrix porosity could provide preferential flow paths to the reservoir fluids, thus enhancing the reservoir permeability. A novel near-wellbore upscaling workflow was used to assess and incorporate these

multi-scale geological features arising from late-burial corrosion more reliably in the field-scale reservoir model and is presented in Chapter 6 and Chapter 7.

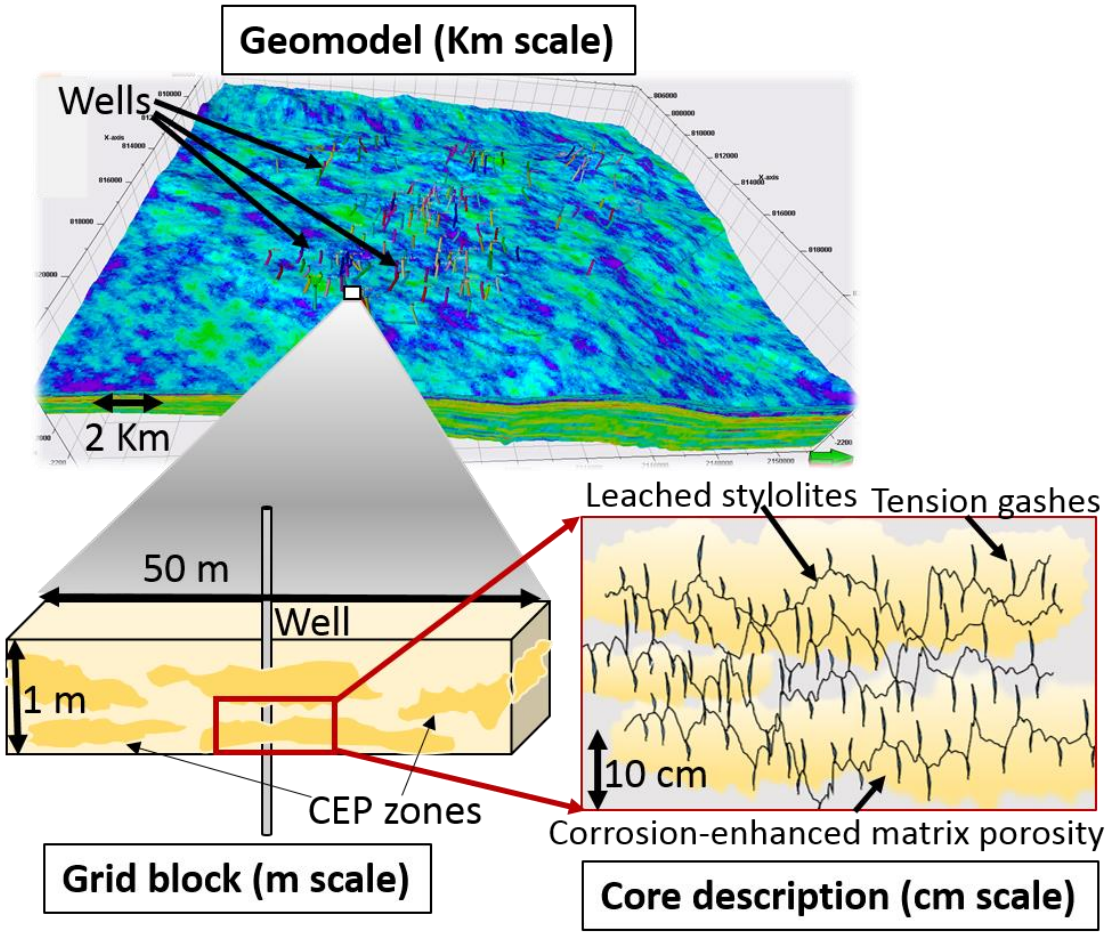

Figure 5.23. Illustration of the conceptual model of multiscale connectivity of the CEP zones across the Field X reservoir. The leached stylolites or tension gashes alone may not act as the high permeability conduits, but rather the combination of the corrosion-enhanced matrix porosity, stylolites and tension gashes is the potential contributor to the enhanced permeability in Field X.

5.6.2. Saturation modelling and initialisation issues

Due to the capillary transition zone present in the oil rim, Field X poses additional challenges for reliable characterisation and simulation of the reservoir flow behaviour. According to earlier studies, the initial hydrocarbons-in-place and the critical oil saturation values are associated with high degrees of uncertainty in Field X. The performance predictions of the reservoir simulation model were found to be highly

sensitive to the volumes of fluids initially-in-place and the critical oil saturation in addition to permeability (Figure 5.19). The irregularities observed between the distributions of fluids based on reservoir simulation predictions and the actual production volumes implied that the fluid-in-place volumes and production characteristics were not properly understood (Calvert & Ballay 2011). Unrealistic water-oil relative permeability endpoints and local initial saturation changes were applied to the original Field X geomodel to obtain history match. These modifications suggested that the distribution of initial oil-in-place and the dependency of residual oil saturation on initial water saturation required better characterisation.

The capillary transition zone plays a vital role in the reservoir flow behaviour in Field X due to the limited thickness of the oil rim. To be able to address the dynamic behaviour of the transition zone, it must be ensured that the reservoir simulator places each simulation grid-block in gravity and capillary equilibrium during initialisation. Particularly in the case of Field X it is necessary to simulate the complex interplay of viscous and gravitational forces accurately to model the gas cap drive correctly, which is the primary recovery mechanism. In order to accomplish reliable initialisation of reservoir simulation model, it must be ensured that the poro-perm distribution, capillary pressure, and relative permeability characteristics are coherent within each grid-block. It was hence deemed necessary to re-evaluate the oil-in-place calculations and improve reservoir model initialisation to obtain more reliable simulation predictions. Chapter 8 describes the near-wellbore upscaling and rock-typing workflow employed to revise the full field geomodel of Field X which incorporates the late-burial corrosion heterogeneities and is initialised for reservoir simulation with consistent static and dynamic reservoir properties.

5.7. Concluding remarks

Field X comprises a giant Palaeogene limestone reservoir with a long production history. The two main hydrocarbon zones, A Zone and B Zone were interpreted to be of different depositional systems and were separated by a shale unit, the 'A/B unconformity'. Late-burial dissolution played a crucial role in the evolution of reservoir static and dynamic properties in Field X. The main porosity types seen in Field X were fractures associated with stylolites, moldic-vuggy porosity and matrix porosity. However, the impact of incorporating the late-burial corrosion model in the reservoir simulation model on production forecasting was uncertain. The key geological

heterogeneities impacting fluid flow needed to be accounted for in both, the geomodel and the simulation model. Chapter 6 presents the workflow adopted to assess and incorporate the multi-scale geological features arising from late-burial corrosion more reliably in the field-scale reservoir model.

Permeability distribution was one of the biggest uncertainties to be resolved in Field X, as exemplified by the need to invoke a range of multipliers which were not based on geological insights. Hence there was a strong need for re-evaluating the permeability model. The following chapters, specifically Chapter 6 and Chapter 7 demonstrate the near-wellbore upscaling workflow that was developed to improve the permeability modelling in Field X. In addition to permeability, initial hydrocarbons-in-place and the critical oil saturation values were also associated with high degrees of uncertainty in Field X. It was hence necessary to re-evaluate the geological-petrophysical model of Field X to increase the reliability of oil-in-place calculations and reservoir model initialisation for simulation predictions. Chapter 8 demonstrates how an integrated near-wellbore rock-typing and upscaling approach improved reservoir initialisation of Field X simulation model. It must be noted that the various simulation sensitivities performed in the later chapters while incorporating the late burial corrosion model have not considered the impact of varying the fault transmissibility values in the reservoir simulator, as this was out of scope of this thesis.

Chapter 6. EVALUATING THE IMPACT OF LATE-BURIAL CORROSION ON THE PERMEABILITY IN FIELD X USING NEAR-WELLBORE MODELLING TOOLS

6.1. Introduction

As discussed in Chapter 5, the permeability of Field X was identified as one of the biggest uncertainties associated with the reservoir simulation model. A reduction in the uncertainty associated with permeability distribution was thus needed to evaluate the feasibility of the next development phase. This chapter describes the approach adopted to resolve these issues through a systematic re-evaluation of the reservoir simulation model, considering, in particular, the field's diagenetic history. The prime aim was to understand the fundamental controls on fluid flow that needed to be adequately captured in the reservoir model. Geological studies carried out by the operator suggested that the key permeability pathways are strongly related to the mechanism of reservoir poro-perm evolution during late-burial corrosion (Wright & Barnett 2011). However, it was unclear how a diagenetic model that accounts for late-burial corrosion should be included in the reservoir simulation model and how such an updated reservoir simulation model could impact production forecasting.

As discussed in Chapter 3, near-wellbore modelling can estimate the effects of geologically realistic millimetre to decimetre scale geological features on permeability (Wen *et al*. 1998; Nordahl *et al*. 2005; Ringrose *et al*. 2008). They also allow us to evaluate how small-scale heterogeneities impact reservoir-scale flow behaviours by incorporating them in sector- and field-scale reservoir models (Nordahl 2004; Elfenbein *et al*. 2005). Chapter 4 demonstrates that near-wellbore modelling tools can be used to simulate the impact of small-scale geological heterogeneities in a highly heterogeneous clastic reservoir and that the inclusion of these heterogeneities in field-scale models leads to better calibrated reservoir models. In the work described in this chapter, SBED^{TM} was used to obtain realistic reservoir property distributions for the millimetre to centimetre-sized geological features in the CEP zones as described in the following sections.

In this chapter, the petrophysical evaluation of the multi-scale geological heterogeneities caused by late-burial corrosion is presented first. Then, the near-wellbore modelling and upscaling approach used to understand the impact of late-burial

corrosion heterogeneities on horizontal and vertical permeability is discussed. Following this, it is described how the aforementioned heterogeneities were represented in the reservoir simulation model through Lucia's (1983) permeability transforms using the results from near-wellbore upscaling. Finally, the sensitivity of simulated cumulative production profiles to several model scenarios that incorporated the modified permeability distributions is analysed.

6.2. Petrophysical description and evaluation of late-burial corrosion in Field X

As discussed in Chapter 5, the main present-day porosity types and probably the majority of the reservoir porosity, originated as a result of late-burial corrosion of A and B Zone limestones, caused by the arrival of burial-derived (hypogene) fluids. To reiterate, the key porosity types are leached stylolites and associated tension gashes, corrosion-enhanced intergranular and vuggy macroporosity, and microporosity. As before, the intervals that contain the porosity types listed above are referred to as corrosion-enhanced porosity (CEP) zones. Hence, the CEP zones comprise well-connected micro and macropore networks with leached stylolite and tension gash porosity, all of which act as a high-permeability network that significantly enhances fluid flow in the reservoir (Figure 6.1).

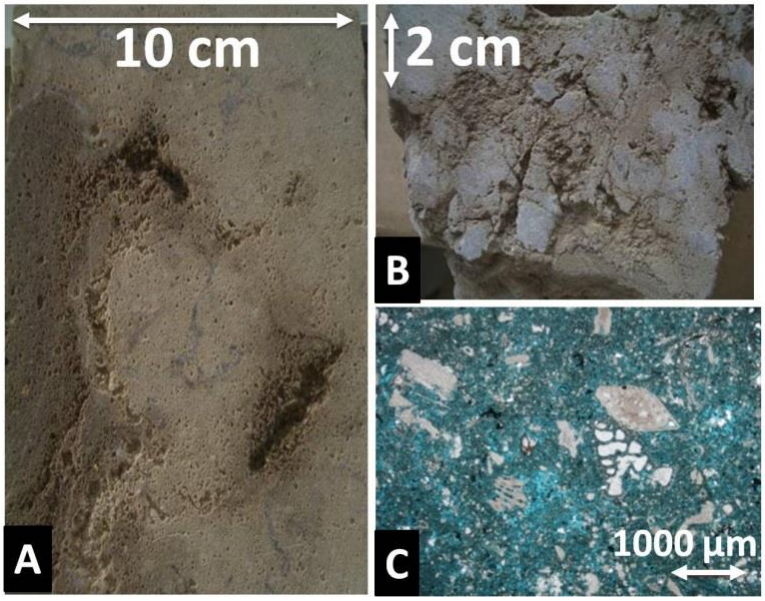

Figure 6.1. Illustration of varying scales of corrosion-enhanced porosity caused by late-burial corrosion within the corrosion-enhanced porosity (CEP) zones in A and B Zones. (a) Vuggy/moldic porosity on core. (b) Leached stylolite and associated tension gashes. (c) Matrix micro and macroporosity observed in thin-section.

Table 6.1 summarises the assessment of the CEP zones based on the available petrophysical data. Over 300 metres of well cores were inspected to obtain detailed core description of the CEP zones, including the spatial and structural aspects of the leached stylolites and tension gashes. Observations from core and thin-sections indicate that the stylolites are Type III stylolites. Type III stylolites are high amplitude and anastomosing stylolites (Aharonov *et al*. 2012). These stylolites are frequently associated with vertical to sub-vertical tension gashes (Figure 6.2). These features are typically leached and coexist with extensive corrosion-enhanced micro and macroporosity halos. These are the CEP zones (Figure 6.1).

Table 6.1. Summary of petrophysical data analysis

Scale	Available data	Resolution	Depth of Investigation	Key Geological Heterogeneities Resolved	Petrophysical Property Inferred
Pore	Special Core Analysis (SCAL)	Few µm-mm	Few µm-mm	- Corrosion-enhanced patchy microporosity - Microstylolites - Depositional facies	- Capillary pressure, P_c, Relative permeability, K_r - Pore throat diameter range - Pore size distribution - Macro and microporosity cut-offs
	Thin-section images	Few µm-mm	Few mm		
Core	Probe permeameter	Few mm-cm	Few mm-cm	- Depositional facies - Corrosion enhanced matrix meso and macroporosities - Vuggy/moldic porosity - Corrosion-enhanced stylolites and tension gashes - Stylobreccia and pervasive dissolution	- Matrix porosity distribution range - Core poro-perm transforms - Flow zone indicators (FZIs)
	Plug poro-perm	5 cm	5 cm		
	Core plug X-Ray Tomography	Few cm	Few cm		
	Core Spectral Gamma Ray	Few cm	Few cm		
	Core description	mm- m	Upto 10 cm		
Wireline	Image Logs	0.5 cm	2.5 cm	- A/B unconformity - Shaly-stylobreccia zones - Fractures/stylolites captured in image log resolution	- Total and Effective porosities - water saturation model - Fluids-in-place calculations
	Density log	46 cm	13 cm		
	Neutron porosity log	30 cm	23 cm		
	Gamma ray log	30.5 cm	61 cm		
	Deep resistivity log	46 cm	81 cm		

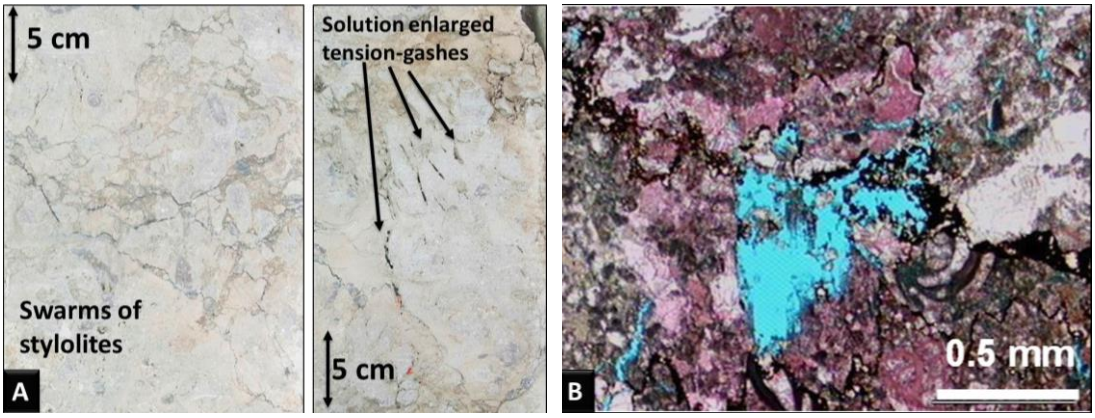

Figure 6.2. (a) Swarms of dissolution-enlarged stylolites (left) and associated small-scale tension gashes (right) observed on core from Well Group 1. (b) Photomicrograph illustrating leached stylolite porosity.

As noted earlier, the available core plug data suffered from sample insufficiency arising from poor core recovery of high-porosity CEP zones as they were probably mechanically weaker. This resulted in a sample bias towards the uncorroded tight limestone. Although the core plug data by itself failed to characterise the permeability distribution in the CEP zones effectively, the core slabs still could be used to obtain probe permeameter data. However, probe permeameter measurements are sensitive to the local pore geometries because of the small sample size of such measurements (Corbett *et al*. 1999). Hence these measurements needed to be evaluated with care as the CEP zones comprised a variety of corrosion-enhanced porosity types, including moldic, vuggy and stylolite porosities. Core and thin-section analysis confirmed that the corrosion-enhanced porosity (CEP) zones showed higher porosity than the surrounding unmodified matrix (Figure 6.3a). The probe permeameter measurements from the CEP zones were over two orders of magnitude higher than those from the surrounding tight limestone (Figure 6.3b).

In addition to the above factors, neither core plug nor the probe permeameter data could measure porosity and/or permeability values for the leached stylolites and tension gashes. Previous studies suggest that stylolites are often localised and laterally extensive planar surfaces (e.g., Peacock & Azzam 2006; Ebner *et al*. 2010; Koehn *et al*. 2012). Stylolites are also bound by rough-walled, non-planar surfaces (e.g., Renard *et al*. 2004; Brouste *et al*. 2006). Using the idealised assumption that stylolites are bound by two planar and smooth surfaces, we calculated the permeability range of the stylolites and tension gashes based on their apertures using the parallel plate solution derived from the

Navier-Stokes equations (Witherspoon *et al*. 1980). This law implies that for laminar flow of fluid with density ρ and viscosity μ, between two fracture walls, the fracture permeability, K, is proportional to the fracture aperture, 2b, squared, and can be estimated as

$$K = \frac{(2b)^2 \rho g}{12\mu} \quad (1)$$

Although this law makes the highly idealised assumptions that fracture walls are smooth and planar, studies have shown that the parallel plate law can provide reasonable permeability estimates for rough-walled and non-planar fracture surfaces with highly heterogeneous flow fields (Dijk *et al*. 1999).

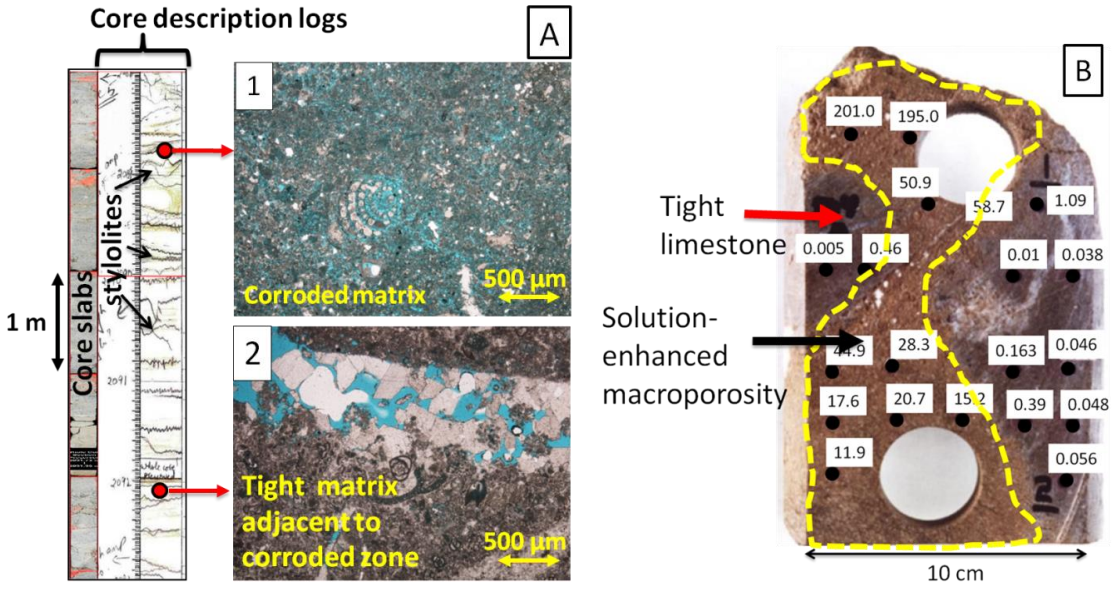

Figure 6.3. (a) Core log with detailed description of the stylolites and associated tension gashes featuring the thin-sections from corroded [1] and unmodified matrix [2].The thin-sections from the corroded zone show much higher porosity than those from the unmodified matrix. (b) Probe permeameter map showing the distribution of permeability between the corroded and unmodified limestone matrix on the core. Note that core plugs were taken towards the tighter matrix.

Another important assumption in the parallel plate law is that the fractures remain open. However, in Field X it was observed that stylolites and tension gashes can be partially filled with dickite and bladed calcite. Dickite is a high-temperature phyllosilicate clay mineral and was precipitated in Field X as a bi-product of mesogenetic dissolution (Wright & Barnett 2011). The impact of dickite and calcite on fracture permeability is

unknown and requires further investigation. A further challenge is that apertures measured in the stylolites and tension gashes at surface conditions are most likely different from the apertures at reservoir conditions. Hence, a heuristic approach was used and the aperture values initially measured in the core were reduced by a factor of 10. Subsequently, the impact of apertures ranging from 0.01 to 0.02 mm was analysed. In summary, the permeability of the stylolites and tension gashes is associated with uncertainty related to the roughness of the stylolite surfaces, the overburden/unloading effect on the apertures and the local precipitation of dickite and calcite within the stylolites and tension gashes. The uncertainty in permeability of the stylolites and tension gashes impacted the upscaled horizontal and vertical permeabilities that were computed in the near-wellbore modelling workflow. These sensitivities were analysed in the later sections when the minimum and maximum apertures were used to obtain the corresponding range of effective permeabilities from near-wellbore upscaling workflow.

The core description logs were used in conjunction with the core plug and probe permeameter data to estimate porosity and permeability of the CEP zones in the wells. Porosity and permeability measurements from a total number of 344 core plugs were available. The wireline porosity log was also used to validate the estimated porosity distribution for the CEP zones. The range of porosity and permeability values in the CEP zones that were obtained from Routine Core Analysis (RCA) and well log data is listed in Table 6.2. The CEP zones typically displayed higher porosity values (Figure 6.4). The probe permeameter values measured in the CEP zones showed permeabilities that were over two orders of magnitude higher relative to those from the surrounding unaltered limestone (Figure 6.5). Even considering the aforementioned uncertainties in permeability measurements for complex pore types (Corbett *et al*. 1999), this difference was significant and indicated that the CEP zones are likely a primary control for fluid flow in Field X. Image logs were correlated readily with core and probe permeameter data and they confirmed the presence and extensive distribution of the corroded zones throughout the well (Figure 6.6). The dark conductive patches on the Formation Micro-Image (FMI) log were consistent with the CEP zones, which in turn corresponded to higher probe permeameter measurements on the core. In contrast, light coloured resistive patches indicated the tight limestone.

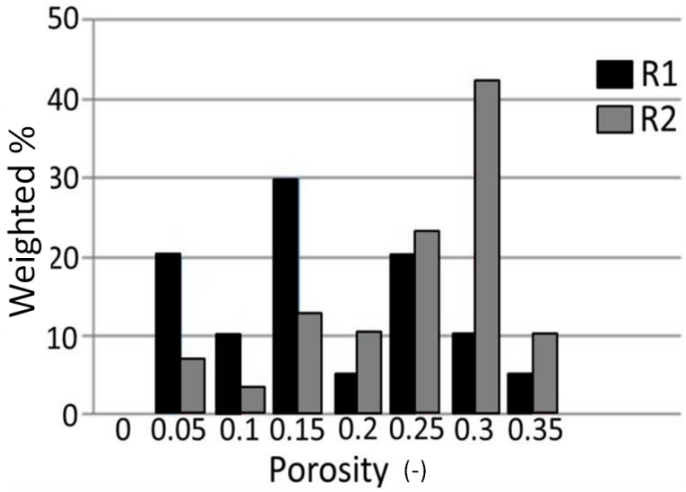

Figure 6.4. Porosity distribution of unmodified matrix and CEP zones, denoted by R1 and R2, respectively. The CEP zones exhibit higher porosity than the tight limestone. Porosity measurements from a total number of 344 core plugs were available

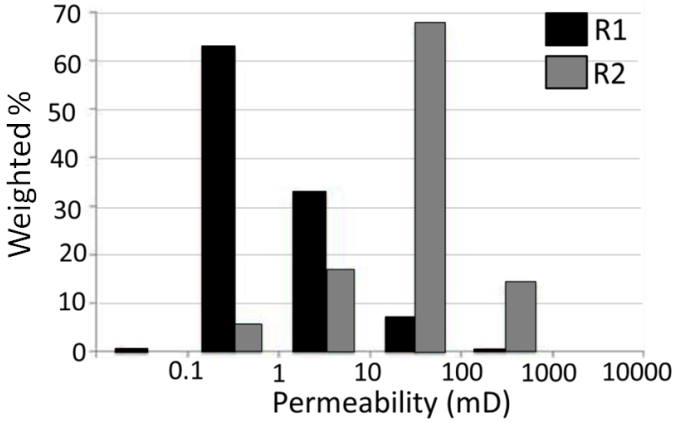

Figure 6.5. Histogram of permeability distribution of unmodified matrix and CEP zones, denoted by R1 and R2, respectively. The CEP zones exhibit higher permeability range than the tight limestone. Permeability measurements from a total number of 344 core plugs were available.

Table 6.2. Poro-perm range of CEP zones from RCA data.

CEP type	Porosity (-)				Permeability (mD)			
	Min	Max	Mean	SDV	Min	Max	Mean	SDV
Matrix-micro porosity	0.04	0.15	0.08	0.03	0.001	7.28	0.4	1
Matrix-macro porosity halos near stylolites	0.12	0.4	0.23	0.04	100	700	300	170
Micro-porosity halo near stylolites	0.08	0.2	0.12	0.07	15	120	50	15
Leached stylolites	0.4	0.8	0.5	0.1	500	2500	1000	100
Leached tension gashes	0.4	0.8	0.5	0.1	5000	25000	10000	500

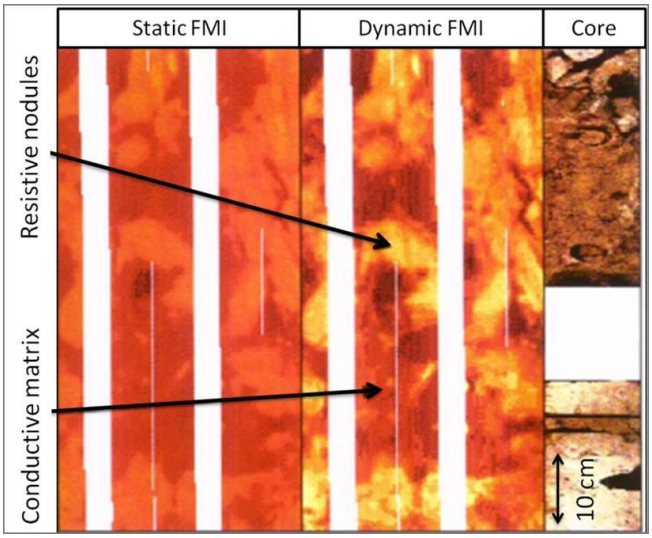

Figure 6.6. Image logs correlated with core; dark coloured conductive matrix represents the corroded zones and light coloured resistive matrix the tight limestone. Note that the lightest area on the image logs corresponds to the light coloured tight rock and the dark patches on the image log are tied to the dark brown areas on the core.

6.3. Near-wellbore upscaling of late-burial corrosion heterogeneities

The wide-spread occurrence of CEP zones in Field X is likely to be a key control for fluid flow in Field X. However, as mentioned before, due to sample bias towards the low-permeability tight limestones, the CEP zones were not included in a geologically consistent way in the reservoir simulation model. Instead, different permeability multipliers were introduced until a satisfactory history match was achieved. Hence an accurate re-evaluation of the horizontal permeability K_h for the CEP zones was needed. Considering the drive mechanism in Field X where the oil rim is produced by expanding the gas cap (Oates *et al*. 2012), it was expected that the ratio of vertical to horizontal permeability, K_v/K_h, needed to be modelled accurately in Field X to capture the main flow mechanisms. It was therefore crucial to disentangle and understand how the different corrosion-enhanced porosity types in the CEP zones, from microporosity to leached stylolites and tension gashes, impact reservoir permeability individually and cumulatively. This challenge was approached using a systematic modelling and upscaling workflow in which near-wellbore modelling tools were employed.

6.3.1. Modelling corroded zones with near-wellbore modelling tools

A range of high-resolution, i.e. centimetre-scale, models were created with SBED™ that represent the CEP zones (Figure 6.7). These models also included the leached stylolites (Figure 6.7a) and associated tension gashes (Figure 6.7b). The methodology

used to construct the models with stylolites and tension gashes can be referred from Chapter 3, in 'Bedding structure modelling' section. Input data for the near-wellbore modelling came from the detailed core description, petrophysical analysis, and probe permeameter data described above. Figure 6.7c illustrates a near-wellbore modelling scenario in which stylolites are surrounded by corrosion-enhanced matrix porosity halos. The spatial and geometrical parameters of the leached stylolites and the vertical to sub-vertical tension gashes were based on the core observations. The near-wellbore model dimensions were selected such that the multi-scale heterogeneities were adequately represented while the resulting K_v/K_h values were appropriate for the reservoir geomodel. The model dimensions for the near-wellbore modelling workflow were $\Delta X = \Delta Y = \Delta Z = 20$ cm. The cell dimensions were $\Delta x = \Delta y = 0.2$ cm. This allowed the representation of the size of the leached stylolites and tension gashes realistically. The cell dimension in the z-direction, Δz, varied between 2 mm to 1 cm, depending on the vertical dimension of the geological structures that were needed to be resolved.

Porosity and permeability statistics that were needed as input for the near-wellbore modelling were obtained from the probe permeameter and core plug data. In this way, three scenarios of CEP zone models were generated with multiple realisations. These models included or excluded stylolites and tension gashes. The density of distribution of the stylolites and tension gashes were also varied to evaluate how different apertures impacted their permeabilities using the minimum and maximum apertures of 0.01 mm and 0.02 mm respectively. It must be noted that only the above mentioned three types of CEP scenarios were evaluated in the work discussed in this chapter. Several additional scenarios of CEP types, with varying distributions of corrosion-enhanced matrix porosity, are also important to perform a full-scale study to characterise field-scale permeability for Field X. However, this was not undertaken due to time constraints in this particular study, but were later carried out as will be discussed in Chapter 7.

6.3.2. Obtaining effective properties for the corroded zones

The near-wellbore models of the small-scale heterogeneities in the CEP zones were upscaled in SBED^{TM} to compute the effective porosity, horizontal permeability and K_v/K_h values using flow-based upscaling, as discussed in Chapter 3. A pressure solver method with periodic and open boundary conditions (Pickup & Sorbie 1996) was used to estimate a more realistic effective full-permeability tensor for the small-scale

heterogeneities. The resulting upscaled properties showed that the effective horizontal permeability was significantly improved in the CEP zones, i.e. when the corrosion-enhanced micro and macroporosity in the matrix, leached stylolites and the tension gashes were accounted for. Effective permeabilities ranged from 1 to 350 mD for corrosion-enhanced micro and macroporosity model scenarios. This was in stark contrast to the original core derived permeability which varied from 0.01 to 50 mD. When stylolites and associated tension gashes were included, the upscaled permeability were as high as 1000 mD. Including stylolites and tension gashes also increased the vertical permeability considerably and led to K_v/K_h ratios that were as high as 2.5. The models that only accounted for corrosion-enhanced matrix porosity yielded K_v/K_h ratios of up to 1. In this context, it must be noted that the K_v/K_h ratio in the original geomodel was a uniform 0.1. Table 6.3 lists the typical upscaling results for all modelled near-wellbore scenarios and indicates that the leached stylolites and associated tension gashes can act as a highly permeable network in conjunction with the surrounding corrosion-enhanced matrix porosity.

Table 6.3. Effective poro-perm of CEP zones from near wellbore upscaling.

CEP Zone scenario	Φ_{eff}	$K_{h\text{-}eff}$	$K_{v\text{-}eff}/K_{h\text{-}eff}$
Corroded matrix with micro and macroporosity	0.23	250	1
Corroded matrix with leached stylolites	0.3	600	1.5
Corroded matrix with leached tension gashes	0.26	300	2
Corroded matrix with leached stylolites and tension gashes	0.35	900	2.5

Table 6.4 presents an example of the comparison between the effective permeability values when calculated using periodic (PBC) versus linear (LBC) boundary conditions (refer to Chapter 3, Section 3.7.2 for more details on flow-based upscaling) and the results calculated by SBED^{TM} using arithmetic, geometric and harmonic averaging. Arithmetic averaging constantly overestimated while the harmonic averaging severely underestimated the effective permeability when compared to flow-based upscaling. The effective permeability values calculated using PBC were on an average around 10% lower than those from LBC. As discussed in Chapter 3, the results from PBC were consider to be accurate than those from LBC and were used throughout this thesis.

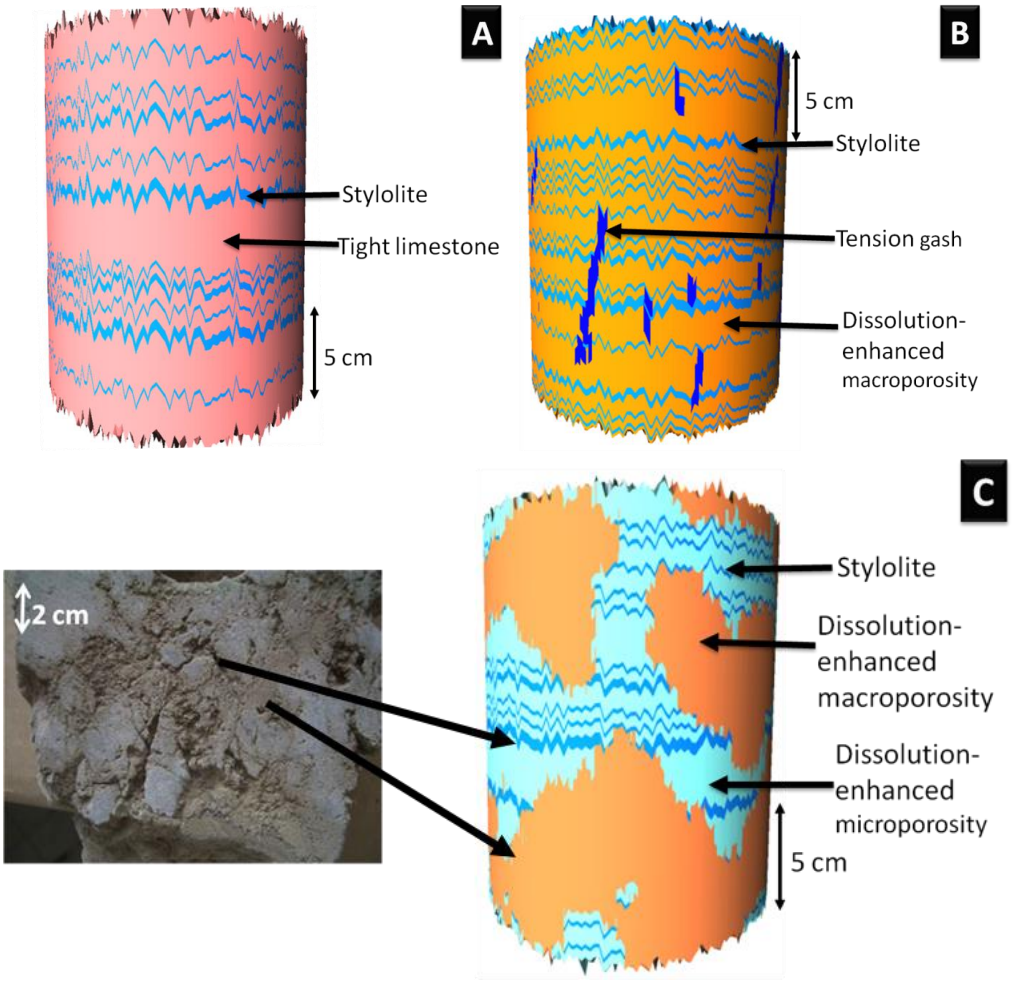

Figure 6.7. (a) Near-wellbore modelling template of stylolites in tight limestone matrix (b) Near-wellbore modelling template of stylolites and associated leached tension gashes surrounded by matrix macroporosity (c) Near-wellbore modelling template with stylolites and halos of matrix macroporosity, mimicking the distribution of the corrosion-enhanced porosity in association with stylolites.

Table 6.4. Comparison of effective permeability values obtained using different boundary conditions

Case	Periodic boundary conditions		Linear boundary conditions		Arithmetic mean	Geometric mean	Harmonic mean
	K_{xx} (mD)	K_{zz} (mD)	K_x (mD)	K_z (mD)	K_x (mD)	K_x (mD)	K_x (mD)
Corroded matrix with micro and macroporosity	84.7	22.67	98.5	90	116	32.53	6.2
Corroded matrix with leached stylolites and tension gashes	612.87	5568.3	790.78	7276.297	1664.092	239.32	212.65

6.4. Translating NWM-derived permeability into reservoir simulation

As discussed earlier, the CEP zones could act as preferential flow paths throughout the reservoir, varying in scale from few centimetres to several meters. One of the objectives of translating the near-wellbore upscaling results into the reservoir simulation model is to account for this scale gap. The conceptual model (Chapter 5, Figure 5.23) of how the CEP zones could be connected throughout the reservoir, in conjunction with near-wellbore upscaling guided the characterisation of porosity-permeability distribution and their inter-relationship. Effective permeability values estimated for the high-resolution near-wellbore models clearly showed an increase in permeability in the CEP zones for all model sensitivities. However, these effective permeability values were still well below the scale of a reservoir simulation grid block and it was hence necessary to translate them to the reservoir simulation grid block scale so as to evaluate how the small-scale permeability enhancement impacted reservoir-scale fluid flow.

The above issue was addressed by comparing the effective near-wellbore modelling-derived porosity and horizontal permeability values for the different models in the CEP zones, i.e. models that included or excluded stylolites and tension gashes, with the porosity-permeability transform derived from the core plug data. Lucia's (1983) class 1, 2 and 3 porosity-permeability transforms at the core plug scale were used, as shown in Figure 6.8.

The original porosity-permeability values measured on the plugs followed Lucia's class 3, which indicated a lower reservoir quality. In contrast, effective porosities and permeabilities from the near-wellbore models of the CEP zones followed Lucia's class 2, indicating much better reservoir quality. This increase in K_h and K_v/K_h associated with Lucia's class 2 transform indicated that the "missing" permeability enhancement in the original reservoir model could be recovered using a different permeability-porosity transform; that is, applying Lucia's class 2 transform may overcome the need to use permeability multipliers to enhance fluid flow in the reservoir simulation model in order to achieve an adequate history match. Lucia's class 2 transform was used to translate porosities measured at the wireline-log scale to permeabilities, and these values were used to update the geological and reservoir simulation models. This approach resulted in new permeability distributions in the geomodel, all of which were guided by near-wellbore modelling and upscaling. These new geomodels accounted for different combinations of small-scale heterogeneities in the CEP zones. As these models

incorporated additional geological information for the CEP zones, it was expected that they should lead to more reliable forecasts of hydrocarbon production and should require less artificial permeability multipliers.

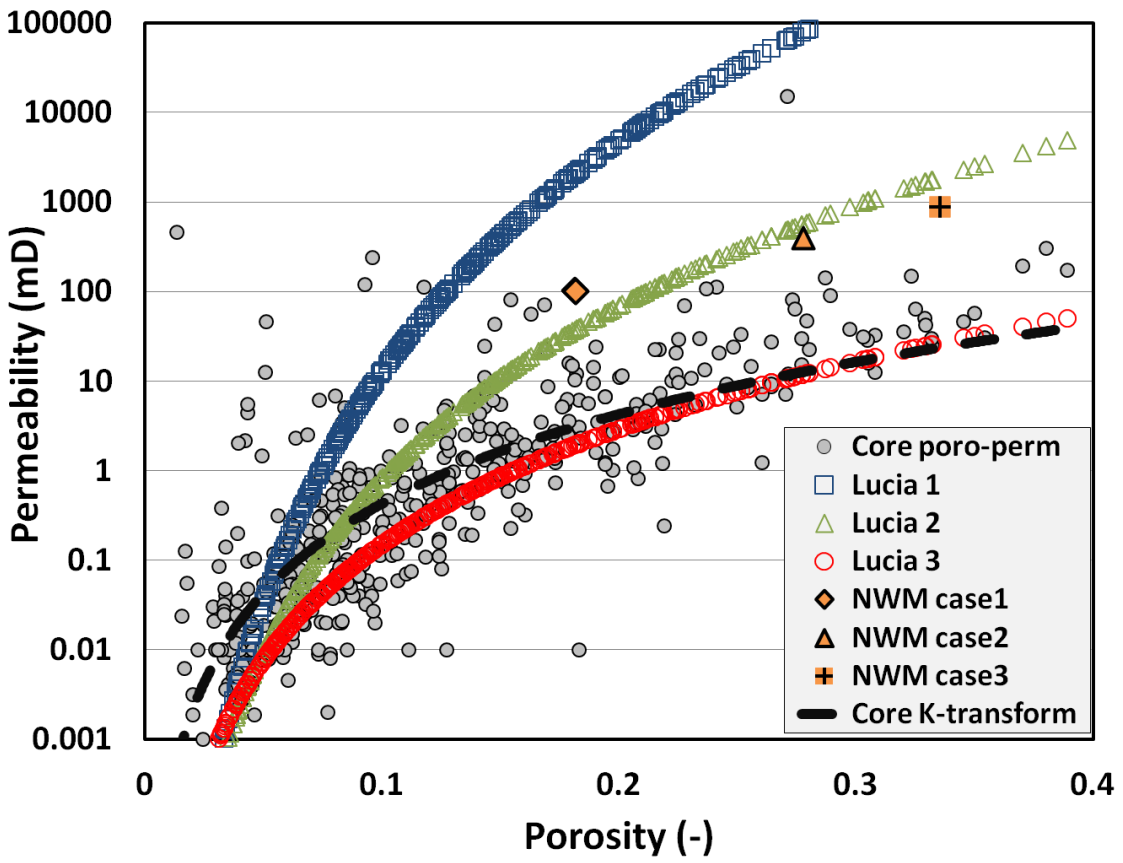

Figure 6.8. Comparison of Field X core porosity and horizontal permeability data with Lucia's (1983) permeability transforms and effective porosity and horizontal permeability values from the near-wellbore upscaling workflow. NWM case 1, case 2 and case 3 represent corroded matrix, corroded matrix with stylolites, and corroded matrix with stylolites and tension gashes, respectively. Note that the original core permeability-transform is closer to Lucia's Class 3 transform, reflecting poor quality matrix. The upscaled properties obtained from the near-wellbore modelling closer to the higher quality Lucia Class 2 and 1 transforms.

Since Field X required a large and complex simulation model (Figure 6.9a) that required considerable computing time, only the geomodels for a sector model containing Well Group 1 (Figure 6.9b) were updated in this chapter. Well Group 1 was selected because it was the well group with the longest production history. It consisted of 12 vertical and 11 horizontal production wells. There were approximately 376,000

active cells in the sector model. Each cell had an average dimension of ΔX = ΔY = 50m and average thickness of ΔZ = 1 m in B Zone and ΔZ = 2 m in A Zone.

The original geomodel, without its permeability multipliers, served as the base case. Recall that this geomodel comprised a permeability distribution that was biased towards the low-permeability, uncorroded matrix. To generate additional geomodel scenarios that represented various late-burial corrosion heterogeneities, a simple reservoir rock-typing scheme was introduced and the tighter uncorroded matrix was defined as rock type R1 and the highly permeable CEP zone as rock type R2. This was in contrast to the original geomodel which did not contain a facies model or any rock types. Rock type R2 was varied to reflect the different small-scale heterogeneities that were observed in the CEP zone. That is, R2 contained varying combinations of corrosion-enhanced matrix porosity, leached stylolites and tension gashes, expressed through variations in effective permeability and porosity as computed from near-wellbore modelling and upscaling.

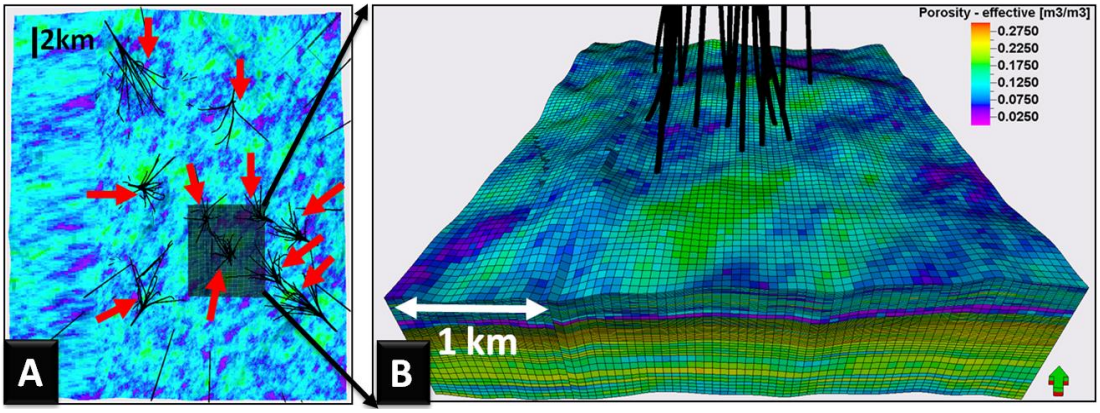

Figure 6.9. (a) Top-view of the field scale geomodel of Field X showing the porosity distribution and the approximate location of all the well groups (see arrows). The field scale geomodel comprises over five million grid blocks with lateral cell dimensions of 50 m x 50 m. Cell sizes in the vertical direction have an average thickness of 2 m, enabling the resolution of reservoir layers and capture the vertical heterogeneity. (b) Close-up showing the sector model containing Well Group 1 used for the simulation study. The location of the sector model is indicated by the grey shaded area in the field scale model. The colour scale for porosity is the same in the sector and in the field scale model.

Rock type logs of R1 and R2 were generated for the near-wellbore region of the wells using available core description. These logs provided density and porosity cut-offs based on the petrophysical log analysis, which allowed us to generate additional rock type logs for the wells without core. These rock type logs were then upscaled into the reservoir grid blocks using weighted averaging. Sequential Indicator Simulation (SIS) (Deutsch & Journel 1998; Deutsch 2002) was used to distribute R1 and R2 away from the wellbore. The porosity distribution was calculated for each model using Sequential Gaussian Simulation (SGS) (Deutsch & Journel 1998; Deutsch 2002) based on the wireline porosities and conditioned to the new rock type distributions. Multiple model scenarios were obtained by varying the lateral correlation lengths of the rock type R2. Due to the limited availability of the geostatistics that were used to build the original porosity model given by the operator, the sensitivities were constricted to varying the correlation lengths of the rock type distributions. Two main types of rock type scenarios were obtained; one by distributing the rock type log from wells in to the grid blocks using SIS, and the other by changing the correlation lengths to generate porosity models from porosity log using SGS- and then applying the porosity cutoff to obtain facies model. Correlation lengths of 50m, 100m and 200m were used in both cases. Subsequently the application of permeability transforms was conditioned to the distribution of the RTs. The geostatistical parameters used to obtain a certain model realisation could also impact the simulated production profiles along with the varying permeability input from near-wellbore upscaling. The geostatistical factors were also hence given consideration while evaluating the production performance of each of the realisations.

For the base case, the porosity-permeability transform from the original core data was used, i.e. the transform that was biased towards a tighter rock matrix and was similar to Lucia's class 3 transform (Figure 6.8). The same transform was also used to calculate permeability within rock type R1. Lucia's class 2 porosity-permeability transform was tested for rock type R2 and was found to represent the permeability derived from the near-wellbore modelling and upscaling of the heterogeneities in the CEP zones more closely (Figure 6.8). The vertical and horizontal permeability values from the near-wellbore modelling and upscaling were used to estimate the respective K_v/K_h ratios for rock type R2. These ratios varied depending on the presence or absence of corrosion-enhanced micro and macroporosity in the matrix, leached stylolites and associated

tension gashes. Over all, this approach resulted in over 25 permeability scenarios, ranging from the original geomodel to geomodels that accounted for all the heterogeneities observed in the CEP zones. This allowed the simulation of a range of production profiles to analyse how small-scale geological heterogeneities caused by late-burial corrosion impacted the dynamic behaviour of Field X. It also allowed the investigation of a geomodel that accounted for the CEP zone if it can provide better history matches without requiring permeability multipliers.

6.5. Impact of late-burial corrosion on reservoir performance

Oil, gas and water production data for the different permeability models were simulated for Well Group 1 (Figure 6.9b), using the original field development strategy, i.e. we used the same well production scheduling and well-controls as in the history matched model. Only the first 10 years of production were simulated. The resulting production profiles were then compared to evaluate which of the different model scenarios had the smallest misfit, i.e. which of the different model scenarios was most likely because its simulated production profiles agreed best with the observed ones.

Figures 6.10, 6.11 and 6.12 demonstrate the simulated versus historic cumulative oil, gas and water production graphs respectively. The respective oil, gas and water production rates are presented in Appendix C. In these three graphs the same symbols and line types were used for the different cases, while the green, orange and blue colours denote the oil, gas and water productions curve graphs respectively. Ideally the choice of simulation parameter to monitor could have been individual production rates. However, the cumulative production profiles were used to compare with historic data due to some prevailing uncertainty associated with the well completions data provided with the original history matched simulation model. The base case, i.e. the geomodel without permeability multipliers, displayed a cumulative oil production that did not match the observed production at all. This mismatch decreased significantly when rock type R2, and hence the small-scale heterogeneities in the CEP zone, was included into the geomodel (Figure 6.10). This indicated that the permeability multipliers in the history match were only needed to recover the "missing" permeability from rock type R2. Case 1 and Case 2 in Figure 6.10 represent two different geomodel scenarios for R2. In both cases the horizontal permeability within rock type R2 was modelled using Lucia's class 2 transform, i.e. the rock type included the combined impact of corrosion-enhanced matrix, stylolite and tension gashes (Figure 6.7b). In both cases, rock type R2

was also modelled using a small correlation length of 50 m, which was equivalent to the simulation grid block size. The key difference was that the K_v distribution for rock types R1 and R2 in Case 1 was computed using the uniform K_v/K_h ratio of 0.1 from the base case. In Case 2, however, the K_v/K_h ratio for R2 was taken from the near-wellbore modelling and upscaling. In other words, the improvement of vertical permeability caused by the network of leached stylolites and tension gashes in conjunction with matrix porosity was not accounted for in Case 1.

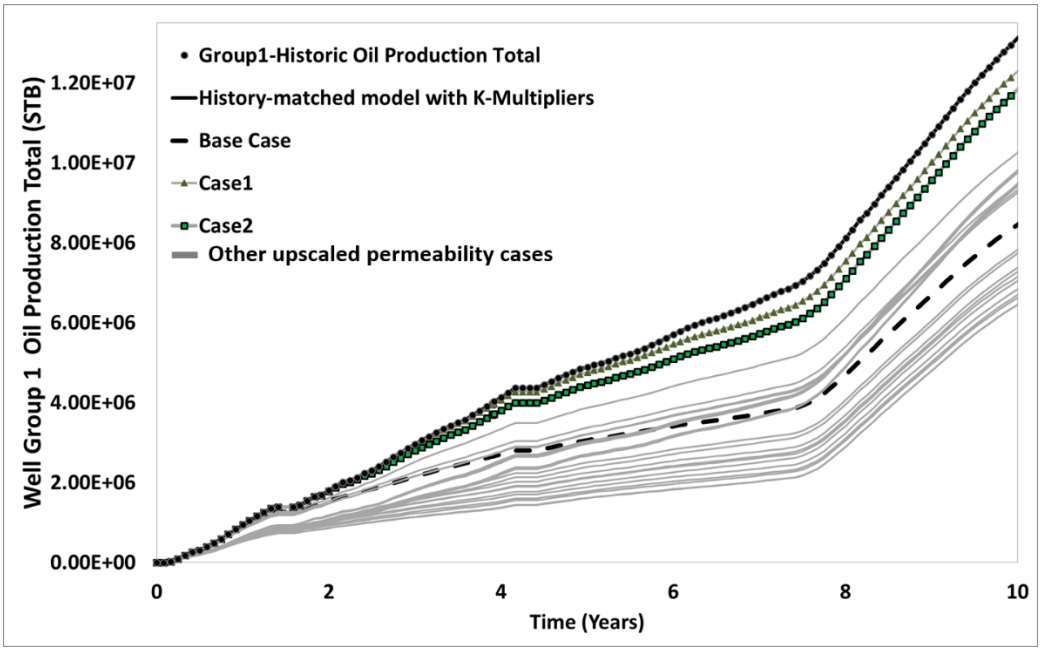

Figure 6.10. Cumulative oil production curves simulated for sector model containing Well Group1. Results are from all geomodel scenarios before and after incorporating facies R2. Note that the history-matched simulation model curves and historic curves are overlapping. In Case 1, the K_v distribution from the base case was used for rock types R1 and R2. In Case 2 the K_v/K_h values estimated from the near-wellbore modelling and upscaling workflow were used for distributing K_v in rock type R2. STB refers to 'Stock Tank Barrels'.

Both, Case 1 and Case 2 showed significantly improved matches between the simulated and historic oil production. This was due to the increase in horizontal permeability, which allowed for additional flow in the reservoir and hence higher oil production rates. However, simulations for Case 1 failed to obtain a successful match of the simulated gas and water production profiles (Figure 6.11 and Figure 6.12). This was due to the reduced K_v/K_h ratio in Case 1. Case 2, which used the K_v/K_h ratio from the near-

wellbore modelling and upscaling, allowed for additional flow in the vertical direction and hence represented the vertical fluid displacement caused by the particular drive mechanism in Field X more adequately. Case 2 therefore showed significantly improved matches for the gas (Figure 6.11) and water production (Figure 6.12). Rock type R2 with the higher K_v/K_h ratio improved the lateral and vertical connectivity in the reservoir by accounting for leached stylolites and associated tension gashes as well as the corrosion-enhanced matrix porosity. This inference provided a valuable insight towards the sensitivity of the simulated production profiles in Field X to the contribution of leached stylolites to the vertical permeability of rock type R2.

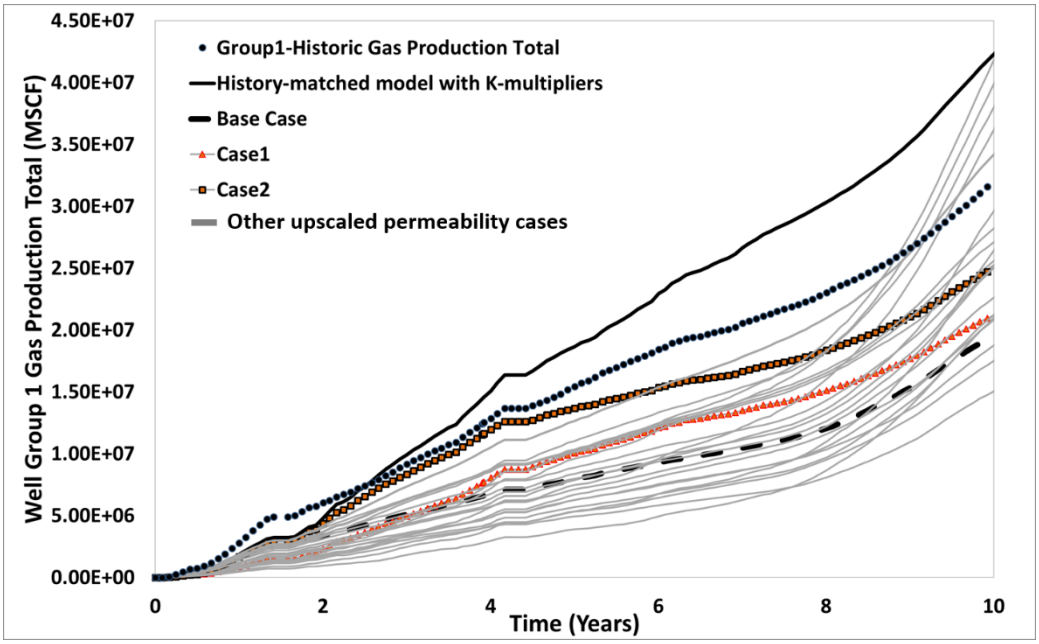

Figure 6.11. Cumulative gas production curves simulated for the sector model containing Well Group1. Results are for all geomodel scenarios before and after incorporating facies R2. Note the divergence between the historic and base case profiles. MSCF refers to 'Thousand Standard Cubic Feet'.

Neither Case 1 nor Case 2 achieved perfect matches to the historic oil production due to several reasons; First, only Lucia's class 2 transform was used as a proxy to estimate the permeability of rock type R2. As noted earlier, Lucia's transforms do not account for fractures and open touching vugs. A better match for the oil production rate could possibly be obtained by generating a new, tailor-made porosity-permeability transform using our near-wellbore modelling and upscaling approach, as well as the available core data and possibly dynamic data. Secondly, there are other major uncertainties associated

with the geomodel of Field X such as initial fluid distributions that can impact the quality of a history match. Lastly, it is very likely that the late-burial corrosion also impacted other properties of Field X such as relative permeability and wettability that will influence, in particular, the oil rates. However, the outcome of the work presented in this chapter significantly improved the understanding towards the role of late-burial corrosion on the permeability of Field X and the reservoir simulation results.

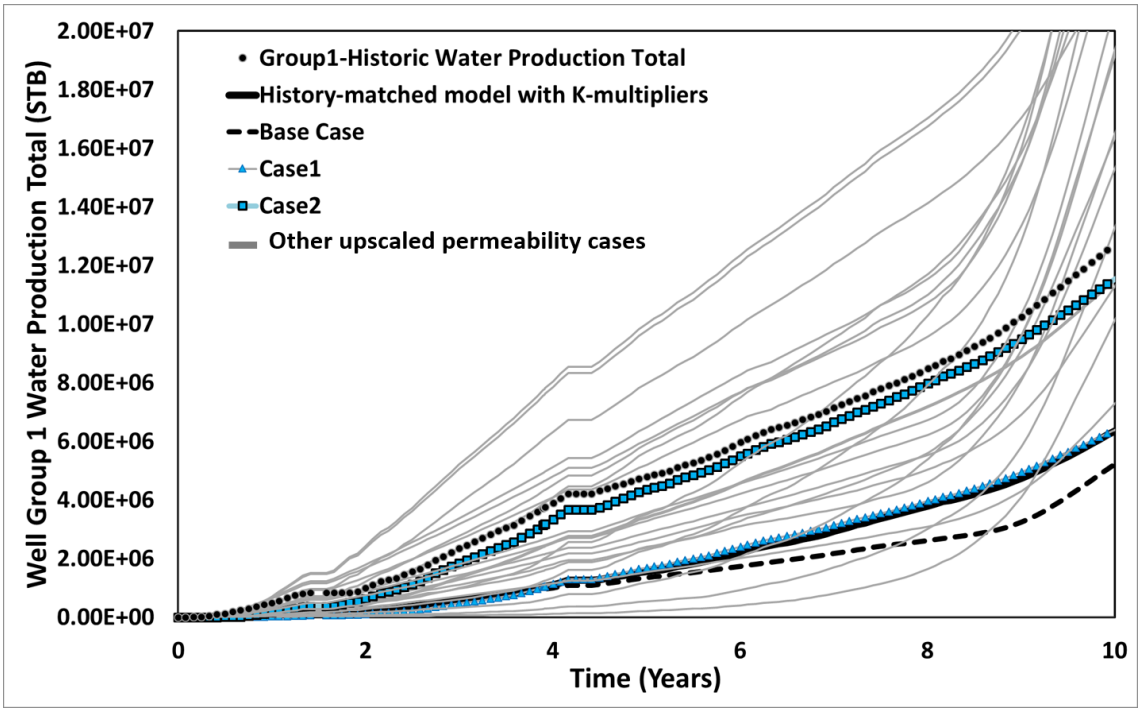

Figure 6.12. Cumulative water production curves simulated for the sector model containing Well Group1. Results are for all geomodel scenarios before and after incorporating facies R2. Note that the base case and Case 1 profiles are overlapping, while Case 2 profile is much closer to the historic data. STB refers to 'Stock Tank Barrels'.

6.6. Conclusions

This chapter describes how NWM workflow was used to evaluate the impact of small-scale geological heterogeneities caused by late-burial corrosion on the reservoir fluid production profiles in Field X. It was demonstrated, using a re-evaluation of the core data, NWM, and reservoir simulation, that corrosion-enhanced matrix micro and macroporosity, leached stylolites and associated tension gashes have a significant impact on reservoir horizontal and vertical permeabilities. A large number of geomodel cases were created, each of which contained different combinations and lateral extents

of these corrosion-enhanced porosity (CEP) zones. The NWU results aided the incorporation of these small-scale heterogeneities in field-scale reservoir simulation models by computing their effective properties from small-scale and high-resolution models. Lucia's permeability transforms, guided by near-wellbore upscaling results, were used as proxies to incorporate the small-scale heterogeneities related to the late-burial corrosion in the permeability model of Field X. Fluid production was simulated for the different reservoir sector models, ranging from the original geomodel to the geomodels which comprised the re-evaluated permeability distributions. Then, the simulated production profiles from the sector models were compared with the historic production data of the corresponding well group. The different geological models were then ranked to evaluate the most likely scenario based on the best match between simulated and observed production data.

The smallest mismatch between simulated and historic production profiles was obtained not only when an increased horizontal permeability was included but when the K_v/K_h anisotropy of the late-burial corrosion features was included in the geomodel. Thus, the investigation presented in this chapter led to a significantly improved characterisation of the late-burial corrosion heterogeneities in Field X and validated their prominent role in improving the permeability distribution. However, it must be noted that although Lucia's class 2 transform matches the effective NWM-derived permeability well, it only accounts for interparticle porosity, i.e. strictly speaking it does not account for fracture or "touching vug" porosity.

While it would be possible, in principle, to derive a new permeability-porosity transform for Field X using only NWU, along with other data such as well-tests and plug measurements, this is beyond the scope of the study presented in this chapter. The following chapter, Chapter 7, describes the workflow and outcome of deriving new permeability transforms for Field X using only NWU tools, in contrast to using Lucia's permeability transforms as proxies.

Chapter 7. NOVEL NEAR-WELLBORE UPSCALING WORKFLOW TO IMPROVE PERMEABILITY MODELLING IN FIELD X

7.1. Introduction

In the previous chapter, the characterisation of multi-scale heterogeneities caused by late-burial corrosion in Field X has been discussed and their impact on fluid flow has been demonstrated using Lucia's permeability transforms as proxies. The current chapter describes the workflow adopted to derive new global permeability transforms for Field X using only near-wellbore modelling and upscaling tools. The reservoir simulation results from a sector model of Field X that employed the permeability transforms derived from near-wellbore upscaling were analysed. In addition, a comparison of the uncertainty analysis results between the original history matched model and the simulation model that employed new permeability transforms has been presented. The main objective of the work described in the following sections is to resolve the uncertainty related to modelling and upscaling horizontal permeability, K_h, and permeability anisotropy ratio, K_v/K_h, in Field X. The following sections describe the near-wellbore modelling and upscaling workflow developed in this study to address the permeability modelling challenges in Field X.

7.2. Modelling late-burial corrosion heterogeneities

As illustrated in Chapter 6, SBED^{TM} is capable of generating representative models and upscaled properties of the geological heterogeneities in Field X. In the work described in this chapter, SBED^{TM} was employed in a robust geostatistical modelling framework in an attempt to capture the extreme variability in the permeability distribution of Field X in the reservoir simulation model. The near-wellbore modelling workflow in SBED^{TM} firstly involved obtaining the geometrical model templates of the multi-scale geological heterogeneities. For this, cores were first used to divide the near-wellbore regions of the wells into centimetre to decimetre scale representative intervals. This exercise was mainly based on the distribution of matrix micro and macroporosity types and presence of leached stylolites and associated tension gashes within the CEP zones. Multiple scenarios of millimetre to centimetre scale miniature stochastic models, hereafter referred to as 'mini-models', were generated in SBED^{TM} using the 'bedding structure modelling' feature for each of these representative intervals. Each mini-model comprised 'sub-model elements', representing the various late-burial corrosion heterogeneities. These 'sub-model elements' were equivalent to the 'lamina type

templates' described in Chapter 3. Figure 7.1 illustrates an example mini-model which represents a CEP zone with corrosion-enhanced matrix macroporosity surrounded by tight limestone matrix. There were hence two 'sub-model elements' in this mini-model, corrosion-enhanced macroporosity and tight matrix.

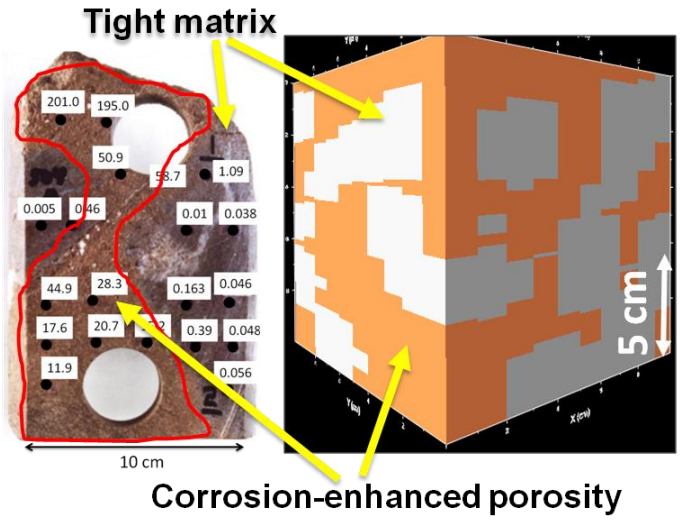

Figure 7.1. Example of a mini-model with corrosion-enhanced macroporosity surrounded by tight matrix. The numbers on the core indicate the probe permeameter measurement at those points.

The dimensions of each mini-model were chosen such that the model volume was comparable to the volume of investigation of the wireline porosity tool. This enabled us to check the quality of the upscaled properties by comparing them to the wireline data. Accordingly, the model dimensions used were $X = Y = Z = 20\ cm$. The typical cell dimensions were $\Delta X = \Delta Y = 0.2\ cm$, and were chosen such that the small-scale geological features such as stylolites and tension gashes could be represented realistically. The cell dimension in the z-direction, Δz, varied between 2 mm to 1 cm, depending on the geometries of the heterogeneities to be represented.

The mini-models were of two main categories, 'matrix only' mini-models and 'stylolite and tension gash' mini-models. In the matrix only mini-models, the key element towards enhancing permeability was the corrosion-enhanced matrix porosity. In the stylolite and tension gash mini-models, the leached stylolites and associated tension gashes were expected to act as a high permeable network in conjunction with the surrounding corrosion-enhanced matrix porosity. Each mini-model scenario consisted of

its own unique set of geometrical parameters from which a large number of equiprobable stochastic realisations were generated for that scenario.

The geometrical and spatial distribution parameters of the sub-model elements related to late-burial corrosion were deduced from core and image log interpretation to define the geological details (e.g. Figure 7.1). The porosity-permeability distributions for the mini-models leveraged the petrophysical analysis discussed in Chapter 6. The mean and standard deviation of porosity and permeability within the various sub-model elements were derived with the aid of careful investigation of core and probe permeameter data (e.g. Figure 7.1). This approach mitigated the core sample bias and incomplete RCA data. Porosity and permeability distributions for each sub-model element in each mini-model realisation were populated by random Gaussian simulation using the mean, standard deviation, minimum and maximum values. Random Gaussian field if the default and only option available in the current SBED^{TM} version used in this thesis for the latter method of property distribution. Alternatively, as discussed in Chapter 3, it could have also been possible to employ a suitable variogram to define the porosity and permeability distributions. When geostatistical data for the variogram are available, the suitable variogram model, trend and poro-perm correlation can be selected accordingly. However, due to limited geostatistical data available from Field X for this study, the Random Gaussian field distribution was hence used for property modelling. The petrophysical parameters input for the sub-model templates of matrix only and stylolite and tension gash mini-model scenarios is summarised in Table 7.1.

Table 7.1. Input parameters used for petrophysical modelling of late-burial corrosion heterogeneities.

Sub-model template	Porosity				Permeability			
	Mean (fraction)	**Std Dev**	**Limit control (Min)**	**Limit control (Max)**	**Mean (mD)**	**Std Dev**	**Limit Control (Min)**	**Limit Control (Max)**
Tight limestone	0.01	0.001	0.005	0.02	0.05	0.005	0.01	0.1
Corrosion-enhanced microporosity	0.08	0.03	0.04	0.15	0.4	1	0.01	7.28
Corrosion-enhanced microporosity halo near stylolites	0.15	0.07	0.12	0.23	25	5	20	30
Corrosion-enhanced macroporosity	0.23	0.04	0.15	0.4	300	170	100	700
Corrosion-enhanced macroporosity near stylolites	0.23	0.04	0.15	0.4	500	60	115	1000
Leached stylolites	0.5	0.1	0.4	0.8	1000		500	5000
Leached tension gashes	0.5	0.1	0.4	0.8	10000		5000	20000

In summary, the mini-models were used to represent the geometrical and petrophysical variability of the late-burial corrosion heterogeneities as accurately as possible in the near-wellbore region. The following sections detail the near-wellbore modelling parameters used for the various mini-model scenarios.

7.2.1. Matrix only mini-models

The main sub-model templates used in the 'matrix-only' mini-model scenarios were tight limestone matrix, corrosion-enhanced macroporosity and corrosion-enhanced microporosity. Different scenarios of matrix microporosity and macroporosity distributions were modelled using the object modelling feature in SBED^{TM} (e.g. Figure 7.2a). The procedure followed during object modelling in SBED^{TM} to superimpose the geometrical models with diagenetic features has been presented in Chapter 3. Figure 7.2b illustrates a network rod object model template, which was used as the sub-model template for superimposing the corrosion-enhanced matrix porosity distribution on the background bedding structure model. Table 7.2 summarises the geometrical parameters used for modelling the micro and macroporosity sub-model templates using the object modelling feature in SBED^{TM}.

The spatial distributions of the micro and macroporosity sub-model templates were controlled in a stochastic framework to impose randomness to the extent of corrosion-enhanced porosity in each mini-model realisation. Two stochastic methods, percentage type and bioturbation index type, were used to regulate the proportions of sub-model templates within each mini-model scenario. As discussed in Chapter 3, the percentage type required the input of mean and standard deviation values of the percent of sub-model template to be modelled in a particular scenario. The bioturbation index type required the input of the upper and lower limits of the percent of sub-model template in the mini-model. Several scenarios of matrix only mini-models were obtained by varying the spatial distribution of the micro and macroporosity sub-model templates from 0 to 100% (Figure 7.3a). 20 equiprobable realisations were generated for each mini-model scenario (e.g. Figure 7.3b). The typical cell dimensions used for matrix only mini-models were $\Delta X = \Delta Y = 0.2\ cm$ in the lateral direction and Δz = 1 cm in the vertical direction. The model dimensions were $X = Y = Z = 20\ cm$

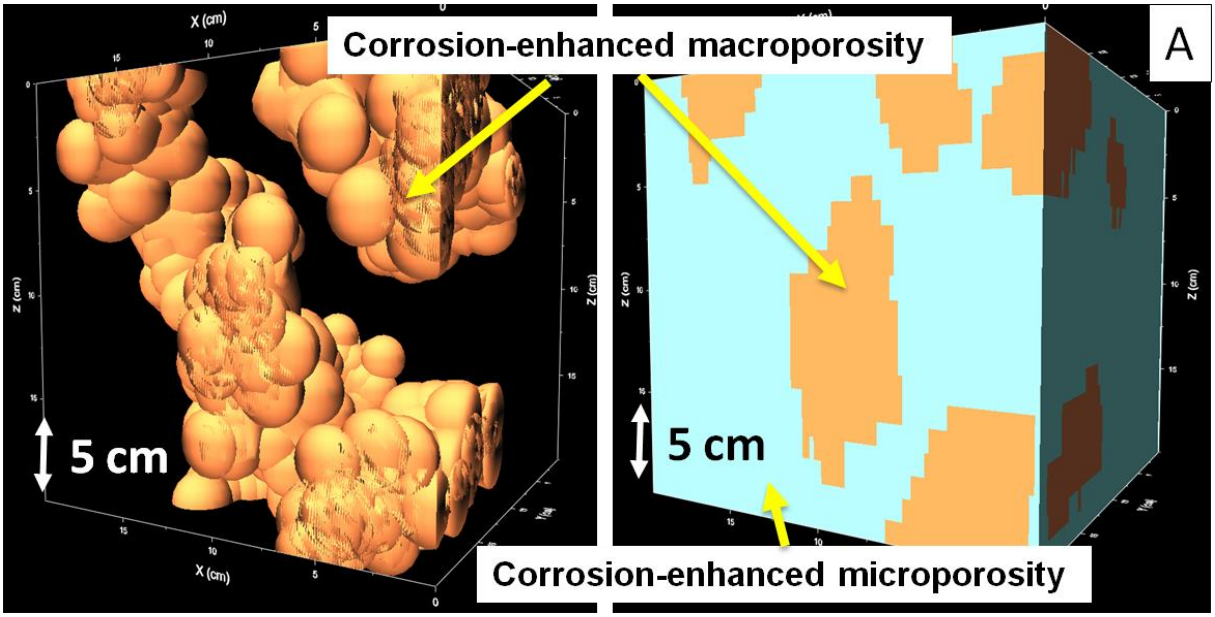

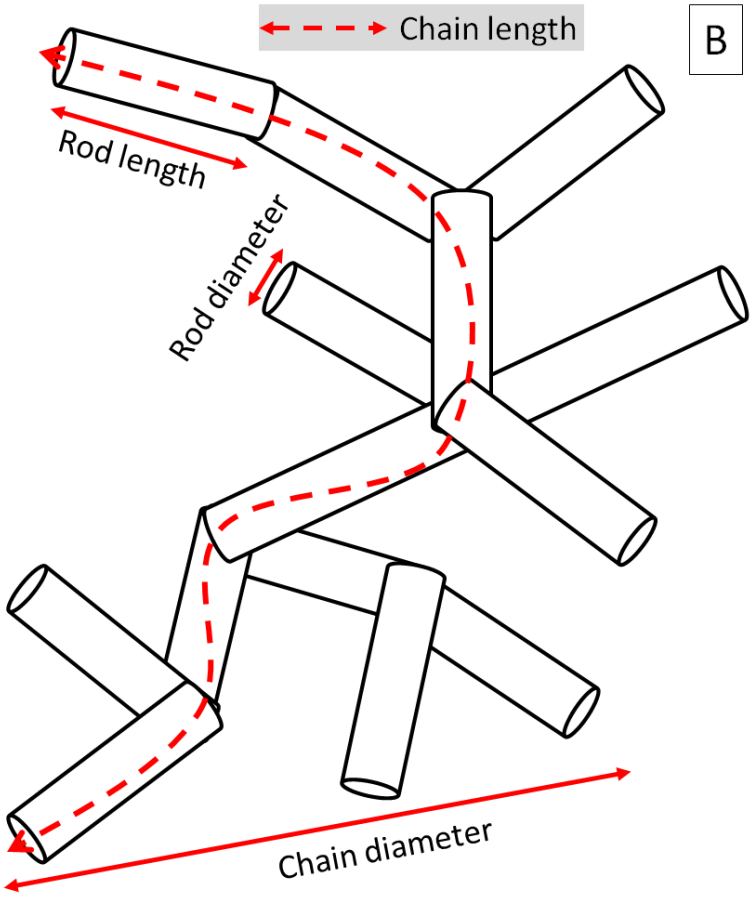

Figure 7.2. **(a)** Example of a mini-model realisation in which corrosion-enhanced macroporosity was modelled as a sub-model element using the object modelling feature in SBED^{TM}. (b) The network rod template used for modelling the distribution of corrosion-enhanced matrix porosity.

Table 7.2. Geometrical parameters used for modelling the corrosion-enhanced matrix porosity. An illustration of network rod template if shown in Figure 7.3b.

Shape	Parameter	Mean	Standard Deviation
Network rod	Azimuth (degree)	0.00	30.00
	Dip (degree)	0.00	30.00
	Rod length (cm)	3.00	1.00
	Chain length (cm)	10.00	2.00
	Rod diameter (cm)	3.00	0.00
	Chain diameter (cm)	2.00	0.00

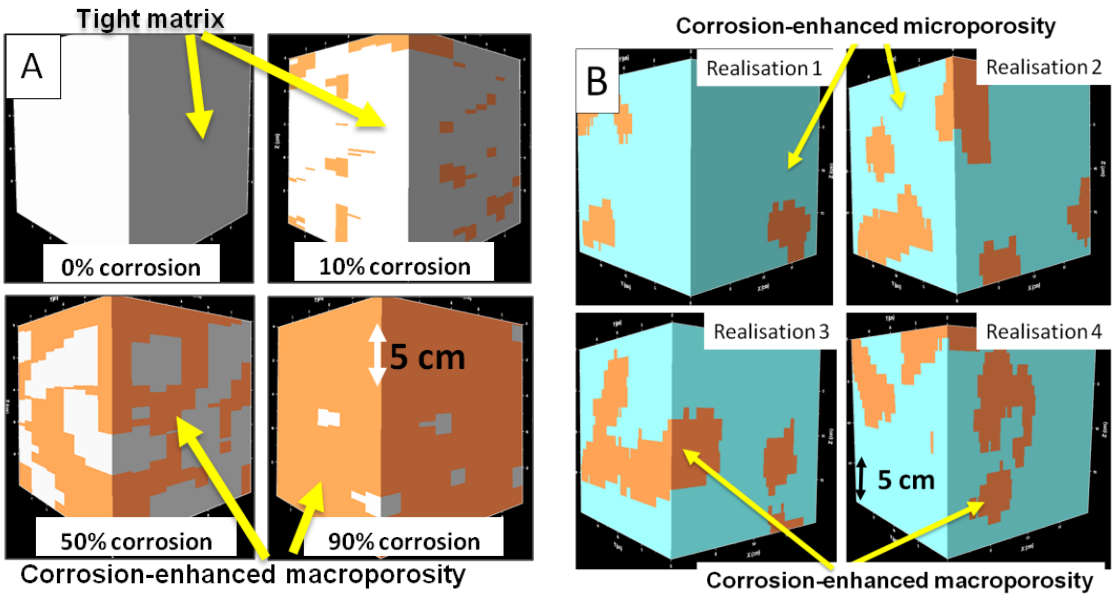

Figure 7.3. (a) Exemplary mini-model scenarios with varying proportions of corrosion-enhanced macroporosity surrounded by a tight background matrix. (b) Examples of equiprobable realisations of a mini-model scenario with constant proportions of corrosion-enhanced macroporosity (in this case 20%) surrounded by microporosity.

7.2.2. Stylolite and tension gash mini-models

In the stylolite and tension gash mini-model scenarios various geometrical and spatial distribution aspects of leached stylolites and associated tension gashes were superimposed on the matrix only cases. As discussed in Chapter 5, the majority of the stylolites were generally associated with corrosion-enhanced macro and microporosity. The main sub-model templates used in the stylolite and tension gash mini-model scenarios were hence corrosion-enhanced macroporosity, corrosion-enhanced microporosity, leached stylolites and leached tension gashes. The stylolites were explicitly modelled by modifying the bedding plane roughness of the geometrical model (Figure 7.4). The leached stylolites that were associated with tension gashes were

normally surrounded by corrosion-enhanced macroporosity. The tension gashes were hence modelled in conjunction with stylolite and corrosion-enhanced macroporosity sub-model templates (Figure 7.5a), based on core description. The description of the tension gashes from core is presented in Chapter 5, in the sub-section 'Stylolite and fracture porosity'. Core description suggests that the tension gashes are upto 6 mm wide, few mm to several centimetres long and are vertical to sub-vertical, originating from the mechanical discontinuity along the stylolite surface and developed nearly parallel to the direction of vertical stress.

Figure 7.5b illustrates the u-shaped body object model template in SBED^{TM}. This object model template was used for superimposing the leached tension gashes on the background bedding structure model. Table 7.3 summarises the geometrical parameters used for modelling the tension gashes. Figure 7.6 illustrates exemplary mini-model realisations with varying spatial distributions and orientations of the tension gashes. Two cases of tension gash lengths were tested using a constant height of 2mm (Figure 7.6b). In the first case the lengths varied from 1 cm to 5cm and in the second case from 3 cm up to 10 cm as shown in Figures 7.6a and 7.6b respectively. Since the tension gashes observed on the core were vertical to sub-vertical, the dip angle was varied from 0^o to 10^o (Figures 7.6c and 7.6e). The azimuth, i.e. orientation of the tension gashes with respect to the x-y plane, was varied from 0^o to 90^o (Figures 7.6d, 7.6e and 7.6f). The spatial distribution of the tension gashes was controlled using the constant method in SBED^{TM}, which required the input value of number of tension gashes to be randomly distributed in a mini-model. Two cases of tension gash distributions were tested. The first case contained 100 tension gashes per cubic metre and the second case contained 200 tension gashes per cubic metre (Figures 7.6a and 7.6f). The former and the latter represented low density of tension gashes and high density of tension gashes, respectively.

Table 7.3. Geometrical parameters used for modelling tension gashes. See Figure 7.6b for u-shaped body template geometry

Shape	**Parameter**	**Mean**	**Standard Deviation**
U-shaped body	Azimuth (degree)	0.00	90
	Dip (degree)	0.00	10
	Width 1 (cm)	1	1
	Width 2 (cm)	1	1
	Height (cm)	0.1	0.00

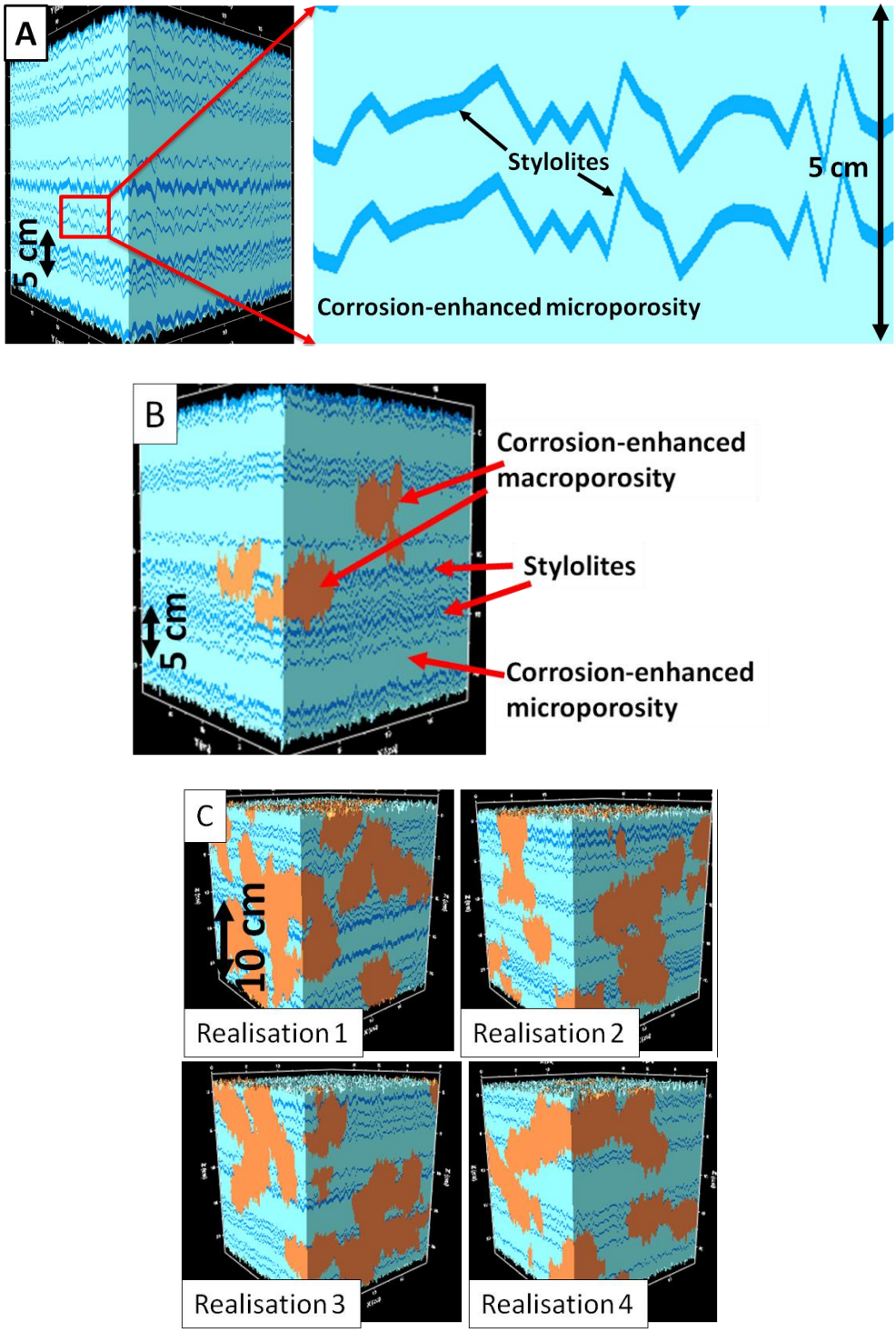

Figure 7.4. (a) Example of a mini-model with stylolites surrounded by corrosion-enhanced microporosity. (b) Example of a mini-model comprising corrosion-enhanced macroporosity and stylolites surrounded by microporosity. (c) Exemplary model realisations of corrosion-enhanced macroporosity and stylolites surrounded by microporosity.

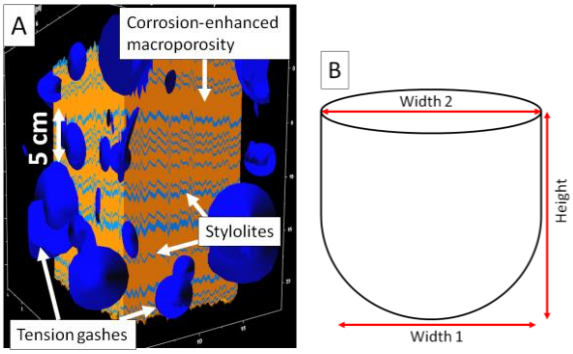

Figure 7.5. (a) Example of a mini-model with tension gashes intersecting leached stylolites and corrosion-enhanced macroporosity. (b) The u-shaped body object template in SBED^{TM} used for modelling the leached tension gashes.

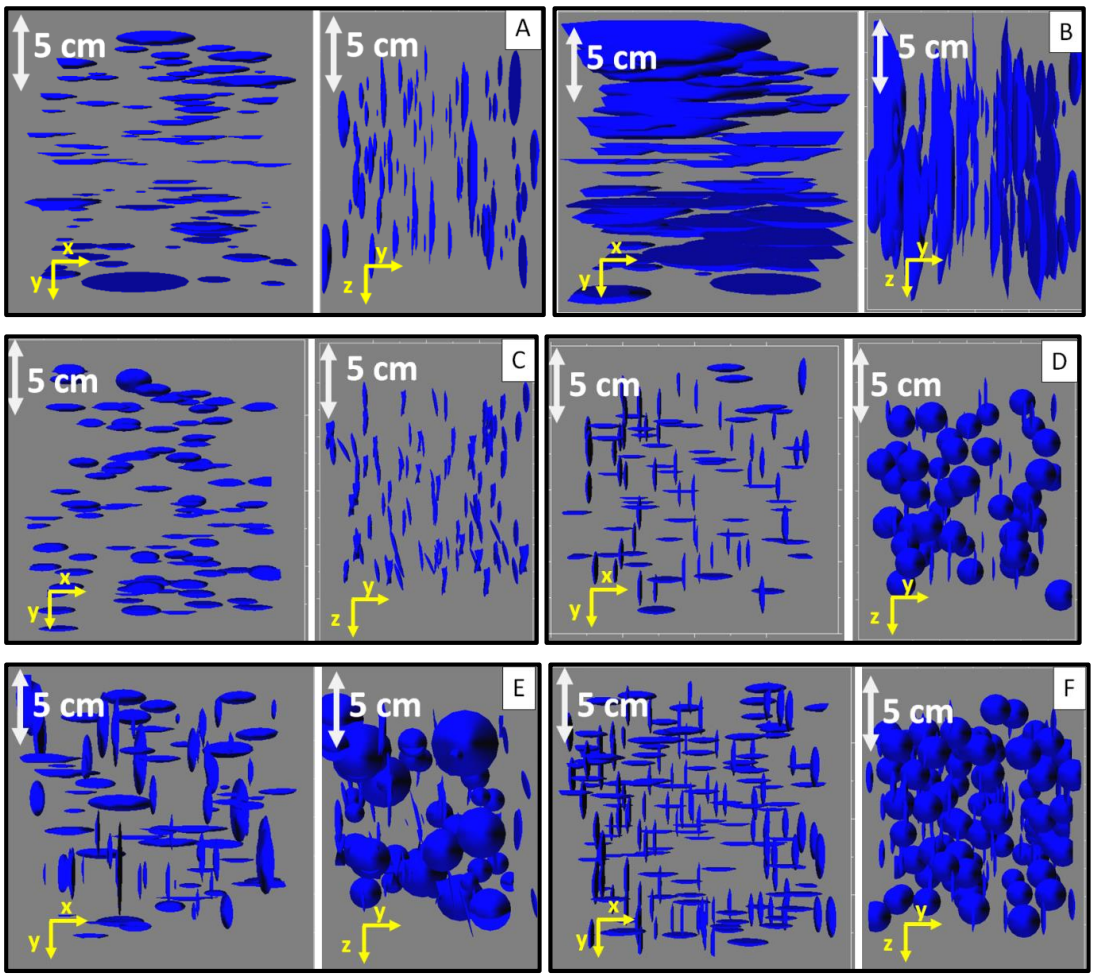

Figure 7.6. Top and side views of sub-model templates used to model tension gashes with varying geomotrical and spatial distributions for the tension gashes. (a) The tension gash lengths varied from 1 cm to 5cm (b) The tension gash lengths varied from 3 cm up to 10 cm (c) The Dip angle varied from 0^o to 30^o (d) The azimuth varied from 0^o to 90^o (e) low density tension gashes with varying dip and azimuth (f) high density of tension gashes with varying dip and azimuth.

7.3. Upscaling porosity and permeability

Once the high resolution unstructured porosity and permeability grids of all the mini-model realisations were obtained, they were subject to single-phase flow-based upscaling (Pickup *et al*. 1995, Christie & Blunt 2001) as discussed in Chapter 3. The K_{eff} estimates of several hundreds of stochastic mini-model realisations constrained to the near-wellbore geology were obtained. The effective porosity, Φ_{eff}, estimates were also calculated. The x- and z- directional permeability estimates K_{xx} and K_{zz} were used to calculate the effective horizontal-vertical permeability anisotropy ratio, $K_{v\text{-}eff}/K_{h\text{-}eff}$, for all these realisations. Figure 7.7 shows the comparison between the calculated effective porosity and permeability values and the core data. As discussed before, the core data was strongly biased to the tighter limestone matrix due to sampling issues. The new results indicated that the matrix only mini-model realisations with various scenarios of micro and macroporosity distributions (scenarios ZA2-ZB6 in Figure 7.7) showed improved permeability compared to the well core data.

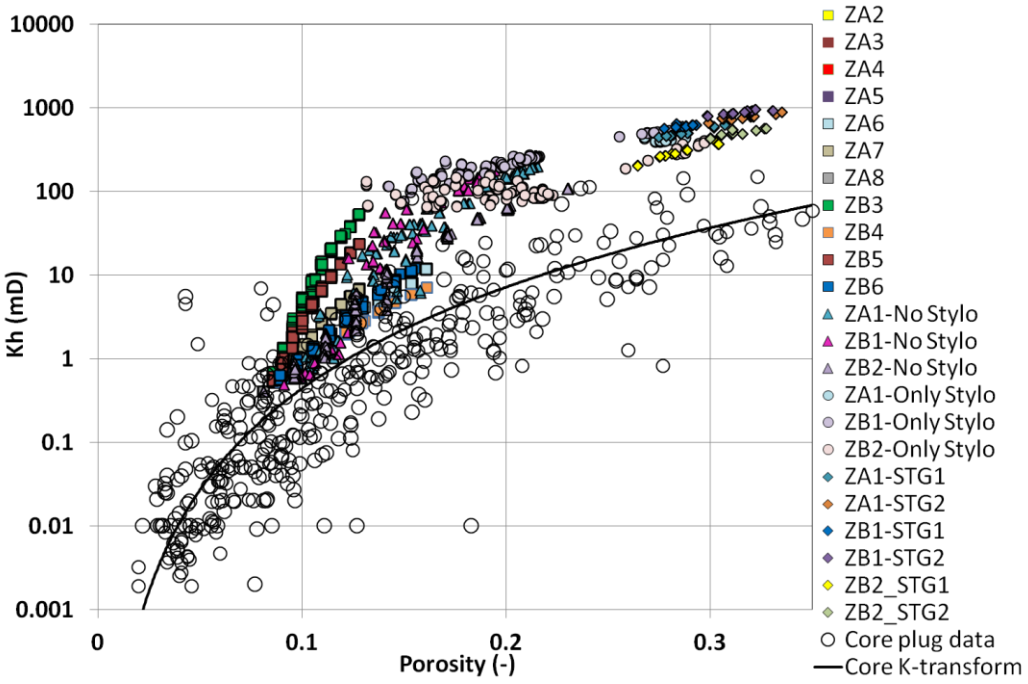

Figure 7.7. Comparison between upscaled porosity and permeability estimates and well core plug data. ZA2 to ZB6 are the various scenarios of matrix only mini-models and ZA1-ZB2 are different scenarios of 'stylolite and tension gash' mini-models with varying geomoetries and spatial distributions of tension gashes.

Incorporating the leached stylolites and associated tension gashes into the mini-models significantly increased the $K_{h\text{-}eff}$ and $K_{v\text{-}eff}/K_{h\text{-}eff}$ values compared to the core data and

even the matrix only scenarios. The $K_{h\text{-}eff}$ and $K_{v\text{-}eff}/K_{h\text{-}eff}$ values thus suggested that the centimetre to decimetre scale geological heterogeneities in Field X could be the primary controls for fluid flow but could not be represented by core data or any RCA data.

The Φ_{eff}, and $K_{h\text{-}eff}$ estimates were then used to calculate the horizontal permeability transform scenario, T_{NWU}. High and low case permeability transforms (Figure 7.8), $T_{NWU\text{-}HIGH}$ and $T_{NWU\text{-}LOW}$ respectively, were also obtained to test the sensitivity of simulated production profiles. A cross-plot between $K_{h\text{-}eff}$ and $K_{v\text{-}eff}/K_{h\text{-}eff}$ was produced in order to understand the relation between the $K_{v\text{-}eff}/K_{h\text{-}eff}$ anisotropy with $K_{h\text{-}eff}$ as shown in Figure 7.9. The near-wellbore upscaled permeability transforms were then used as input for the global horizontal permeability modelling in the geomodel while the $K_{v\text{-}eff}/K_{h\text{-}eff}$ versus $K_{h\text{-}eff}$ relation was applied to calculate the global vertical permeability. High and low cases were also tested for the second order relation obtained between $K_{v\text{-}eff}/K_{h\text{-}eff}$ and $K_{h\text{-}eff}$ to understand the impact of permeability anisotropy on the simulated reservoir production profile. This provided valuable insights towards improving the reservoir permeability model, as demonstrated through the flow simulation sensitivity study described in the following sections.

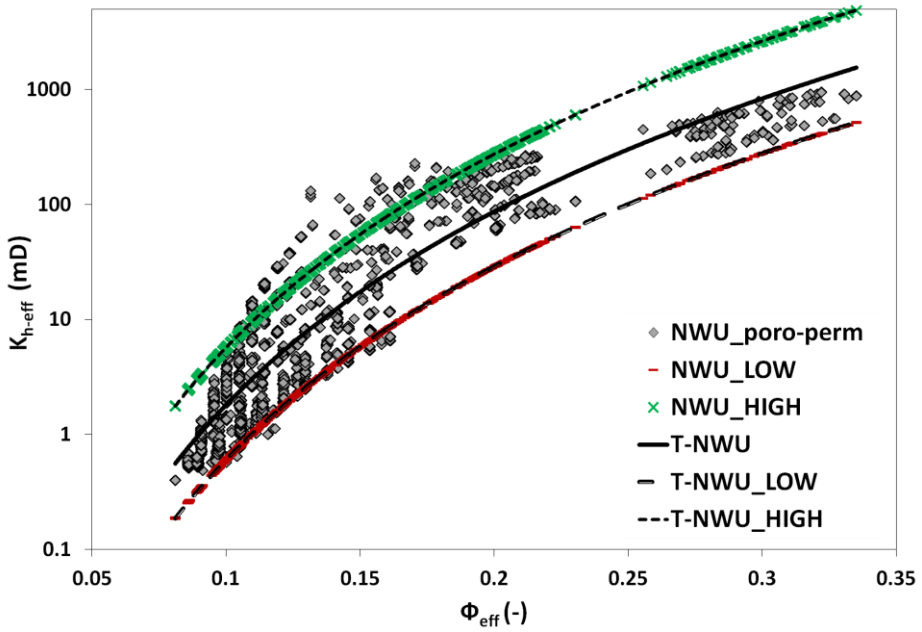

Figure 7.8. Cross-plot between calculated effective porosity, Φ_{eff}, and effective horizontal permeability, $K_{h\text{-}eff}$, and the corresponding trend line, T_{NWU}. T_{NWU_HIGH} and T_{NWU_LOW} are the trend lines of the high (NWU_HIGH) and low (NWU_LOW) near-wellbore upscaled (NWU) transform cases, respectively, used to populate the reservoir simulation model.

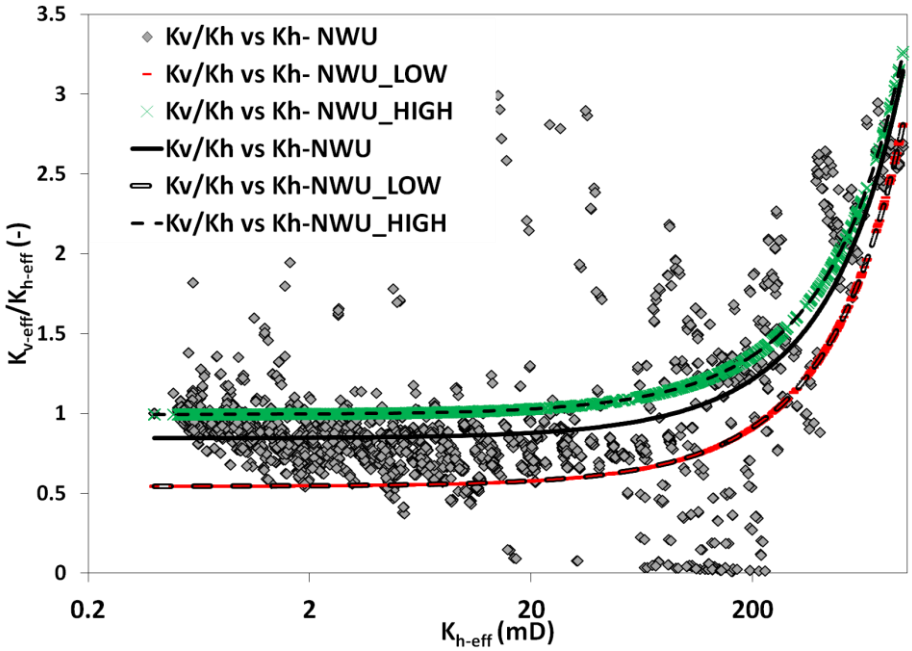

Figure 7.9. Cross-plot between calculated $K_{h\text{-}eff}$ and effective permeability anisotropy ratio, $K_{v\text{-}eff}/K_{h\text{-}eff}$. A second order polynomial was used to fit this distribution and calculate the global vertical permeabilty $K_{v\text{-}eff}$. Note the high $K_{v\text{-}eff}$ values correspond to the facies that incorporate leached stylolites and tension gashes. A high and a low case was also obtained to populate the simulation model.

7.4. Reservoir Scale Permeability Modelling

A sector model of Field X comprising Well Group 1was used to simulate production and analyse how the various combinations of upscaled small-scale heterogeneity, i.e. the new permeability transforms derived from near-wellbore modelling workflow, impacted cumulative production. Several scenarios of sector models were generated by using the new global permeability transform cases (e.g. Figure 7.8) and $K_{v\text{-}eff}/K_{h\text{-}eff}$ cases (e.g. Figure 7.9) in conjunction with the original porosity model of Field X. Figure 7.10 illustrates the sector models showing the original porosity model and the permeability model obtained using the core permeability transform. Figure 7.11 shows a permeability model scenario derived from the T_{NWU}. The sector model dimensions were X=Y= 4 Km and Z= 180 m and the cell dimensions were $\Delta X = \Delta Y = 25\ m$ and $\Delta Z = 1\ m$.

The resulting sector model realisations were then used for reservoir simulation by maintaining the same development strategy as the history-matched model, which was to drain the oil leg under depletion controlled by oil rate. The cumulative oil production curves thus obtained for the various realisations of the sector model are shown in Figure

7.12. The simulated production curves that were obtained by using the NWU permeability transforms were compared to those using the original permeability distribution without any permeability multipliers i.e. the permeability transforms that were derived purely from the core data.

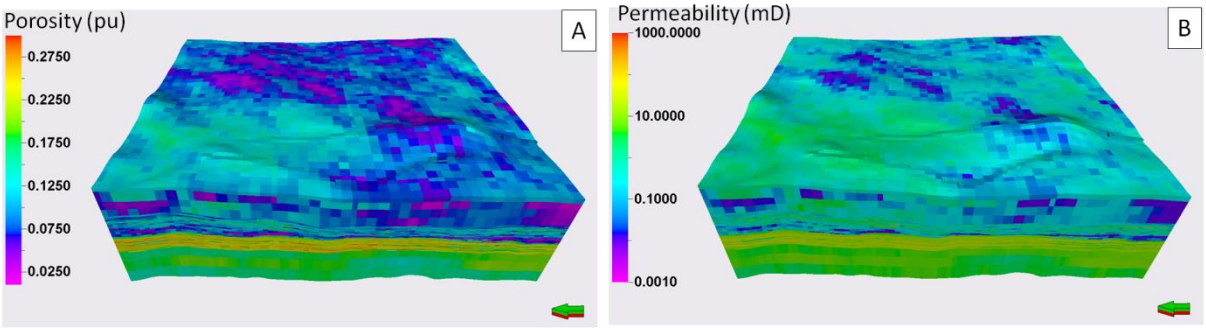

Figure 7.10. (a) Porosity distribution of Field X sector model (b) Permeability model derived from core permeability transform.

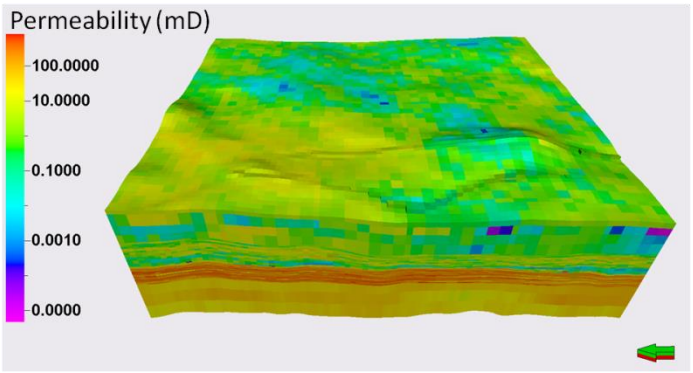

Figure 7.11. Permeability model obtained by using the permeability transform T_{NWU}, derived from near-wellbore upscaled poro-perm values.

The new global permeability transforms calculated from the near-wellbore upscaling workflow did not require any artificial permeability multipliers and yet led to cumulative oil production curves that showed significantly better agreement with the historic oil production data compared to OPT3 (Figure 7.12). This was because of the following reasons; the improved horizontal and vertical permeability distribution in the revised models provided increased production profiles. The improved match for models using the NWU permeability transforms corroborates that the high-permeable corroded facies, leached stylolites and tension gashes play an important role in enhancing the vertical and lateral connectivity of Field X not only at core-scale, but also at the simulation grid block scale. Through the NWU workflow, we were able to model and

upscale these small-scale heterogeneities so that they could be incorporated into the permeability model at simulation grid-block scale. While the original reservoir simulation model required excessive use of permeability multipliers in order to match the historic production data, the new permeability model obtained from near-wellbore upscaling largely eliminated the need for such multipliers. In addition, the improved permeability models also reduced the simulation runtimes significantly.

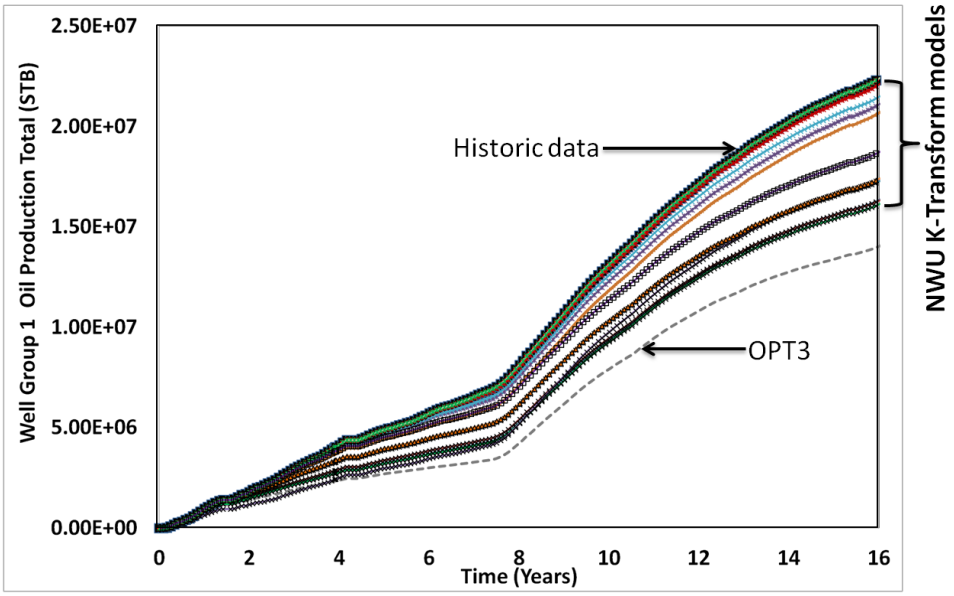

Figure 7.12. Cumulative oil production curves of Well Group 1 obtained from simulations using the various scenarios of near wellbore upscaled (NWU) permeability transforms and $K_{v\text{-}eff}/K_{h\text{-}eff}$ values. OPT3 is the simulated oil production after removing the well productivity multipliers in addition to the zone and well permeability multipliers.

In addition to the sector model study discussed above, an uncertainty analysis was conducted using two full field models of Field X as base cases: 1) the original history matched simulation model and 2) the simulation model comprising the permeability model resulting from near-wellbore upscaling workflow. The aim of this work was to investigate the sensitivity of cumulative oil production to the various reservoir simulation parameters by changing one parameter at a time. The reservoir simulation parameters used for this uncertainty analysis have been summarised in Table 7.4. The results corroborated that the range of uncertainty associated with permeability in Field X was reduced significantly in base case that employed T_{NWU} compared to the original

history matched model. The reduction in permeability uncertainty is demonstrated in the tornado charts shown in (Figure 7.13).

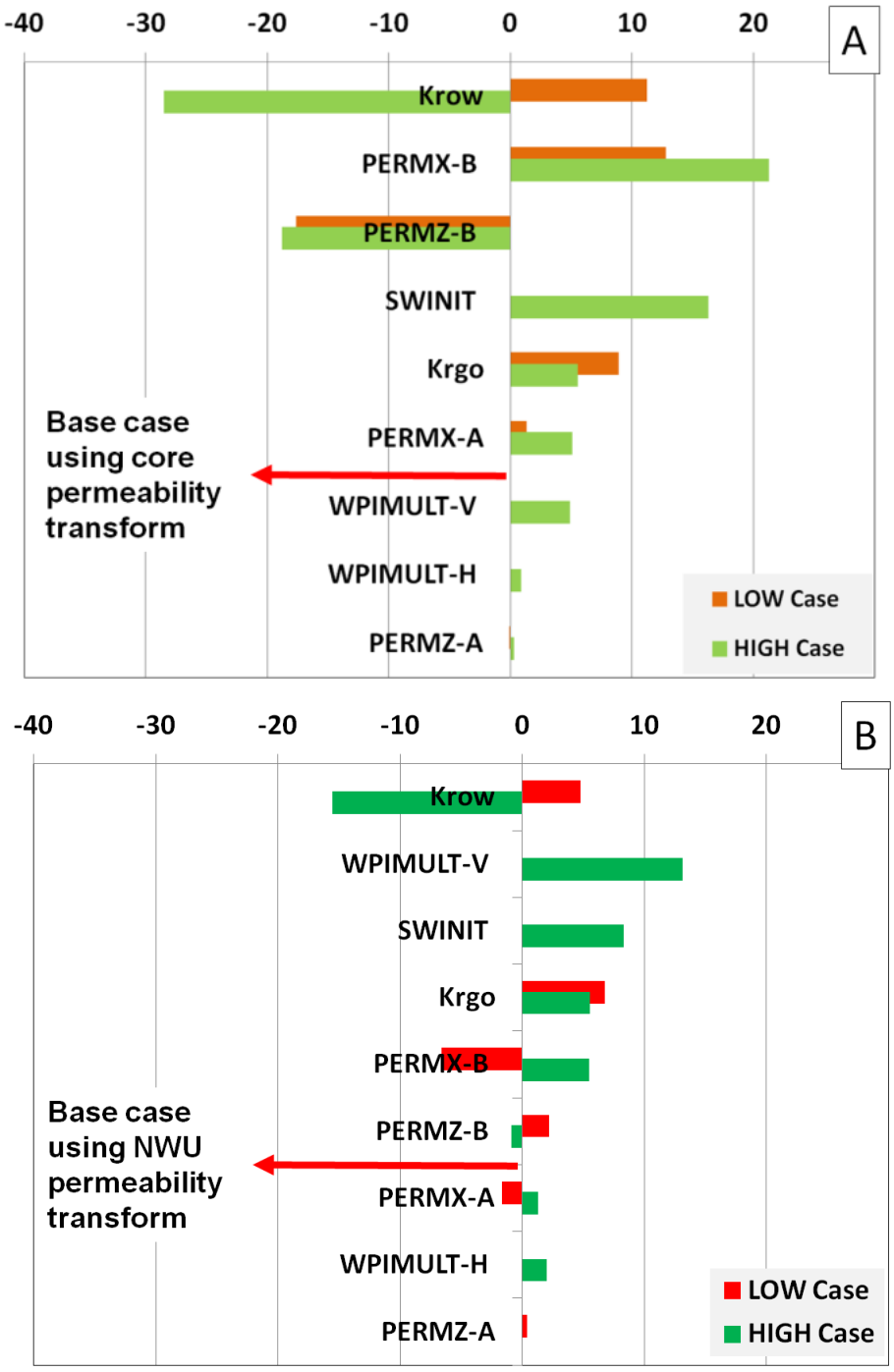

Figure 7.13. Tornado charts showing the percent change of cumulative oil for apermeability model that employed (a) core permeability transform and (b) T_{NWU} . Note that the sensitivity of the simulation results to relative permeability is significantly lower in the T_{NWU} case, due to the improved permebility characterisation and removal of permeability multipliers.

Table 7.4. Reservoir simulation parameters used for uncertainty analysis

Code	Model Parameters	Comments	Base case		High Case	Low Case
			Original model	NWU model		
PERMX-B	Horizontal permeability of B Zone	Horizontal permeability transform in B Zone, equivalent to layers 18-36 in reservoir model	Core permeability transform	NWU permeability transform, T_{NWU}	$T_{NWU-HIGH}$	$T_{NWU-LOW}$
PERMX-A	Horizontal permeability of A Zone	Horizontal permeability transform in A Zone, equivalent to layers 1-17 in reservoir model	Core permeability transform	NWU permeability transform, T_{NWU}	$T_{NWU-HIGH}$	$T_{NWU-LOW}$
PERMZ-B	Vertical permeability of B Zone	Vertical permeability transform in B Zone, equivalent to layers 18-36 in reservoir model	$K_v = 0.1 \times K_h$	$K_{v\text{-}eff}/K_{h\text{-}eff}$ vs. $K_{h\text{-}eff}$ correlation	$K_{v\text{-}eff}/K_{h\text{-}eff}$ vs. $K_{h\text{-}eff}$ High	$K_{v\text{-}eff}/K_{h\text{-}eff}$ vs. $K_{h\text{-}eff}$ Low
PERMZ-A	Vertical permeability of A Zone	Vertical permeability transform in A Zone, equivalent to layers 1-17 in reservoir model	$K_v = 0.1 \times K_h$	$K_{v\text{-}eff}/K_{h\text{-}eff}$ vs. $K_{h\text{-}eff}$ correlation	$K_{v\text{-}eff}/K_{h\text{-}eff}$ vs. $K_{h\text{-}eff}$ High	$K_{v\text{-}eff}/K_{h\text{-}eff}$ vs. $K_{h\text{-}eff}$ Low
WPIMULT-H	Horizontal well productivity index multipliers	Horizontal well productivity index multipliers	OFF	OFF	ON	OFF
WPIMULT-V	Vertical well productivity index multipliers	Vertical well productivity index multipliers	OFF	OFF	ON	OFF
KRow	Maximum water relative permeability	Maximum water relative permeability	0.224	0.224	0.34	0.26
	Critical oil in water saturation	The maximum oil saturation at which oil relative permeability is zero	0.1	0.1	0.32	0.4
KRgo	Maximum relative permeability to gas	Maximum relative permeability to gas	0.736	0.736	0.6815	0.323
	Critical gas saturation	The maximum gas saturation at which gas relative permeability is zero	0.05	0.05	0.05	0.055
SWINIT	Initial water saturation model	The simulator keyword 'SWINIT' was used to honour the given initial saturation model during initialisation	ON	ON	ON	OFF

Overall, the base case scenario that employed the T_{NWU} (Figure 7.13b) showed less sensitivity to variations in reservoir parameters compared to the original history matched model (Figure 7.13a). In both cases, the simulated cumulative oil production was most sensitive to changes in the water-oil relative permeability, i.e. the maximum water relative permeability and critical oil saturation. The second most influential parameters in the model that used core permeability transform were the horizontal and vertical permeability distributions in the B Zone. In contrast, the model with T_{NWU} was more sensitive to the vertical well productivity multipliers and the initial water saturation distribution. Representing the late-burial corrosion heterogeneities in the form of T_{NWU} thus reduced the uncertainty associated with permeability modelling in Field X.

7.5. Conclusions

Using a novel near-wellbore upscaling workflow, the effective global permeability transforms and permeability anisotropy ratios (K_v/K_h) that reflected the impact of small-scale geological heterogeneities on fluid flow in Field X were calculated. The new permeability transforms, T_{NWU}, improved the permeability modelling at the field scale because they represented the high-permeability late-burial corrosion heterogeneities that were originally undersampled in the well data. These high-permeability heterogeneities were solution-enhanced matrix porosity, leached stylolites and associated tension gashes that were only partly represented by the Routine Core Analysis data. Hence, the original permeability transform used for modelling the reservoir permeability in Field X was severely biased towards the poor quality limestone matrix. The new, upscaled permeability transforms mitigated the core sample bias and bridged the gap between core and wireline scales by accounting for multi-scale heterogeneities that could be represented by core plugs. The permeability transforms obtained from near-wellbore upscaling were therefore more appropriate for field scale permeability modelling. Simulation results suggested that the models that employed T_{NWU} yielded cumulative production curves that produced an improved match with the historic production data but did not require artificial permeability multipliers.

Similar reservoir simulation study that was conducted using the full field model of Field X concurred with the results from the sector model study. The sensitivity of cumulative oil production profiles to various reservoir simulation parameters was investigated using two full field models as base cases. The base case was compared to the original history

matched model and the new simulation model comprising T_{NWU}. The reservoir simulation results were observed to be most sensitive to the relative permeability characteristics and distribution of initial water saturations in both the base cases. However, the uncertainty associated with the permeability distribution in Field X was significantly reduced when T_{NWU} was used compared to the original history matched model.

The outcome of this study led to a significantly improved characterisation and modelling of the permeability distribution in the field, which is now much better constrained to the reservoir geology. The next chapter demonstrates the near-wellbore rock-typing and upscaling workflow, which was developed with the specific aim of integrating the static and dynamic reservoir properties with regard to late-burial corrosion and incorporating them in the reservoir simulation model.

Chapter 8. EFFECTIVE INTEGRATION OF RESERVOIR ROCK-TYPING AND SIMULATION USING NEAR-WELLBORE UPSCALING

8.1. Introduction

The uncertainty associated with permeability modelling in Field X was discussed in Chapters 6 and 7, where it was demonstrated that re-evaluating the permeability model of Field X with considerations to late diagenetic corrosion can significantly improve the reservoir simulation model. The aim of the work discussed in this chapter is to revise the full field geomodel by incorporating the late-burial corrosion heterogeneities, and to obtain a properly initialised reservoir simulation model with consistent static and dynamic reservoir properties. In order to revise the geomodel of Field X with considerations to the proposed late-burial corrosion model (Wright & Barnett 2011), it was essential to obtain a fit-for-purpose rock-typing scheme that adequately incorporated the late-burial corrosion heterogeneities. However, conventional rock-typing workflows may not be appropriate to Field X due to the difficulties associated with the petrophysical characterisation and data sampling of the key porosity types such as leached stylolites and associated tension gashes. Besides, upscaling these sub-grid-scale heterogeneities to incorporate them adequately into the reservoir simulation model was another major challenge. To address these issues, a novel rock-typing method was adapted in conjunction with near-wellbore upscaling (NWU) workflow, which involved characterisation, representation and upscaling of key small-scale heterogeneities into reservoir grid-block scale. The rock-typing and upscaling methodology described in this work involves the geological-petrophysical classification of multi-scale heterogeneities through systematic evaluation of the key paragenetic events with consideration to the crucial parameters of near-wellbore modelling (NWM) and upscaling workflow.

8.2. Field X rock-typing

Figure 8.1 illustrates the rock-typing methodology that was developed in this chapter. In order to facilitate the effective description of this workflow, some key terminology is defined at the outset. ‘Lithofacies’ is defined as depositional facies classified based on sedimentary texture, grain types and depositional structure (Dunham 1962). A ‘geological rock type’, GeoRT, is a division of a lithofacies type that went through similar diagenetic processes and whose pore network has the same genetic origin. A ‘near-wellbore rock type’, NWRT, is a bin of GeoRTs that have similar petrophysical

properties at core scale and NWM aspects. A 'Geological-Porosity Derived System', GeoPODS, is a geologically realistic equivalent of the 'hydraulic flow unit' (c.f. Amaefule *et al*. 1993) at reservoir grid-block scale and consists of a bin of NWRTs that went through NWU workflow and display similar static and dynamic properties.

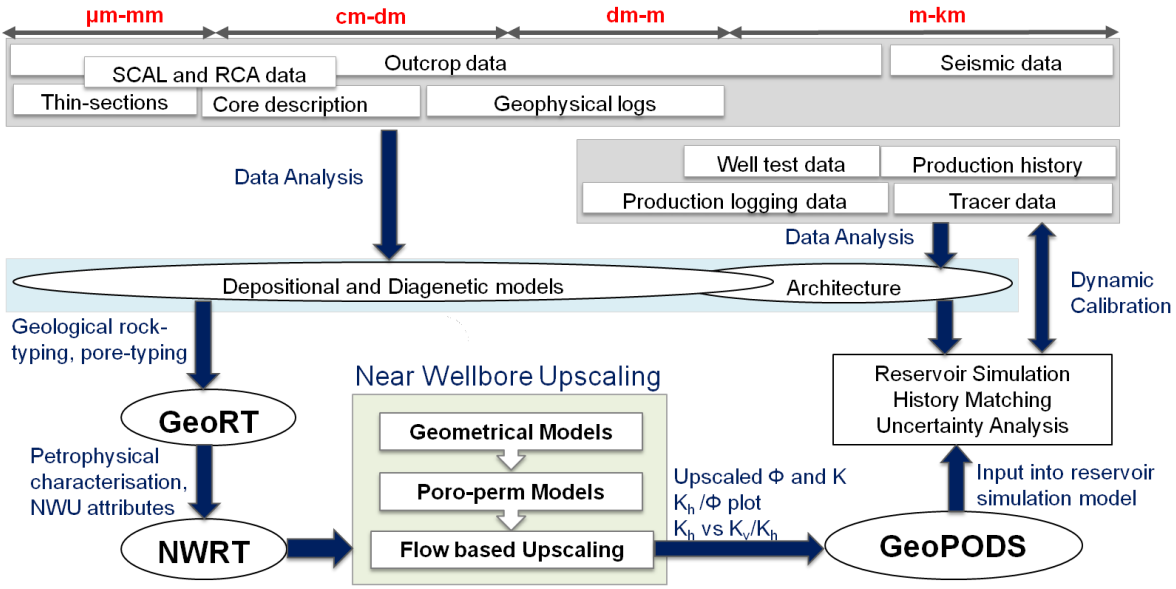

Figure 8.1. Summary of the integrated near-wellbore rock-typing and upscaling workflow. A geological rock type, GeoRT, is a division of a lithofacies type that went through similar diagenetic processes. A near-wellbore rock type, NWRT, is a bin of GeoRTs that have similar petrophysical properties at core scale and near-wellbore modelling parameters. A Geological-Porosity Derived System, GeoPODS, is equivalent to a Global Hydraulic Element consisting of a bin of NWRTs grouped based on the upscaled poro-perm.

The rock-typing approach adopted in this study was iterative to ensure seamless integration of the multi-scale and multi-disciplinary datasets. First, the geological rock types, hereafter referred to as GeoRTs, were classified by characterising and grouping the gross depositional facies and the key porosity types associated with late-burial dissolution. This was guided by the depositional model and interpretation of paragenetic sequences that occurred in the reservoir. The GeoRTs in this study are hence comparable to the rock types developed by Hollis *et al*. (2010), who grouped the lithofacies of the same genetic origin and pore network, to ensure that the entire geological evolution of the rock (including the diagenetic history) was incorporated into the rock type definition. The GeoRTs were then grouped into 'near-wellbore rock types', hereafter referred to as NWRTs, based on their petrophysical characterisation

using the Routine Core Analysis (RCA) and Special Core Analysis (SCAL) data. The capillary pressure and relative permeability data used in this chapter were part of the measured SCAL data provided by the operator. This was done with consideration to the NWM aspects of the GeoRTs to facilitate their input into the NWU workflow. NWU yielded averaged petrophysical properties at the reservoir simulation grid-block scale.

Following NWU, the centimetre-scale NWRTs were further binned into reservoir-scale 'Geological-Porosity Derived Systems', hereafter referred to as GeoPODS, based on their upscaled petrophysical properties. GeoPODS emphasise the geological basis for the grouping and upscaling of rock types and are coherent with the definition of Porosity Derived Systems ("PODS") (Kazemi *et al*. 2012) at reservoir grid block scale. Thus, GeoPODS represent the impact of sub-grid scale heterogeneities on fluid flow at the reservoir grid-block scale and help define the Global Hydraulic Elements (Corbett & Potter 2004) concept at the appropriate modelling scale for full field simulation models. The evolution of GeoPODS is strongly linked to geological rock types (GeoRTs), which in turn are based on the depositional and diagenetic models of the field. The GeoPODS are conditioned to the near-wellbore data and at the same time spatially-commensurate with the reservoir dynamic simulator for distributing the dynamic properties away from the wells. The following sections describe how the integrated near-wellbore rock-typing and upscaling workflow (Figure 8.1) was applied to Field X. A series of 'roadmaps' (Figures 8.2, 8.3 and 8.9) highlighting the steps of the workflow have been included in every corresponding section to describe the workflow more effectively.

8.3. Obtaining geological rock types (GeoRTs)

The specific types and distributions of the pores present within the reservoir rocks impart strong control on the production and stimulation characteristics of carbonate reservoirs (e.g., Chilingarian *et al*. 1992; Honarpour *et al*. 1992; Jodry 1992; Wardlaw 1996; Mazullo 2004). It is often the case that the types of fabric-selective pores coincide with the depositional environment of the rock. Understanding the crucial links between depositional and diagenetic models can provide valuable guidance towards unravelling the relationships between lithofacies and petrophysical groups (Gomes *et al*. 2008), and towards the evaluation of the reservoir flow properties (Mazullo 2004). Hence the prime incentive for obtaining the GeoRTs was to capture the key relationships between the depositional and diagenetic features with considerations to their impact on reservoir

flow properties. Figure 8.2 illustrates the summary of the integrated near-wellbore rock-typing and upscaling workflow highlighting the steps taken to obtain GeoRTs.

Overall, 16 GeoRTs in A Zone and 16 in B Zone were identified based on the relationships observed between the main lithotypes, presence of leached stylolites and associated tension gashes, and the extent of matrix microporosity and macroporosity (see Section 5.5, Chapter 5) (Table 8.1). The GeoRT logs were used to divide the near-wellbore region of the wells into centimetre to decimetre scale intervals. These GeoRTs were then further grouped into NWRTs based on petrophysical analysis. The NWRTs were then upscaled in the NWU workflow for input in the reservoir simulation model.

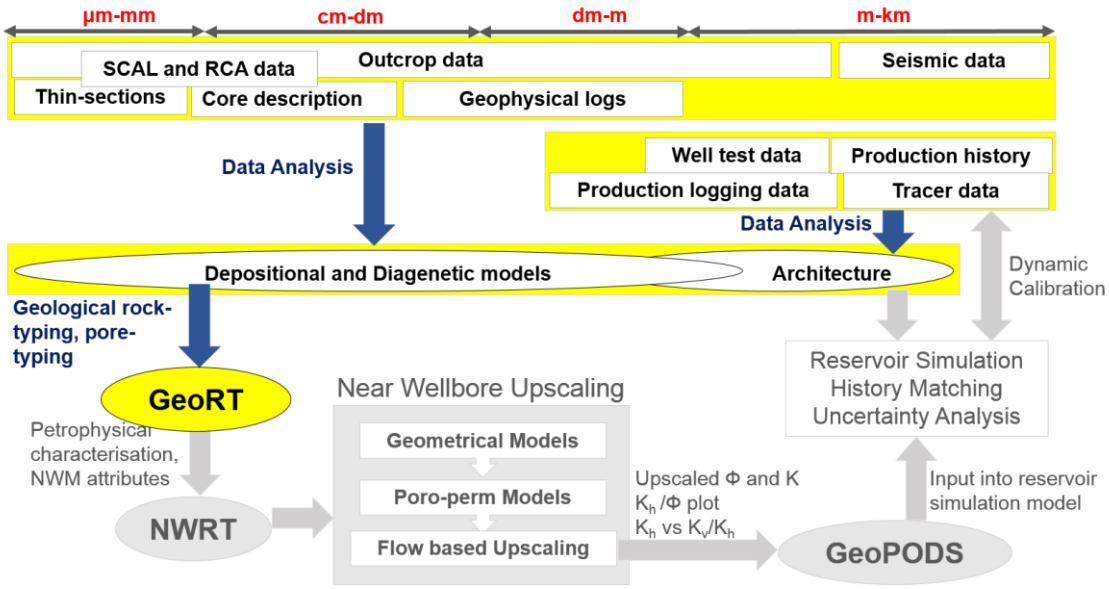

Figure 8.2. Summary of the integrated near-wellbore rock-typing and upscaling workflow highlighting the steps taken to obtain GeoRTs.

Table 8.1. Summary of GeoRTs present in A Zone and B zone.

GeoRT A Zone	Description	GeoRT B Zone	Description
1	Shale	**1**	Inner ramp Coskinolia grainstone with CEP1
2	Mid-ramp Rotalid packstone	**2**	Inner ramp Coskinolia packstone with CEP1
3	Outer ramp Nummulitide packstone	**3**	Shallow mid-ramp Coskinolina Hash packstone-wackstone with CEP1
4	Outer ramp Nummulite wackestone-packstone	**4**	Mid-ramp-Rotalid-Packstone with CEP1
5	Shallow mid-ramp floatstone with platy corals	**5**	Inner-ramp Coskinolina grainstone with CEP1 and LAS
6	Shallow mid-ramp floatstone with CEP1	**6**	Inner ramp Coskinolia packstone with CEP1 and LAS
7	Mid-ramp Rotalid packstone with CEP1	**7**	Shallow mid-ramp Coskinolina Hash packstone-wackstone with CEP1 and LAS
8	Outer ramp Nummulitide packstone with CEP1	**8**	Shallow mid ramp framestone with LAS and CEP1
9	Outer ramp Nummulite wackestone-packstone with CEP1	**9**	Shallow mid ramp floatstone with LAS and CEP1
10	Shallow mid-ramp floatstone with LAS and CEP1	**10**	Mid-ramp Rotalid packstone with LAS and CEP1
11	Mid-ramp Rotalid packstone with LAS and CEP1	**11**	Inner ramp Coskinolia grainstone with HAS and CEP2
12	Outer ramp Nummulitide packstone with LAS and CEP1	**12**	Inner ramp Coskinolia packstone with HAS and CEP2
13	Outer ramp Nummulite grainstone-wackestone with LAS and CEP1	**13**	Shallow mid-ramp Coskinolina Hash packstone-wackstone with HAS and CEP2
14	Outer ramp Nummulite wackestone-packstone with LAS and CEP1	**14**	Shallow mid ramp framestone with HAS and CEP2
15	Shallow mid-ramp floatstone with HAS and CEP2	**15**	Shallow mid ramp floatstone with HAS and CEP2
16	Outer ramp Nummulite grainstone-wackestone with HAS and CEP2	**16**	Mid-ramp Rotalid packstone with HAS and CEP2

LAS = Low amplitude stylolites
HAS= High amplitude stylolites
CEP1= Corrosion-enhanced micro- and mesoporosity
CEP2= Corrosion-enhanced macroporosity including leached stylolites and tension gashes

8.4. Near-wellbore upscaling of GeoRTs for reservoir simulation

Figure 8.3 illustrates the summary of the integrated near-wellbore rock-typing and upscaling workflow highlighting the steps taken to NWRTs from GeoRTs and upscaling them using NWU tools.

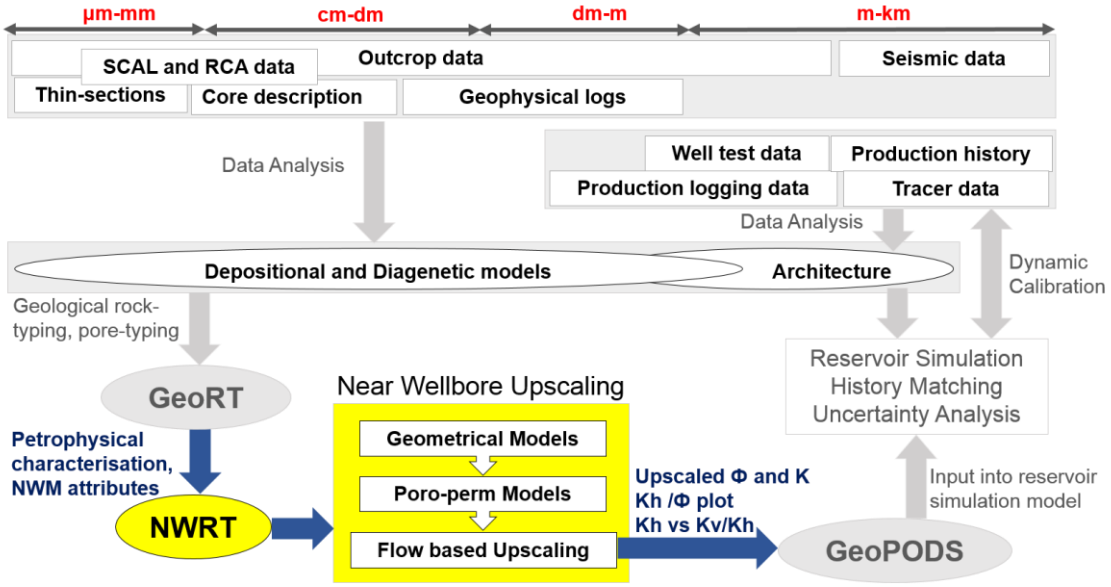

Figure 8.3. Summary of the integrated near-wellbore rock-typing and upscaling workflow highlighting the steps taken to obtain Near Wellbore Rock Types (NWRTs) from GeoRTs and upscaling them using NWU tools.

The GeoRTs represent the geological-petrophysical heterogeneity of the reservoir rock at the pore-core scale. This scale is well below the practical size of a reservoir simulation grid-block. It is hence necessary to efficiently upscale the GeoRTs to the field scale so that they can be used in reservoir simulation studies. It was demonstrated in the earlier chapters that near-wellbore modelling can effectively capture and upscale centimetre to decimetre scale geological features in large reservoir simulation models and improves the dynamic calibration of geomodels. The main input required for NWM are the spatial and geometrical parameters and petrophysical property statistics of the heterogeneities associated with the GeoRTs. To facilitate the input of the GeoRTs into NWU, they were further grouped into NWRTs. This was based on petrophysical characterisation of the GeoRTs using Routine Core Analysis (RCA) and Special Core Analysis (SCAL) data and with consideration to the geometrical modelling aspects of the associated sub-grid scale heterogeneities. For instance, the presence of high proportions of leached high-amplitude stylolites could strongly influence the effective

flow properties of the simulation grid-block. Hence, these stylolites were modelled explicitly using the appropriate geometrical and petrophysical descriptors in the NWU software. The following sections describe the characterisation of porosity-permeability distributions, capillary pressure profiles and relative permeability curves of the GeoRTs.

8.4.1. Porosity and permeability characterisation of GeoRTs

The GeoRT logs from the near-wellbore regions were used in conjunction with the core plug and probe permeameter data to estimate porosity and permeability of the GeoRTs in the studied wells. As mentioned before, the available core plug data suffered from sample insufficiency due to poor core recovery of the well intervals containing GeoRTs with high proportion of CEP types. This was because the reservoir rock was mechanically weak as it was strongly altered by corrosive fluids. This resulted in a sample bias of RCA and SCAL data towards the GeoRTs that mainly contained the uncorroded lithofacies. However, probe permeameter measurements supplemented the core plug data and provided an estimate of the upper and lower bounds of the permeability range. The uncertainties associated with the probe permeameter data (Corbett *et al*. 1999) and the issues related to the measurement of stylolite and tension gash porosity-permeability were discussed in Chapter 6. Based on probe permeameter and core plug data, the GeoRTs were binned into 7 poro-perm groups in A Zone and 7 in B Zone (Table 8.2).

Table 8.2. Porosity-permeability groups in A Zone and B Zone. See Table 8.1 for GeoRT descriptions.

A Zone		**B Zone**	
GeoRT	**Poro-perm Group**	**GeoRT**	**Poro-perm Group**
1	K-0	1	K-0
2,3,4,5	K-A1	4, 10	K-B1
7	K-A2	8	K-B2
6, 8, 11, 12	K-A3	16	K-B3
10, 9	K-A4	1, 2, 3, 7	K-B4
13, 14	K-A5	5,6, 9, 12	K-B5
15, 16	K-A6	11, 13, 14, 15	K-B6

The range of probe permeameter measurements and the porosity-permeability cross-plots of the poro-perm groups are shown in (Figure 8.4). Due to the highly heterogeneous distribution of the CEP types even at core scale, a wide range of poro-perm values were obtained for the GeoRTs. Nevertheless, there was a visible trend of increasing poro-perm values that correlated to the increase in intensity of late-burial corrosion. Overall, groups K-A6 and K-B6 (Table 8.2) showed the highest poro-perm

range in A Zone and B Zone respectively (Figure 8.4). These groups constituted the GeoRTs with higher proportion of CEP2 type porosity, i.e. vuggy and moldic macroporosity associated with leached stylolites and tension gashes. Groups K-A1 from A Zone and K-B1 from B Zone (Table 8.2), containing GeoRTs with no or low presence of any CEP types recorded much lower poro-perm range (Figure 8.4).

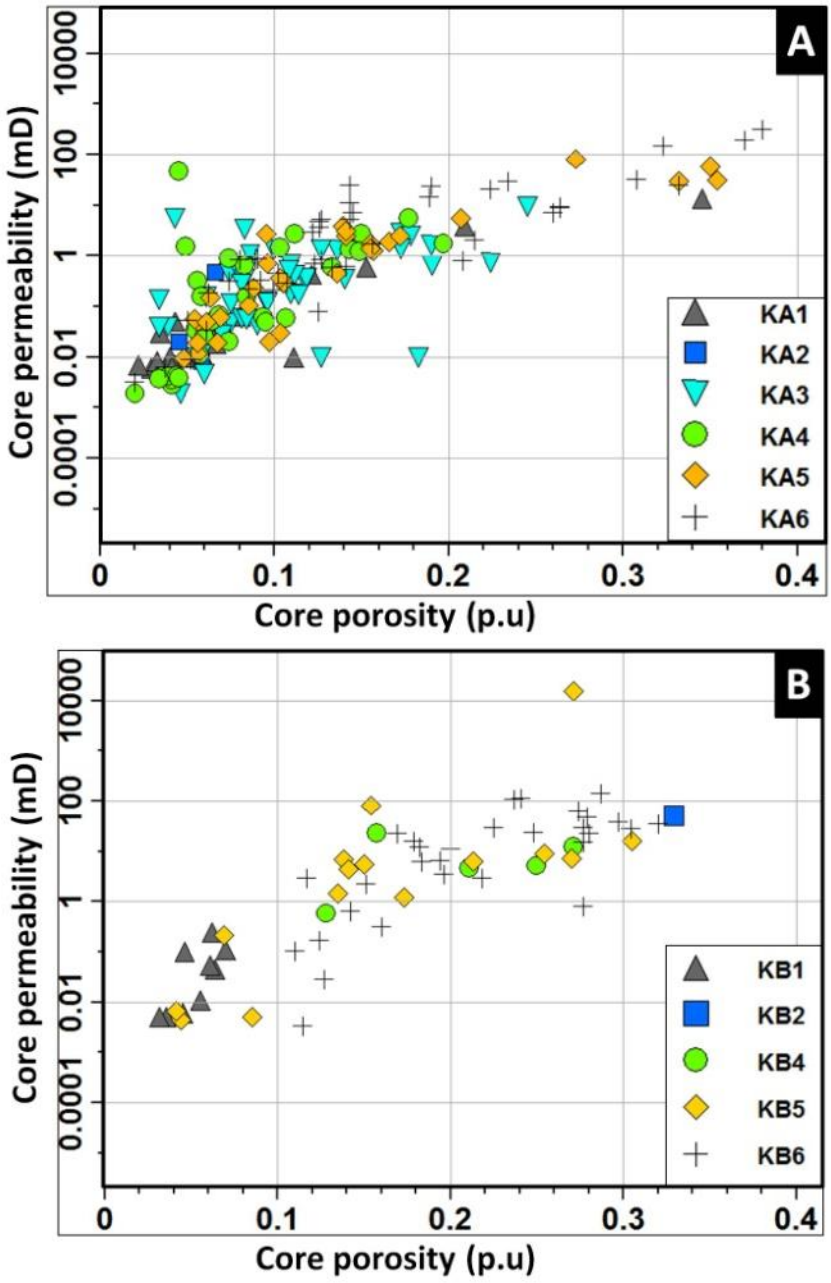

Figure 8.4. Porosity-permeability cross-plots for the poro-perm groups from (a) A Zone and (b) B Zone. Groups K-A1 and K-B1 (Table 8.2), containing no or low presence of any CEP types, show much lower poro-perm compared to groups K-A6 and K-B6 (Table 8.2) that represent vuggy and moldic macroporosity.

8.4.2. GeoRT capillary pressure characteristics

Capillary pressure (P_c) data provides information about pore throat diameters, pore connectivity and their impact on fluid flow in the reservoir. With respect to reservoir simulation, the applications of P_c curves are mainly two-fold. First, P_c curves are used to distribute the initial saturations in the grid-blocks during initialisation of the simulation model. Second, P_c curves contribute to the fluid-flow equations in the form of gradients of the phase pressures. The former is one of the most crucial contributors to the initial hydrocarbons-in-place calculations in the reservoir simulation model. The GeoRTs corresponding to high proportion of corrosion-enhanced porosity displayed low threshold entry pressures of less than 2.25 psia. In contrast, the GeoRTs associated with no or low corrosion displayed threshold entry pressures higher than 100 psia. The GeoRTs associated with tight matrix without any corrosion-enhanced porosity displayed high initial water saturation values and steep saturation-height curves. The GeoRTs with CEP1 type porosity displayed higher initial saturation values compared to those GeoRTs that contained CEP2. The former GeoRTs were abundantly present in the A Zone and represented intermediate quality rock with patchy microporosity grading into larger meso-pores. The GeoRTs with CEP2 type porosity generally represented the best quality rock in the reservoir and were dominated by macro-pores. These GeoRTs were abundantly present in B Zone and characterised by broadly shaped saturation curves and low initial water saturation values. Consequently, the saturation-height functions were broadly classified into three main groups based on the corrosion-enhanced porosity of the GeoRTs. The saturation-height function curves corresponding to GeoRTs with tight matrix without any corrosion-enhanced porosity types and GeoRTs with CEP1 and CEP2 are shown in Figure 8.5.

8.4.3. Relative permeability characterisation of GeoRTs

The relative permeability characteristics of reservoir rock types, namely the saturation and relative permeability end-points, and the fractional flow behaviour are fundamentally important for reliable estimation of ultimate hydrocarbon recovery. Note that the fractional flow curves are not discussed here since the flow is gravity dominated and the fractional flow effects are not evident. The residual oil saturation value varied between 0.19-0.36 pv for the samples from B Zone, in which the oil rim is located. The initial water saturation values varied between 0.17-0.47 pv for the samples from A Zone and 0.37-0.308 pv for those from B Zone. The cross point of the water-oil relative

permeability curves occurred at less than 50% water saturation for over 95% of the SCAL samples. The water relative permeability values at maximum water saturation ranged from 0.30 up to 0.70 in A Zone and from 0.13 to 0.41 in B Zone.

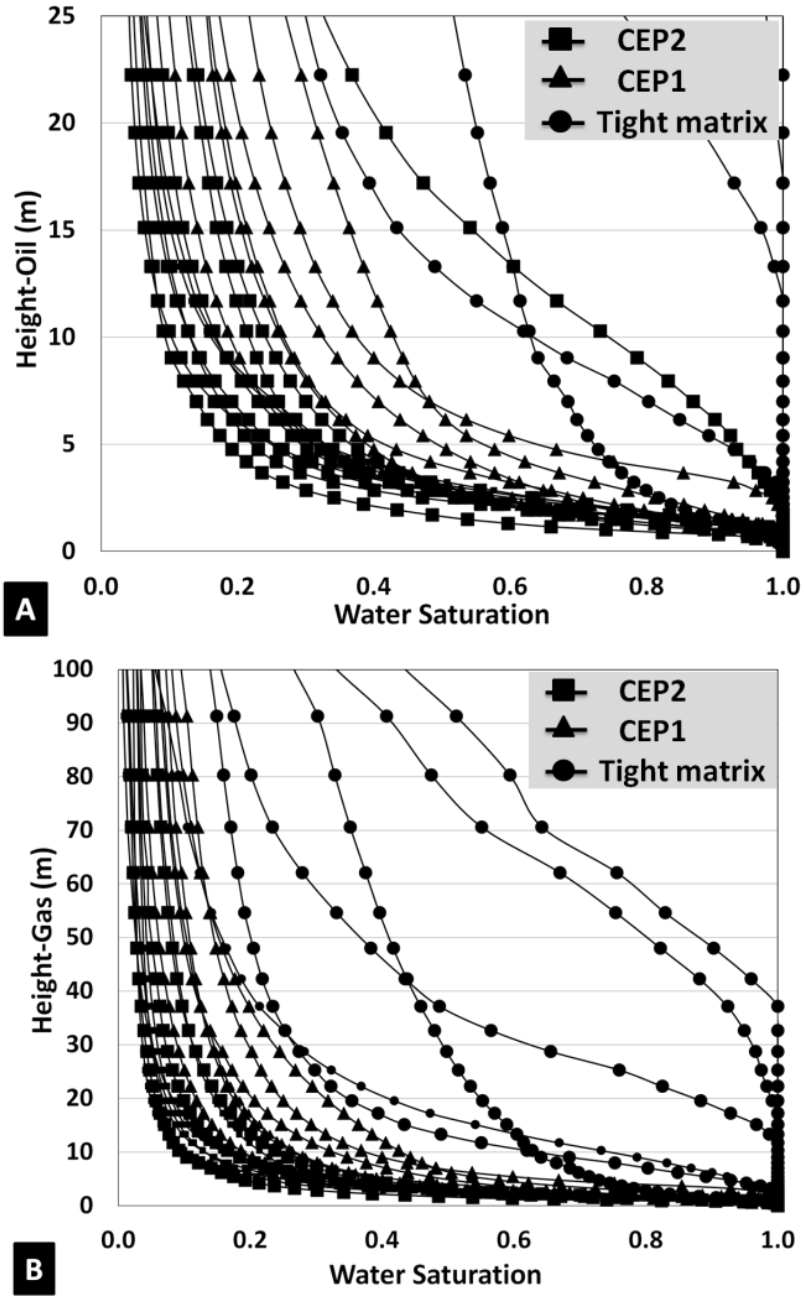

Figure 8.5. Groups of saturation-height functions of GeoRTs of Field X based on the corrosion-enhanced porosity types CEP1 (a) and CEP2 (b).

It was indeed very challenging to characterise each GeoRT with its own set of relative permeability curves due to the limited availability of SCAL data samples. Nevertheless, it was possible to obtain some general inferences regarding the potential relationship between the extent of late-burial corrosion and the relative permeability characteristics

of the GeoRTs. It appeared that the samples from the wells that are located away from the East-fault zone, Wells G11 and G1, showed lower end-point water permeability compared to Wells G6 and G5, which are closer to the fault zone (See Figure 5.1, Chapter 5). This trend could be associated with the role of the East-fault zone in the distribution of corrosion-enhanced porosity in Field X, causing higher proportions of CEP2 type porosity in the regions closer to the fault zone compared to the flank of the reservoir. Figure 8.6 shows the groups of relative permeability curves of the GeoRTs based on corrosion-enhanced porosity types CEP1 and CEP2. It was observed that the critical oil saturation values of the GeoRTs had the tendency to decrease with the increase in the proportion of CEP2 type porosity. Due to the lack of wettability index data, more detailed analysis of any possible trends of wettability with respect to the GeoRTs could not be pursued.

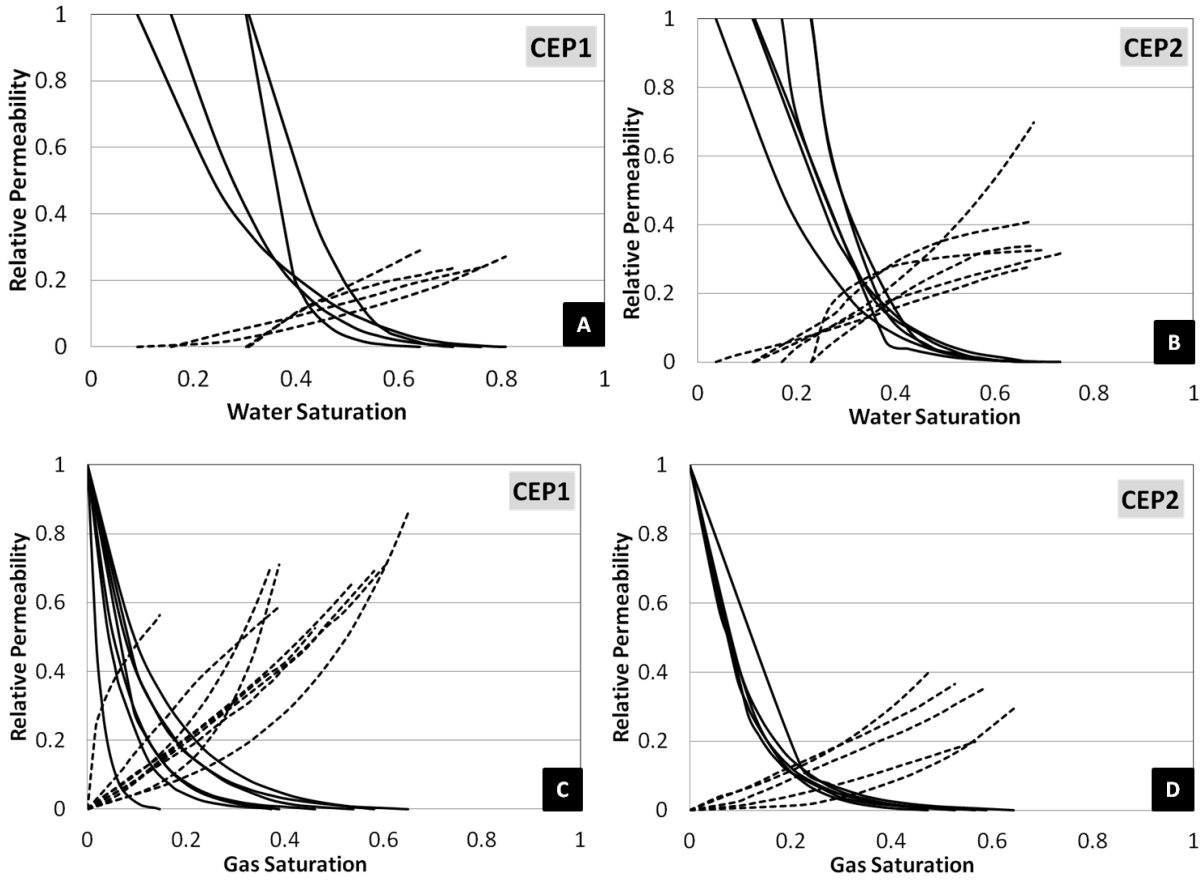

Figure 8.6. Groups of water-oil and gas-oil relative permeability curves of the GeoRTs based on the corrosion-enhanced porosity types CEP1 and CEP2.

8.4.4. Near-wellbore upscaling of GeoRTs

Based on the petrophysical analysis discussed in the previous sections and the associated NWM (NWM) parameters, the GeoRTs were grouped into 7 NWRTs in A Zone (Table 8.3) and 7 in B Zone (Table 8.4). The NWM parameters considered for the grouping of GeoRTs are listed in Tables 8.3 and 8.4. The NWRTs were then modelled using the NWM software SBED^{TM} using the workflow described in Chapter 7. The resulting centimetre-decimetre scale near-wellbore geological models were aimed to be realistic representations of the geometries and distributions of the core-scale geological features corresponding to the GeoRTs, for example the CEP types with the leached stylolites and tension gashes. Figure 8.7 illustrates some of the corresponding near-wellbore model realisations. As shown in Chapter 7, leached stylolites and tension gashes were explicitly modelled within the respective NWRTs in order to represent their impact on effective permeability. Multiple stochastic realisations of high resolution porosity and permeability grids were produced for each NWRT scenario using the mean, standard deviation, minimum and maximum values of poro-perm distributions within each of the NWRTs. Thus, the numerous geometrical and petrophysical realisations of the NWRTs were aimed to capture the extremes of the geological-petrophysical heterogeneities in Field X that were observed from well data. The high-resolution NWRTs at the core scale were then upscaled into the reservoir scale using single-phase flow based upscaling to obtain the effective porosity and permeabilities of each NWRT realisation (Figure 8.8). This yielded the upscaled poro-perm and K_v/K_h distributions for the NWRTs, conditioned to the near-wellbore region.

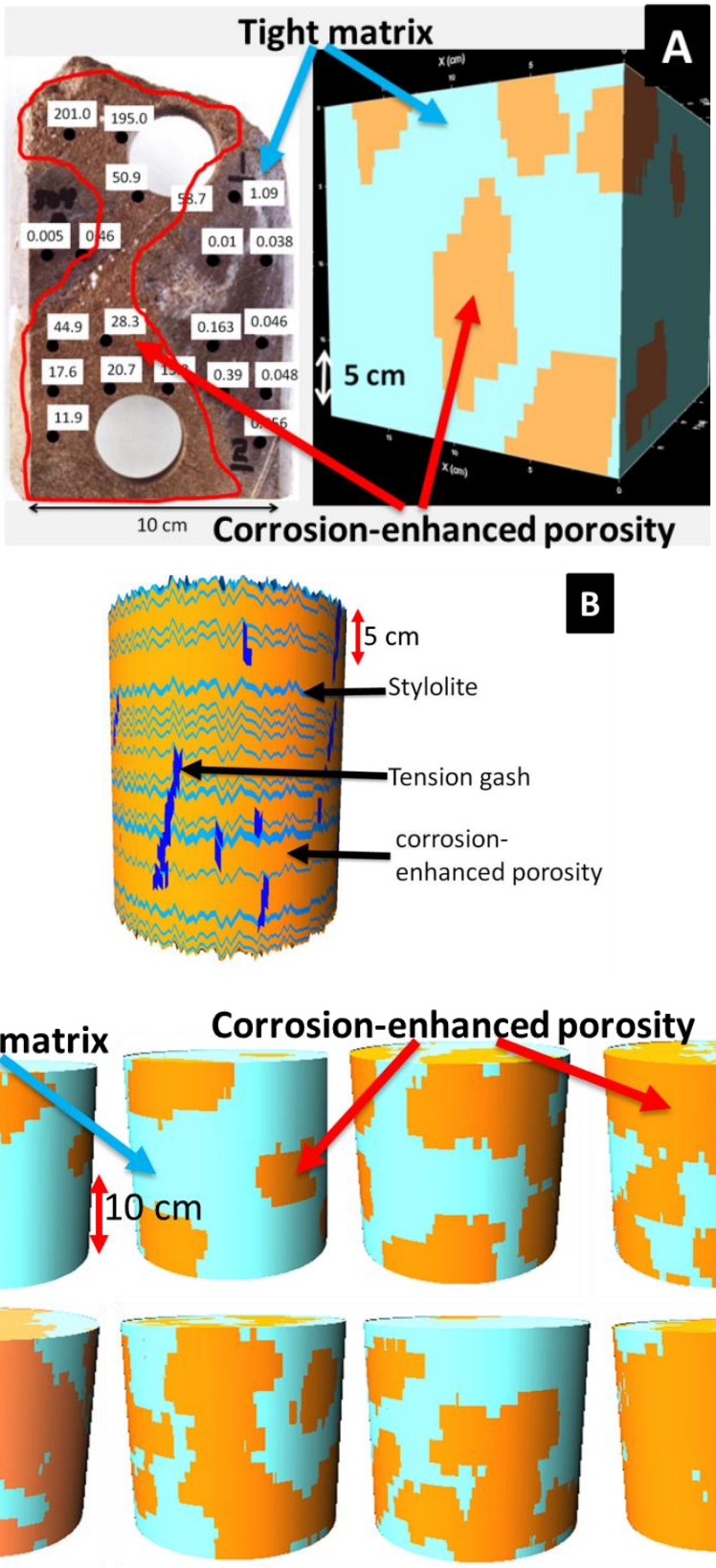

Figure 8.7. (**a**) Near-wellbore model representing distribution of corrosion-enhanced porosity surrounded by a tight matrix (**b**) Example of a near-wellbore model when stylolites and associated tension-gashes are explicitly modelled. (**c)** Example model realisations of solution-enhanced porosity and tight matrix scenarios

Table 8.3. Summary of NWRTs present in A Zone. See Table 8.1 for GeoRT descriptions.

#	NWRT	GeoRT A Zone	Poro-perm group	Saturation-height group (Figure 8.5)	Near-wellbore modelling aspects
0	NWRT-A0	1	K-A0	-	Shale lamina
1	NWRT-A1	2,3,4,5	K-A1	Tight matrix	Tight matrix, multiple poro-perm scenarios
2	NWRT-A2	7	K-A2	CEP1	Multiple realisations of K-A2 overprinted on tight matrix
3	NWRT-A3	6, 8, 11, 12	K-A3	CEP1	Multiple realisations of K-A3 overprinted on tight matrix
4	NWRT-A4	10, 9	K-A4	CEP1	Multiple realisations of K-A4 overprinted on KA3
5	NWRT-A5	13, 14	K-A5	CEP2	Multiple realisations of K-A5 overprinted on KA3
6	NWRT-A6	15, 16	K-A6	CEP2	Multiple realisations of K-A5, explicitly modelled leached stylolites and tension gashes overprinted on KA3

Table 8.4. Summary of NWRTs present in B Zone. See Table 8.1 for GeoRT descriptions.

#	NWRT	GeoRT B Zone	Poro-perm group	Saturation-height group (Figure 8.5)	Near-wellbore modelling aspects
0	NWRT-B0	1	K-B0	-	Shale lamina
1	NWRT-B1	4, 10	K-B1	Tight matrix	Multiple realisations of of KB1 overprinted on tight matrix
2	NWRT-B2	8	K-B2	CEP1	Multiple realisations of of KB2 overprinted on tight matrix
3	NWRT-B3	16	K-B3	CEP1	Multiple realisations of KB4 overprinted on tight matrix
4	NWRT-B4	1, 2, 3, 7	K-B4	CEP1	Multiple realisations of KB4 overprinted on KB3
5	NWRT-B5	5,6, 9, 12	K-B5	CEP2	Multiple realisations of K-B5, explicitly modelled leached stylolites and tension gashes overprinted on KB4
6	NWRT-B6	11, 13, 14, 15	K-B6	CEP2	Multiple realisations of K-B6, explicitly modelled leached stylolites and tension gashes overprinted on KB4

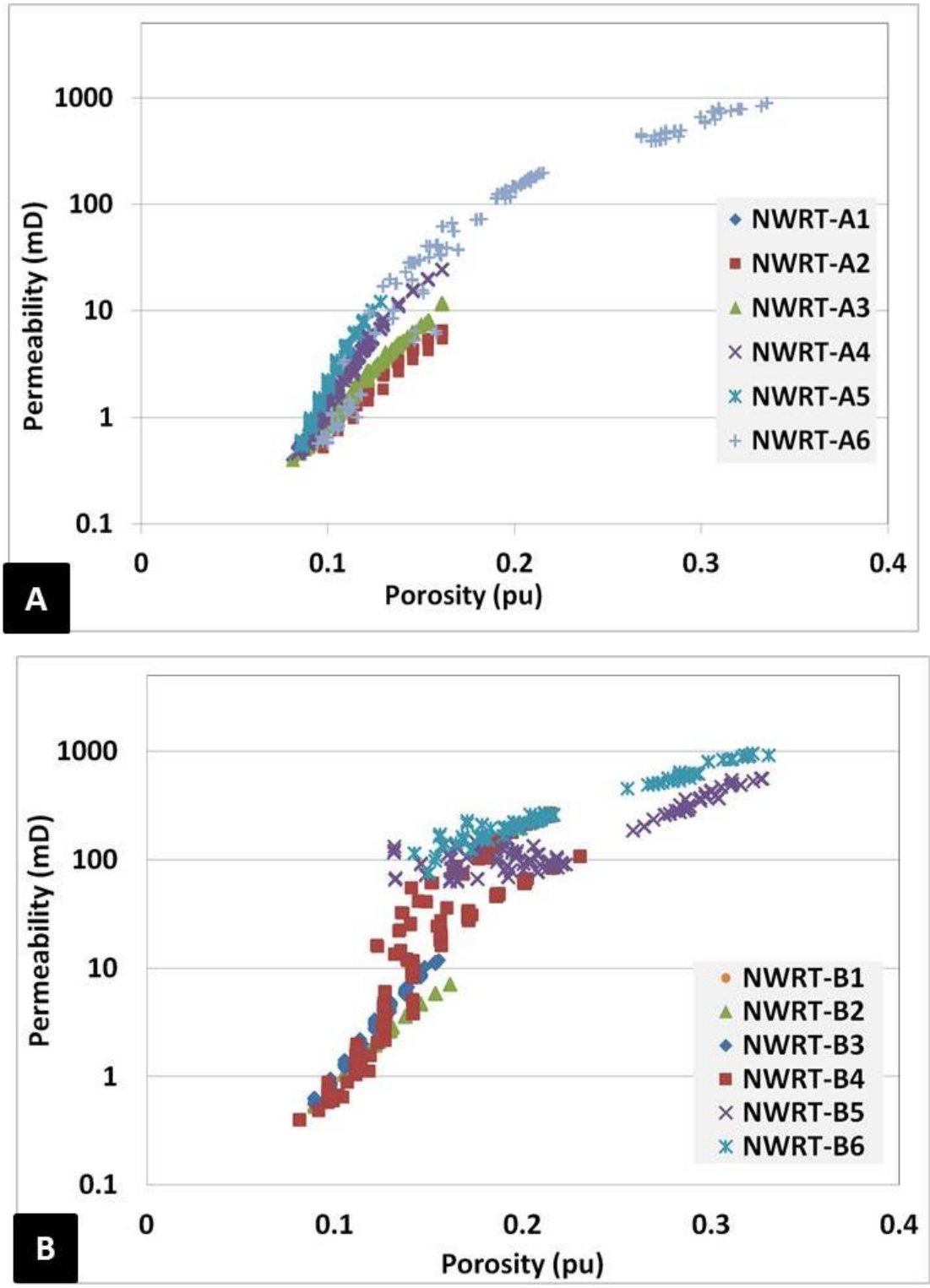

Figure 8.8. Cross-plot between effective porosity and effective horizontal permeability calculated using flow-based upscaling for the various near-wellbore rock types (NWRTs) from A Zone (a) and B Zone (b).

8.5. Geological-Porosity Derived Systems (GeoPODS)

Figure 8.9 illustrates the summary of the integrated near-wellbore rock-typing and upscaling workflow highlighting the steps taken to obtain Geological Porosity Derived Systems (GeoPoDS) from NWRTs and incorporating them into reservoir simulation studies.

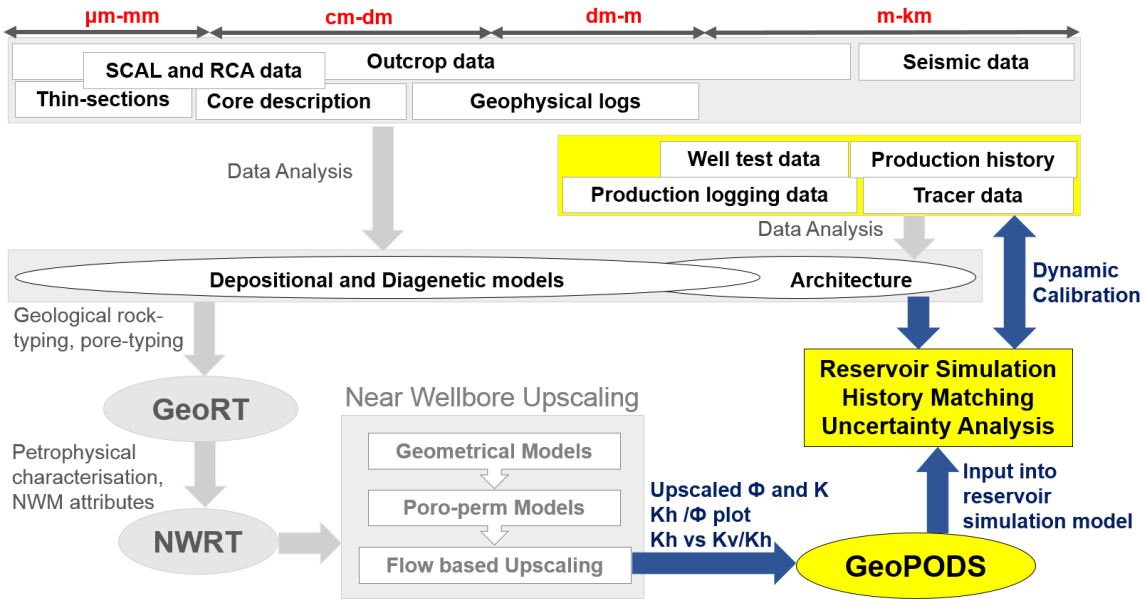

Figure 8.9. Summary of the integrated near-wellbore rock-typing and upscaling workflow highlighting the steps taken to obtain Geological Porosity Derived Systems (GeoPoDS) from NWRTs and incorporating them into reservoir simulation studies.

The level of reservoir model complexity is generally case dependent, based on the objectives of the reservoir simulation study and the associated uncertainties. It is necessary to achieve a healthy balance between the robustness of the reservoir simulation model and the accuracy of the simulation results. The upscaled NWRTs from each zone (Tables 8.3 & 8.4) could have been used as the reservoir rock types of Field X and directly input into the reservoir model. However, this would have resulted in a relatively large number of rock types; Field X would have comprised a total of 12 reservoir rock types, resulting from 6 NWRTs in A Zone and 6 in B Zone. As a consequence, the complexity of the reservoir modelling and simulation workflows could have increased significantly. This issue was addressed by further grouping the NWRTs into GeoPODS. The GeoPODS are then used in the reservoir simulation model.

In this study, the effective porosity and permeability values resulting from NWU and the predominant poro-perm trends were the main basis for grouping the NWRTs into

GeoPODS. Overall, the NWRTs were binned into four GeoPODS in Field X: shale, G0, G1 and G2 (Table 8.5). Figure 8.10a illustrates the cross-plot obtained from near-wellbore upscaled porosity and horizontal permeability values used to obtain GeoPODS. This cross-plot was used to calculate the global permeability transforms of the GeoPODS. High and low case permeability transforms were also obtained for each of the GeoPODS to test their impact on production profiles. The cross-plot used to obtain the correlation between near-wellbore upscaled K_v/K_h anisotropy and horizontal permeability is shown in Figure 8.10b. This correlation was used to calculate the vertical permeability of the GeoPODS. Figure 8.11a shows the comparison between the GeoPODS porosity-permeability crossplot and Lucia's (1983) permeability transforms for nonvuggy carbonate fabrics.

The GeoPODS permeability transforms superimposed on the 'Global Hydraulic Elements' (GHE) plot (Corbett & Potter 2004) is shown in Figure 8.11b. G0 mainly constituted the NWRTs derived from GeoRTs with tight matrix while G1 was dominated by NWRTs derived from GeoRTs with CEP1, i.e. corrosion-enhanced micro and meso porosity types. The porosity-permeability distribution of GeoPODS G0 was coherent with Lucia's (1983) Class 3 nonvuggy rock-fabric type (Figure 8.11a) and is equivalent to GHE 3 (Figure 8.11b). The porosity-permeability distribution of G1 was spread between Lucia's (1983) class 2 and class 3 (Figure 8.11a) and showed equivalence to GHE 4 (Figure 8.11b). The GeoPODS G2 comprised the NWRTs that corresponded to GeoRTs with high CEP2, which included leached stylolite and tension gash porosity types. G2 porosity-permeability distribution varied between Lucia's class 1 and class 2 rock fabric types (Figure 8.11a) and was equivalent to GHE 6 (Figure 8.11b). The comparison of GeoPODS porosity-permeability relation with GHE in Figure 8.11b corroborates the presence of three main porosity types in Field X at the reservoir grid-block scale. Table 8.5 summarises the GeoPODS and their petrophysical attributes that were derived from the integrated near-wellbore rock-typing and upscaling workflow. Table 8.5 also lists the saturation-height function and relative permeability groups corresponding to the GeoPODS based on the characterisation of GeoRTs.

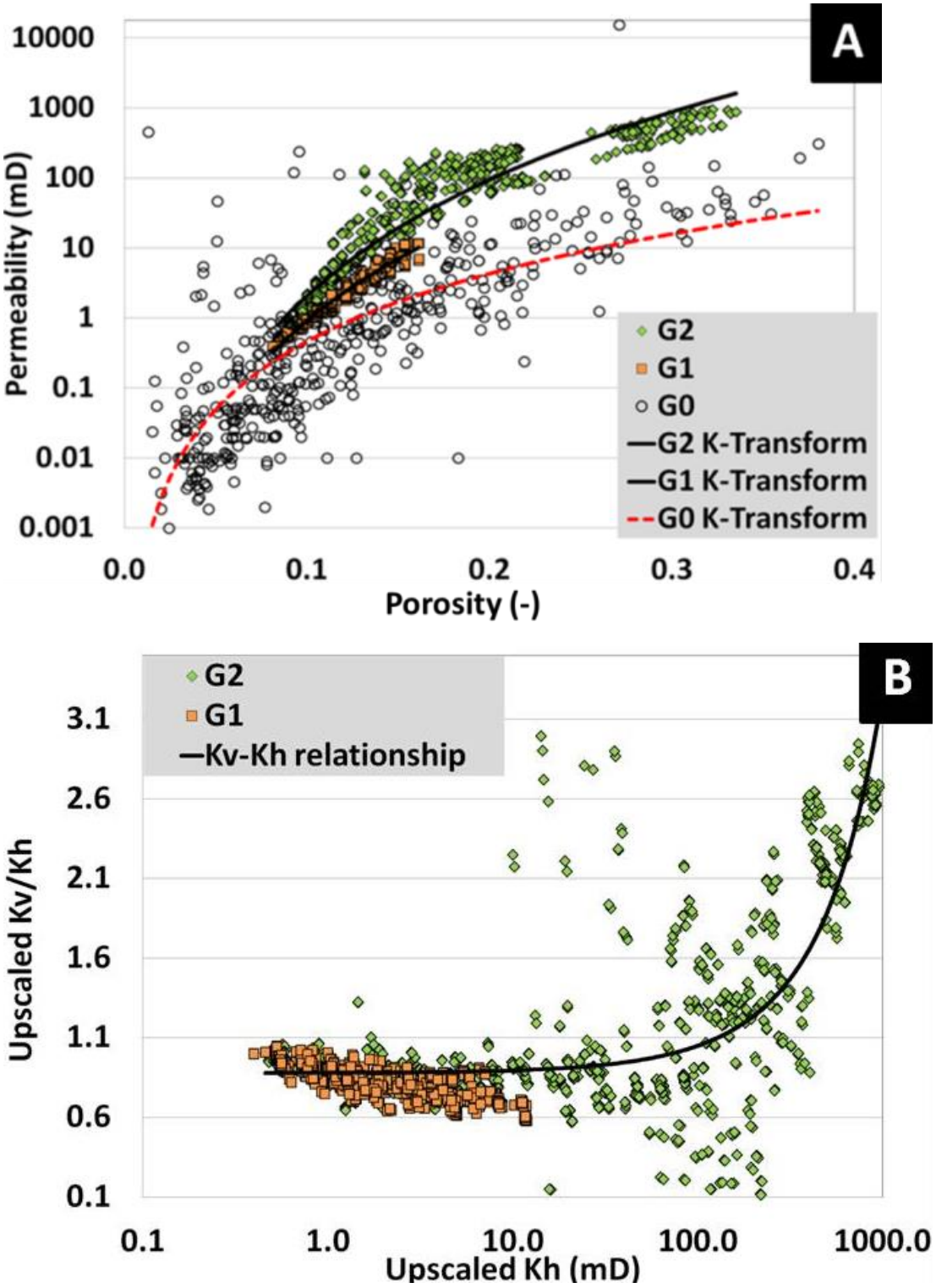

Figure 8.10. (a) Cross-plot between effective porosity and effective horizontal permeability of GeoPODS. (b) Cross-plot between calculated effective horizontal permeability and effective K_v/K_h anisotropy ratio of the GeoPODS.

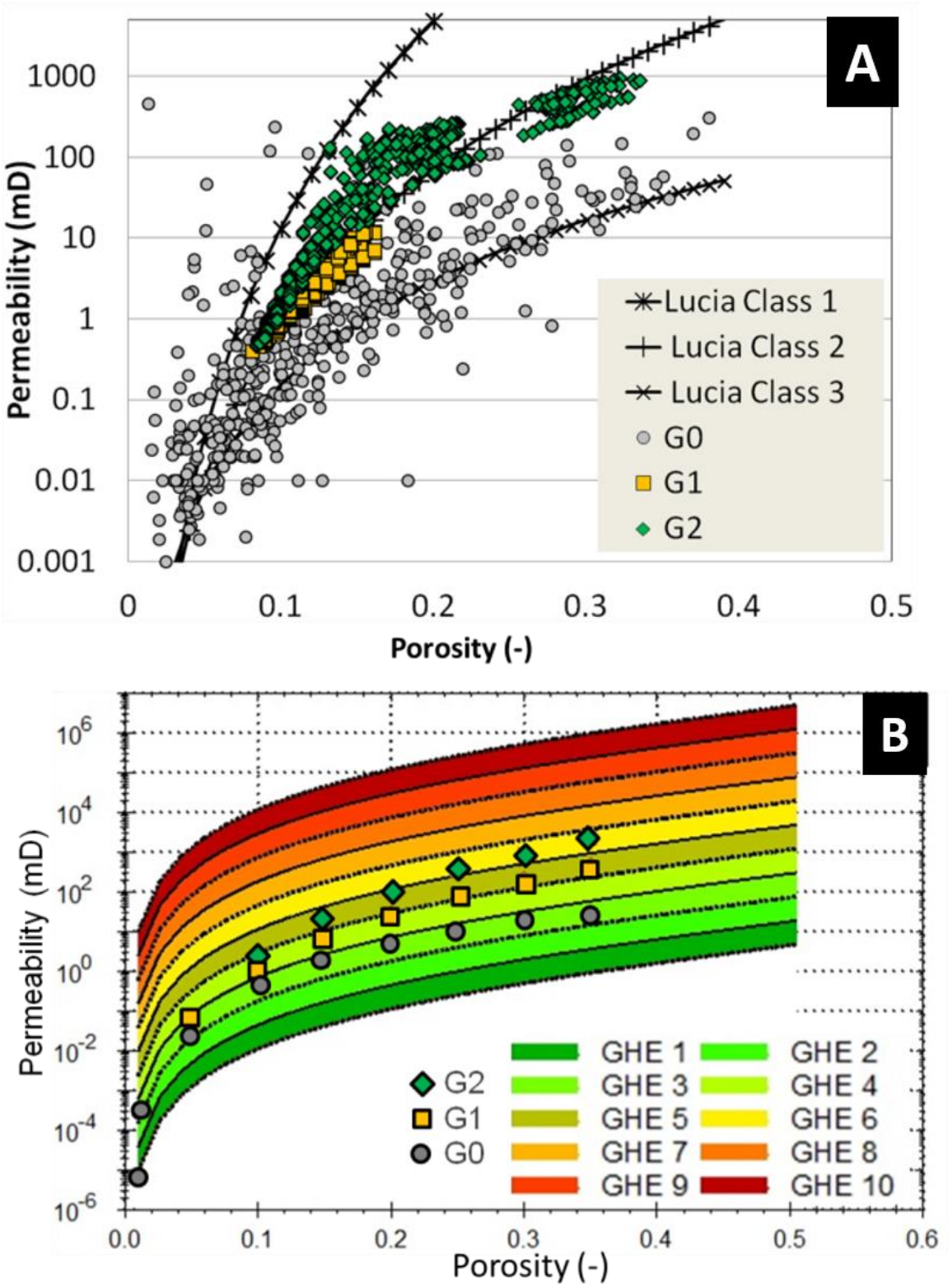

Figure 8.11. (a) Comparison between the GeoPODS porosity-permeability crossplot and Lucia's (1983) permeability transforms for nonvuggy fabrics. (b) GeoPODS permeability transforms superimposed on the 'Global Hydraulic Element' (Corbett & Potter 2004) plot.

Table 8.5. Summary of GeoPODS and their petrophysical attributes input into reservoir simulation. Figures 8.5 and 8.6 can be referred for the Sw-H and Kr groups.

GeoPODS	PHIE	Permeability Transform	K_v/K_h anisotropy	Sw-H group	Kr group
Shale	<0.01	$K = 0.001$	$K_v = K_h$	CEP0	CEP0
G0	[0.01, 0.05)	$K = 766.42 * \Phi^{3.2229}$	$\frac{K_v}{K_h} = 8\text{x}10^{17} * K_h^2 + 0.0016 * K_h + 0.878$	CEP0	CEP0
G1	[0.05, 0.15)	$K = 101278 * \Phi^{5.0483}$	$\frac{K_v}{K_h} = 8\text{x}10^{17} * K_h^2 + 0.0016 * K_h + 0.878$	CEP1	CEP1
G2	>0.15	$K = 663749 * \Phi^{5.5071}$	$\frac{K_v}{K_h} = 8\text{x}10^{17} * K_h^2 + 0.0016 * K_h + 0.878$	CEP2	CEP2

8.6. Employing GeoPODS in reservoir simulation

As discussed earlier, not only the reservoir permeability of Field X, but also the initial hydrocarbons-in-place and the critical oil saturation values were associated with high degrees of uncertainty. Due to the capillary transition zone present in the oil rim, Field X poses additional challenges for reliable characterisation and simulation of the reservoir behaviour. The unrealistic water relative permeability endpoints and local initial saturation changes applied to the original Field X geomodel to obtain history match suggested that the distribution of initial-oil-in-place and the dependency of residual oil saturation on initial water saturation require better characterisation. In order to accomplish this, it was ensured that the poro-perm distribution, capillary pressure, and relative permeability characteristics were coherent within each GeoPODS. This was vital to maintain the internal consistency of the reservoir static and dynamic properties in the simulator. The steps to incorporate the static and dynamic properties of the GeoPODS into the reservoir simulator are discussed in the next section.

8.6.1. Field X Permeability and rock quality index

First, the porosity cut-offs (Table 8.5) for each GeoPODS were obtained from upscaled poro-perm cross-plots (Figure 8.8) and were reconciled with the wireline effective porosity logs in the near-wellbore regions. The porosity cut-offs were then applied to the Field X porosity model, originally supplied by the operator, to obtain the GeoPODS model. Following this, the respective permeability and K_v/K_h transforms (Table 8.5) were applied to the porosity model to calculate the horizontal and vertical permeability distributions within each GeoPODS. Figure 8.12 shows the comparison between the permeability model derived from conventional core poro-perm transform and the

permeability model resulting from the GeoPODS model. The reservoir rock quality index (RQI) in Field X was calculated as (Amaefule *et al*. 1993)

$$RQI = 0.0314\sqrt{\frac{k}{\Phi}}, \qquad (1)$$

where k is permeability and Φ is porosity. The RQI calculated for the GeoPODS inherently capturesd the enhanced flow properties caused by late-burial corrosion that could not be modelled by conventional rock-typing. The characterisation of RQI in Field X hence significantly improved due to the implementation of GeoPODS (Figure 8.13b) compared to the original geomodel (Figure 8.13a). This improvement in RQI characterisation would have strong implications towards the calculation of initial water saturation in the simulation model when J function approach was used for saturation modelling.

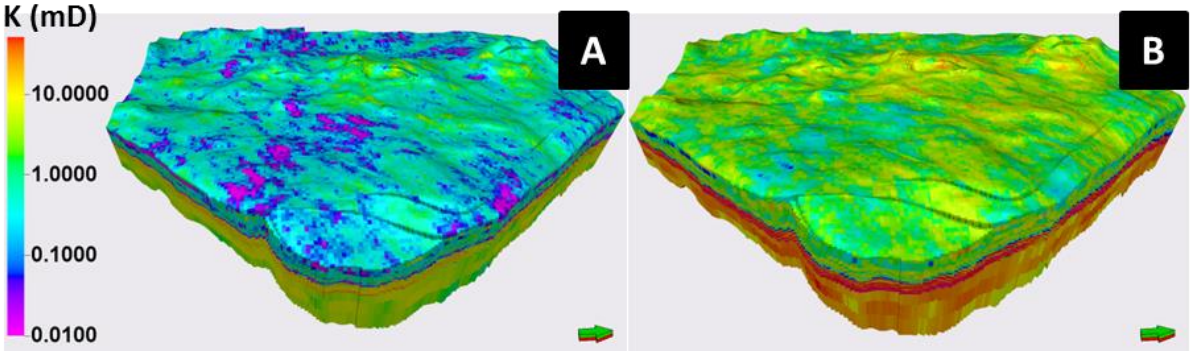

Figure 8.12. (a) Permeability model derived from core permeability transform (b) Permeability model obtained from the permeability transforms of the GeoPODS.

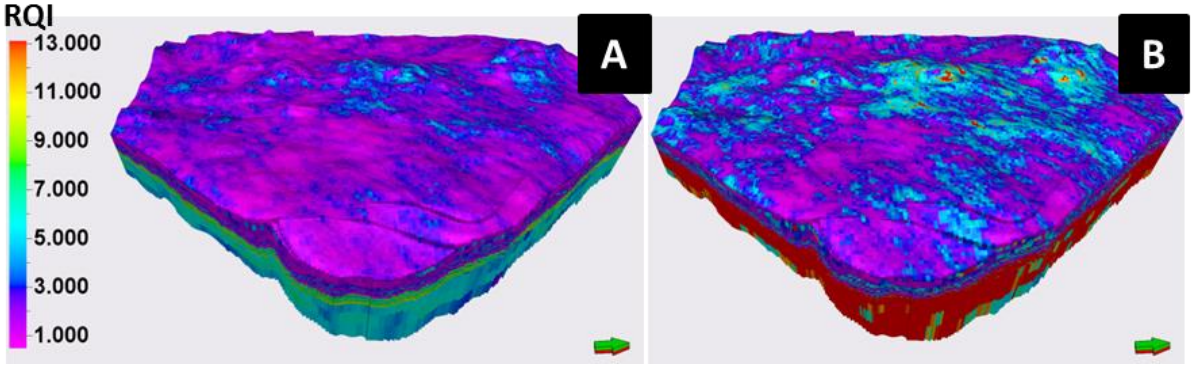

Figure 8.13. (a) Reservoir rock quality index calculated using the permeability model derived from core permeability transform (b) Reservoir quality index calculated using the permeability model obtained from the permeability transforms of the GeoPODS.

8.6.2. Relative permeability curves

Despite the limited number of SCAL samples that were available for this study, it was possible to obtain a general understanding of the relative permeability characteristics of the GeoRTs (Figure 8.6). These relative permeability curve groups were 'averaged' and assigned to the GeoPODS. The relative permeability curves from each CEP group were averaged using the commercial software application called SCAL, which is a plug-in to the reservoir simulator ECLIPSE. The relative permeability curves were first normalised to remove the effect of the different initial water saturation values and residual oil saturation values of the samples of the same group. Then the normalised curves were averaged to obtain a single relative permeability curve, which was used as the representative of the group. Figure 8.14 shows the representative water-oil and gas-oil relative permeability curves of the GeoPODS compared with those originally used for Field X history matching.

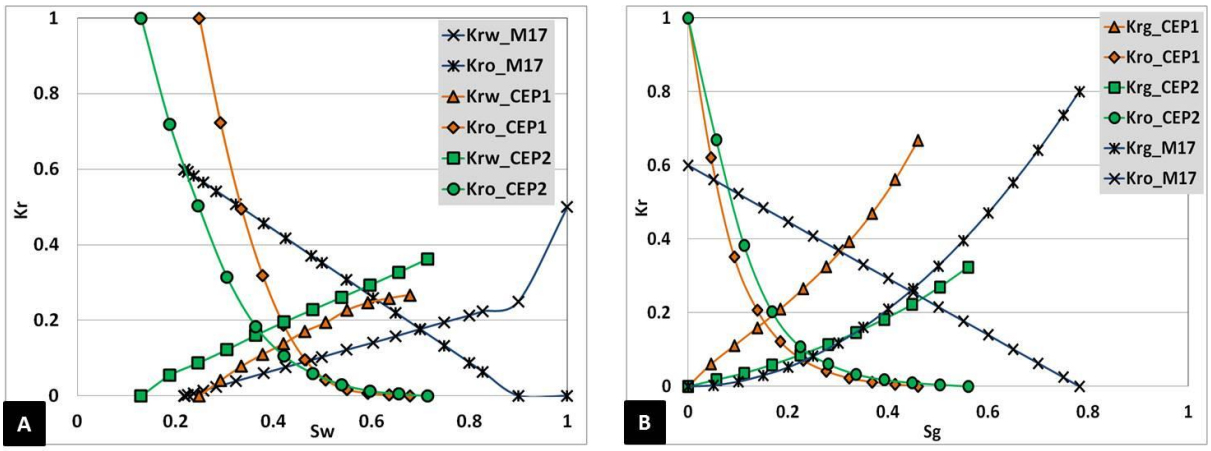

Figure 8.14. (a) Average water-oil relative permeability curves obtained for the GeoPODS (CEP1 and CEP2) compared with those used for history matching (M17). (b) Average gas-oil relative permeability curves obtained for the GeoPODS (CEP1 and CEP2) compared with those used for history matching (M17).

8.6.3. Capillary pressure-saturation correlations

The three main groups of saturation-height functions that were obtained during the characterisation of GeoRTs were used to obtain the relationship between initial water saturation and capillary pressure for the GeoPODS. Two methods were tested to derive the relationship between capillary pressure and saturation to be implemented in reservoir simulation. In the first method a P_c-S_w correlation was obtained for each GeoPODS based on the correlation between the logarithm of capillary pressure and

water saturation (Figure 8.15a). In the second method (Figure 8.15b) the relationship between J function, P_c and water saturation was used as

$$J = \frac{0.218\ P_c}{\sigma \mathrm{Cos}\ \theta} \sqrt{\frac{k}{\Phi}}, \qquad (2)$$

Here σ and θ are interfacial tension and contact angle between oil and water at reservoir condition, respectively. Thus, the J function allowed the scaling of capillary pressure to account for the variation in porosity and permeability in the reservoir, i.e, the RQI. Some of the capillary pressure curves from G0 group, which represented the poor quality reservoir rock in Field X, were concave due to the micritic nature of the rock. The normalised capillary pressure curve of the GeoPODS G0 (Figure 8.15a) could not represent this phenomenon adequately. In contrast, these curves were better characterised by the J functions (Figure 8.15b), which accounted for the rock quality index of the GeoPODS.

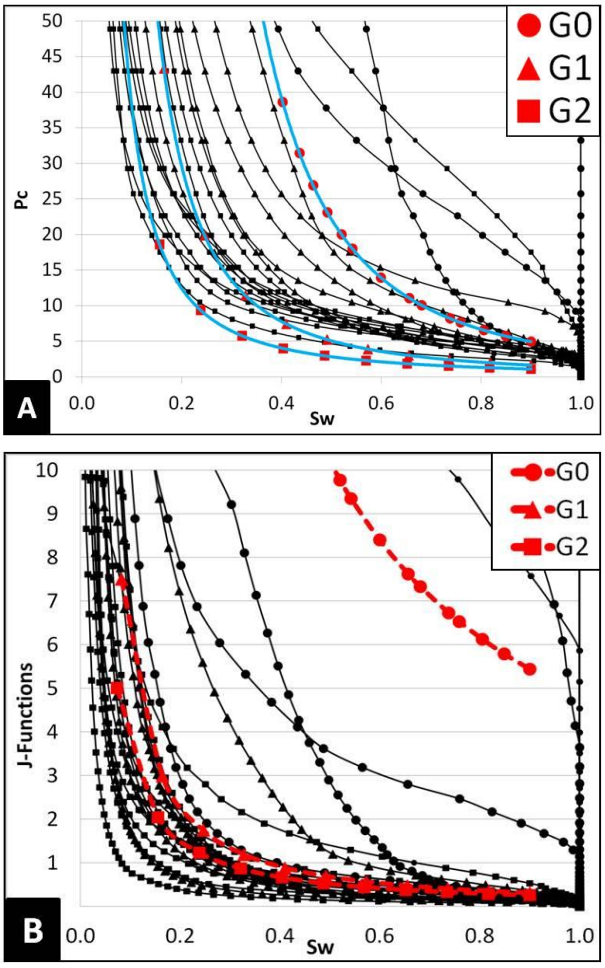

Figure 8.15. (a) Average capillary pressure-saturation correlation curves obtained for the GeoPODS. (b) Average J functions obtained for the GeoPODS.

8.7. Implications towards fluid-in-place calculations and reservoir simulation

During reservoir simulation, the capillary pressure-saturation curves are used to compute the initial water saturation in the reservoir simulation model, which provides the initial fluid volumes in the grid-blocks. The capillary pressure-saturation relationships obtained for the GeoPODS using the two different methods discussed in the previous section were input as tables into the simulation model to test how this impacts the fluids-in-place volumes. The capillary pressure- and J function-saturation correlations were applied to the saturation column from the relative permeability-saturation tables to calculate the P_c and J functions, respectively, for each of the GeoPODS. The input of J function-saturation tables was used by the simulator to compute the P_c values as

$$P_c = CF * J * T \cos\theta * \sqrt{\frac{\Phi}{k}}, \qquad (3)$$

Where CF is the conversion factor and for capillary pressure in Psi, CF = 4.61678.

The impact of the different capillary pressure- and J-saturation correlations on the distribution of initial water saturation and therefore on the fluids-in-place calculation is demonstrated in Table 8.6. A difference of over 150 million STB of oil-in-place and up to 700 million MSCF of gas-in-place was observed. The impact of varying capillary pressure and J function on the reservoir flow simulation results is shown in Figure 8.16. The J function approach was tested using two GeoPODS permeability cases, one using the near-wellbore upscaled permeability transform shown in Figure 8.8a and one using the high permeability transform case. The simulation scenarios that incorporated GeoPODS and employed the respective J functions showed better agreement of simulated and observed cumulative oil production compared to the simulation case that did not involve any rock-typing (Figure 8.16). The simulation scenario employing J function with high permeability transform case showed upto 22% increment in the cumulative oil production compared to the simulation case without rock-typing. These differences can be explained as follows: When the J function-saturation correlations were used, the effect of block dependent porosity and permeability was accounted for during initialisation in the reservoir simulator (equation 3). This approach produced a spatially varying transition zone which was not only a result of spatially varying capillary pressures but also the RQI. The RQI was in turn conditioned to the distribution of GeoPODS. Therefore, using the J function approach to employ GeoPODS in

reservoir simulation provided internal consistency of the static reservoir properties, i.e., porosity and permeability as well as the dynamic behaviour associated with capillary pressure and relative permeability in the reservoir simulation model. Subsequently, the simulation model was reinforced by the improved characterisation of RQI during near-wellbore rock-typing and upscaling, which yielded more reliable saturation modelling and reservoir initialisation for reservoir simulation studies. As a result, the simulation model predictions involving near-wellbore rock-typing and upscaling were in better agreement with the historic production data compared to the scenario without rock-typing.

It must be noted that the process of history matching yields a non-unique solution. For instance, similar production curves as discussed above probably could have been resulted by a model with higher fault transmissibility multipliers and using only the lower NWU permeability case. However, since the characterisation of the faults in Field X was out of scope of the work presented here, this issue was not touched. It is hence strongly suggested that during the full-fledged history matching study to follow the fault transmissibility values must be included in the sensitivity analysis during the evaluation of history matching parameters. On the other hand, similar results could have also been obtained by simply adding permeability multipliers in the simulation model and/or manipulating the relative permeability end-points or the fault transmissibility values. However, such manipulations, when done without any geological-petrophysical rationale impose additional uncertainty to the model and render it unreliable for reservoir management and development studies. The near-wellbore rock-typing and upscaling workflow discussed in this chapter presents a practical solution to characterise and initialise the reservoir model prior to history-matching such that the requirement for such numerical multipliers and manual modifications to the simulation model are minimised.

Table 8.6. Sensitivity of volumes of oil- and gas-in-place to Pc-Sw correlation.

Correlation method	STOIIP[*10^6 STB]	GIIP [*10^6 MSCF]
Capillary pressure-saturation	1138.9	2721.3
J-saturation using NWU permeability	965.7	2029
J-saturation using NWU permeability high case	1252.9	2685.2

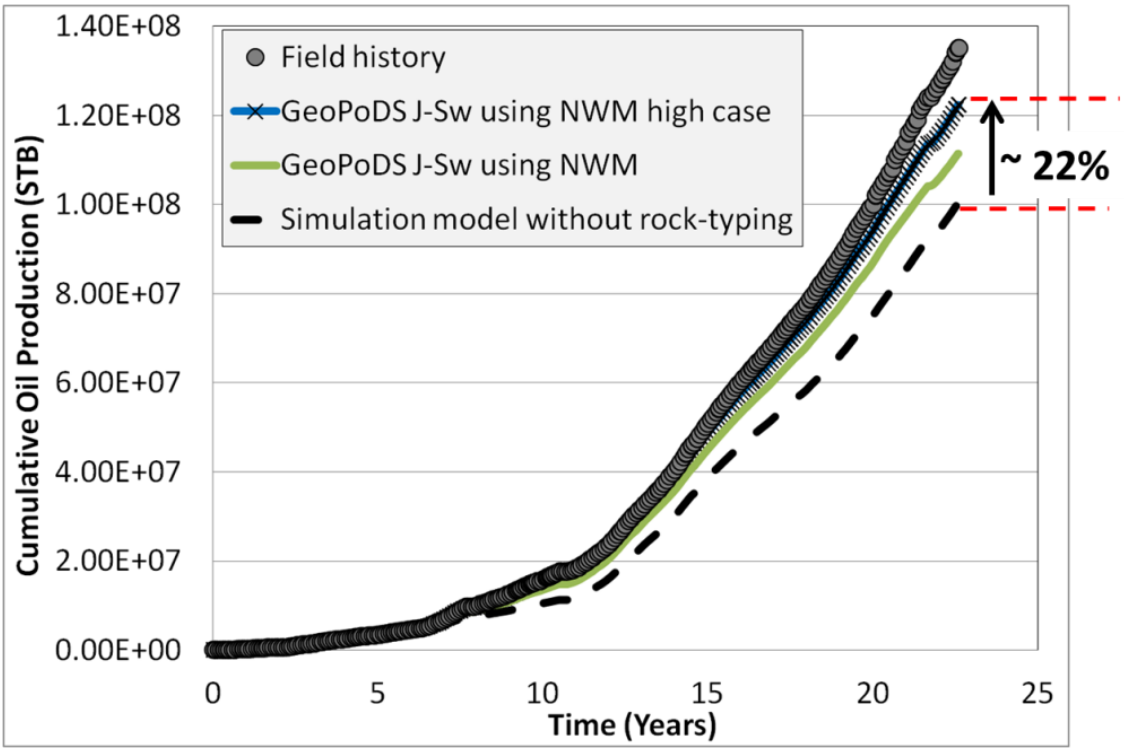

Figure 8.16. Observed and simulated cumulative oil production curves in Field X. The GeoPODS scenarios employing J-saturation method shows better agreement with historic data compared to the simulation model that does not involve a near-wellbore rock-typing and upscaling workflow.

8.8. Conclusions

The key challenges associated with integrating reservoir rock-typing and simulation were addressed in this study by employing a novel rock-typing workflow in conjunction with NWU. The near-wellbore rock-typing and upscaling workflow involved characterisation, modelling and upscaling of key small-scale geological-petrophysical heterogeneities into reservoir grid-block scale. This approach was applied to Field X, to improve reservoir characterisation and simulation of the field. The geological rock types, GeoRTs, were generated with the specific aim to account for the impact of late-burial corrosion, the crucial diagenetic phase in Field X, on the evolution of reservoir properties. This was approached with considerations to the crucial links between the depositional and diagenetic features and their impact on reservoir flow properties. Petrophysical characterisation of GeoRTs enabled their grouping into near-wellbore rock types, NWRTs, which were then upscaled to the reservoir grid block scale using the NWU workflow. The upscaled porosity-permeability cluster was used to group the NWRTs with same poro-perm trends into Geological-Porosity Derived Systems,

GeoPODS. GeoPODS are equivalent to upscaled plug-scale Hydraulic Flow Units (Amaefule *et al*. 1999) and help to further define the Global Hydraulic Elements (Corbett & Potter 2004) concept at the appropriate modelling scale for full field simulation models. The resulting GeoPODS scenarios hence incorporated the small-scale depositional and diagenetic heterogeneities in Field X. The GeoPODS were ultimately used to populate the reservoir geomodel and ensure that the static and dynamic reservoir properties are internally consistent within each GeoPODS. The porosity-permeability transforms, saturation-height functions and relative permeability curves individually tailored for each GeoPODS were employed in the simulation model. This yielded consistent initialisation of reservoir simulation model and therefore improved the calculation of volumes of fluids-in-place. Simulation results indicated that using GeoPODS in conjunction with J functions led to cumulative production curves that agreed well with the historic production data.

Overall, this chapter illustrated a new way of integrating multi-scale static and dynamic data pertinent to heterogeneous carbonate reservoirs seamlessly into a reservoir simulation model for improved characterisation and dynamic calibration. The new simulation model is now much better constrained to the reservoir geology and can provide an improved geological-prior for history matching.

Chapter 9. SUMMARY, CONCLUSIONS AND FUTURE WORK

This thesis demonstrated a set of workflows that employed high-resolution near-wellbore modelling and upscaling tools to improve the integration of multi-scale geological-petrophysical data seamlessly for reservoir characterisation and simulation of highly heterogeneous reservoirs. An important advantage of these workflows is that they can be easily plugged into the conventional reservoir modelling and simulation workflows that are generally used in the industry. Overall, results confirmed the strong impact of centimetre to decimetre scale geological heterogeneities on the reservoir performance of the studied fields. It was shown that NWM tools can capture multi-scale heterogeneities in the near-wellbore region in a geomodel and can aid the study of skin effects in a numerical modelling environment.

A major portion of this thesis was devoted to the implementation of NWU tools to address the critical modelling and simulation challenges associated with carbonate reservoirs. This thesis demonstrated, with the help of NWU tools that the reservoir performance of the studied carbonate field was strongly controlled by the distribution of late burial diagenetic heterogeneities. Stylolites and associated tension gashes are among the most commonly observed diagenetic features in carbonate reservoirs, varying laterally in size from few centimetres to several meters, and often they impact the fluid flow paths by acting as either inhibitors or enhancers to flow. This thesis presented a novel way of incorporating stylolites and tension gashes in reservoir scale models, using near-wellbore upscaling tools. Furthermore, a new methodology to upscale the porosity-permeability transforms into the reservoir scale from the core plug scale was presented. Additionally, a novel near-wellbore rock-typing and upscaling approach was presented, which addressed the crucial challenges of integrating reservoir rock-typing and simulation in carbonate reservoirs. Altogether, this thesis provides valuable insights to the means by which a geologically consistent field-level history match can be achieved for complex carbonate reservoirs. The key results and conclusions presented in the chapters from Part I and Part II of this thesis are summarised in the next section, followed by recommendations for future work.

9.1. Summary and conclusions

In Part I of this thesis, the near-wellbore modelling (NWM) tools were applied to a heterogeneous braided fluvial reservoir, Field A, to improve the calibration of the

reservoir model of Field A with well test data. The key conclusions that can be drawn from Part I are:

- NWM tools were used to build more representative geomodels in the near-wellbore region and to capture a wide range of multi-scale heterogeneities in a reservoir. Such geomodels reinforced the study of skin effects in a numerical modelling environment and allowed to simulate the real pressure transients more accurately.

- Using local grid refinement to fuse high-resolution near-wellbore models with field scale geomodelling minimised numerical artefacts in the early time region during reservoir simulation. This resolved the near-wellbore geology at scales that are typically not achieved in conventional reservoir simulation and hence provided clear information on skin effects.

- Choosing the optimum grid cell size of the NWM grid enabled the replication of the highly conducting cross bedded channel fills in the near-wellbore region of Well A in Field A. Subsequently, these high-permeability channels were reflected in the well test simulation results.

- The NWM workflow employed in Field A ideally requires good Early Time Region (ETR) data sampling in the well-test for dynamic calibration. In the event of sparsely sampled ETR, the skin value and the derivative rise observed from the Middle Time Region (MTR) can be used as a measure of dynamic calibration of the geostatistical NWM.

- Overall, a fit-for-purpose geoengineering workflow that included NWM in conventional sector-scale models enhanced reservoir characterisation of Field A.

In Part II, the NWM workflow was extended to Field X, which is a heterogeneous carbonate reservoir with complex diagenetic history. The reservoir simulation parameters that are associated with the highest uncertainty in Field X are permeability, volumes of fluids initially in place and critical oil saturation. The following conclusions can be deduced from the chapters presented in Part II:

- In Chapter 6, NWM was used in conjunction with petrophysical data to demonstrate that late-burial corrosion heterogeneities, i.e., solution-enhanced

matrix micro- and macro-porosity, leached stylolites and associated tension gashes, have a significant impact on the reservoir properties of Field X. Lucia's transforms were used as proxies to incorporate the small-scale heterogeneities related to the late-burial corrosion in the permeability model of Field X. The investigation presented in this chapter led to a significantly improved characterisation of the late-burial corrosion heterogeneities in Field X and validated their prominent role in improving the permeability distribution.

- In Chapter 7, the NWU workflow was used to calculate the upscaled global permeability transforms and vertical-horizontal permeability anisotropy ratios (K_v/K_h) that reflected the impact of solution-enhanced matrix porosity, leached stylolites and associated tension gashes on fluid flow. The new, upscaled permeability transforms mitigated the core sample bias caused by oversampling of the low-permeability facies. The new transforms further bridged the gap between core and wireline scales by accounting for multi-scale heterogeneities that cannot be represented by core plugs. Reservoir simulation results suggested that the incorporation of the small scale geological heterogeneities into the permeability leads to cumulative production curves that had reduced misfit compared to the historic oil production data, although they do not require artificial permeability multipliers.
- The key challenges associated with integrating reservoir rock-typing and simulation were addressed in Chapter 8 by employing a novel rock-typing workflow in conjunction with near-wellbore upscaling. This yielded consistent initialisation of reservoir simulation model and therefore improved the calculation of volumes of fluids-in-place. On the whole, Chapter 8 illustrated a new way of integrating multi-scale static and dynamic data pertinent to heterogeneous carbonate reservoirs seamlessly into a reservoir simulation model for improved characterisation and dynamic calibration. The new simulation model is now much better constrained to the reservoir geology and provides an improved geological-prior for history matching.

The near-wellbore upscaling workflow and results discussed in Part II rely on a basic assumption that the porosity model given by the operator is sufficiently accurate to proceed with. The NWU workflows developed for this thesis were successfully tested and implemented for Field X using the given porosity model and the results confirmed

that the proposed workflows can significantly improve the reservoir simulation of Field X. Nevertheless, the uncertainty possibly associated with the porosity model should be given due consideration while performing the history matching study. In addition, it is strongly suggested that the uncertainty associated with the Field X well completion data must be evaluated and addressed in any future studies. Further recommendations for future work are presented in the following section. Overall, the study presented in Part II has led to a substantially improved characterisation of the reservoir simulation parameters in Field X, which are now much better constrained to the reservoir geology. While the original reservoir simulation model required excessive use of permeability multipliers in order to match the historic production data, the new model has largely eliminated the need for such multipliers. This also resulted in a significant decrease in the computational time. It is hence expected that the new model, which accounts for small-scale heterogeneities, will require significantly less efforts to be fully calibrated to dynamic data using advanced (assisted) history matching techniques. The updated reservoir model is therefore better suited to contribute to the ongoing development plans and to help forecast incremental oil recovery more accurately.

9.2. Future work

The following ideas are proposed for future work based on the work presented in this thesis:

- New methods to enhance the modelling of leached stylolites and tension gashes should be explored such that the anastomosing stylolites are represented much more realistically in contrast to the simpler models developed in this thesis. The lateral and vertical connectivity of these features can then be represented more robustly, yielding more accurate effective permeability values.
- The impact of leached stylolites and tension gashes on multiphase flow behaviour was not investigated thoroughly in this thesis. Pore-scale studies of these features can be helpful to understand how they might impact secondary and tertiary recovery processes, for example, water flooding or WAG.
- The J function method was employed in Chapter 8 of this thesis to describe the capillary pressure-saturation relations in the reservoir simulator. However, the investigation of various methods of characterising and averaging capillary pressure data was not done exhaustively and should be looked into.

- The water saturation model described in Chapter 8 was calculated purely from capillary-gravity equilibrium method and should be calibrated with that calculated from wireline logs. This is to ensure that the natural variability of the reservoir fluid saturations is accounted for.
- The rock-typing work presented in Chapter 8 provided some insights based on the SCAL data about the link between the extent of diagenetic corrosion and wettability of the rock. It is suggested that these inferences be substantiated through a robust study focusing on characterising the relative permeability wettability index data of Field X.
- It is highly recommended to perform a full field history matching study of Field X using the improved reservoir simulation model resulting from the work presented in Part II of this thesis. The fault transmissibility values should be included in the sensitivity analysis while evaluating the history matching parameters.
- Along with long production history data, Field X also has tracer data. It is hence recommended to monitor the tracer data during assisted history matching studies to improve the characterisation of the lateral and vertical connectivity of the reservoir.

Appendix

A. Static Model Transient Analysis Results

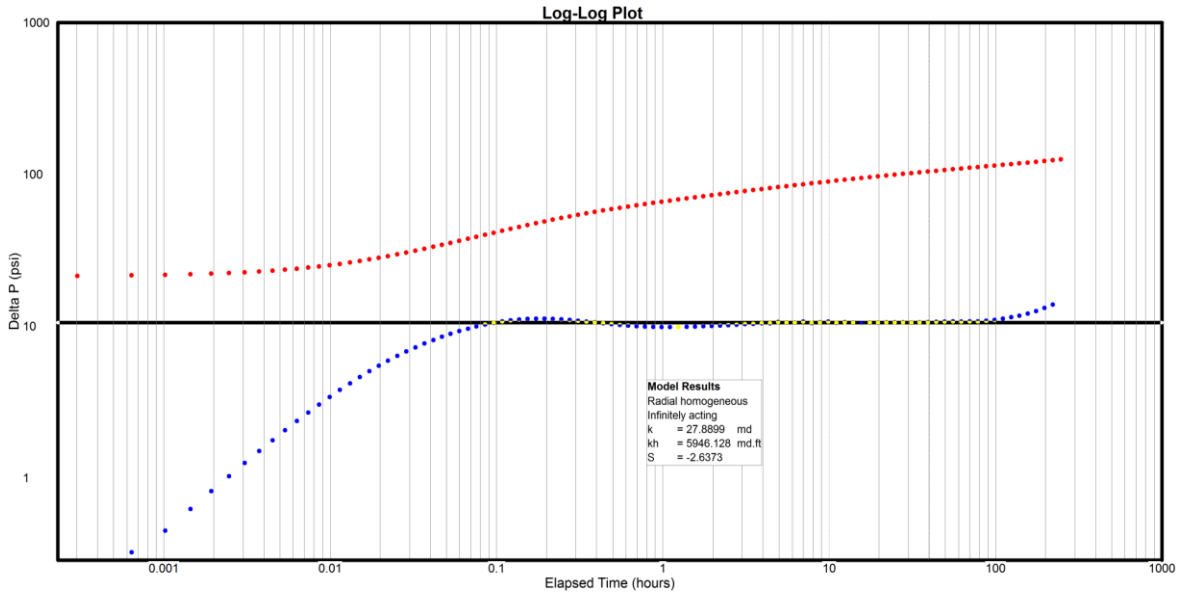

Figure A1. Static model transient analysis of the coarse sector model.

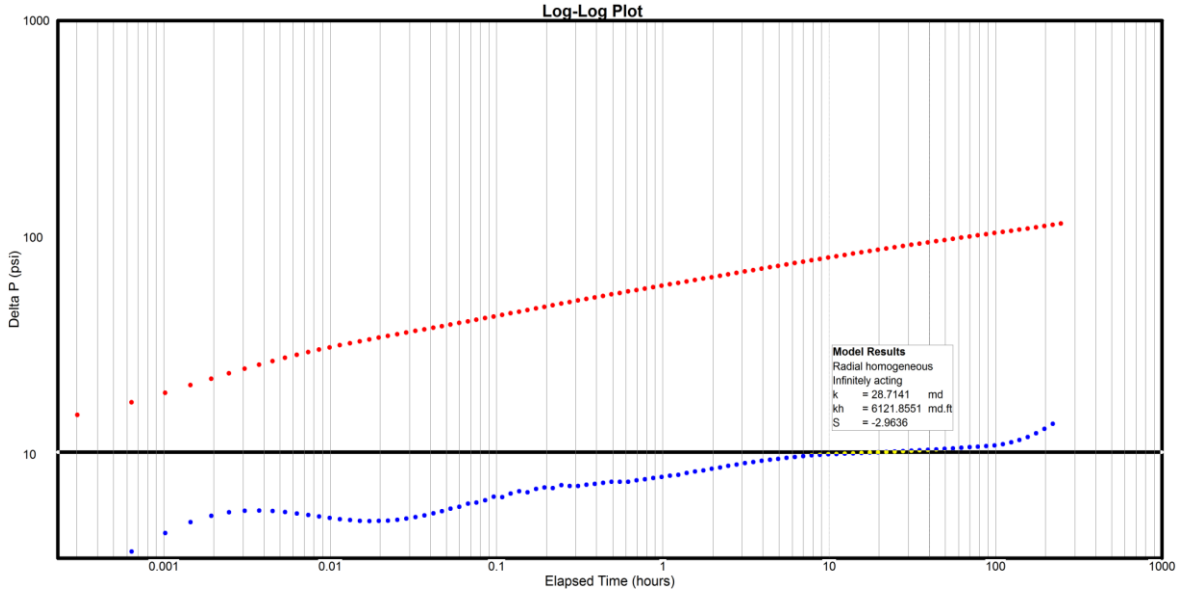

Figure A2. Static model transient analysis of the sector model with local grid refinement (LGR3).

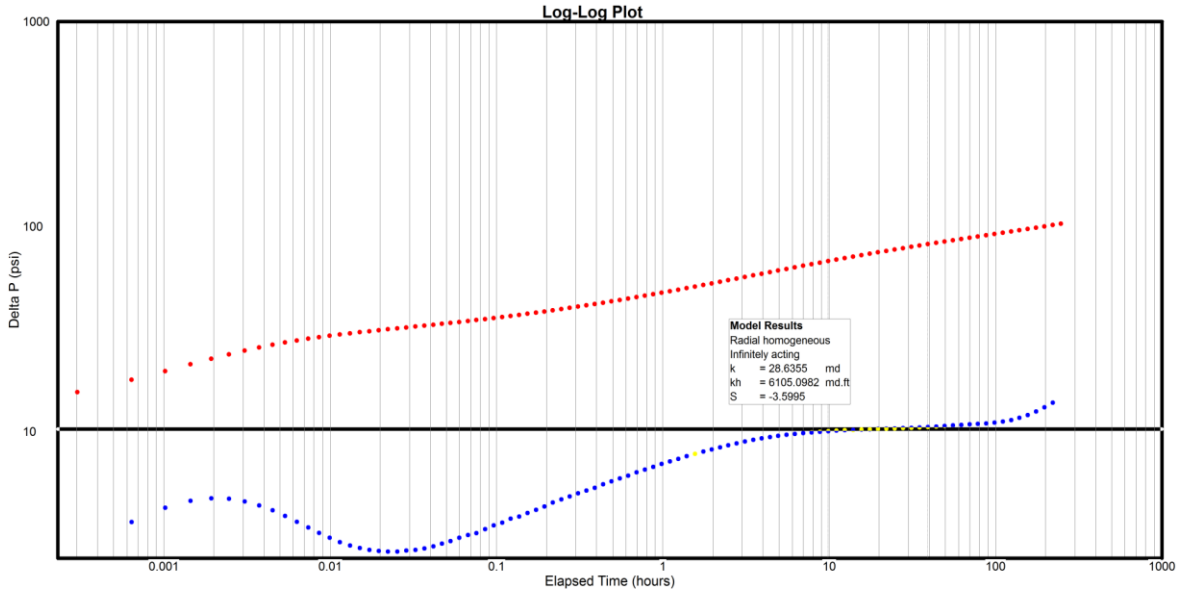

Figure A3. Static model transient analysis of the sector model with local grid refinement embedded with NWM (LGR3+NWM-A1).

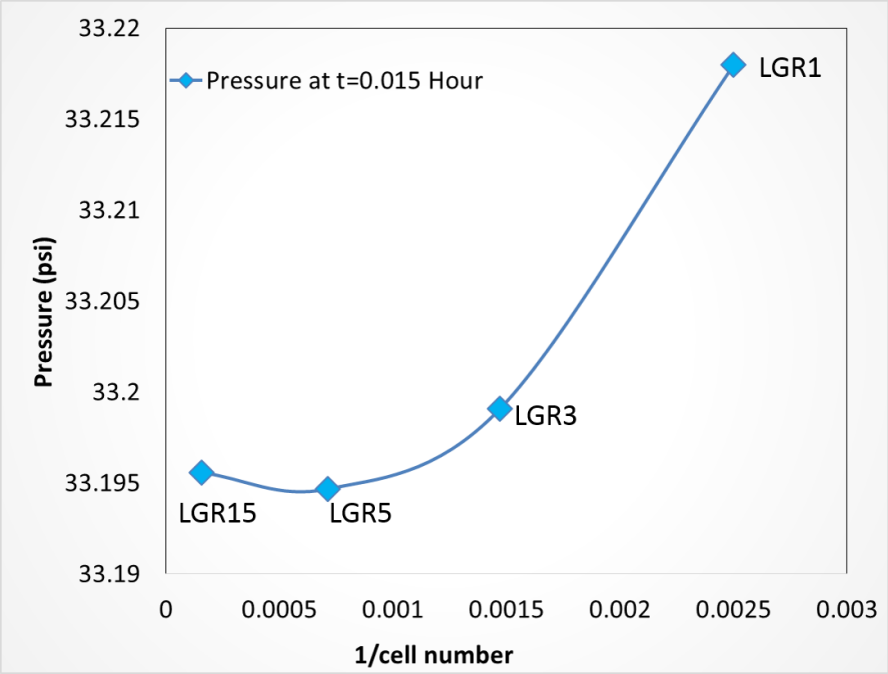

Figure A4. Plot of pressure at a point of time in the ETR versus the inverse of number of cells within the local grid refinement zone of each LGR scenario. LGR3 is considered the best case scenario to proceed further to optimise the simulation run time versus quality of convergence.

B. Field X Saturation Height and Relative Permeability Curves

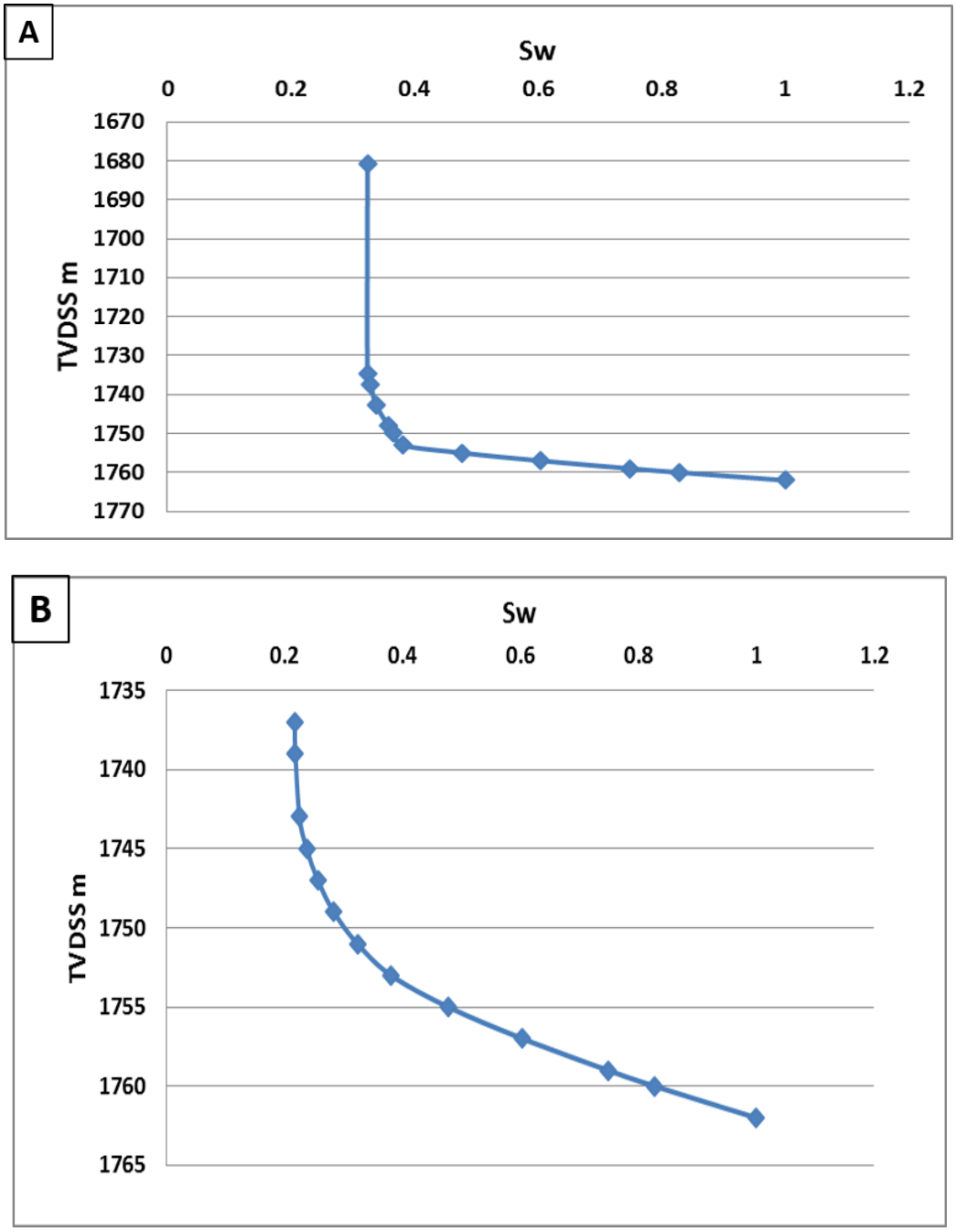

Figure B1. Saturation height functions used by the Field X operator for initialising the reservoir simulation model for a) A Zone and b) B Zone.

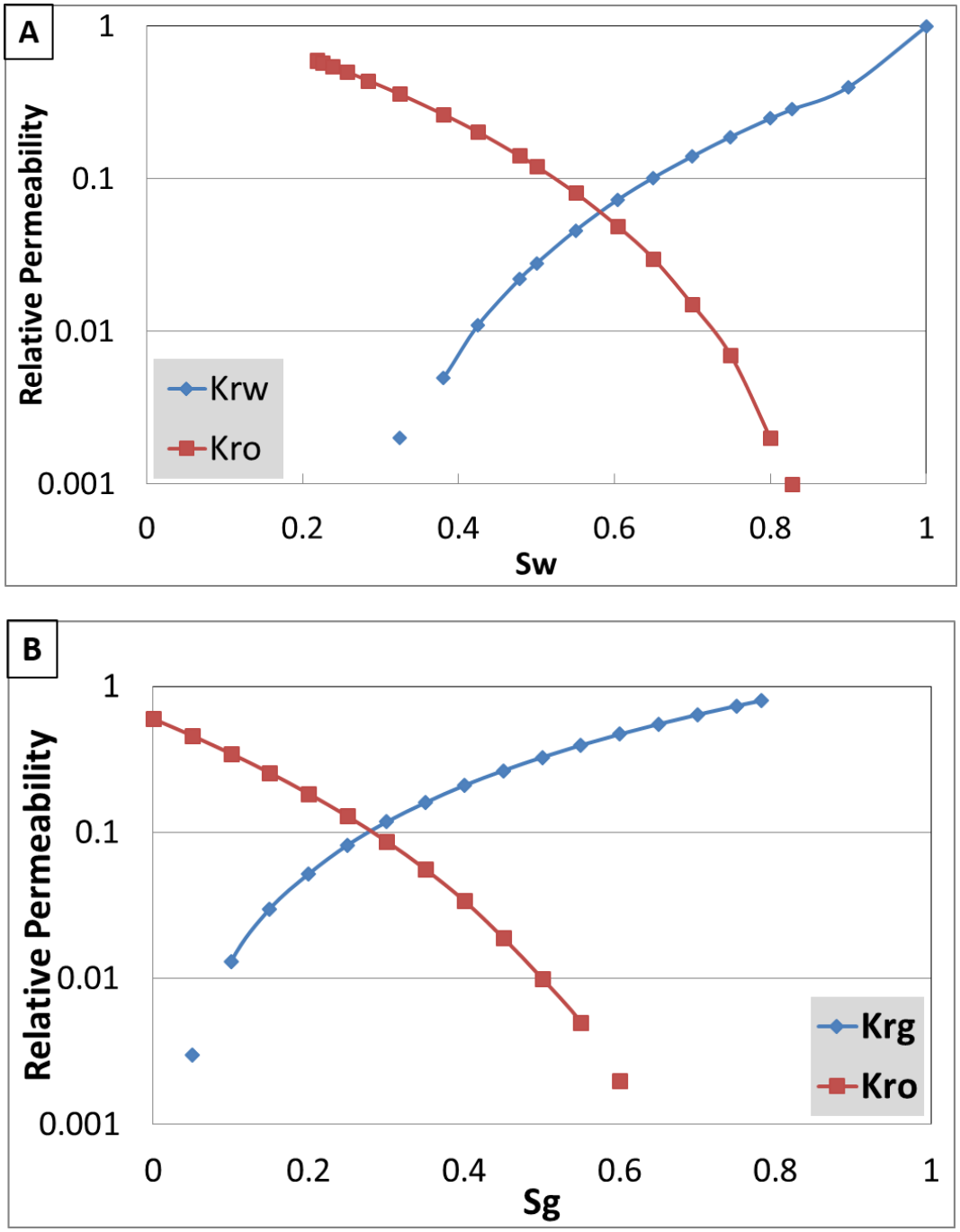

Figure B2. Relative permeability curves used by the Field X operator in the reservoir simulation model for a) water-oil and b) gas-oil. Here, the value of Corey coefficient used for oil is 3, and that for water is 3, the critical water saturation value is 21.8% and critical oil saturation value is 10%.

C. Field X Well Group 1 Simulated versus Historic Fluid Production Rates

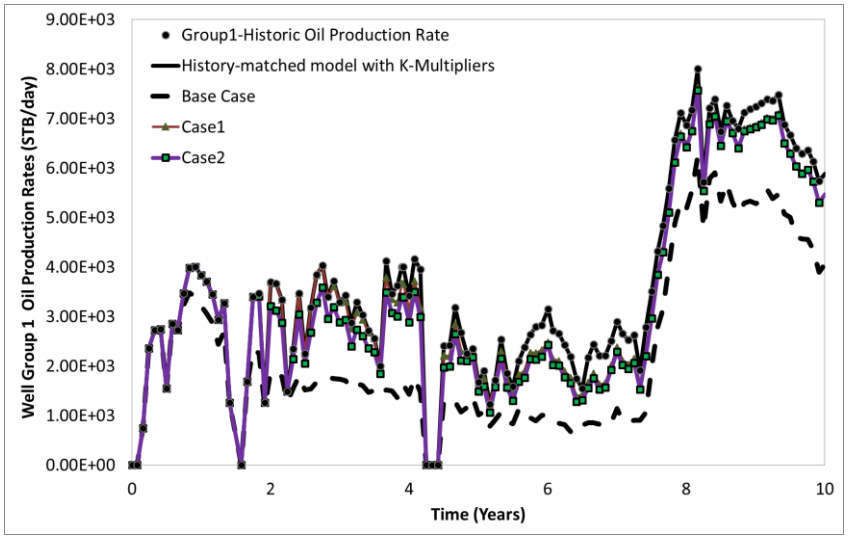

Figure C1. Oil production rate curves simulated for sector model containing Well Group1. Results compare geomodel scenarios before and after incorporating facies R2. Note that the history-matched simulation model curves and historic curves are overlapping. In Case 1, the K_v distribution from the base case was used for rock types R1 and R2. In Case 2 the K_v/K_h values estimated from the near-wellbore modelling and upscaling workflow were used for distributing K_v in rock type R2. STB refers to 'Stock Tank Barrels'.

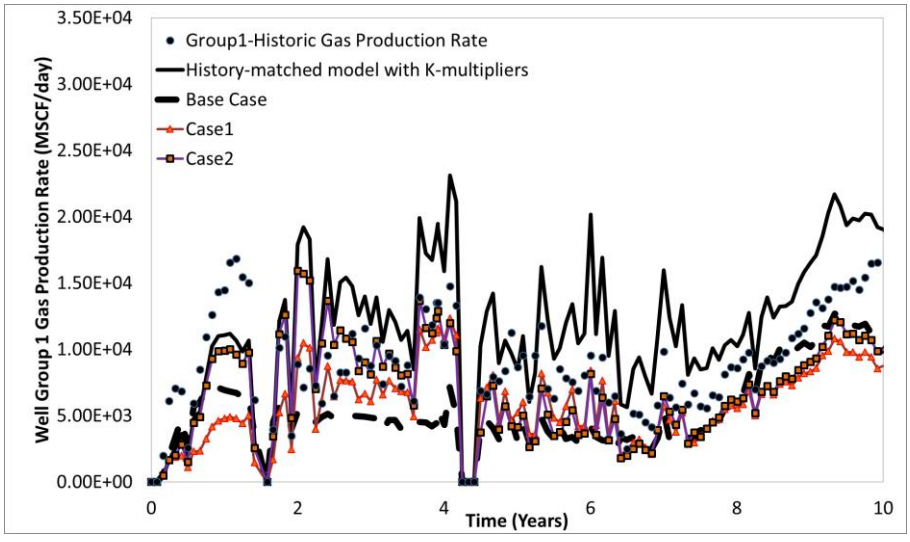

Figure C2. Gas production rate curves simulated for sector model containing Well Group1. Results compare geomodel scenarios before and after incorporating facies R2. Note the divergence between the historic and base case profiles. MSCF refers to 'Thousand Standard Cubic Feet'.

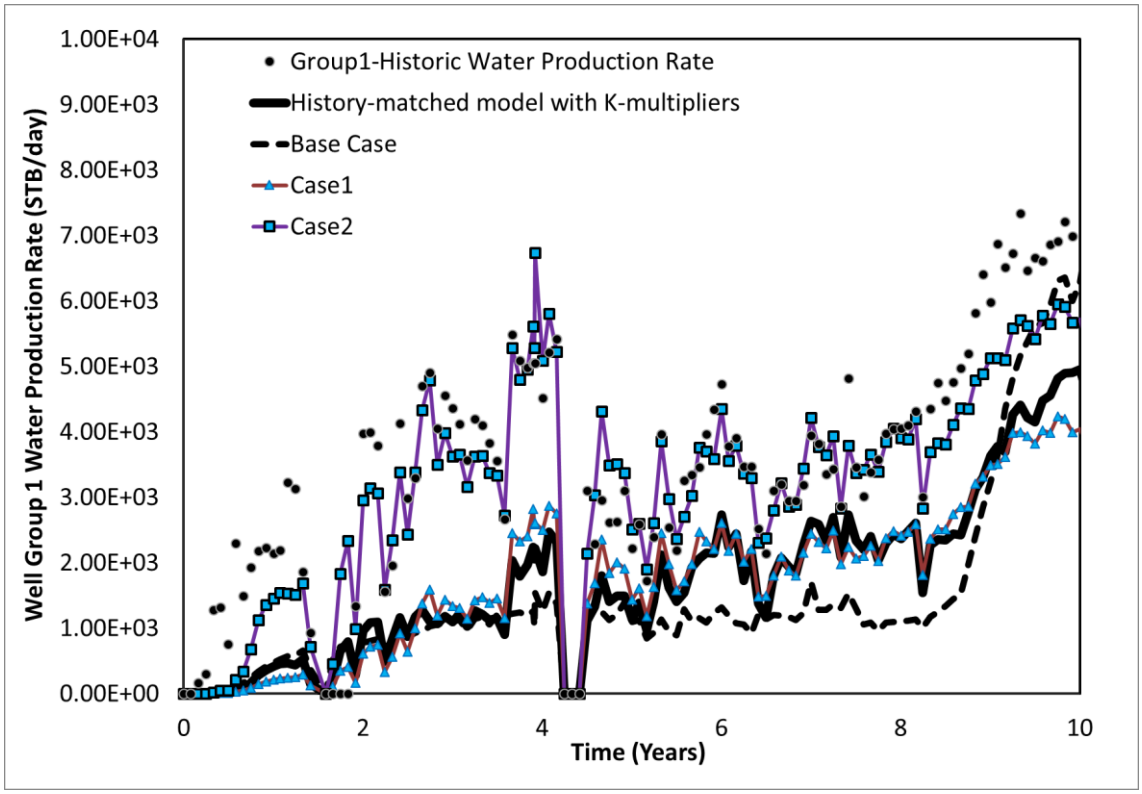

Figure C3. Water production rate curves simulated for sector model containing Well Group1. Results compare geomodel scenarios before and after incorporating facies R2. Note that the Case 2 simulation model curves are closer to the historic curves compared to the original 'history matched' simulation curves. STB refers to 'Stock Tank Barrels'.

D. Unit Conversion Tables

Unit	Multiplied by	Approximate Conversion Factor	equals	Unit
barrels of oil (bbl)	X	0.1589873	=	cubic metres (m3)
barrels of oil equivalent (boe)	X	5,658.53	=	cubic feet (f3) of natural gas
cubic feet (f3)	X	0.02831685	=	cubic metres (m3)
cubic feet (f3) of natural gas	X	0.0001767	=	barrels of oil equivalent (boe)
pounds (lb)	X	0.45359237	=	kilograms (kg)
kilograms (kg)	X	2.2046	=	pounds (lb)
feet (ft)	X	0.3048	=	meters (m)
inches (in)	X	2.54	=	Centimeters (cm)
square feet (ft2)	X	0.09290304	=	square meters (m2)
square inches (in2)	X	6.4516	=	square centimeters (cm2)
Psi	X	6.89476	=	kpascal

$$Specific\ gravity = \frac{141.5}{131.5 + \ ^\circ API}$$

BIBLIOGRAPHY

AARNES, J. E., KROGSTAD, S. & LIE, K. 2008. Multiscale mixed/mimetic methods on corner-point grids. *Computational Geosciences*. doi:10.1007/s10596-007-9072-8.

AGARWAL, R. G. 1980. A new method to account for producing time effects when draw-down type curves are used to analyse pressure buildup and other test data. *Society of Petroleum Engineers of AIME,* SPE 9289.

AHARONOV, E., LARONNE, B. L., KARCZ, Z., TOUSSAINT, R., KADORI, M. & SAGY, A. 2012. *Large-scale distributions of sedimentary stylolites in carbonates: Field observations and emerging insights regarding evolution, strain and dissolution.* AAPG Search and Discovery Article #120034, Proceedings of AAPG Hedberg Conference Fundamental Controls on Flow in Carbonates, Saint-Cyr Sur Mer, Provence, France, July 8-13, 2012.

AHARONOV, E. & KATSMAN, R. 2009. Interaction between pressure solution and clays in stylolite development: Insights from modelling. *American Journal of Science*, 09/2009; 309:2009. DOI: 10.2475/07.2009.04.

AHARONOV, E. & ROTHMAN, D. H. 1996. Growth of correlated pore-scale structures in sedimentary rocks: A dynamical model. *Journal of Geophysical Research*, **101**, doi: 10.1029/95JB03209. issn: 0148-0227.

ALLEN, J. R. L. 1968. Current Ripples. Their relation to patterns of water and sediment motion. North-Holland Publishing Company, Amsterdam.

ALSHARHAN, A. S. & SADD, J. 2000. Stylolites in lower Cretaceous carbonate reservoirs. U.A.E. *Society of Economic Paleontology and Mineralogy Special Publication*, **69**, 185–207.

ALSHARHAN, A. S. 1990. Geology and reservoir characteristics of Lower Cretaceous Kharaib Formation in Zakum Field, Abu Dhabi, United Arab Emirates. *In:* Brooks, J. (ed), *Classic Petroleum Provinces*. Geological Society Special Publications, **50**, 299–316.

AMAEFULE, J. O., ALTUNBAY, M., TIAB, D., KERSEY, D. G., & KEELAN, D. K. 1993. Enhanced Reservoir Description: Using Core and Log Data to Identify Hydraulic

(Flow) Units and Predict Permeability in Uncored Intervals/Wells. Society of Petroleum Engineers. doi:10.2118/26436-MS.

AKBAR, M., VISSARPRAGADA, B., ALGHAMDI, A. H., ALLEN, D., HERRON, M., CARNEGIE, A., DUTTA, D., OLESEN, J.-R., CHOURASIYA, R. D., LOGAN, D., STEIF, D., NETHERWOOD, R., RUSSELL, S. D. & SAXENA, K. 2001. A snapshot of carbonate reservoir evaluation. *Oilfield Review,* **12**, 20-41.

AKBAR, M., PETRICOLA, M., WATFA, M., BADRI, M. A., CHARARA, M., BOYD, A., CASSELL, B., NURMI, R., DELHOMME, J.-P., GRACE, M., KENYON, B. & ROESTENBURG, J. W. 1995. Classic interpretation problems; evaluating carbonates. *Oilfield Review,* **7**, 38-57.

ATES, H., BAHAR, A., SALEM, S. E. A., CHARFEDDINE, M., & KELKAR, M. G. 2005. Ranking and Upscaling of Geostatistical Reservoir Models Using Streamline Simulation: A Field Case Study. Society of Petroleum Engineers. doi:10.2118/81497-PA.

BARNETT, A., WRIGHT, V. P. & KHANNA, M. 2010. Porosity Evolution in the Bassein Limestone of Panna and Mukta Field, Offshore Western India: Burial Corrosion and Microporosity Development. Proceedings of AAPG New Orleans**.**

BAYLY, B. 1986. A mechanism for development of stylolites, *Journal of Geology*, **94**, 431– 435.

BEAR, J. 1972. Dynamics of Fluids in Porous Media. Elsevier, New York.

BEGG, S. H., CARTER, R. R. & DRANFIELD, P. 1989. Assigning effective values to simulator gridblock parameters for heterogeneous reservoirs, *SPE Reservoir Engineering*, **4** (4), 455-463.

BLACKBOURN, G. A. 1990. Cores and core logging for geologists. Whitless Publishing, ISBN: 1-870325--25-7.

BOURDET, D. 2002. Well test analysis: The use of advanced interpretation models. Elsevier Science B. V.

BOWMAN, M. B. J., McCLURE, N. M. & WILKINSON, D. W. 1993. Petroleum Geology of Northwest Europe: Proceedings of the 4th Conference. *In:* J. R. Parker (ed) *Petroleum Geology '86 Ltd*. The Geological Society, London, 1513-1517.

BRAITHWAITE, C. J. R. 1989. Stylolites as open fluid conduits: *Marine and Petroleum Geology*, **6**, 93-96.

BRANDSÆTER, I., WIST, H. T., NÆSS, A., LIA, O., ARNTZEN, O.J., RINGROSE, P.S., MARTINIUS A.W. & LERDAHL, T.R. 2001. Ranking of stochastic realizations of complex tidal reservoirs using streamline simulation criteria. *Petroleum Geoscience*, **7**, 53-63.

BRAYSHAW, A. C., DAVIES, G. W. & CORBETT, P. W. M. 1996. Depositional controls on primary permeability and porosity at the bedform scale in fluvial reservoir sandstone. *In*: CARLING. P. A. AND DAWSON, M. R. (eds.) *Advances in Fluvial Dynamics and Stratigraphy*, 373-394.

BROMLEY, R. G. 1996. Trace Fossils. Biology, Taphonomy and Applications, 2nd ed. Chapman & Hall. ISBN 0 412 61480 4.

BRONS, F. & MARTING, V. E. 1961. The effect of restricted fluid entry on well productivity. *Journal of Petroleum Technology*. **13 (**2), 171-174.

BROUSTE, A., RENARD, F., GRATIER, J. & SCHMITTBUHL, J. 2006. Variety of stylolites' morphologies and statistical characterisation of the amount of heterogeneities in the rock. *Journal of Structural Geology*, **29**, 422-434, doi:10.1016/j.jsg.2006.09.014.

BRUSH, L. M. JR. 1965. Sediment sorting in alluvial channels. *In*: Middleton (ed.), *Primary sedimentary structures and their hydrodynamic interpretation*, Society of Economic Paleontologists and Mineralogists Special Publication, **12**, 25-33.

BUITING, J. J. 2011. Upscaling Saturation-Height Technology for Arab Carbonates for Improved Transition-Zone Characterization. Society of Petroleum Engineers. doi:10.2118/125492-PA.

BURCHETTE, T. P. 2012. Carbonate rocks and petroleum reservoirs: a geological perspective from the industry. *Geological Society of London*, Special Publications, **370**, doi 10. 1144/SP370. 14.

BURGESS, C. J. & PETER, C.K. 1985. Formation, Distribution, and Prediction of Stylolites as Permeability Barriers in the Thamama Group, Abu Dhabi, SPE paper 13698.

BURRUSS, R. C., CERCONE, K. R. & HARRIS, P. M. 1985. Timing of hydrocarbon maturation- Evidence from fluid inclusions in calcite cements, tectonics and burial history. *In:* Schneidermann, N. & Harris, P. M (eds) *Carbonate cements*. Tulsa: Society for Sedimentary Geology, SEPM special publication, **36**, 277-289.

CALVERT, S., & BALLAY, G. 2011. Basic logs unlock complex carbonate pore properties. Society of Petrophysicists and Well-Log Analysts. *SPWLA-2011-MM.*

CAMPBELL, C. V. 1967. Lamina, laminaset and bedset. *Sedimentology*, **8**, 7-26.

CEREPI, A., BARDE, J. & LABAT, N. 2003. High-resolution characterisation and integrated study of a reservoir formation: the danian carbonate platform in the Aquitaine Basin (France). *Marine and Petroleum Geology*, **20**, 1161-1183.

CHANDRA, V., CORBETT, P. W. M., HAMDI, H. & GEIGER, S. 2013. Improving Reservoir Characterisation and Simulation with Near Wellbore Modeling. *SPE Reservoir Evaluation & Engineering*, **16 (2)**,183-193, SPE Journal Paper 148104-PA.

CHILINGARIAN, G. V., TORABZADEH, J., RIEKE, H. H., METGHALCHI, M., & MAZZULLO, S. J. 1992. Interrelationships among surface area, permeability, porosity, pore size, and residual water saturation. *In:* Chilingarian, G.V., Mazzullo, S.J. & Rieke, H. H. (eds) *Carbonate Reservoir Characterization: A Geologic-Engineering Analysis, Part I*: Elsevier Publ. Co., Amsterdam, Developments in Petroleum Science, **30**, 379-397.

CHOQUETTE, P. W. & PRAY, L. C. 1970. Geologic Nomenclature and Classification of Porosity in Sedimentary Carbonates. *AAPG Bulletin*, **54** (2), 207-250.

CHRISTIE, M. A. & BLUNT, M. J. 2001. Tenth SPE comparative solution project: A comparison of upscaling techniques, *SPE Reservoir Evaluation & Engineering.* **4** (4), 308-317.

COLTER, V. S. & HARVARD, D. J. 1981. The Wytch Farm Oil Field, Dorset. *In:* ILLING, L.V. & HOBSON, G.D. (eds) *Petroleum Geology of the Continental Shelf of North-West Europe*. Heyden, London, 494–503.

CORBETT, P. W. M., GEIGER, S., BORGES, L., GARAYEV, M., & CAMILO, V. 2012. The third porosity system: understanding the role of hidden pore systems in well-test interpretation in carbonates. *Petroleum Geoscience*, **18**, 73-81,

CORBETT, P. W. M., GEIGER, S., BORGES, L., GARAYEV, M., GONZALEZ, J. G. & VALDEZ, C. 2010. Limitations in numerical well test modelling for fractured carbonate rocks. SPE paper 130252.

CORBETT, P. W. M. 2009. Petroleum Geoengineering: Integration of Static and Dynamic Models, SEG/EAGE Distinguished Instructor Series, **12**, 100. ISBN 978-1-56080-153-5.

CORBETT, P. W. M. & POTTER, D. K. 2004. Petrotyping: A basemap and atlas for navigating through permeability and porosity data for reservoir comparison and permeability prediction. Paper presented at International Symposium of the Society of Core Analysts, *SCA2004-30*.

CORBETT, P., ELLABAD, Y., MOHAMMED, K. & POSOSYAEV, A. 2003. Global hydraulic elements - elementary petrophysics for reduced reservoir modelling. Presented at the 65th EAGE Conference and Exhibition, paper F-26.

CORBETT, P., ANGGRAENI, S. & BOWEN, D. 1999. The use of the probe permeameter in carbonates- addressing the problems of permeability support and stationarity. *The Log Analyst*, **40** (5), 316-326.

CORBETT, P. W. M., JENSEN, J. L. & SORBIE, K. S. 1998. A review of up-scaling and cross-scaling issues in core and log data interpretation and prediction. *In*: Harvey, P. K. and Lovell, M. A. (eds) *Core-Log Integration*, Geological Society Special Publication, **136**, 9-16.

CORBETT, P. W. M., MESMARI, A. & STEWART, G. 1996. A method for using the naturally-occurring negative geoskin in the description of fluvial reservoirs, SPE Paper 36882.

CORBETT, P. W. M., STROMBERG, S. G., BRENCHLEY, P. J. & GEEHAN, G. 1994. Laminaset geometries in fine grained shallow marine sequences: core data from the Rannoch Formation (North Sea) and from outcrop data from the Kennilworth Member (Utah, USA) and the Bencliff Grit (Dorset, UK). *Sedimentology*, **41**, 729-745.

CORBETT, P. W. M. & JENSEN, J. L. 1993a. Application of probe permeametry to the prediction of two-phase flow performance in laminated sandstones (lower Brent Group, North Sea). *Marine and Petroleum Geology*, **10**, 335-346.

CORBETT, P. W. M. 1993b. *Reservoir characterisation of a laminated sediment. The Rannoch Formation Middle Jurassic, North Sea*. Unpubl. PhD thesis, Heriot-Watt University, Edinburgh.

CORBETT, P. W. M. & JENSEN, J. L. 1992a. Variation of reservoir statistics according to sample spacing and measurement type for some intervals in the Lower Brent Group. *The Log Analyst*, 22-41.

CORBETT, P. W. M. & JENSEN, J. L. 1992b. Estimating the mean permeability: how many measurements do we need? *First Break*, **10** (3). 10.3997/1365-2397.1992006.

CORBETT, P. W. M., RINGROSE, P. S., JENSEN, J. L., SORBIE, K. S. 1992c. Laminated clastic reservoirs; the interplay of capillary pressure and sedimentary architecture. 67th annual technical SPE conference, Washington DC, 4–7 October 1992. SPE 24699.

CORRE, B. P., THORE, V., FERAUDY, D. E. & VINCENT, G. 2000. Uncertainty Assessment for Project Evaluation and Risk Analysis, SPE European Petroleum Conference, 24-25 October 2000, Paris, France.

CORREIA, M., MASCHIO, C., SCHIOZER, D. J. & SANTOS, M. 2011. Upscaling Technique Applied to Naturally Fractured Carbonate Reservoirs. Society of Petroleum Engineers. doi:10.2118/143150-MS.

CREUSEN, A., MAAMARI, K. K., TULL, S., VAHRENKAMP, V., MOOKERJEE, A. & VAN RIJEN, M. F. J. 2007. Property Modelling Small Scale Heterogeneity of Carbonate Facies. Society of Petroleum Engineers. doi:10.2118/111451-MS.

DABEK, L. B. & KNEPP, R. 2011. *Bioturbation and its effects on permeability in wave-dominated shoreface rocks of the spring canyon member, Blackhawk Formation, Utah, USA.* AAPG Search and Discovery Article # 50425. Proceedings of AAPG Annual Convention and Exhibition, Houston, Texas, USA, April 10-13, 2011.

DAGAN, G. 1979. Models of groundwater flow in statistically homogeneous porous formations. *Water Re- sour Res* 15(1), 47–63.

DAVIES, D.K., WILLIAMS, B.P.J. & VESSELL, R.K. 1992. Models for Meandering and Braided Fluvial Reservoirs With Examples From the Travis Peak Formation, East Texas. 67th Annual Technical Conference and Exhibition of the Society of Petroleum Engineers, Washington.

DAWSON, W.C. 1988. Annual meeting of the American Association of Petroleum Geologists, Houston, TX, USA, 20 Mar 1988, CONF-880301.

DELHOMME, J. P., BEDFORD, J., COLLEY, N. M. & KENNEDY, M. C. 1996. Permeability and Porosity Upscaling in the Near-Wellbore Domain: The Contribution of Borehole Electrical Images. Society of Petroleum Engineers. doi:10.2118/36822-MS.

DESBARATS, A.J. 1993. Geostatistical analysis of inter well transmissivity in heterogeneous aquifers, *Water Re- sour Res* 2 (9), 1239-12461.

DEUTSCH., C. V. 2010. Estimation of Vertical Permeability in the McMurray Formation, Journal of Canadian Petroleum Technology, SPE Paper 142894.

DEUTSCH C.V. 2002. Geostatistical Reservoir Modeling. Oxford University Press.

DEUTSCH C.V. & JOURNEL A.G. 1998. GSLIB. Geostatistical Software Library and User's Guide. N.Y., Oxford University Press.

DIJK, P., BERKOWITZ, B. & BENDEL, P. 1999. Investigation of flow in water-saturated rock fractures using nuclear magnetic resonance imaging (NMRI). *Water Resources Research*, **35 (2)**, 347-360.

DRANFIELD, P., BEGG, S. H. & CARTER, R. R. 1987. Wytch Farm Oilfield: reservoir characterisation of the Triassic Sherwood Sandstone for input into reservoir simulation studies. *In:* BROOKS, J. AND GLENNIE, K. W. (eds) *Petroleum Geology of North West Europe,* Graham & Trotman, London, 149-160.

DREYER, T. SCHEIE, Å. & WALDERHAUG, O. 1990. Minipermeameter-based study of permeability trends in channel sand bodies. *The American of Petroleum Geologist Bulletin*, **74**, 359-374.

DROSER, M. L. & BOTTJER, D. J. 1986. A semiquantitative field classification of ichnofabric. *Journal of Sedimentary Research*, **56**, 558–559.

DRUMMOND, C. & SEXTON, D. 1998. Fractal structure of stylolites. *Journal of Sedimentary Research*, **68**, 8-10.

DUNHAM, R. J. 1962. Classification of Carbonate Rocks According to Depositional Texture. *In*: W.E. HAMM (ed), *Classification of Carbonate Rocks*, A Symposium. American Association of Petroleum Geologists, 108-121.

DYKSTRA, H. & PARSONS, R. L. 1950. The prediction of oil recovery by waterflooding. In Secondary Recovery of Oil in the United States, second edition, ed. 160-174. Washington, DC: API.

EBANKS, W. J. 1987. Geology in enhanced oil recovery. *In*: TILLMAN, R. W. AND WEBER, K. J. (eds), *Reservoir sedimentology*, SEPM Special Publication, **40**, 1-14.

EBNER, M., PIAZOLO, S., RENARD, F. & KOEHN, D. 2010. Stylolite interfaces and surrounding matrix material: Nature and role of heterogeneities in roughness and microstructural development. *Journal of Structural Geology,* **32**, 1070-1084, doi:10.1016/j.jsg.2010.06.014.

EHRENBERG, S. N., WALDERHAUG, O. & BJØRLYKKE, K. 2012. Carbonate porosity creation by mesogenetic dissolution: Reality or illusion? *AAPG Bulletin*, **96 (2)**, 217–233.

ELFENBEIN, C., RINGROSE, P. S. & CHRISTIE, M. 2005. Small-scale reservoir modeling tool optimizes recovery offshore Norway. *World Oil*, **226** (10), 45–50.

EMBRY, A. F. & KLOVAN, J. E. 1971. A late Devonian reef tract on northeastern Banks Island. *N. W. T. Bulletin. Canadian Petroleum Geology*. **19**, 730-781.

EREN, M. 2005. Origin of stylolite related fractures in Atoka bank carbonates, Eddy county, New Mexico, U.S.A. *Carbonates and Evaporites*, **20** (1), 42-49.

ESTEBAN, M. & TABERNER, C. 2003. Secondary porosity development during late-burial in carbonate reservoirs as a result of mixing and/or cooling of brines. *Journal of Geochemical Exploration*, **78–79**, 355–359.

ESTEBAN, M. & TABERNER, C. 2002. Reconstructing fluid flow evolution from compressional to extensional regimes. *Late corrosive fluids: a key factor for porosity formation and enlargement*. Proceedings of AAPG Hedberg Conference, Austin, 234.

EWING, R. E. & LAZAROV, R. D.1988. Adaptive Local Grid Refinement, SPE Paper 17806.

FLETCHER, R. A. & POLLARD, D. D. 1981, Anticrack model for pressure solution surfaces, *Geology*, **9**, 419– 424.

GAL, D., NUR, A. & AHARONOV, E. 1998. Stability analysis of a pressure-solution surface, *Geophysics Research Letters*, **25**, 1237– 1240.

GHAFOORI, M. R., ROOSTAERIAN, M. & SAJJADIAN, V. A. 2008. Secondary porosity; a key parameter controlling the hydrocarbon production in heterogeneous carbonate reservoirs (case study). SPWLA 49th Annual Logging Symposium, May 25-28, 2008. Edinburgh, Scotland: SPWLA.

GHEDAN, S. G., GUNNINGHAM, T. W., EHMAID, B. H., & AZER, S. R. 2002. Upscaling of Multimillion Cell Geological Model into a Practical Simulation Model of a Major Carbonate Oil Reservoir in Offshore Abu Dhabi. Society of Petroleum Engineers. doi:10.2118/78578-MS.

GIBBONS, K., HALVORSEN, C. & SIRING, E. 1993. Vertical and horizontal permeability variation within a sandstone reservoir based on minipermeameter measurements. *Marine and Petroleum Geology*, **10**, 325-334.

GLOVER, J.E. 1968. Significance of stylolites in dolomitic limestones: *Nature*, **217**, 835-836.

GOGGIN, D. J., THRASHER, R. L. & LAKE, L. W. 1988. A theoretical and experimental analysis of minipermeameter response including gas-slippage and high-velocity flow effects. *In Situ*, **12**, 79-116.

GOLDMAN, M.I. 1940. Stylolites. *Journal of Sedimentary Petrology*, **10**, 146-147.

GOMES, J. S., RIBEIRO, M. T., STROHMENGER, C. J., NEGAHBAN, S. & KALA, M. Z. 2008. Carbonate reservoir rock typing- The link between geology and SCAL. SPE Paper 118284.

GOSWAMI B. G., SINGH H., BHATNAGAR A. K., SINHA A. K. & SINGH R. R. 2007. *Petroleum Systems of the Mumbai Offshore Basin, India.* AAPG Search and Discovery Article #10154. Proceedings of AAPG Annual Convention, Long Beach California, April 1-4, 2007.

GREDER, H. N., DIVER, P. Y., DANQUIGNY, S. & PELLERIN, F. M. 1996. Determination Of Permeability Distribution At Log Scale In Vuggy Carbonates. Society of Petrophysicists and Well-Log Analysts.

GRINGARTEN, A. C. 2008. From straight lines to deconvolution: The evolution of the state of the art in well test analysis. *SPE Reservoir Evaluation & Engineering*. **11** (1), 41- 62. doi.org/10.2118/102079-PA.

GRINGARTEN, A. C. 1986. Computer-aided well test analysis. SPE Paper 14099, presented at the SPE International Meeting on Petroleum Engineering, Beijing, 17-20 March. DOI: 10.2118/14099-MS.

GRINGARTEN, A. C., BOURDET, D., LANDEL, P. A. & KNIAZEFF, V. 1980. A comparison between different skin and wellbore storage type-curves for early-time transient analysis. SPE Paper 8205, September 1979.

GULBRANSEN, A. F., HAUGE, V. L. & LIE, K. 2010. A multiscale mixed finite-element method for vuggy and naturally fractured reservoirs. *SPE Journal*, 395-403.

HALDORSEN, H. H. 1986. Simulator parameter assignments and the problem of scale in reservoir engineering, *In*: LAKE, L. W. AND CAROLL, H. B. (eds) *Reservoir Characterization*. Academic Press, Orlando, 293-340.

HALVORSEN, C. & HURST, A. 1990. Principles practice and applications of laboratory minipermeametry. *In*: WORTHINGTON (ed), *Advances in Core Evaluation*, 521-549.

HAMDI, H. 2012. Illumination of channelised fluvial reservoirs using geological well-testing and seismic modelling, Unpublished PhD Thesis, Heriot-Watt University, UK.

HANOR, J. S. 1987. Origin and migration of subsurface sedimentary brines. SEPM Short Course Lecture Notes no. 21. Tulsa: Society of Economic Paleontologists and Mineralogists. ISBN 0 918985 75 7.

HAY, R. L. & REEDER, R. J. 1978. Calcretes of Olduvai Gorge and the Ndolanya Beds of northern Tanzania. *Sedimentology*, **25**, 649-673.

HEYDARI. E. 2000. Porosity loss, fluid flow, and mass transfer in limestone reservoirs: Application to the Upper Jurassic Smackover Formation, Mississippi. *AAPG Bulletin*, **84**, 100-118.

HEYDARI, E. & MOORE, C. H. 1989, Burial diagenesis and thermochemical sulphate reduction, Smackover Formation, southeastern Mississippi salt basin. *Geology*, **17**, 1080-1084.

HOGG, A. J. C., EVANS, I. J., HARRISON, P. F., MELING, T., SMITH, G. S., THOMPSON, S. D. & WATTS, G. F. T. 1999. Reservoir management of the Wytch Farm Oil Field, Dorset, UK: providing options for growth into later field life. *Petroleum Geology Conference series*, **5**, 1157-1172.

HOLLIS, C., VAHRENKAMP, V., TULL, S., MOOKERJEE A., TABERNER, C. & HUANG, Y. 2010. Pore system characterisation in heterogeneous carbonates: An alternative approach to widely-used rock-typing methodologies. *Marine and Petroleum Geology*, **27**, 772-793.

HONARPOUR, M.M., CHILINGARIAN, G.V. & MAZZULLO, S.J. 1992. Permeability and relative permeability of carbonate reservoirs, *In:* CHILINGARIAN, G.V., MAZZULLO, S.J. AND RIEKE, H.H. (eds) *Carbonate Reservoir characterization: A Geologic-Engineering Analysis, Part I,* Elsevier Publ. Co., Amsterdam, Developments in Petroleum Science, **30**, 399-416.

HURST, A. & GOGGIN, D. 1995. Probe permeability: An overview and bibliography, *AAPB Bulletin*, **79**, 463-473.

HURST, A. 1993. Sedimentary flow units in hydrocarbon reservoirs: some shortcomings and a case for high-resolution permeability data. *In*: FLINT, S. AND BRYANT, I. D. (eds) *The geological modelling of hydrocarbon reservoirs and outcrop*

analogues, Special Publication Number **15** of the International Association of Sedimentologists, 191-204.

JACKSON, M. D., YOSHIDA, S., MUGGERIDGE, A. M. & JOHNSON, H. D. 2005. Three-dimensional reservoir characterization and flow simulation of heterolithic tidal sandstones. *AAPG Bulletin*, **89** (4), 507 – 528,

JACKSON, M. D., MUGGERIDGE, A. YOSHIDA, H. S. & JOHNSON, H. D. 2003. Upscaling permeability measurements within complex heterolithic tidal sandstones. *Mathematical Geology*, **35** (5), 499–520.

JACKSON, M. D., YOSHIDA, S., JOHNSON, H.D., MUGGERIDGE, A.H., NÆSS, A. & RINGROSE, P. S. 1999. Upscaling complex three-dimensional bedfoamscale sedimentary structures within tidal sandstone reservoirs. *In:* LIPPARD, S. J., NÆSS, A., SINDING-LARSEN, R. (eds) *Proceedings of 5th Annual Conference on the International Association for Mathematical Geology*. Trondheim, Norway, 6–11.

JACKSON, J. A. & BATES, R. L. (eds). 1997. Glossary of geology. 4th edition. American Geological Institute, Alexandria, USA.

JAMESON, J. 1994. Models of Porosity Formation and Their Impact on Reservoir Description, Lisburne Field, Prudhoe Bay, Alaska. *AAPG Bulletin*, **78** (11), 1651–1678.

JENSEN, J. L. 1990. A model for small scale permeability measurement with applications to reservoir description. SPE paper no. 20265, presented at the 7th SPE/DOE Symposium on EOR, Proceedings, Society of Petroleum Engineers, Dallas, 891-900.

JIAN, F. X., CHORK, C. Y., TAGGERT, I. J., MCKAY, D. M. & BARTLETT, R. M. 1994. A genetic approach to prediction of petrophysical properties. *Journal of Petroleum Geology*, **17** (1), 71-88.

JODRY, R. L. 1992. Pore geometry of carbonate rocks and capillary pressure curves (basic geologic concepts). *In:* CHILINGARIAN, G.V., MAZZULLO, S.J. & RIEKE, H. H. (eds) *Carbonate Reservoir Characterization: A Geologic-Engineering Analysis, Part I*, Elsevier Publ. Co., Amsterdam, Developments in Petroleum Science, **30**, 331-377.

JOHNSON N. M. & DREISS, S. J. 1989. Hydrostratigraphic interpretation using indicator geostatistics. *Water Resources Research*, **25**, 2501-2510.

JOURNEL, A. & HUIJBREGTS, C. J., 1978, Mining Geostatistics. Academic Press, London, 600.

KAPLAN, M. Y. E. 1976. Origin of stylolites. Dokl. Acad. Sci. USSR, Earth Science Section **211**, 205-207.

KARCZ, Z., MUTLU, O., ALBERT, R. & DEGRAFF, J. The Formation and Propagation of Stylo-Fractures. 2011. *Geophysical Research Abstracts,* **13**, EGU2011-7930, 2011, EGU General Assembly 2011.

KARCZ, Z. & C. H. SCHOLZ. 2003. The fractal geometry of some stylolites from the Calcare Massiccio Formation, Italy. *Journal of Structural Geology*, **25**, 1301– 1316.

KAZEMI, A., CORBETT, P. W. M. & WOOD, R. 2012. New approach for geomodeling and dynamic calibration of carbonate reservoirs using porosity determined system (PODS). Presented at 74th EAGE conference and Exhibition, Copenhagen, Denmark, 4-7 June 2012.

KAZEMI, A., SHAIKHINA, D. S., PICKUP, G. E. & CORBETT, P. W. M. 2012. Comparison of Upscaling Methods in a Heterogeneous Carbonate Model. Society of Petroleum Engineers. doi:10.2118/154499-MS.

KEEHM, Y. & MUKERJI, T. 2004. Permeability And Relative Permeability From Digital Rocks: Issues On Grid Resolution And Representative Elementary Volume. Society of Exploration Geophysicists.

KHALILI, A. D., ARNS, J. Y., HUSSAIN, F., CINAR, Y., PINCZEWSKI, W. & ARNS, C. H. 2013. Permeability Upscaling for Carbonates From the Pore Scale by Use of Multiscale X-Ray-CT Images. Society of Petroleum Engineers. doi:10.2118/152640-PA

KOEHN, D., EBNER, M., RENARD, F., TOUSSAINT, R. & PASSCHIER, C. W. 2012. Modelling of stylolite geometries and stress scaling. Earth and Planetary Science Letters, **341–344**, 104–113, http://dx.doi.org/10.1016/j.epsl.2012.04.046.

KOEPNICK, R.B. 1984. Distribution and Vertical Permeability of Stylolites within a Lower Cretaceous Carbonate Reservoir, Abu Dhabi, United Arab Emirates. Stylolites and Associated Phenomena: Relevance to Hydrocarbon Reservoirs, Abu Dhabi Natl. Reservoir Research Foundation (1984) 261-78.

KOLTERMANN, C. E. & GORELICK, S. M. 1996. Heterogeneity in sedimentary deposits: A review of structure imitating, process-imitating and descriptive approaches. *Water Resources Research*, **32** (9), 2617-2658.

KULANDER, B.R, BARTON, C.C. & DEAN, S.L. 1979. The application of fractography to core and outcrop fracture investigations: Morgantown, West Virginia, DOE METC/ SP-7913, 174.

LAMBERT, L., DURLET, C., LOREAU, J. & MARNIER, G. 2006. Burial dissolution of micrite in Middle East carbonate reservoirs (Jurassic–Cretaceous): keys for recognition and timing. *Marine and Petroleum Geology*, **23**, 79-92.

LARONNE, B.L., AHARONOV, E., KARCZ, Z., KADURI, M. & TOUSSAINT, R. 2014. Sedimentary stylolite networks and connectivity in Limestone: Large-scale field observations and implications for structure evolution. *Journal of Structural Geology*, **63**, 106-123.

LONOY, A. 2006. Making sense of carbonate pore systems. *AAPG Bulletin*, **90**, 1381-1405.

LUCIA, F. J. 1999. Carbonate reservoir characterisation. Springer, Germany.

LUCIA, F. J. 1995. Rock-fabric/petrophysical classification of carbonate pore space for reservoir characterisation. *AAPG Bulletin*, **79**, 1275-1300.

LUCIA, F. J. 1983. Petrophysical parameters estimated from visual description of carbonate rocks: a field classification of carbonate pore space. *Journal of Petroleum Technology*, **35**, 626-637.

MACHEL, H.G. 2003. Dolomites and dolomitization. *In:* MIDDLETON, G.V. (ed) *Encyclopedia of Sediments and Sedimentary Rocks*, Kluwer Academic Publishers, Dordrecht, 235–243.

MAZZULLO, L. J. & HARRIS, E. M. 1991. An overview of dissolution porosity development in the deep-burial environment, with examples from carbonate reservoirs in the Permian Basin. *In:* CANDELLARIA, M.E (ed) *Permian Basin Plays-Tomorrow's Technology Today*. Geological Society Publication, **91-89**, 125-138.

MAZULLO, S. J. 2004. Overview of porosity evolution in carbonate reservoirs. *Kansas Geological Society Bulletin*, **79**, 1-2.

MCKEE, E. D. 1965. Experiments on ripple lamination. *In:* MIDDLETON G.V. (ed) *Primary sedimentary structures and their hydrodynamic interpretation*, Society of Economic Paleontologists and Mineralogists Special Publication, **12**, 66-83.

MCKENNA S. A., & POETER, E. P. 1994. Simulating geological uncertainty with imprecise data for groundwater flow and advective transport modelling. *In:* YARUS, Y. M., and Chambers, R. L. (ed), *Stochastic Modeling and Geostatistics Principles, Methods and Case Studies*, AAPG Computational. Geol, **3**, 241-248.

MCKENNA S. A. & POETER, E. P. 1995. Field example of data fusion in site characterization, *Water Resources Research*, **31**, 3229-3240.

MCKIE, T., AGGETT, J. & HOGG, A. J. C. 1998. Reservoir architecture of the upper Sherwood Sandstone, Wytch Farm field, southern England. *Geological Society, London, Special Publications*, **133 (1)**, 399-406.

MCKINLEY, J. M., LLOYD, C. D. & RUFFELL, A. H. 2004. Use of variography in permeability characterization of visually homogeneous sandstone reservoirs with examples from outcrop studies. *Mathematical Geology*, **36**, 761-779.

MILLIKEN, K. L. 2003. Diagenesis. *In:* MIDDLETON G. V. (ed) *Encyclopedia of Sediments and Sedimentary Rocks*, Kluwer Academic Publishers, Dordrecht, 214–219.

MONICARD, R. P. 1980. Properties of reservoir rocks: Core analysis. Institut Francais du Pétrole Publications, Editions Technip ISBN: 2-7108-0387-9.

MOORE, C. H. 1989. Carbonate diagenesis and porosity. Elsevier, *Developments in Sedimentology*, **46**, 338.

MOORE, C. H. & DRUCKMAN, Y. 1981. Burial diagenesis and porosity evolution, Upper Jurassic Smackover, Arkansas and Louisiana. *AAPG Bulletin*, **65**, 597-628.

MORTON, K., THOMAS, S., CORBETT, P. W. M. & DAVIES, D. 2002. Detailed analysis of probe permeameter and interval pressure transient test permeability measurements in a heterogeneous reservoir. *Petroleum Geoscience*, **8**, 209–216.

MOSHIER, S. O. 1989. Development of microporosity in a micritic limestone reservoir, Lower Cretaceous, Middle East. *Sedimentary Geology*, **63**, 217–240.

NELSON, R. A. 1981. Significance of Fracture sets associated with stylolite zones. *AAPG Bulletin*, **65 (11)** (1981), 217–2425.

NEWELL, A. J. 2006. Calcrete as a source of heterogeneity in Triassic fluvial sandstone aquifers (Otter Sandstone Formation, SW England). *Geological Society, London*, Special Publications, **263**, 119-127.

NICHOLS, G. 2009. Sedimentology and Stratigraphy. Blackwell Science Ltd, Oxford.

NORDAHL, K., & RINGROSE, P. S. 2008. Identifying the representative elementary volume for permeability in heterolithic deposits using numerical rock models. *Mathematical geosciences*, **40 (7)**, 753-771.

NORDAHL, K., RINGROSE, P. S. & WEN, R. 2005. Petrophysical characterization of a heterolithic tidal reservoir interval using a process-based modelling tool. *Petroleum Geoscience*, **11**(1), 17–28.

NORDAHL, K. 2004. A petrophysical evaluation of tidal heterolithic deposits: application of a near wellbore model for reconciliation of scale dependent well data. Ph.D. thesis. Norwegian University of Science and Technology, Trondheim

OATES, M., MISHRA, G., SULTANA, N. & NATH, G. 2012. Resolving a permeability mismatch in a mature carbonate field. Proceedings of SPE Oil and Gas India Conference and Exhibition, Mumbai, March 2012, SPE Paper 155458.

PANFILI, P., COMINELLI, A., CALABRESE, M., ALBERTINI, C., SAVITSKY, A. & LEONI, G. 2012. Advanced Upscaling for Kashagan Reservoir Modeling. Society of Petroleum Engineers. doi:10.2118/146508-PA.

PEACEMAN, D.W. 1977. Interpretation of well – block pressures in numerical reservoir simulation. SPE - AIME 52nd Annual Fall Technical Conference and Exhibition, Denver, Colorado, Oct. 1977. SPE paper 6893.

PEACOCK, D. C. P. & AZZAM, I. N. 2006. Development and scaling relationships of a stylolite population. *Journal of Structural Geology*, **28**, 1883-1889, doi:10.1016/ j.jsg.2006.04.008.

PICKUP, G. E., STEPHEN, K. D., MA, J., ZHANG, P., & CLARK, J. D. 2005. Multi-stage upscaling: selection of suitable methods. In: Das, D. B. and Hassanizadeh, S. M., eds. Upscaling multiphase flow in porous media: from pore to core and beyond. Dordrecht: Springer.

PICKUP, G. E., RINGROSE, P. S. & SHARIF, A. 2000. Steady-state upscaling: from lamina-scale to full-field model. *SPE Journal*, **5**(2), 208–217.

PICKUP, G. E., & STEPHEN, K. D. 2000. Assessment of steady-state scale-up for small-scale geological models. *Petroleum Geoscience*, **6(3)**, 203-210.

PICKUP, G. E. & SORBIE, K. S. 1996. The scaleup of two-phase flow in porous media using phase permeability tensors. *SPE Journal*, **1**(4), 369–382.

PICKUP, G. E. & CARRUTHERS, D. 1996. Effective flow parameters for 3D reservoir simulation. Proceedings of European 3-D Reservoir Modelling Conference, Stavanger, Norway. SPE Paper 35495.

PICKUP, G. E., RINGROSE, P. S., CORBETT, P. W. M., JENSEN, J. L. & SORBIE, K. S. 1995. Geology, geometry and effective flow. *Petroleum Geoscience*, **1**(1), 37–42.

PICKUP, G. E., RINGROSE, P. S., FORRESTER, M. M., JENSEN, J. L., & SORBIE, K. S. 1994. The Geopseudo Atlas: Geologically Based Upscaling of Multiphase Flow. Society of Petroleum Engineers. doi:10.2118/27565-MS.

POPOV, P., QIN, G., BI, L., EFENDIEV, Y., EWING, R. E., & LI, J. 2009. Multiphysics and Multiscale Methods for Modeling Fluid Flow Through Naturally Fractured Carbonate Karst Reservoirs. Society of Petroleum Engineers. doi:10.2118/105378-PA.

PRASAD, R. S. S., AL-ATTAR, E. H., & AL-JASMI, A. K. 1996. Reservoir Permeability Upscaling Indicators From Welltest Analysis. Society of Petroleum Engineers. doi:10.2118/36175-MS

RADKE, B. M. & MATHIS, R. L. 1980. On the formation and occurrence of saddle dolomite. *Journal of Sedimentary Petrology*. **50**, 1149-68.

RAMEY, H. J. JR. 1992. Advances in practical well-test analysis. *Journal of Petroleum Technology*, **44** (6): 650-659. SPE-20592-PA. DOI: 10.2118/20592-PA.

RAMEY, H. J. JR. 1982. Pressure transient testing. *Journal of Petroleum Technology*, **34**, (7), 1407-1413.

RAMEY, H. J. JR. 1980. Practical use of modern well test analysis. Pressure transient testing methods, Reprint Series. Richardson, Texas: SPE, **14**, 46-67.

RAMEY, H. J. JR. 1970. Short-time well test data interpretation in the presence of skin effect and wellbore storage. *Journal of Petroleum Technology*, **22** (1): 97-104. SPE-2336-PA. DOI: 10.2118/2336-PA.

READING, H. 1996. Sedimentary environments: Processes, Facies and Stratigraphy. Blackwell Science Ltd, Oxford.

REBELLE, M., UMBHAUER, F., & POLI, E. 2009. Pore to Grid Carbonate Rock-Typing. International Petroleum Technology Conference. doi:10.2523/13120-MS.

REINECK, H. E. & SINGH, I. B. 1980. Depositional sedimentary environments. With reference to terrigenous clastics. Second version. Springer-Verlag.

RENARD, P, H. & MARSILY, D. E. G. 1997. Calculating equivalent permeability: a review. *Advances in Water Resources*, **20** (5-6), 253-278.

RENARD, F., J. SCHMITTBUHL, J. P. GRATIER, P. MEAKIN. & E. MERINO. 2004. Three-dimensional roughness of stylolites in limestones. *Journal of Geophysical Research*, **109**, B03209, doi:10.1029/2003JB002555.

RINGROSE, P.S., ALLARD, W., MARTINIUS, A. W. & JOSTEIN, A. 2008. Multiscale geological reservoir modeling in practice. *Geological Society, London*, Special Publications, **309**, 123-134, doi:10.1144/SP309.9.

RINGROSE, P.S., NORDAHL, K., & WEN, R. 2005. Vertical permeability estimation in heterolithic tidal deltaic sandstones. *Petroleum Geoscience*, **11** (1), 29-36.

RINGROSE, P. S., SKJETNE, E. & ELFENBEIN, C. 2003. Permeability estimation functions based on forward modeling of sedimentary heterogeneity. SPE paper 84275, presented at SPE Annual Technical Conference and Exhibition, Denver, USA, October 5–8.

RINGROSE, P. S. 2007. Myths and Realities in Upscaling Reservoir Data and Models. Society of Petroleum Engineers. doi:10.2118/106620-MS.

RITZI, R. W., DOMINIC, JR., D. F., BROWN, N. R., KAUSCH, K. W., MCALENNEY, P. J. & BASIAL, M. J. 1995. Hydrofacies distribution and correlation in the Miami Valley aquifer system, *Water Resources Research*, **31**, 3271-3281.

ROSALIND, A. & YILDIZ T. 2001. Transient well index for numerical well test analysis. SPE Paper 71572.

RUBIN, D. M. 2003. Cross-stratification. *In:* MIDDLETON, G. V. (ed) *Encyclopedia of Sediments and Sedimentary Rocks*. Kluwer Academic Publishers, Dordrecht, The Netherlands, 170–173.

RUBIN, D. M. 1987. Cross-bedding, bedforms, and paleocurrents. *Concepts in Sedimentology and Paleontology*. Special Publication 1. Society of Economic Paleontologists and Mineralogists, Tulsa, Oklahoma.

SAMANTRAY, A. K., DASHTI, Q. M., MA, E. & KUMAR, P. S. 2006. Upscaling and 3D Streamline Screening of Several Multimillion-Cell Earth Models for Flow Simulation. Society of Petroleum Engineers. doi:10.2118/81496-PA.

SATTLER, U., ZAMPETTI, V., SCHLAGER, W. & IMMENHAUSER, A. 2004. Late leaching under deep burial conditions: a case study from the Miocene Zhujiang Carbonate Reservoir, South China Sea. *Marine and Petroleum Geology*, **21**, 977-992.

SIMONS, D. B., RICHARDSON, E. V. & NORDIN, C. F. JR. 1965. Sedimentary structures generated by flow in alluvial channels. *In:* MIDDLETON, G. V. (ed) *Primary sedimentary structures and their hydrodynamic interpretation*, Society of Economic Paleontologists and Mineralogists Special Publication, **12**, 34-52.

SKALINSKI, M. & KENTER, J. A. M. 2014. Carbonate petrophysical rock typing: Integrating geological attributes and petrophysical properties while linking with

dynamic behaviour. *Fundamental Controls on Fluid Flow in Carbonates: Current Workflows to Emerging Technologies*. Geological Society, London, Special Publications, **406**, doi: 10.1144/SP406.6

SOETAERT, K., HERMAN, P. M. J. & MIDDELBURG, J. J. 1996. A model of early diagenetic processes from the shelf to abyssal depths. *Geochimica et Cosmochimica Acta*, **60** (6), 1019–1040.

SOUTHARD, J. B. & BOGUCHWAL, L. A. 1973. Flume experiments on the transition from ripples to lower flat bed with increasing sand size. *Journal of Sedimentary Petrology*, **43** (4), 1114-1121.

STEPHEN, K. D., CLARK, J. D. & PICKUP, G. E. 2002. Modeling and flow simulations of a North Sea turbidite reservoir: sensitivities and upscaling. Paper presented at SPE European Petroleum Conference, Aberdeen, United Kingdom.doi:10.2118/78292-MS.

STOW, D. A. V., READING, H. G. & COLLINSON, J. D. 1996. Deep seas. *In:* READING, H. G. (ed) *Sedimentary environments: processes, facies and stratigraphy*. 3rd edition. Blackwell Publishing, Oxford, UK, 395–453.

SUZUKI, K., ASADA, J., YOSHIDA, K. & NOMURA, M. 2004. Accelerated History Matching Through Process Independent Scale-up Techniques in a Giant Carbonate Reservoir. Society of Petroleum Engineers. doi:10.2118/87012-MS.

THOMAS, A. R, SUSAN, D. A, GREG, P. P., WILLIAM, M. D. & ROBERT, M. M. *Stylolitization and Resulting Porosity Reduction in the Norphlet Formation, Offshore Alabama.* AAPG Search and Discovery Article #90928©1999.

TIAB, D. & DONALDSON, E. C. 1996. Petrophysics: Theory and practice of measuring reservoir rock and fluid transport properties. Gulf Publishing Company, Houston, Texas, ISBN: 0-88415-634-6.

TORO-RIVERA M. L. E., CORBETT P. W. M., & GEORGE S. 1994. Well test interpretation in a heterogeneous braided fluvial reservoir. SPE Paper 28828.

TORSÆTER, O. & ABTAHI, M. 2003. Experimental reservoir engineering, laboratory workbook. Dept. of Petroleum Eng. and Applied Geophysics, Norwegian University of Science and Technology.

TUCKER, M. & WRIGHT, V. 1990. Carbonate sedimentology. Blackwell Science Ltd, Oxford.

VAN DER LAND, C., WOOD, R. A., WU, K., VAN DIJKE, MIJ., JIANG, Z, CORBETT, P. W. M. & COUPLES, G. D. 2013. Modelling the permeability evolution of carbonate rocks. *Marine and Petroleum Geology*. **48**, 1-7, doi:10.1016/j.marpetgeo.2013.07.006.

WALLS, R. A.; HARRIS, W. B. & NUNAN, W. E. 1975, Calcareous crust (caliche) profiles and early subaerial exposure of Carboniferous carbonates, northeastern Kentucky. *Sedimentology*, **22**, 417-440.

WANG, F. P., LUCIA, F. J., & KERANS, C. 1994. Critical Scales, Upscaling, and Modeling of Shallow-Water Carbonate Reservoirs. Society of Petroleum Engineers. doi:10.2118/27715-MS.

WARDLAW, N. C. 1996. Factors affecting oil recovery from carbonate reservoirs and prediction of recovery. in G. V. CHILINGARIAN, S.J. MAZZULLO, and H.H. RIEKE, eds., Carbonate Reservoir Characterization: A geologic-Engineering Analysis, Part II: Elsevier Publ. Co., Amsterdam, Developments in Petroleum Science, **44**, 867-903 .

WASSERMAN M. L. 1987. Local grid refinement for three-dimensional simulators. SPE Paper 16013.

WEBER, K. J. 1982. Influence of common sedimentary structures on fluid flow in reservoir models. *Journal of Petroleum technology*, **44**, 665-672.

WEISSMANN, G. S. & FOGG, G. E. 1999. Multi-scale alluvial fan heterogeneity modeled with transition probability geostatistics in a sequence stratigraphic framework. *Journal of Hydrology*, **226** (1), 48-65.

WEN, R., MARTINIUS, A. W., NÆSS, A. & RINGROSE, P. 1998. Three-dimensional simulation of small-scale heterogeneity in tidal deposits– a process-based stochastic simulation method. In: Buccianti, A., G. Nardi, and R. Potenza [eds.], Proceedings of

the 4th Annual Conference of the International Association of Mathematical Geosciences, Ischia, Italy, 129–134.

WEN, R. 1997. Modeling and simulation of small-scale sedimentary heterogeneity in tidal deposits. Statoil Report 98A06X43.

WILSON, M. E. J. & EVANS, M. J. 2002. Sedimentology and diagenesis of Tertiary carbonates on the Mangkalihat Peninsula, Borneo: implications for subsurface reservoir quality. *Marine and Petroleum Geology*, **19**, 873-900.

WITHERSPOON, P. A., WANG, J. S. Y., IWAI, K. & GALE, J. E. 1980. Validity of cubic law for fluid flow in a deformable rock fracture. *Water Resources Research*, **16**, 1016-1024.

WRIGHT, V.P. & BARNETT, A.J. 2011. Burial corrosion and porosity formation: from the seismic to micropore scale, but what processes do we blame? Carbonate Geochemistry: Reactions and Processes in Aquifers and Reservoirs. Karst Waters Institute Special Publication, **16**, 81-83.

ZAMPETTI, V., SATTLER, U. & BRAAKSMA, H. 2005. Well log and seismic character of Liuhua 11-1 Field, South China Sea; relationship between diagenesis and seismic reflections. *Sedimentary Geology*, **175**, 217-236.

ZHANG, P., PICKUP, G. E. & CHRISTIE, M. A. 2008. A New Practical Method for Upscaling in Highly Heterogeneous Reservoir Models. Society of Petroleum Engineers. doi:10.2118/103760-PA.